NASA CONTRACTOR REPORT

NASA CR-2215

NASA CR-2215

TWO-DIMENSIONAL WIND-TUNNEL TESTS OF A NASA SUPERCRITICAL AIRFOIL WITH VARIOUS HIGH-LIFT SYSTEMS

Volume II - Test Data

by E. Omar, T. Zierten, M. Hahn, E. Szpiro, and A. Mahal

Prepared by
THE BOEING COMPANY
Seattle, Wash. 98124
for Langley Research Center

NATIONAL AERONAUTICS AND SPACE ADMINISTRATION • WASHINGTON, D. C. • SEPTEMBER 1973

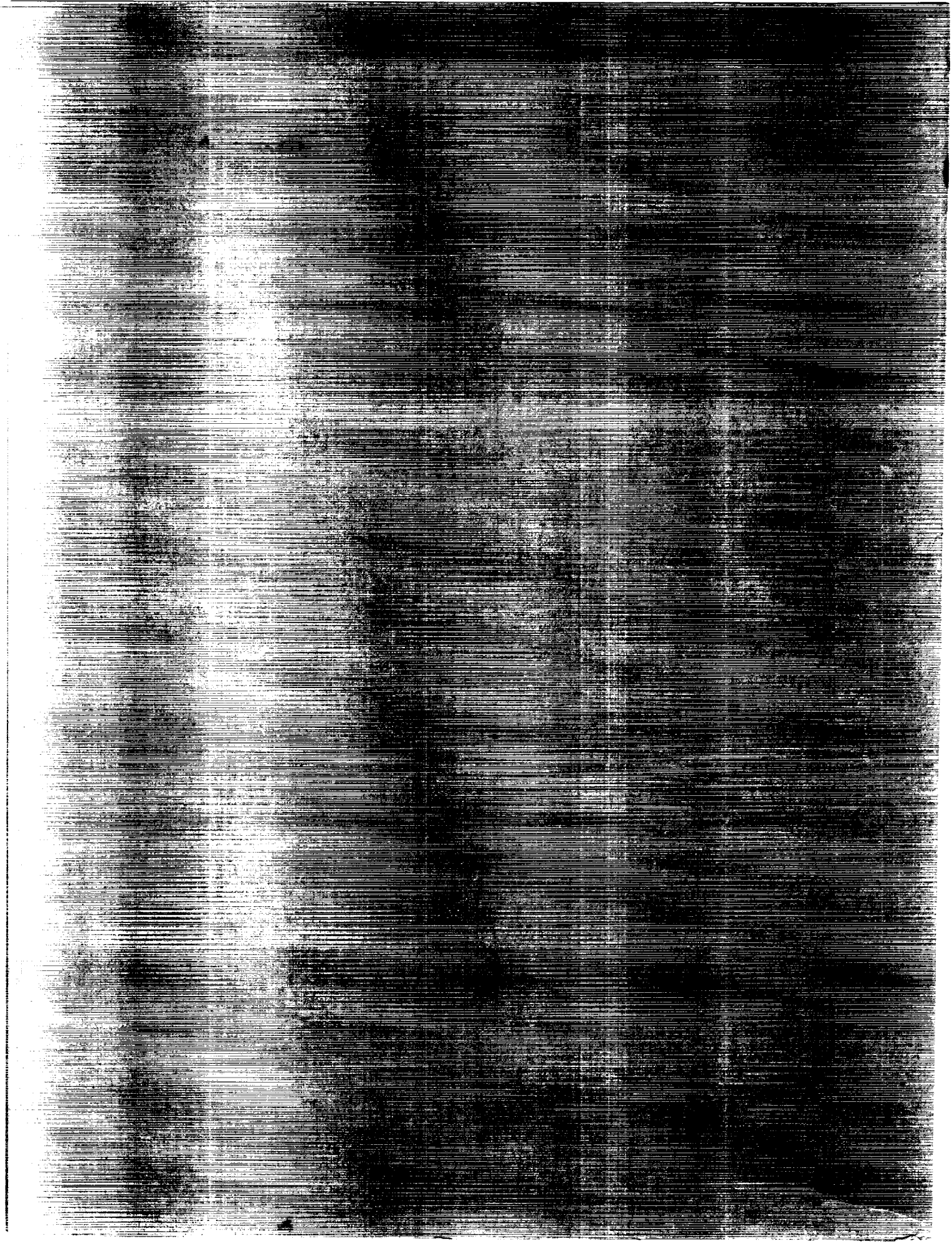

[redacted]

1. Report No.	2. Government Accession No.	3. Recipient's Catalog No.
NASA CR-2215		

4. Title and Subtitle	5. Report Date
TWO-DIMENSIONAL WIND-TUNNEL TESTS OF A NASA SUPER-CRITICAL AIRFOIL WITH VARIOUS HIGH-LIFT SYSTEMS VOLUME II- TEST DATA	September 1973
	6. Performing Organization Code
7. Author(s) E. Omar, T. Zierten, M. Hahn, E. Szpizo, and A. Mahal	8. Performing Organization Report No. D6-41063-2
	10. Work Unit No. 760-64-60-01
9. Performing Organization Name and Address The Boeing Company Commercial Airplane Group Seattle, Washington 98124	11. Contract or Grant No. NAS1-10824
	13. Type of Report and Period Covered Contractor Report
12. Sponsoring Agency Name and Address National Aeronautics and Space Administration Washington, D. C. 20546	14. Sponsoring Agency Code

15. Supplementary Notes

This is a final report.

16. Abstract

In fulfillment of NASA contract NAS1-10824, "Two-Dimensional Wind Tunnel Tests of a NASA Supercritical Airfoil With Various High-Lift Systems," three high-lift systems for a NASA 9.3-percent blunt-based, supercritical airfoil were designed, fabricated, and wind tunnel tested. In addition, a method furnished by NASA for calculating the viscous flow about two-dimensional multicomponent airfoils was evaluated by comparing its predictions with test data.

The primary objective of this program was to determine whether high-lift systems derived from supercritical airfoils would have performance comparable to high-lift systems derived from conventional airfoils. The high-lift system for the supercritical airfoil were designed to achieve maximum lift and consisted of: (1) a single-slotted flap, (2) a double-slotted flap and a leading-edge slat, and (3) a triple-slotted flap and a leading-edge slat.

This volume contains the experimental wind-tunnel data obtained for these high-lift systems. Aerodynamic force and moment data and surface pressure data are presented for all configurations and boundary-layer and wake profiles for the single-slotted flap configuration. This volume also contains discussions of the wind-tunnel models, test facilities and instrumentation, data reduction procedures, and data two dimensionality.

17. Key Words (Suggested by Author(s))	18. Distribution Statement
Supercritical airfoil High-Lift flap systems Two-Dimensional data	[redacted]ilable to U.S. Government Agencies and their contractors only

19. Security Classif. (of this report)	20. Security Classif. (of this page)	21. No. of Pages	22. Price
[redacted]	Unclassified	234	

[redacted]

CONFIDENTIAL CLASSIFIED

LaRC

SUBJECT TO GEN[redacted] CLASSIFICATION EXECUTIVE [redacted]652 AUTOMATICALLY DOWNGRADED AT TW[redacted] INTERVALS AND DECLASSIFIED ON DEC 31 1979

Unauth[redacted] ject to Criminal Sanctions

[redacted]

CONTENTS

Page

INTRODUCTION 1

SYMBOLS 2

TEST SETUP AND DATA REDUCTION 5
- Model Description 5
- Test Facilities 5
- Data Description 7
- Data Reduction 9

TWO-DIMENSIONALITY 12

APPENDIX A—Airfoil Section Characteristics 47

APPENDIX B—Wake/Boundary-Layer Measurements—Model B 97

APPENDIX C—Pressure Distributions 117

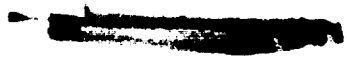

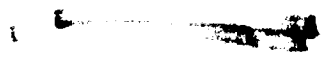

[redacted]

TWO-DIMENSIONAL WIND-TUNNEL TESTS OF A NASA SUPERCRITICAL AIRFOIL WITH VARIOUS HIGH-LIFT SYSTEMS

Volume II–Test Data

By E. Omar, T. Zierten, M. Hahn, E. Szpiro, and A. Mahal
The Boeing Company
Commercial Airplane Group

INTRODUCTION

This document is the second volume of a two-volume technical report on NASA contract NAS1-10824, "Two-Dimensional Wind Tunnel Tests of the NASA Supercritical Airfoil With Various High-Lift Systems," awarded to The Boeing Company in May 1971. While this volume is complete in itself as a data report, it is also intended to complement volume I, which presents the evaluation and analysis portion of the contract study.

The data presented in this volume include:

- Aerodynamic data in the form of C_ℓ versus α, C_d, and $C_{m_{0.25c}}$
- Surface pressures in the form of C_p versus x/c
- Boundary-layer and wake profiles of a single-slotted flap configuration
- Tables of the locations of boundary-layer transition and separation obtained through flow visualization

This volume also includes discussions of:

- Wind tunnel models
- Test facilities and instrumentation
- Data reduction procedures
- Data two-dimensionality

[redacted]

SYMBOLS

All geometric airfoil parameters defined below are illustrated in figure 1.

AR	wing aspect ratio
c	airfoil reference chord length, meters
c'	camber-line length of a deployed high-lift system measured from the wing leading edge (0,0) to the trailing edge of the last flap component, meters
c'_f	camber-line length of a deployed trailing-edge flap, meters
c_f	chord length of a retracted flap, meters
$c_{\ell e}$	chord length of a deployed leading-edge device, meters
C_d	section drag coefficient, $C_d = D/q_\infty S$
C_{D_i}	wing induced-drag coefficient
ΔC_{d_B}	increment in drag due to buoyancy force
C_ℓ	section lift coefficient, $C_\ell = L/q_\infty S$
$C_{\ell_{max}}$	maximum lift coefficient an airfoil configuration generates as angle of attack is varied
C_L	wing lift coefficient
$C_{m_{0.25c}}$	section pitching moment coefficient about a moment center located at (0.25c, 0), $C_{m_{0.25c}} = m/q_\infty Sc$
C_p	pressure coefficient, $(P_L - P_\infty)/q_\infty$
D	drag, newtons
G	slot gap size, meters
h	wind tunnel test section height, meters
H	boundary-layer shape factor, $H = \delta^*/\theta$
L	lift, newtons

[redacted]

m	pitching moment, newton-meters
M_∞	freestream Mach number
P_L, P_S	local static pressure, newtons per square meter
P_T	local total pressure, newtons per square meter
P_{T_e}	total pressure at the outer edge of wake or boundary layer, newtons per square meter
P_∞	freestream static pressure, newtons per square meter
q_∞	freestream dynamic pressure, $q_\infty = \rho_\infty U_\infty^2/2$, newtons per square meter
Re	Reynolds number based on airfoil reference chord length
S	arc length, meters
t	airfoil maximum thickness, meters
U	local velocity (see eq. (1) and fig. B2), meters per second
U_∞	freestream velocity, meters per second
U_P	local potential velocity (see eq. (2) and fig. B2), meters per second
U_e	velocity at the outer edge of the wake or boundary layer (see fig. B2), meters per second
x, y	horizontal and vertical cartesian coordinates, meters
x_o, y_o	location of the leading-edge point of a high-lift component in a deployed position, meters
Δx	airfoil component overlap measured parallel to the chord line of the most forward of two overlapping components, meters
Y_t	elevation (measured from the wing chord line) of the trailing edge of a leading-edge device, meters

[redacted]

[redacted]

α	airfoil angle of attack, degrees
α_i	wing induced angle of attack, degrees
δ	boundary-layer thickness, meters
δ_f	trailing-edge flap deflection measured from the wing chord line to the flap component chord line, degrees
$\delta_{f_{eq}}$	equivalent plain flap deflection angle; the deflection of a plain flap having the same chord and producing the same potential flow lift as a deployed slotted trailing-edge flap, degrees
$\delta_{\ell e}$	deflection of a leading-edge device measured from the wing chord line to the device chord line, degrees
δ^*	boundary-layer displacement thickness, meters
θ	boundary-layer momentum thickness, meters
ρ	local fluid density, kilograms per cubic meter
ρ_∞	freestream density, kilograms per cubic meter

[redacted]

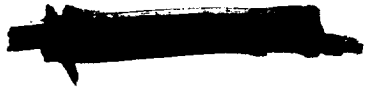

TEST SETUP AND DATA REDUCTION

MODEL DESCRIPTION

The wind tunnel model was machined of 4340 steel, heat treated to 112.5 kN/m^2 (160,000 psi) for the basic section and SAE 06 tool steel, heat treated to 105.5 kN/m^2 (150,000 psi) for the high-lift devices to achieve the strength necessary for proposed future high Reynolds number testing. The 0.6096-m (24-in.) chord by 0.9144-m (36-in.) span basic model (fig. 2) was built with detachable leading and trailing edges to allow incorporation of combinations of high-lift devices. The contours of the model components were maintained at tolerance levels of ±0.025 mm (±0.001 in.) near the leading edge and ±0.076 mm (±0.003 in.) elsewhere on the model. An 8.13 micron (32 μin.) finish was maintained on the surface of the model parts. The ordinates of the model components are presented in tables 1 through 6.

The high-lift devices, when tested, were mounted in the tunnel by attaching them to the turntables using steel end plates (fig. 3) so the flow over the model would be affected as little as possible by the attachment system. The leading-edge slats and the vane of the trailing-edge flaps were equipped with brackets at 33% and 67% span, in addition to the end plates, to restrict the deflections at midspan due to aerodynamic loads. The brackets (fig. 4) were constructed such that they were kept as far as possible from the slot entrances to minimize their effects on slot flow.

All of the model components contain a chordwise array of surface static pressure orifices along the centerline of the model. In addition, models A, B, and C (with the exception of the vane), contain chordwise arrays of surface static pressure orifices located 50.8 and 101.6 mm (2 and 4 in.) from the tunnel wall to verify two-dimensionality. All three models also contained spanwise arrays of surface static pressure orifices. The locations of the orifices in all of the model components are listed in table 7.

TEST FACILITIES

Wind Tunnel

The tests were conducted in the Boeing research wind tunnel (BRWT) at Seattle. The BRWT is a single-return closed-circuit tunnel designed and built as a two-dimensional high-lift test facility. The test section of BRWT is 0.9144 m (36 in.) wide by 2.4384 m (96 in.) high and has a length of 6.0961 m (20 ft). The contraction ratio of the tunnel bellmouth is 12.1 to 1. The wind tunnel is vented to atmospheric pressure immediately aft of the test section. The freestream turbulence level in the test section is 0.07. The general arrangement of the wind tunnel is shown in figure 5.

The model, which spanned the width of the test section, was rigidly mounted on two 0.9144-m (36-in.) diameter turntables that were completely flush with the sidewalls. The entire assembly of the model and turntables was rotated (pitched) about the axis of the turntables, which is coincident with the balance center, to vary the angle of attack of the model.

Two-stage wall boundary-layer control (BLC) was applied by means of tangential blowing upstream of the model and at critical locations on the turntables to ensure two-dimensional flow over the model. A layout of the model/turntable/BLC system is shown on figure 6.

Instrumentation

The two primary instrumentation modes used during the test were the balance and the pressure measurement system.

Located below the test section is a six-component external strain-gage balance that was used for measuring the forces and moments on the model. The model and turntable assembly were attached to the balance box beam by means of a box-beam stanchion arrangement on both sides of the test section (fig. 7). The balance was used to measure the aerodynamic lift, drag, and pitching moment acting on the model. Since the balance drag measurements include the skin friction drag of the turntables, their measurements are only used for backup. Accurate drag measurements were made with an integrating wake rake.

The pressure measurement systems used during the test consisted of the integrating wake rake and the surface static pressure orifices.

The integrating wake rake (fig. 6) consists of a vertical row of small-diameter total-pressure tubes having high line loss and vented to a common plenum. The difference between the pressure in the common plenum and freestream total pressure has been calibrated against drag values calculated on the basis of static and total-pressure surveys through the wake. Hence, measurements of this pressure difference readily yield an accurate measurement of profile drag. The wake rake was located 2.5 model chords aft of the model leading edge and was remotely positioned vertically such that the rake was centered on the wake. The rake was also traversed spanwise such that the drag could be averaged across the span.

Transducers coupled with scanivalves were used for the measurement of the surface static pressures on the model components. The tunnel test section total and static pressures were measured using permanently installed transducers that were calibrated frequently during the test.

Measurement of the geometric angle of the model was achieved by use of a potentiometer. The tunnel total temperature was measured by means of a chromel-alumel thermocouple.

The measurements of the boundary layer and wake discussed under "Data Reduction" and presented in appendix A were made using pitot and static pressure probes and a hot-wire anemometer A flattened pitot probe was used for the boundary-layer survey, and a round-tip pitot tube of 1.02 mn (0.04 in.) outside diameter and 0.76 mm (0.03 in.) inside diameter was used for the wake survey (fig. 8). These two probes were stacked in a rake fashion and mounted on a traversing drive mechanism. The distance between the two probe tips was varied from 11.4 mm to 19.1 mm (0.45 in. to 0.75 in.). The static probe was used to measure the static pressure in both the boundary layer and the wake (fig. 8). The probe has four static-pressure holes of 0.05 mm (0.002 in.) diameter at 90° intervals around a 1.0 mm (0.04 in.) outside diameter tube. The holes were located 10 diameters downstream of the hemispherical tip of the probe.

A constant-temperature hot-wire anemometer was used to measure velocities where flow angularity might prevent accurate measurement with the pitot and static probes, as at the slot gap and minimum C_p region on the flap.

The accuracy of the instrumentation is discussed under "Data Reduction."

DATA DESCRIPTION

Force and Moment Data

The airfoil section aerodynamic data presented in this volume consists of the section lift, drag, and pitching moment data for each of the models tested (app. A); the boundary-layer and wake data obtained on model B (app. B); and the surface pressure distribution on the airfoil section components of each model (app. C). The data logs, tables 8 through 11, contain details of the configurations for which the data are presented.

The section lift and pitching moment coefficients presented in the figures of appendix A are the corrected balance data. The corrections applied to these data are discussed under "Data Reduction." The section drag coefficients presented are the data obtained using the integrating wake rake.

The force and moment data for the basic airfoil section (model A) are presented in figures A1, A2, and A3. Figures A4 through A6 present the force and moment data obtained on the single-slotted flap configuration (model B). The double-slotted flap configuration with slat 1 (model C) data are presented in figures A7 through A16. The force and moment data for the triple-slotted trailing-edge flap configuration with slat 2 (model D) or with slat 1 are presented in figures A17 through A26.

The relationships of the force and moment figures to the various studies in the wind tunnel test are presented in table A1. The boundary-layer transition locations determined by the sublimation technique using a kerosene-kaolin mixture on the various model configurations are presented in table A2.

Boundary-Layer Data

The boundary-layer and wake data obtained on the single-slotted flap configuration (model B) are presented in figures B1 through B16. The significant test parameters are presented in table B1.

The location of the wake/boundary-layer survey stations and a schematic of the various wake/boundary-layer components are presented in figures B1 and B2, respectively. The local "potential velocity" distribution obtained from the measured local static pressure and the wake/boundary-layer edge total pressure at the survey locations are presented in figures B3, B4, and B5. The variation of the potential velocity along the upper surface of the flap is presented in figure B6. The wake/boundary-layer velocity profiles, nondimensionalized with the local potential velocity, are presented in figures B7, B8, and B9. The velocities measured with the hot-wire anemometer and pitot and static probes at the three survey stations where the static pressure variation is significant are presented in figures B10, B11, and B12.

The variations of displacement thickness, momentum thickness, and shape factor of the boundary layer along the upper surface of the flap and the wake over the flap are presented in figures B13, B14, and B15. The variations of the boundary-layer displacement thickness and momentum thickness in the cove of the wing are presented in figure B16.

Surface Pressure Data

The pressure distributions on the airfoil components are presented in figures C1 through C29. The data consist of the corrected surface static pressure data obtained on the four models tested. The manner in which these data were corrected is discussed in the next section.

The pressure data for the basic airfoil (model A) are presented in figures C1 through C4. Figures C5, C6, and C7 present the pressure data for the single-slotted flap configuration (model B). The double-slotted flap configuration with slat 1 (model C) data are presented in figures C8 through C18. The pressure data for the triple-slotted flap configuration with slat 2 (model D) or with slat 1 are presented in figures C19 through C29.

The relationships of the pressure figures to the various studies in the wind tunnel test are presented in table C1.

DATA REDUCTION

Corrections to Force, Moment, and Pressure Data

The acquired data, discussed in the previous section, were corrected for wind tunnel boundary effects and test apparatus characteristics. These corrections have been verified, where applicable, by an accurate potential-flow analysis and are considered applicable to the high-lift configurations investigated in this test.

The wind tunnel boundary corrections that have been applied include:

- Corrections to the freestream dynamic pressure due to solid and wake blockage
- Lift, pitching moment, and angle-of-attack corrections due to the effects of floor and ceiling constraints on streamline curvature
- Compressibility effects for freestream dynamic pressure

Other corrections that have been applied are:

- Balance interactions obtained by experimental calibrations
- Lift and pitching-moment corrections due to the reactions of turntable blowing boundary-layer control obtained experimentally at wind-off conditions
- Wall boundary-layer control effects on the tunnel freestream dynamic and static pressures, which were also obtained experimentally

The corrections that were considered but not applied are:

- The buoyancy force, which for this test has a negligible effect on the freestream dynamic pressure and the drag ($\Delta C_{d_B} = 0.0002$)
- The boundary effects on the model pressure distribution, which is negligible if the chord of the model is less than 0.7 tunnel height as was the case for this test (chord/height = 0.25)
- The induced angle of attack caused by the trailing vortices that are shed in the wall boundary layer

Wake/Boundary-Layer Data Reduction

Due to the nature of the flow field in the immediate region of the flap, where the wake and boundary-layer measurements were taken, special consideration had to be given in the reduction of the data. The static pressure variation at a given survey station was obtained with the static probe while making a special effort to align the axis of the probe with the estimated local streamline. The measured local static and pitot pressures were then used to calculate the local velocity in the boundary layer and wake using the equation:

$$U = \sqrt{\frac{2\,(P_T - P_S)}{\rho}} \qquad (1)$$

A local equivalent potential velocity was determined using the measured local static pressure and a constant total pressure measured at the outside edge of wake and boundary layer at each survey station such that:

$$U_p = \sqrt{\frac{2\,(P_{T_\infty} - P_S)}{\rho}} \qquad (2)$$

This velocity term was used to determine the wake/boundary-layer parameters as described below. The relationships of these velocities are illustrated in figure A2.

In the present case, where there are large static-pressure variations in the transverse direction, the ordinary definition of boundary-layer displacement and momentum thickness cannot be applied. For this reason, the displacement thickness and momentum thickness were defined as follows:

$$\text{Displacement thickness} = \frac{1}{(\overline{\rho U})_p} \int_0^\delta [(\rho U)_p - \rho U]\, dy$$

$$\text{Momentum thickness} = \frac{1}{(\overline{\rho U^2})_p} \int_0^\delta \rho U\, [U_p - U]\, dy$$

where subscript p indicates equivalent potential values.

The shape factor, H, was defined in the usual manner:

$$H = \delta^*/\theta$$

[redacted]

Data Accuracy

The accuracy of the final corrected data is listed below. The probable errors are those that exit at or near the severest conditions.

	Parameter	Accuracy
Forces and moments	C_ℓ	±0.01
	C_d	±0.001
	$C_{m_{0.25}}$	±0.005
Pressures	C_P	±0.01
	q	±2.45 N/m^2 (±0.05 psf)
Boundary-layer data	U	±2.0 m/sec (±6.56 fps)
Geometry	α	±0.1°
	x_o, y_o, Δx, G	±0.0001c
	δ_f, $\delta_{\ell e}$	±0.05°

[redacted]

TWO-DIMENSIONALITY

The degree of two-dimensionality is of particular importance when obtaining data to be used as a standard for developing and evaluating two-dimensional theoretical methods. Phenomena that affect two-dimensionality include:

- Flow separation in the juncture of the model and test section wall
- Shedding of vorticity in the wall boundary layer
- Nonuniformity of the locations of boundary-layer transition and separation
- Longitudinal vortices in the model boundary layer

The effects of the first two phenomena are demonstrated in figure 9. In one case, the wall boundary layer is allowed to separate due to the influences of the model pressure field. In the other case, the wall boundary layer is reenergized by tangential injection of high-energy air from discrete slots located in the wind tunnel walls forward and along the model juncture. With wall boundary-layer control applied, the full-span lift measured by the strain-gage balance and the center-span lift calculated from center-span pressure distributions compare well. In the BLC-off case, the juncture lift loss due to wall boundary-layer separation is represented by the difference in center-span and full-span lift. In addition, there is an appreciable difference in center-span lift between the BLC-on and BLC-off cases. This difference is due to an induced down wash created by juncture vortices emanating from the separated juncture region.

The effects of BLC on spanwise surface pressures are presented in figure 10. The juncture lift loss is evident at survey stations 2, 3, and 4 where the BLC-off pressures tend to become more positive as the wind tunnel walls are approached. The significant difference in pressure levels at stations 1, 2, and 3 reflects the effects of the induced down wash.

Since drag measurements have been made by strain-gage balance and by wake-drag surveys, the downwash effect can readily be verified. For the BRWT test setup, the strain-gage drag measurements include profile drag, induced drag, and turntable skin friction drag. The turntable drag has been determined to be on the order of 0.01. Subtracting this and the wake drag measurements from the strain-gage drag leaves only the induced drag. From induced-drag and lift measurements, the effective aspect ratio and the center-span induced angle of attack have been determined from the relationship $C_{D_i} = \alpha_i C_L = C_L^2/2\pi$ AR for wings with uniform lift distribution for the configuration presented in figure 9. Typical aspect ratios of 56 and 9, and induced down-wash angles of 0.6 and 3.4 were calculated for BLC on and off, respectively. As shown in figure 11, the center-span lift curves compare

considerably better when the induced angle-of-attack correction has been made. Insufficient drag data are available at high angles of attack to properly determine the induced down wash; hence, the discrepancy in center-span lift near stall is still large.

The effect of juncture vortices on drag is also demonstrated in figure 9. As the juncture vortices progress downstream, they draw in low-energy air from the wake; hence, wake drag measurements with BLC off are extremely low, compared with the BLC-on drag measurements.

The BLC requirements for two-dimensional flow have been found to be dependent upon model configuration. Each model (A, B, C, and D) was investigated to ensure two-dimensionality before any data were recorded. Center-span and full-span lift measurements for representative configurations of models A, B, and C are presented in figures 12 through 14. With the exception of model A, the two lift measurements compare well.

The boundary-layer characteristics of each model were observed by use of china clay. In all cases, the location of transition was found to be uniform across the span. Local premature transition does occur in narrow regions following flap support brackets and in the vicinity of the wall BLC jets. Flow visualizations of the leading- and trailing-edge high-lift components of configuration D at $C_{\ell_{max}}$ are presented in figures 15 through 17. Figure 15 shows the transition locations on the leading-edge slat and the main airfoil components. The main airfoil transition occurs at its leading edge. The two discontinuities in the flow pattern occurring at x/c = 0.2 and x/c = 0.65 are seams at which the three main airfoil segments that are joined together. The fluid that seeps into these seams does not readily evaporate and gives the appearance of a transition line. A closeup of the leading edge is presented in figure 16. The details of the transition zone are clearly visible as are the effects of the slat 2 support brackets and the wall BLC jet. The transition locations on the trailing-edge flaps are shown in figure 17. As in the case of the leading edge, the transition is uniform across the span of each flap component with the exception of the local premature turbulence resulting from flap support brackets and wall BLC jets.

The effects of longitudinal vortices introduced by flap support brackets on wake drag measurements was investigated. It was found that only the leading-edge support brackets produce significant vortices. Spanwise surveys of wake drag are presented in figure 18 for several angles of attack for configuration D, with and without leading-edge support brackets. In both cases, the trailing-edge support brackets are in position. At all angles of attack except -4 , the effects of the leading-edge brackets appear very prominent. The effect on the averaged drag, however, is negligible, as shown in figure 19. At angles of attack above 8 , the longitudinal vortices have a slightly favorable effect on drag while below 8 the effect is adverse. They have no appreciable effect on lift and pitching moments.

TABLE 1.–MODEL COMPONENT COORDINATES–BASIC AIRFOIL

N_1WT		
	Y	
X	Upper	Lower
0.0	0.0	–
0.035	0.350	-0.350
0.15	0.750	-0.750
0.40	1.185	-1.185
0.70	1.50	-1.50
1.25	1.87	-1.87
2.00	2.22	-2.22
3.25	2.63	-2.63
5.00	3.04	-3.04
7.50	3.46	-3.46
11.00	3.86	-3.86
11.667	–	-3.91
15.0	4.16	-4.16
20.0	4.41	-4.41
25.0	4.56	-4.56
30.0	4.63	-4.63
35.0	4.65	-4.65
40.0	4.62	-4.62
45.0	4.56	-4.55
50.0	4.44	-4.43
55.0	4.29	-4.23
60.0	4.09	-3.89
65.0	3.84	-3.31
70.0	3.53	-2.43
75.0	3.17	-1.63
80.0	2.74	-0.99
85.0	2.22	-0.52
90.0	1.61	-0.28
94.0	1.02	-0.32
97.0	0.53	-0.58
98.5	0.26	-0.765
99.5	0.07	-0.91
100.0	-0.02	-1.00

X and Y in percent of wing chord

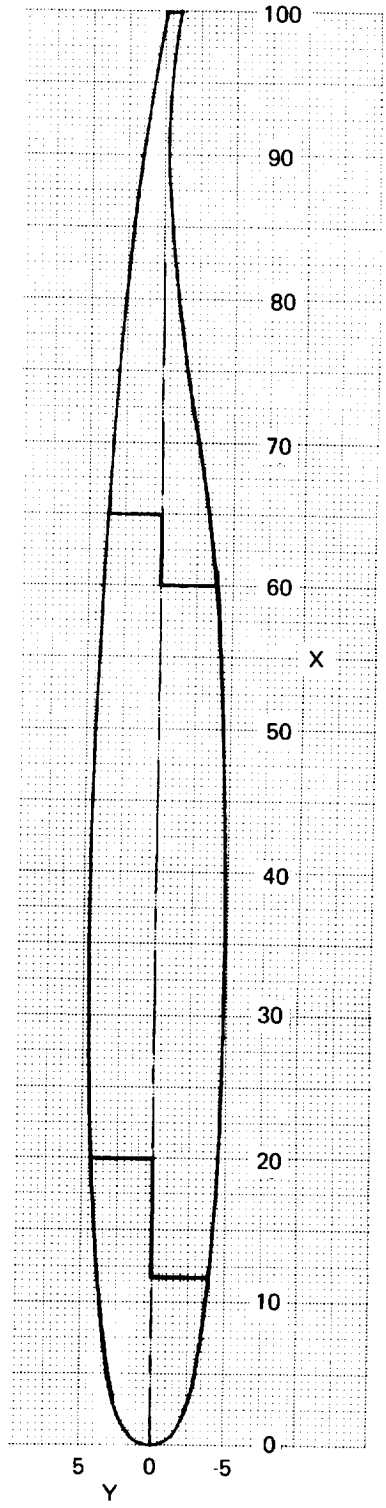

TABLE 2.–MODEL COMPONENT COORDINATES–N_2 AND C_1

N_2			
Upper		Lower	
X	Y	X	Y
3.52	-2.030	–	–
3.61	-1.621	3.54	-2.336
3.83	-1.060	3.70	-2.642
4.25	-0.412	4.0	-2.831
5.0	0.384	4.5	-2.941
5.9	1.113	5.5	-3.141
7.1	1.868	7.5	-3.460
8.5	2.511	11.0	-3.860
9.8	2.991	11.667	-3.910
11.2	3.394	–	–
12.5	3.705	–	–
14.0	3.960	–	–
15.0	4.083	–	–
16.0	4.190	–	–
17.5	4.300	–	–
20.0	4.410	–	–

C_1			
Upper		Lower	
X	Y	X	Y
–	–	60.0	-3.89
65.0	3.840	65.0	-3.31
67.5	3.690	67.5	-2.87
70.5	3.520	67.5	-2.60
73.0	3.325	67.5	-2.00
75.5	3.125	67.85	-1.00
77.5	2.960	69.0	0.23
79.0	2.813	70.7	1.20
80.25	2.705	73.0	1.95
81.3	2.605	75.5	2.35
82.1	2.530	77.5	2.49
82.5	2.490	79.0	2.52
–	–	80.25	2.52
–	–	81.3	2.50
–	–	82.1	2.45
–	–	82.5	2.41

X and Y in percent of wing chord

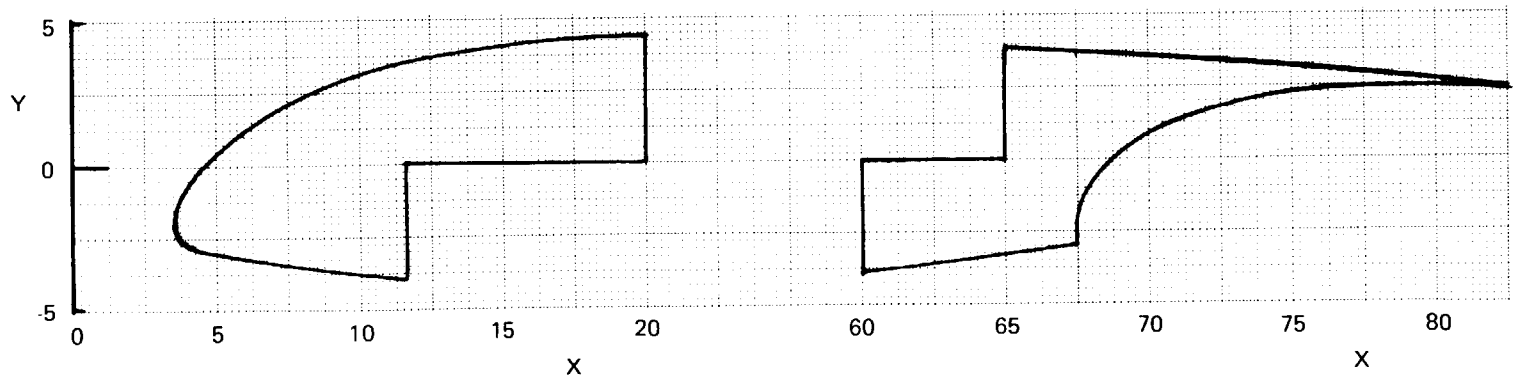

TABLE 3.–MODEL COMPONENT COORDINATES–C_2 AND C_3

C_2			
Upper		Lower	
X	Y	X	Y
–	–	60.0	–3.89
65.0	3.840	62.5	–3.64
67.5	3.690	64.0	–3.40
70.5	3.520	65.0	–3.20
73.0	3.325	66.5	–2.80
75.5	3.125	67.5	–2.55
77.5	2.960	68.5	–2.20
79.0	2.813	69.5	–1.84
80.25	2.705	70.5	–1.52
81.3	2.605	71.5	–1.11
82.1	2.530	72.5	–0.70
82.5	2.490	74.0	–0.01
–	–	75.5	0.588
–	–	77.0	1.08
–	–	78.5	1.62
–	–	80.0	2.00
–	–	81.5	2.30
–	–	82.5	2.40

C_3			
Upper		Lower	
X	Y	X	Y
–	–	60.0	–3.89
65.0	3.840	62.5	–3.64
67.5	3.690	64.0	–3.40
70.5	3.520	65.0	–3.20
73.0	3.325	66.5	–2.80
75.5	3.125	67.5	–2.55
77.5	2.960	67.5	–2.00
79.0	2.813	67.85	–1.00
80.25	2.705	69.0	0.23
81.3	2.605	70.7	1.20
82.1	2.530	73.0	1.95
82.5	2.490	75.5	2.35
–	–	77.5	2.49
–	–	79.0	2.52
–	–	80.25	2.52
–	–	81.3	2.50
–	–	82.1	2.45
–	–	82.5	2.41

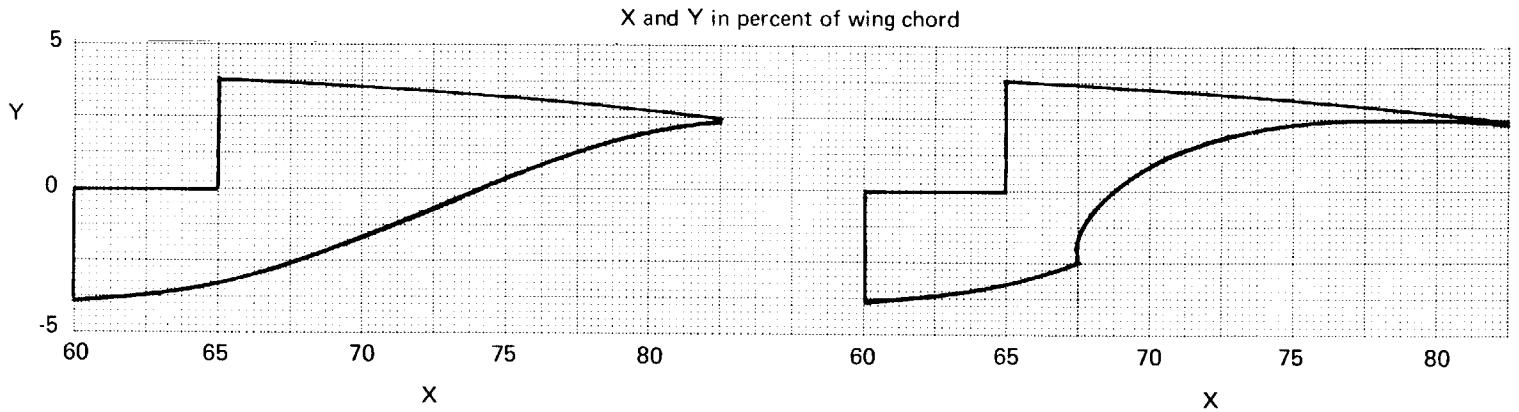

TABLE 4.–MODEL COMPONENT COORDINATES–L_1 AND L_2

L_1			
Upper		Lower	
X	Y	X	Y
0.0	0.200	–	–
0.082	0.580	0.037	−0.120
0.263	0.940	0.163	−0.372
0.563	1.321	0.323	−0.505
0.983	1.684	0.552	−0.564
1.593	2.032	0.983	−0.510
2.398	2.307	3.063	−0.350
3.400	2.451	5.143	−0.200
4.400	2.426	7.183	0.042
5.598	2.297	9.313	0.104
7.095	2.123	11.396	0.250
8.587	1.920	13.480	0.400
10.587	1.588	13.996	0.408
12.581	1.157	14.313	0.333
14.074	0.703	14.733	0.250
15.067	0.288	15.063	0.123
15.563	0.0	15.563	−0.080

L_2			
Upper		Lower	
X	Y	X	Y
0.0	0.001	–	–
0.017	0.417	0.101	−0.490
0.093	0.760	0.287	−0.884
0.237	1.082	0.791	−1.440
0.471	1.425	1.641	−1.800
0.845	1.760	2.441	−1.750
1.229	1.965	3.891	−1.130
1.867	2.143	5.141	−0.375
2.689	2.240	5.819	−0.080
4.005	2.237	7.880	0.418
5.491	2.114	9.827	0.574
7.057	1.912	11.605	0.534
8.699	1.622	12.933	0.411
10.180	1.322	14.141	0.205
11.651	0.993	15.141	0.015
12.923	0.699	15.641	−0.080
14.189	0.386	–	–
15.157	0.129	–	–
15.641	0.0	–	–

X and Y in percent of wing chord

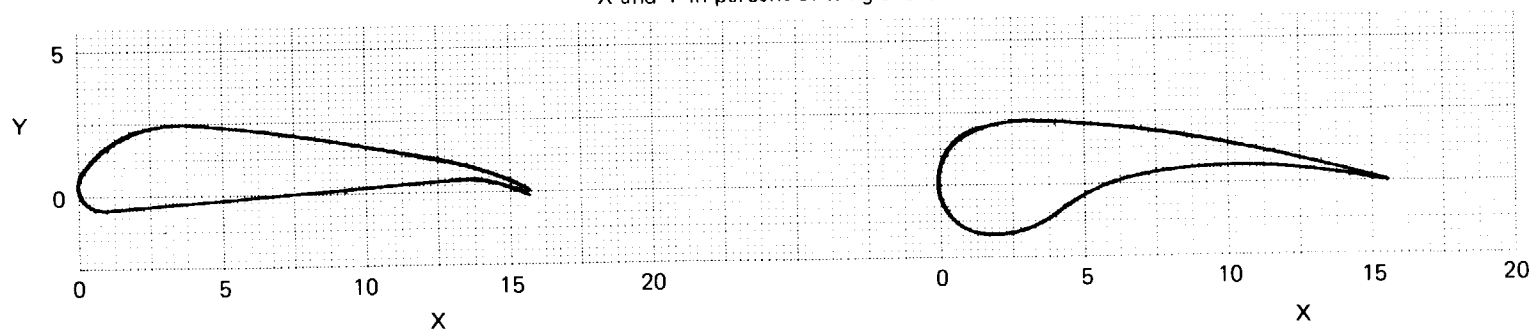

TABLE 5.–MODEL COMPONENT COORDINATES–$F_{2.1}$ AND $F_{2.2}$

$F_{2.1}$			
Upper		Lower	
0.0	−0.062	–	–
0.017	0.144	0.060	−0.261
0.080	0.333	0.256	−0.410
0.233	0.599	0.645	−0.505
0.558	0.973	1.271	−0.488
1.226	1.495	2.188	−0.268
1.854	1.823	3.597	0.314
3.352	2.256	5.226	0.927
4.981	2.396	6.969	1.186
7.049	2.272	8.898	1.182
9.039	1.916	10.827	0.957
10.986	1.400	12.799	0.548
12.836	0.800	13.865	0.265
13.936	0.420	14.533	0.056
14.576	0.184	14.923	−0.038
14.949	0.038	–	–

$F_{2.2}$			
Upper		Lower	
0.0	−0.027	–	–
0.011	0.193	0.059	−0.210
0.093	0.439	0.186	−0.327
0.275	0.732	0.404	−0.377
0.593	1.080	0.787	−0.330
1.052	1.447	1.592	−0.230
2.100	2.062	3.001	−0.079
3.643	2.703	5.518	0.189
5.672	3.240	9.537	0.488
7.687	3.552	13.551	0.682
9.695	3.714	17.559	0.736
11.698	3.741	21.557	0.611
13.693	3.578	24.549	0.364
15.681	3.291	26.538	0.097
18.164	2.869	28.027	−0.166
21.636	2.214	29.018	−0.385
24.610	1.618	29.513	−0.499
26.591	1.180	–	–
28.076	0.842	–	–
29.066	0.604	–	–
29.560	0.479	–	–

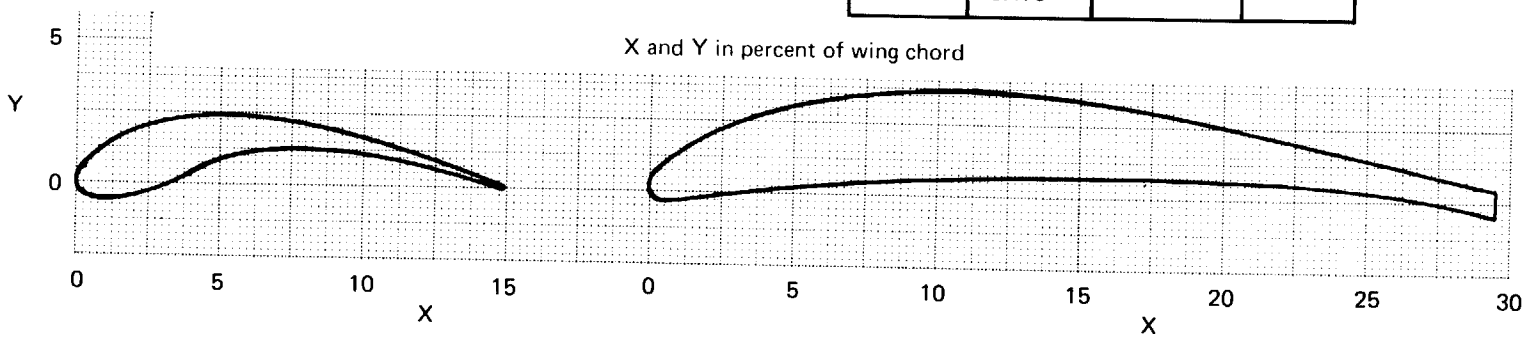

TABLE 6.–MODEL COMPONENT COORDINATES–$F_{3.2}$ AND $F_{3.3}$

$F_{3.2}$			
Upper		Lower	
X	Y	X	Y
0.0	0.046	–	–
0.028	0.265	0.043	-0.140
0.130	0.505	0.160	-0.267
0.335	0.783	0.373	-0.335
0.683	1.100	0.760	-0.320
1.172	1.428	1.570	-0.285
2.269	1.958	2.987	-0.248
3.860	2.472	5.516	-0.186
5.925	2.843	9.547	-0.214
7.955	2.990	13.563	-0.346
9.965	2.989	16.064	-0.501
11.965	2.854	17.262	-0.597
13.939	2.530	17.562	-0.616
15.898	2.082	17.588	-0.418
18.338	1.461	17.720	-0.183
20.774	0.809	18.162	0.112
22.233	0.397	19.205	0.379
23.012	0.184	20.722	0.413
23.497	0.040	22.209	0.218
–	–	22.995	0.055
–	–	23.487	-0.040

$F_{3.3}$			
Upper		Lower	
X	Y	X	Y
0.0	-0.069	–	–
0.020	0.082	0.049	-0.192
0.090	0.215	0.192	-0.250
0.312	0.442	0.491	-0.226
0.758	0.711	0.990	-0.184
1.449	0.981	1.789	-0.146
2.293	1.182	2.988	-0.094
3.439	1.302	4.987	-0.034
4.941	1.295	6.989	-0.055
6.946	1.170	8.994	-0.155
8.956	0.930	10.499	-0.292
10.464	0.717	11.505	-0.427
11.470	0.562	12.007	-0.500
11.973	0.480	–	–

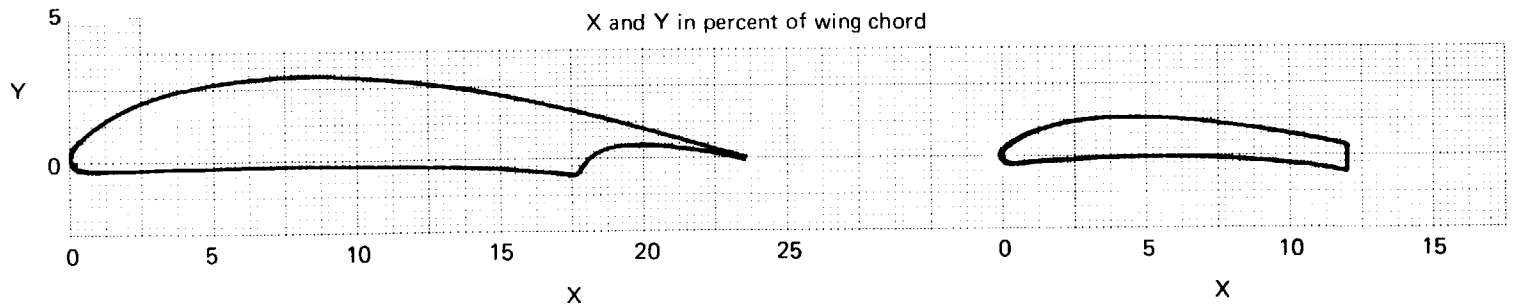

[redacted]

TABLE 7.–MODEL PRESSURE ORIFICE LOCATIONS

N_1WT	
X, percent of wing chord	
Upper	Lower
0.0	–
0.035	–
0.15	0.15
0.40	–
0.70	0.70
1.25	–
2.00	2.00
5.00	5.00
10.0	–
20.208	20.0
30.0	30.0
40.0	40.0
50.0	50.0
60.0	59.792
70.0	70.0
80.0	80.0
90.0	90.0
95.0	95.0
98.5	98.5
100.0	100.0

N_2	
X, percent of wing chord	
Upper	Lower
3.52	–
3.83	4.0
5.0	5.0
7.1	–
10.0	10.0
12.5	–
15.0	–

C_1 and C_3	
X, percent of wing chord	
Upper	Lower
–	65.0
–	67.375
–	67.5
70.0	69.0
75.0	75.5
80.0	80.25
81.3	–
82.1	82.1

C_2	
X, percent of wing chord	
Upper	Lower
–	65.0
–	67.375
–	68.958
70.0	70.542
–	72.083
–	73.417
75.0	74.833
–	76.167
–	77.750
80.0	79.167
81.3	–
82.1	82.1

[redacted]

[redacted]

TABLE 7.–Concluded

L_1
X, percent of wing chord
Upper
0.49
1.35
2.60
5.18
10.10
13.72
15.14

L_2	
X, percent of wing chord	
Upper	Lower
0.093	0.101
0.471	–
0.845	–
1.229	1.641
2.689	–
5.491	5.819
8.699	–
11.651	12.933
14.189	–
15.157	15.141

$F_{2.1}$	
X, percent of wing chord	
Upper	Lower
0.080	–
0.233	0.256
0.558	–
1.226	–
1.854	2.188
3.352	–
4.981	–
7.049	6.969
9.039	–
10.986	–
12.836	12.799
14.576	14.533

$F_{2.2}$	
X, percent of wing chord	
Upper	Lower
0.0	–
0.093	–
0.593	0.404
2.100	–
3.643	–
5.672	5.518
7.687	–
11.698	–
15.681	17.559
21.636	–
26.591	26.538
29.560	29.513

$F_{3.2}$
X, percent of wing chord
Upper
0.10
1.40
4.37
10.10
16.87
22.70

$F_{3.3}$
X, percent of wing chord
Upper
0.18
1.36
3.03
6.31
9.36
11.73

[redacted]

TABLE 8.–DATA LOG–MODEL A

Force figure number	Pressure figure number	Configuration	Symbol	M_∞	Re x 10^{-6}
A1a	C1a	N_1WT	⊙	0.284	4.02
↓	1b	↓	△	0.259	3.66
↓	1c	↓	⊡	0.201	2.83
A1b	C1c	N_1WT	⊡	0.201	2.83
↓	1d	↓	△	0.142	2.01
↓	1e	↓	⊙	0.080	1.10
A2	C1c	N_1WT	⊡	0.201	2.83
A2	C2	↓	△[a]	0.201	2.83
A3	C4	L_1N_1WT	⊙[b]	0.201	2.83

[a] $(x/c)_{trip_U}$ and $(x/c)_{trip_L}$ = 0.1.

[b] δ_{le} = 43.9 ; $x_{o_{le}}/c$ =–0.1242; $y_{o_{le}}/c$ =–0.0749.

TABLE 9.–DATA–MODEL B

M_∞ = 0.201; Re = 2.83 x 10^6

Force figure number	Pressure figure number	Configuration	Symbol	$\delta_{f_{eq}}$, deg	$\delta_{f_{eq}}$, deg	x_{o_1}/c	y_{o_1}/c
A4a	C5a	$N_1WC_1F_1$	⊙	20	20.0	0.8240	–0.0073
↓	b	↓	⊡	↓	19.9	0.7983	–0.0136
↓	c	↓	△	↓	20.0	0.8398	+0.0306
A4b	C5d	$N_1WC_1F_1$	⊙	20	20.0	0.8241	–0.0228
↓	e	↓	⊡	↓	↓	0.7989	–0.0274
↓	f	↓	△	↓	↓	0.8235	+0.0096
A4c	C5g	$N_1WC_1F_1$	⊙	20	20.0	0.8299	+0.0136
↓	h	↓	⊡	↓	↓	0.7990	+0.0016
↓	i	↓	△	↓	↓	0.8242	–0.0024
A5	C6a	$N_1WC_1F_1$	⊙	38	40.0	0.8150	+0.0123
↓	b	↓	⊡	29	30.0	0.8205	+0.0095
↓	c	↓	△	47	50.0	0.8160	+0.0143
A6	C7	$N_1WC_2F_1$	⊙	20	20.0	0.8141	–0.0052

TABLE 10.–DATA LOG–MODEL C

$M_\infty = 0.201$; $Re = 2.83 \times 10^6$

Force figure number	Pressure figure number	Configuration	Symbol	δ_{le}, deg	$x_{o_{le}}/c$	$y_{o_{le}}/c$	$\delta_{f_{eq}}$, deg	δ_f, deg	x_{o_1}/c	y_{o_1}/c	x_{o_2}/c	y_{o_2}/c
A7a	C9a	$L_2N_2WC_1F_2$	⊙	47.2	−0.0627	−0.0918	44	30.0/49.7	0.8298	+0.0133	0.9473	−0.0811
↓	b	↓	⊡	42.1	−0.0633	−0.0750	↓	↓	↓	↓	↓	↓
↓	c	↓	△	37.0	−0.0633	−0.0591	↓	↓	↓	↓	↓	↓
↓	d	↓	◇	45.0	−0.0636	−0.0850	↓	↓	↓	↓	↓	↓
A7b	C9e	$L_2N_2WC_3F_2$	⊙	45.0	−0.0809	−0.0901	44	28.5/50.2	0.8300	+0.0139	0.9368	−0.0826
↓	f	↓	⊡	50.2	−0.0774	−0.1079	↓	↓	↓	↓	↓	↓
↓	g	↓	△	55.0	−0.0745	−0.1250	↓	↓	↓	↓	↓	↓
A8a	C10a	$L_2N_2WC_1F_2$	⊙	45.0	−0.0636	−0.0850	44	30.0/49.7	0.8258	+0.0132	0.9439	−0.0813
↓	b	↓	⊡	44.9	−0.0767	−0.0958	↓	↓	↓	↓	↓	↓
↓	c	↓	△	45.0	−0.0507	−0.0762	↓	↓	↓	↓	↓	↓
A8b	C10d	$L_2N_2WC_1F_2$	⊙	45.0	−0.0604	−0.0923	44	30.0/49.7	0.8258	+0.0132	0.9439	−0.0813
↓	e	↓	⊡	45.0	−0.0724	−0.1033	↓	↓	↓	↓	↓	↓
↓	f	↓	△	44.9	−0.0676	−0.0790	↓	↓	↓	↓	↓	↓
A8c	C10g	$L_2N_2WC_1F_2$	⊙	45.2	−0.0810	−0.0934	44	30.0/49.7	0.8258	+0.0132	0.9439	−0.0813
↓	h	↓	⊡	45.0	−0.0903	−0.1011	↓	↓	↓	↓	↓	↓
↓	i	↓	△	45.0	−0.0875	−0.0863	↓	↓	↓	↓	↓	↓
A8d	C10j	$L_2N_2WC_1F_2$	⊙	45.2	−0.0981	−0.0983	44	30.0/49.7	0.8258	+0.0132	0.9439	−0.0813
↓	k	↓	⊡	45.0	−0.1029	−0.1020	↓	↓	↓	↓	↓	↓
A8e	C10l	$L_2N_2WC_1F_2$	⊙	44.9	−0.1026	−0.0927	44	30.0/49.7	0.8258	+0.0132	0.9439	−0.0813
↓	m	↓	⊡	45.0	−0.1100	−0.1108	↓	↓	↓	↓	↓	↓
A8f	C10n	$L_2N_2WC_3F_2$	⊙	50.0	−0.0877	−0.1233	44	28.5/50.2	0.8300	+0.0139	0.9368	−0.0826
↓	C8	↓	⊡	50.0	−0.0974	−0.1208	↓	↓	↓	↓	↓	↓
↓	C10o	↓	△	50.1	−0.0859	−0.1009	↓	↓	↓	↓	↓	↓

TABLE 10.– Continued

Force figure number	Pressure figure number	Configuration	Symbol	δ_{le}, deg	$x_{o_{le}}/c$	$y_{o_{le}}/c$	$\delta_{f_{eq}}$, deg	δ_f, deg	x_{o_1}/c	y_{o_1}/c	x_{o_2}/c	y_{o_2}/c
A8g	C10p	$L_2N_2WC_3F_2$	⊙	50.1	−0.1068	−0.1215	44	28.5/50.2	0.8300	+0.0139	0.9368	−0.0826
↓	q	↓	⊡	50.1	−0.1004	−0.1383	↓	↓	↓	↓	↓	↓
	r		△	50.0	−0.1100	−0.1381						
A9	C11a	$L_2N_2WC_1F_2$	⊙	45.0	−0.0813	−0.0910	44	25.0/51.2	0.8253	+0.0084	0.9522	−0.0745
↓	b	↓	⊡	↓	↓	↓	↓	34.9/48.4	0.8260	+0.0188	0.9348	−0.0856
A10a	C12a	$L_2N_2WC_1F_2$	⊙	45.0	−0.0813	−0.0910	44	28.5/50.2	0.8258	+0.0121	0.9467	−0.0788
↓	b	↓	⊡	↓	↓	↓	↓	↓	0.8258	+0.0180	0.9467	−0.0893
	c		△						0.8260	−0.0095	0.9466	−0.1010
A10b	C12d	$L_2N_2WC_1F_2$	⊙	45.0	−0.0813	−0.0910	44	28.5/50.1	0.8153	+0.0076	0.9362	−0.0835
↓	e	↓	⊡	↓	↓	↓	↓	28.5/50.2	0.8152	−0.0022	0.9362	−0.0934
	f		△					28.5/50.2	0.8259	+0.0069	0.9472	−0.0839
A10c	C12g	$L_2N_2WC_1F_2$	⊙	45.0	−0.0813	−0.0910	44	28.5/50.1	0.8300	+0.0140	0.9503	−0.0773
↓	h	↓	⊡	↓	↓	↓	↓	28.5/50.2	0.8321	+0.0047	0.9532	−0.0867
	i		△					28.4/50.2	0.8329	+0.0183	0.9545	−0.0726
A10d	C12j	$L_2N_2WC_1F_2$	⊙	45.0	−0.0813	−0.0910	44	28.5/50.2	0.8347	+0.0222	0.9556	−0.0685
↓	k	↓	⊡	↓	↓	↓	↓	↓	0.8328	+0.0132	0.9540	−0.0751
	l		△						0.8299	+0.0181	0.9508	−0.0727
A11a	C13a	$L_2N_2WC_1F_2$	⊙	45.0	−0.0813	−0.0910	44	28.5/50.2	0.8329	+0.0183	0.9497	−0.0804
↓	b	↓	⊡	↓	↓	↓	↓	28.5/50.5	↓	↓	0.9686	−0.0698
	c		△					28.5/50.2			0.9590	−0.0655
A11b	C13d	$L_2N_2WC_1F_2$	⊙	45.0	−0.0813	−0.0910	44	28.5/50.2	0.8329	+0.0183	0.9417	−0.0705
↓	e	↓	⊡	↓	↓	↓	↓	↓	↓	↓	0.9395	−0.0784
	f		△								0.9353	−0.0933

TABLE 10.—Concluded

Force figure number	Pressure figure number	Configuration	Symbol	δ_{le}, deg	$x_{o_{le}}/c$	$y_{o_{le}}/c$	$\delta_{f_{eq}}$, deg	δ_f, deg	x_{o_1}/c	y_{o_1}/c	x_{o_2}/c	y_{o_2}/c
A11c	C13g	$L_2N_2WC_1F_2$	⊙	45.0	−0.0813	−0.0910	44	28.5/50.2	0.8329	+0.0183	0.9350	−0.0847
↓	h	↓	⊡	↓	↓	↓	↓	↓	↓	↓	0.9296	−0.0748
A11d	C13i	$L_2N_2WC_3F_2$	⊙	45.0	−0.0809	−0.0901	44	28.5/50.2	0.8323	+0.0180	0.9190	−0.0795
↓	j	↓	⊡	↓	↓	↓	↓	↓	↓	↓	0.9234	−0.0718
A12a	C14a	$L_2N_2WC_1F_2$	⊙	45.0	−0.0813	−0.0910	12	−5.0/15.0	0.7941	−0.0221	0.9272	−0.0479
↓	b	↓	⊡	↓	↓	↓	30	14.0/33.0	0.8147	−0.0009	0.9417	−0.0668
	c		△				55	30.0/65.0	0.8297	+0.0190	0.9494	−0.0734
A12b	C14d	$L_2N_2WC_1F_2$	⊙	45.0	−0.0813	−0.0910	44	25.0/50.0	0.8028	+0.0006	0.9168	−0.0808
A13	C15a	$L_2N_2WC_1F_2$	⊙	45.0	−0.0813	−0.0910	49	30.0/57.0	0.8295	+0.0158	0.9473	−0.0778
↓	b	↓	⊡	↓	↓	↓	↓	35.2/55.7	0.8283	+0.0169	0.9328	−0.0916
	c		△					33.5/56.0	0.8285	+0.0166	0.9368	−0.0872
A14	C16	$L_2N_2WC_1F_2$	⊙	45.0	−0.0813	−0.0910	49	30.0/57.0	0.8316	+0.0187	0.9367	−0.0774
A15	C17a	$L_2N_2WC_3F_2$	⊙	50.0	−0.0977	−0.1213	15	0.0/16.0	0.8268	−0.0046	0.9653	−0.0403
↓	b	↓	⊡	↓	↓	↓	↓	0.0/16.1	0.8337	+0.0009	0.9740	−0.0335
	c		△					−5.2/17.0	0.8363	−0.0079	0.9687	−0.0274
A16	C18	$N_1WC_1F_2$	⊙	—	—	—	13	−5.0/15.0	0.7947	−0.0264	0.9271	−0.0421

TABLE 11.–DATA LOG–MODEL D

M_∞ = 0.201; Re = 2.83 x 10^6

Force figure number	Pressure figure number	Configuration	Symbol	δ_{le}, deg	$x_{o_{le}}/c$	$y_{o_{le}}/c$	δ_{te}, deg	δ_f, deg	x_{o_1}/c	y_{o_1}/c	x_{o_2}/c	y_{o_2}/c	x_{o_3}/c	y_{o_3}/c
A17	C20a	$L_1N_1WC_1F_3$	⊙	44.0	−0.1147	−0.0764	46	20.0/44.7/64.7	0.8243	+0.0077	0.9451	−0.0645	1.1045	−0.2370
	b		□	49.0	−0.1078	−0.0883								
	c		△	39.0	−0.1183	−0.0635								
	d		◇	54.0	−0.1000	−0.1006								
A18a	C21a	$L_1N_1WC_1F_3$	⊙	43.9	−0.1011	−0.0700	46	20.0/44.7/64.7	0.8243	+0.0077	0.9451	−0.0645	1.1045	−0.2370
	b		□	44.0	−0.1244	−0.0890								
A18b	C21c	$L_1N_1WC_1F_3$	⊙	43.9	−0.1202	−0.0709	46	20.0/44.7/64.7	0.8243	+0.0077	0.9451	−0.0645	1.1045	−0.2370
	d		□		−0.1314	−0.0845								
	e		△		−0.1044	−0.0625								
	f		◇		−0.1244	−0.0747								
A18c	C21g	$L_1N_1WC_1F_3$	⊙	44.1	−0.1253	−0.0669	46	20.0/44.7/64.7	0.8243	+0.0077	0.9451	−0.0645	1.1045	−0.2370
	h		□	44.0	−0.1382	−0.0805								
A19a	C22a	$L_1N_1WC_1F_3$	⊙	43.9	−0.1244	−0.0747	46	15.0/45.8/65.8	0.8247	+0.0049	0.9530	−0.0510	1.1102	−0.2263
	b		□					25.0/43.2/63.2	0.8253	+0.0101	0.9377	−0.0747	1.1013	−0.2431
A19b	C22c	$L_1N_1WC_1F_3$	⊙	43.9	−0.1244	−0.0747	46	20.0/49.7/60.5	0.8244	+0.0076	0.9479	−0.0590	1.0911	−0.2440
	d		□					20.0/39.7/68.3			0.9446	−0.0660	1.1195	−0.2241
A20	C23a	$L_1N_1WC_1F_3$	⊙	43.9	−0.1244	−0.0747	46	20.0/44.7/64.7	0.8285	+0.0106	0.9495	−0.0617	1.1086	−0.2343
	b		□						0.8327	+0.0147	0.9537	−0.0575	1.1129	−0.2300
	C19		△						0.8356	+0.0193	0.9563	−0.0533	1.1153	−0.2255
	C23c		◇						0.8369	+0.0230	0.9579	−0.0493	1.1170	−0.2218
A21	C24a	$L_1N_1WC_1F_3$	⊙	43.9	−0.1244	−0.0747	46	20.0/44.7/64.7	0.8356	+0.0193	0.9674	−0.0542	1.1263	−0.2228
	b		□								0.9549	−0.0578	1.1133	−0.2301

TABLE 11.—Concluded

Force figure number	Pressure figure number	Configuration	Symbol	δ_{le}, deg	$x_{o_{le}}/c$	$y_{o_{le}}/c$	$\delta_{f_{eq}}$, deg	δ_f, deg	x_{o_1}/c	y_{o_1}/c	x_{o_2}/c	y_{o_2}/c	x_{o_3}/c	y_{o_3}/c
A22	C25a	$L_1N_1WC_1F_3$	⊙	43.9	-0.1244	-0.0747	46	20.0/44.7/64.7	0.8356	+0.0193	0.9549	-0.0578	1.1093	-0.2286
↓	b	↓	□	↓	↓	↓	↓	↓	↓	↓	↓	↓	1.1105	-0.2342
A23	C26a	$L_1N_1WC_1F_3$	⊙	43.9	-0.1244	-0.0747	53	25.0/55.0/77.3	0.8337	+0.0166	0.9493	-0.0643	1.0586	-0.2630
↓	b	↓	□	↓	↓	↓	↓	28.4/55.0/75.0	0.8320	+0.0159	0.9410	-0.0736	1.0663	-0.2716
A24	C27a	$L_1N_1WC_1F_3$	⊙	43.9	-0.1244	-0.0747	16	-4.9/10.0/25.0	0.7947	-0.0260	0.9268	-0.0421	1.1548	-0.0944
↓	b	↓	□	↓	↓	↓	↓	↓	↓	↓	↓	↓	↓	↓
A25	C28a	$L_2N_2WC_1F_3$	⊙	45.0	-0.0816	-0.0909	16	-4.9/10.0/25.0	0.7947	-0.0260	0.9268	-0.0421	1.1548	-0.0944
↓	C3	L_2N_2WT	□	↓	-0.0816	-0.0909	0	–	–	–	–	–	–	–
↓	C28b	$L_2N_2WC_1F_3$	△	↓	-0.0813	-0.0910	46	20.0/44.7/64.7	0.8243	+0.0077	0.9451	-0.0645	1.1045	-0.2370
A26	C29	$N_1WC_1F_3$	⊙	–	–	–	16	-5.0/10.0/25.0	0.7947	-0.0264	0.9271	-0.0421	1.1551	-0.0951

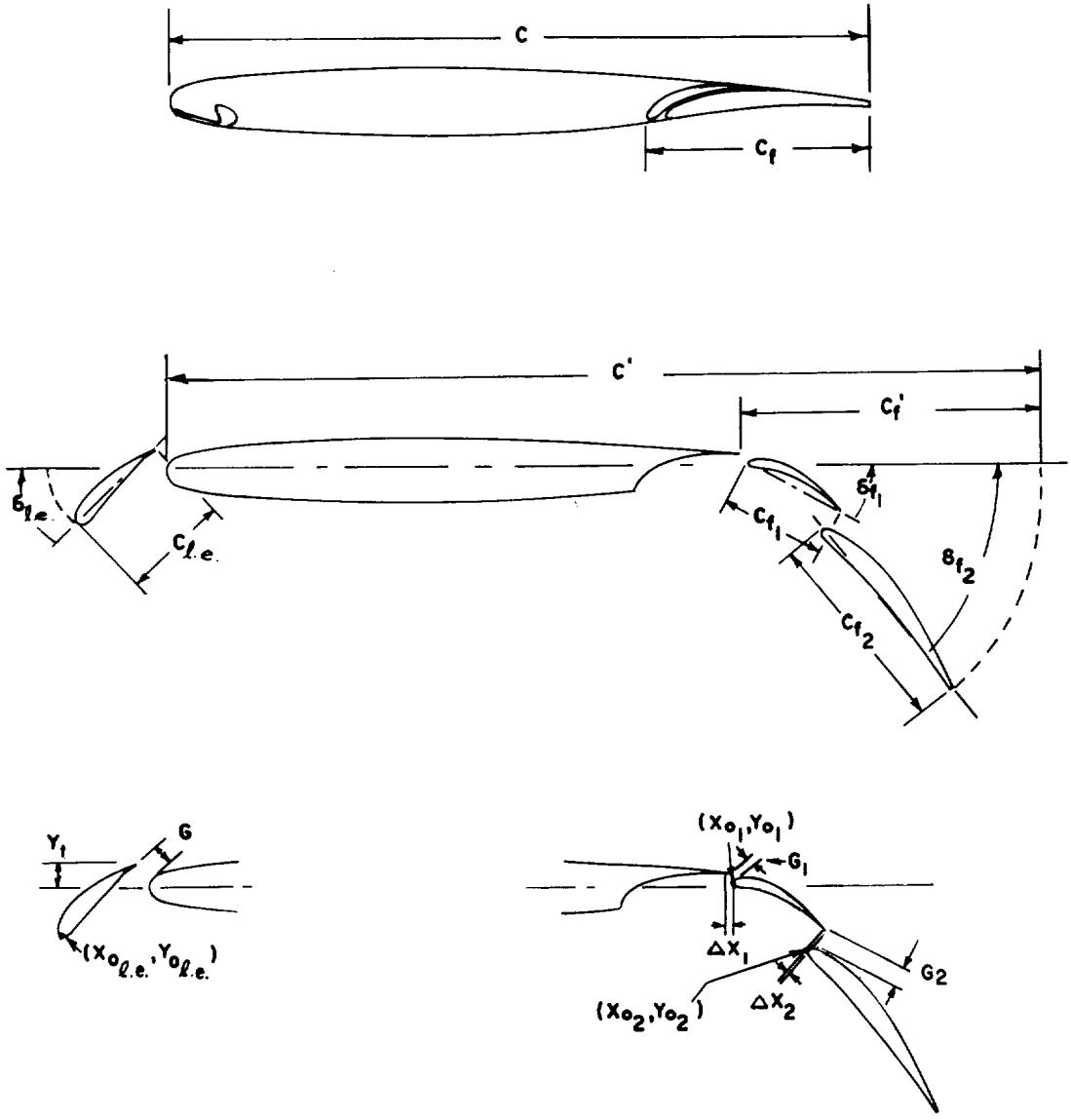

FIGURE 1.—HIGH-LIFT SYSTEM CONFIGURATION NOMENCLATURE

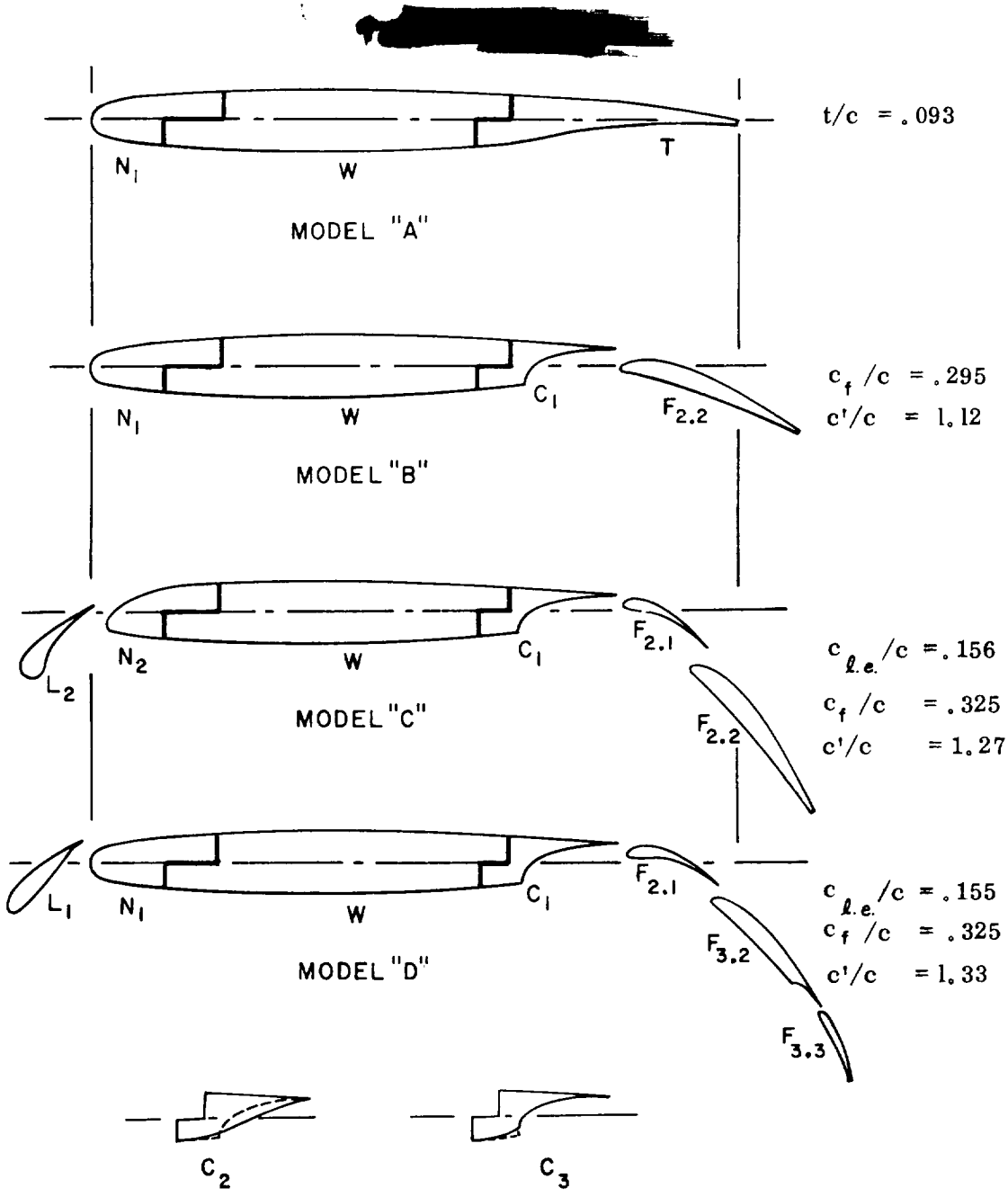

N - Wing Leading Edge
W - Wing Spar
T - Basic Trailing Edge

C - Cove
L - Leading Edge Device
F - Trailing Edge Flap

FIGURE 2.–MODEL COMPONENTS

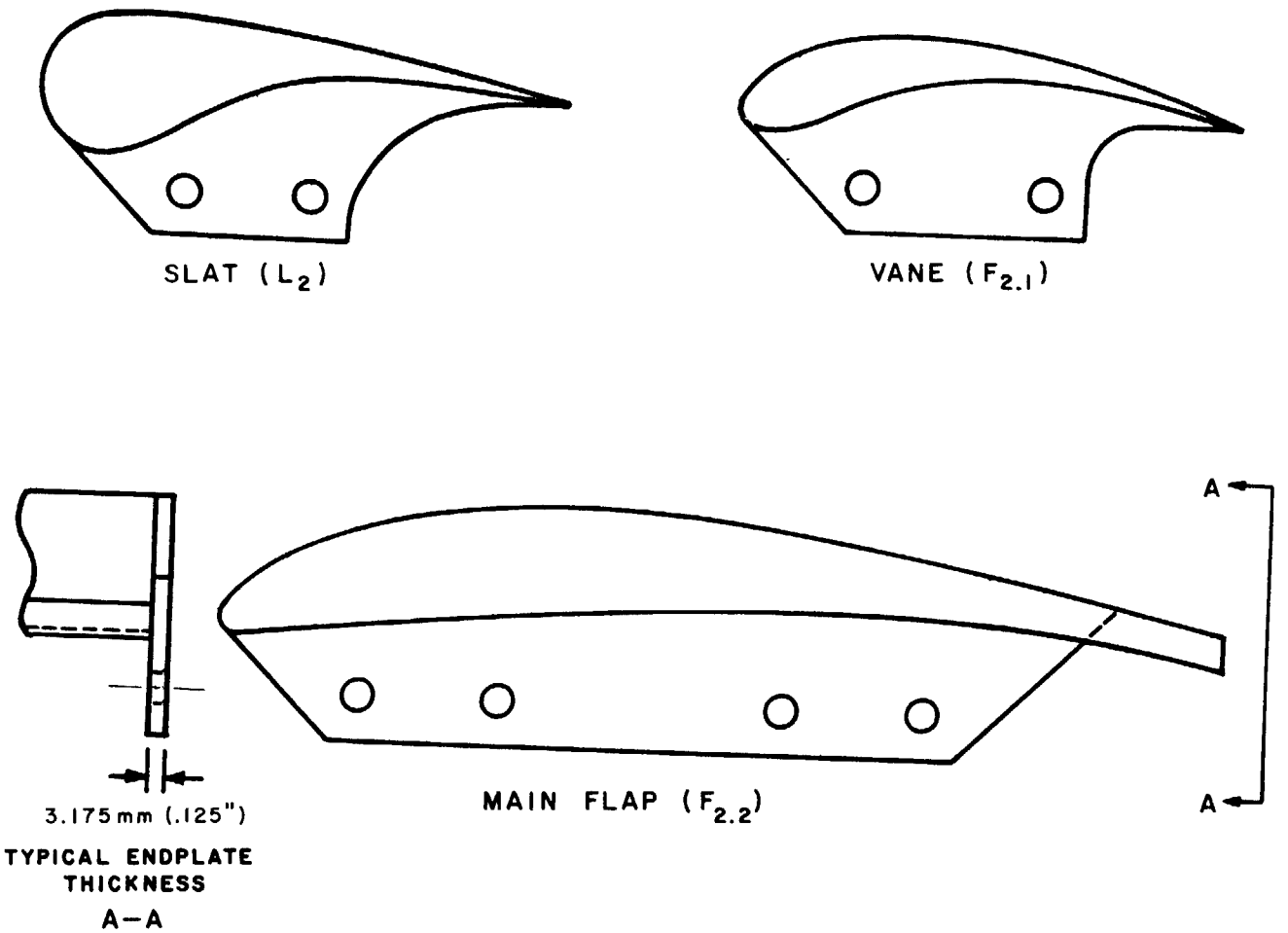

FIGURE 3.–TYPICAL HIGH-LIFT COMPONENT END PLATES

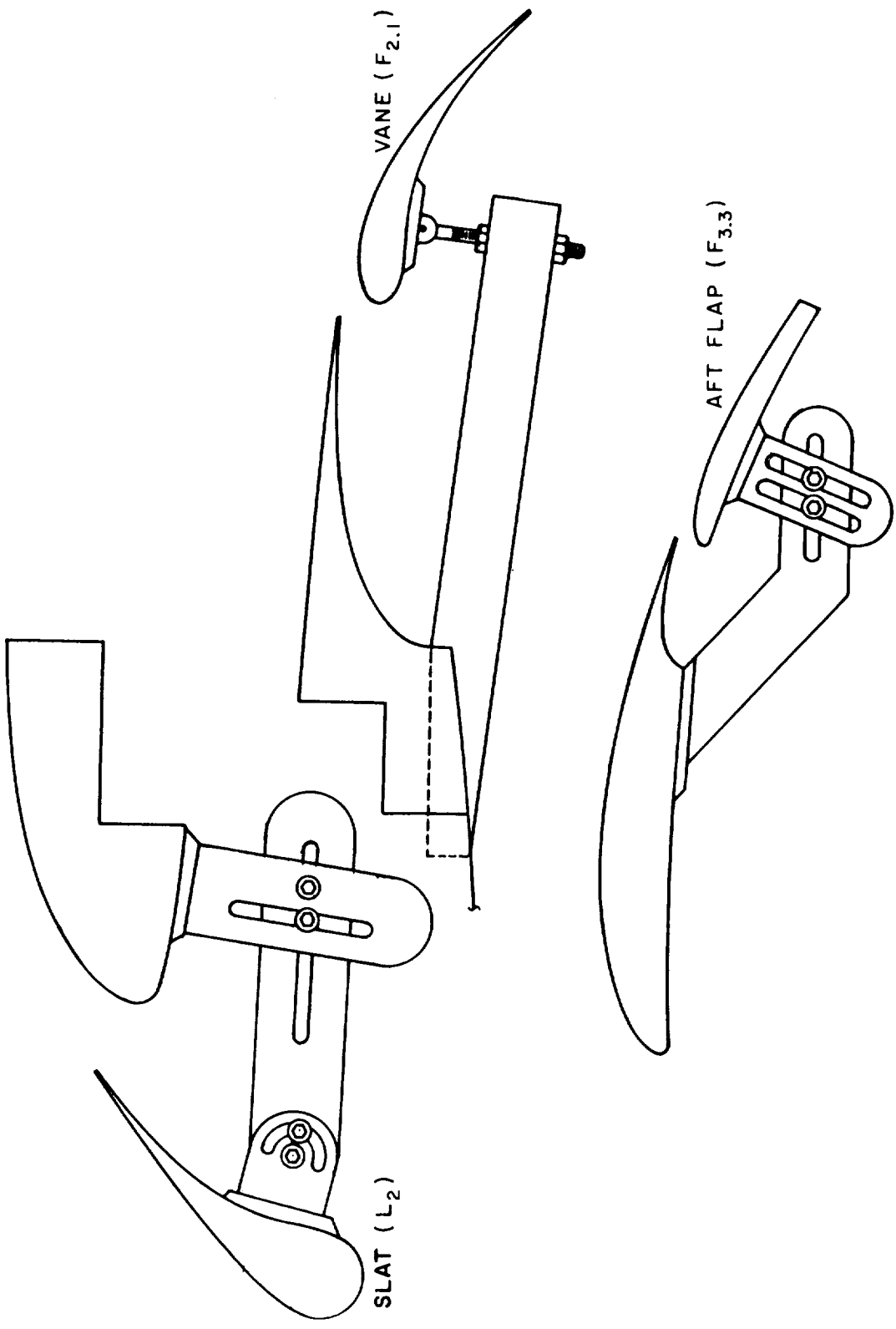

FIGURE 4.–TYPICAL HIGH-LIFT COMPONENT BRACKETS

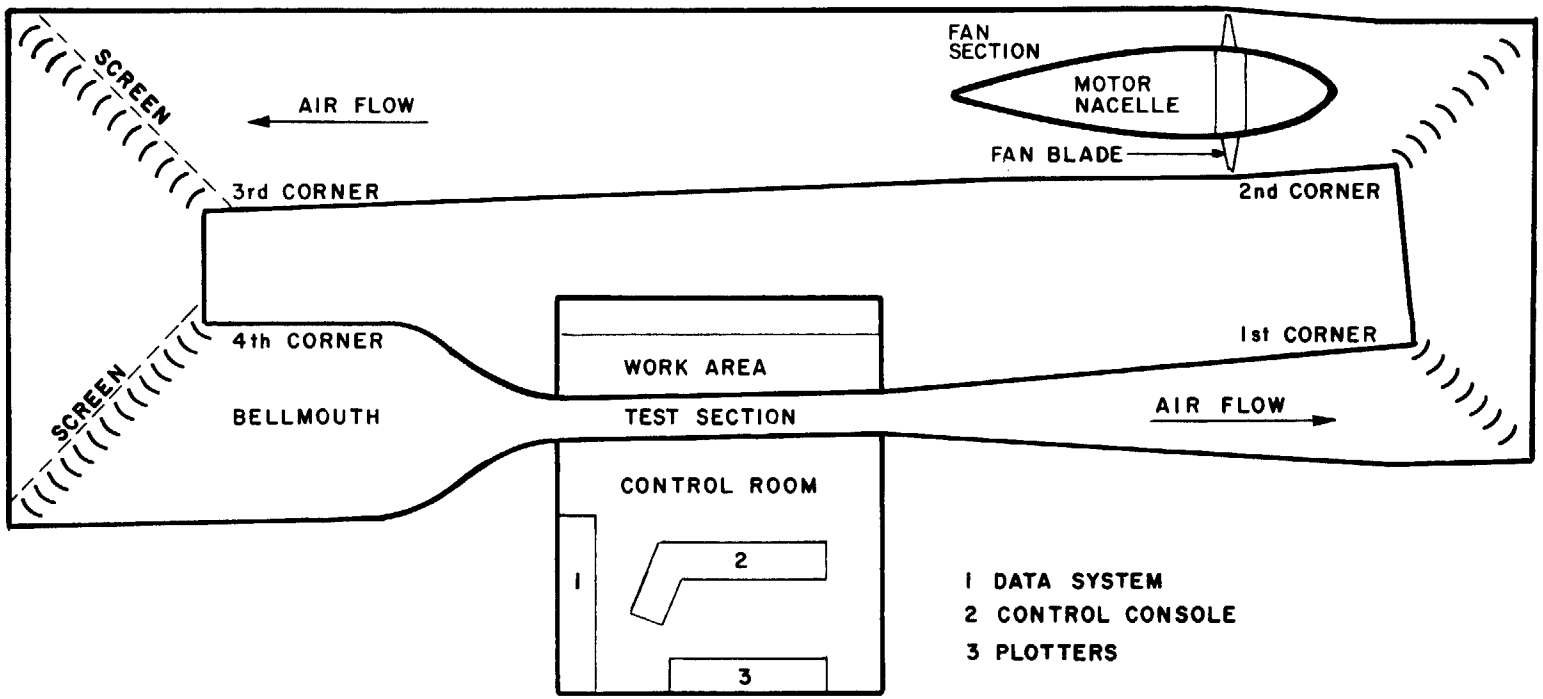

FIGURE 5.–GENERAL ARRANGEMENT OF BRWT

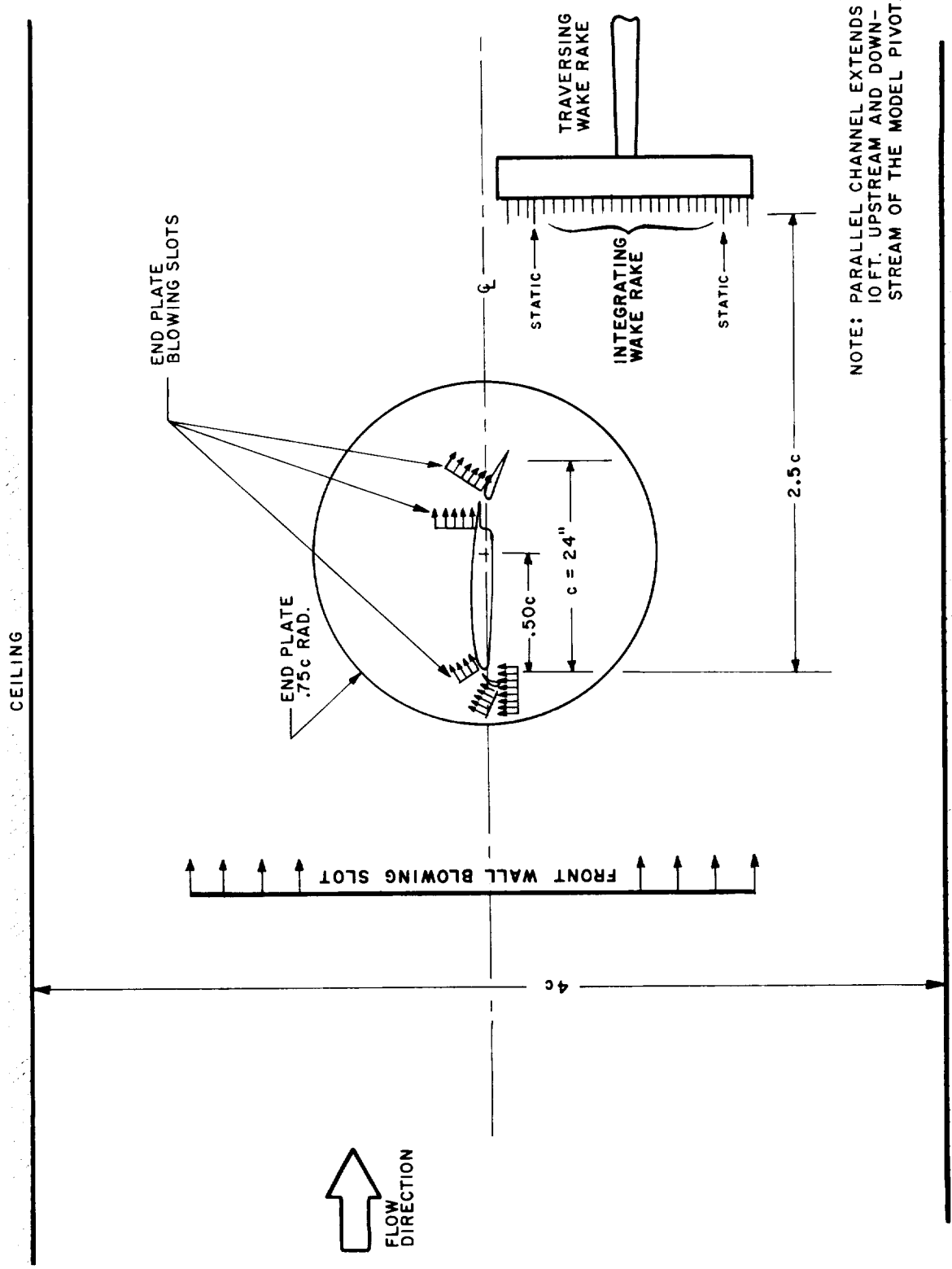

FIGURE 6.– TEST SECTION SHOWING BLC SYSTEM AND INTEGRATING WAKE RAKE

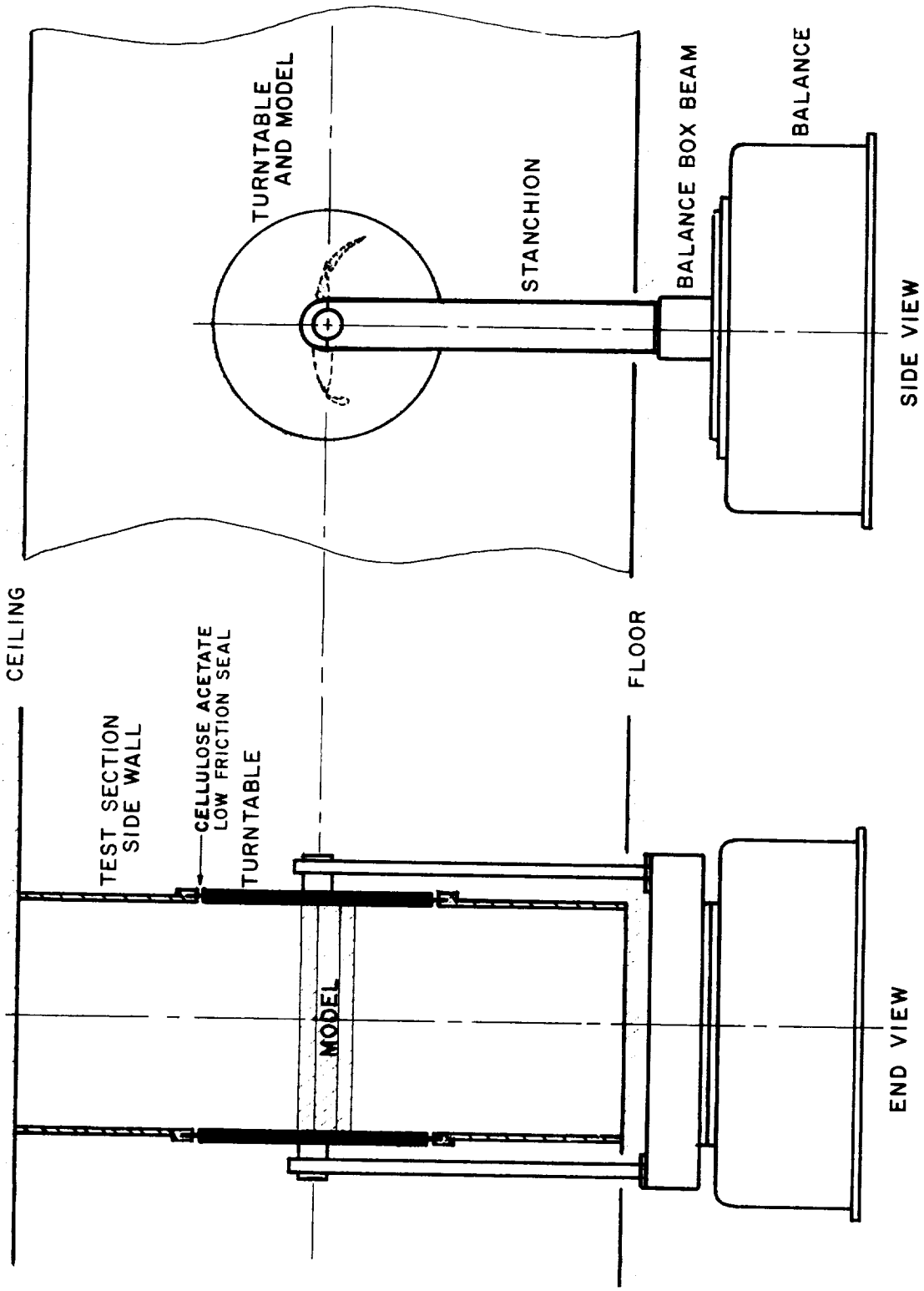

FIGURE 7.–MODEL AND BALANCE STANCHION ARRANGEMENT

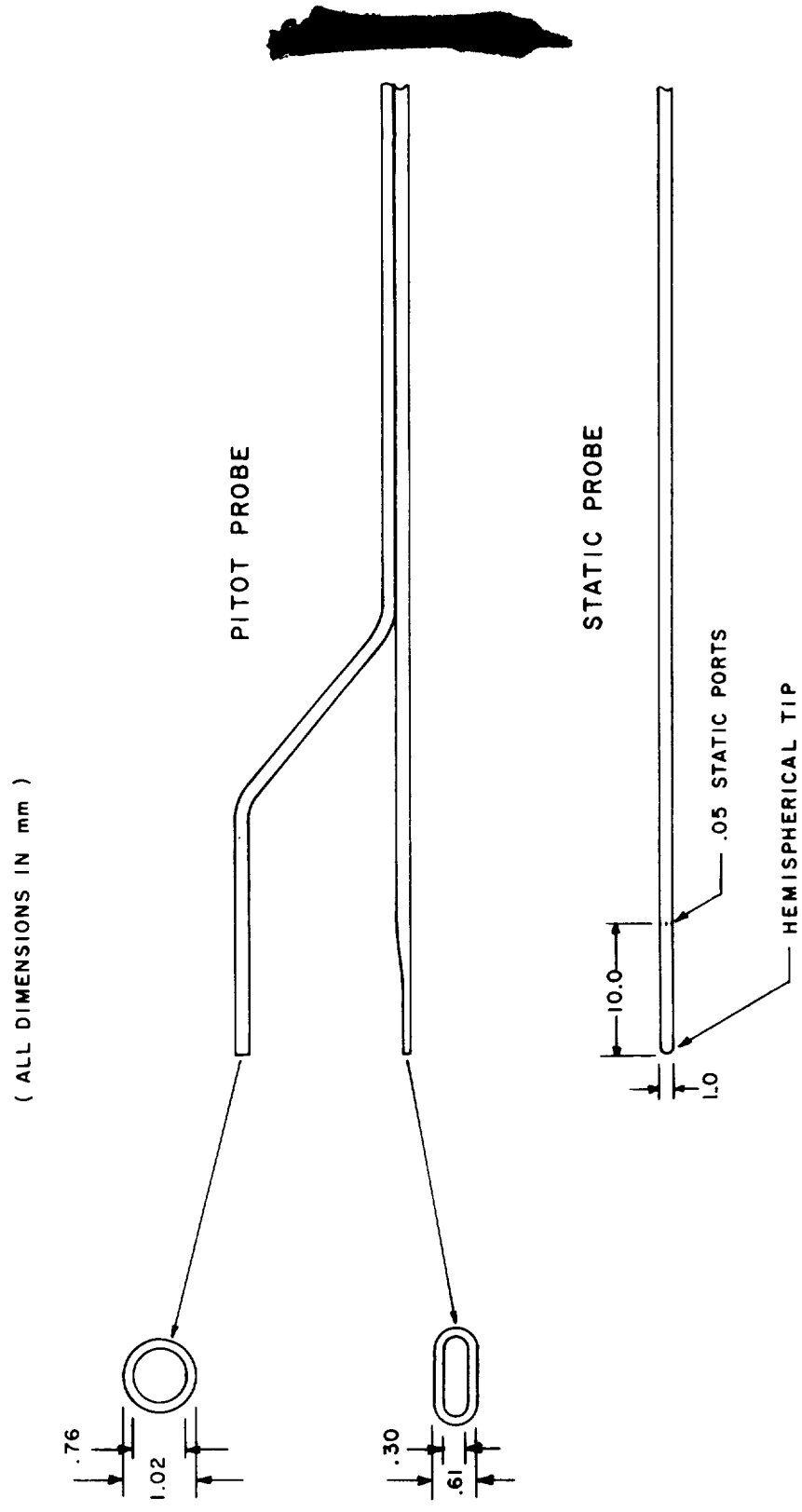

FIGURE 8.–WAKE/BOUNDARY-LAYER PROBES

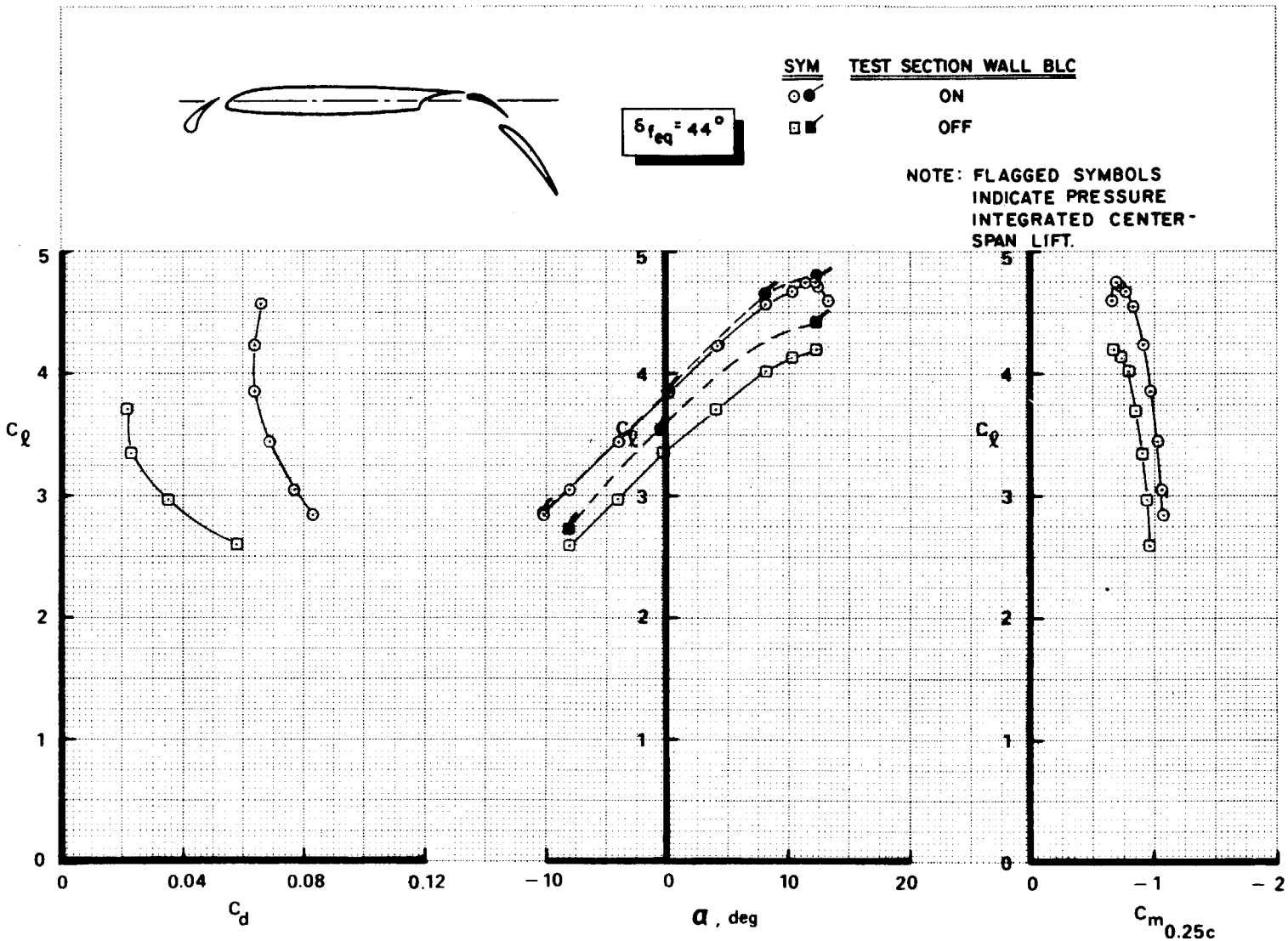

FIGURE 9.–EFFECTS OF TEST SECTION WALL BLC ON AERODYNAMIC CHARACTERISTICS OF MODEL C

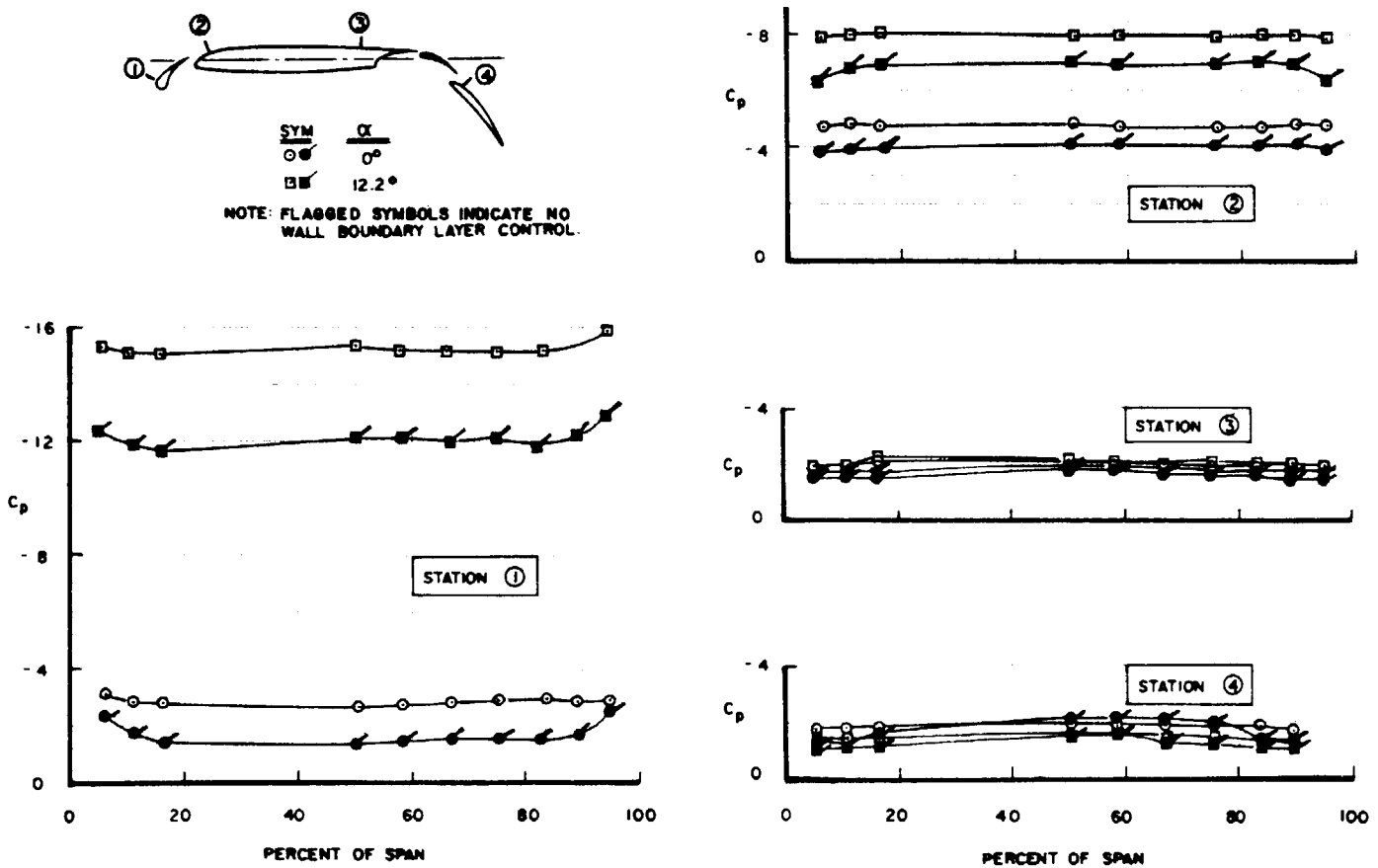

FIGURE 10.—EFFECTS OF TEST SECTION WALL BLC ON SPANWISE PRESSURES OF MODEL C

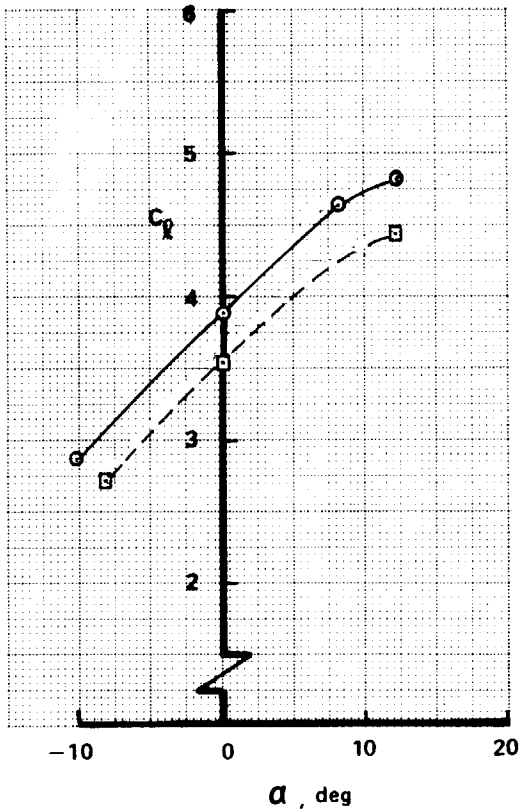

(a) NO DOWNWASH CORRECTIONS

⊙ WITH WALL BLC
⊡ NO WALL BLC

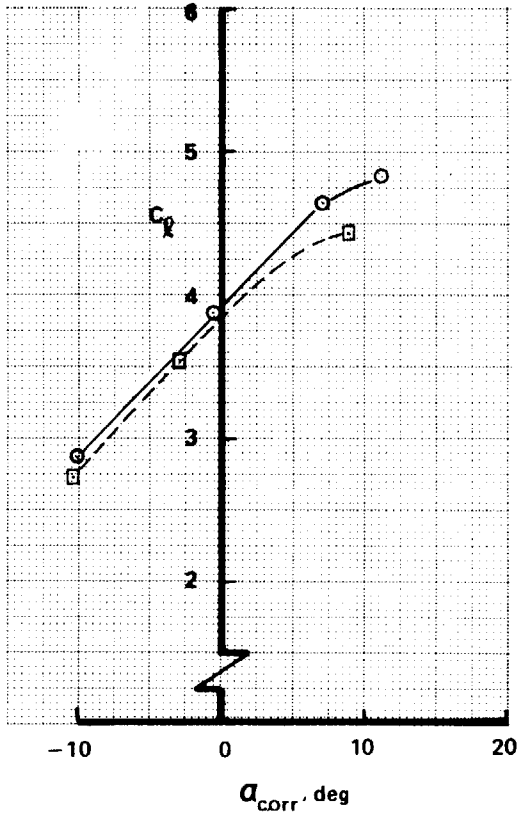

(b) ANGLE-OF-ATTACK CORRECTED FOR INDUCED DOWNWASH

FIGURE 11.—EFFECTS OF INDUCED DOWNWASH ON CENTER-SPAN LIFT MEASUREMENTS

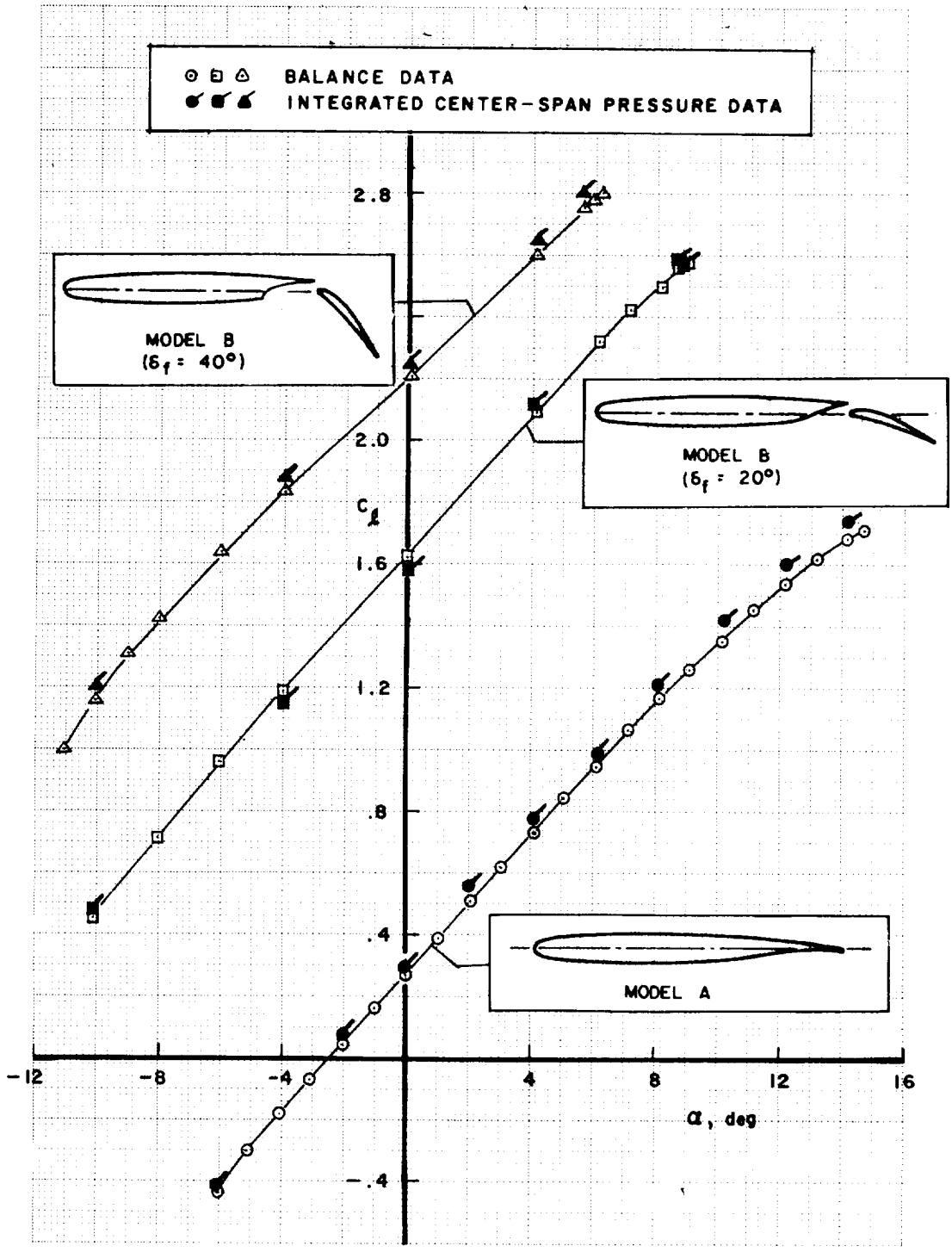

FIGURE 12.–COMPARISON OF CENTER-SPAN AND FULL-SPAN LIFTS OF MODELS A AND B

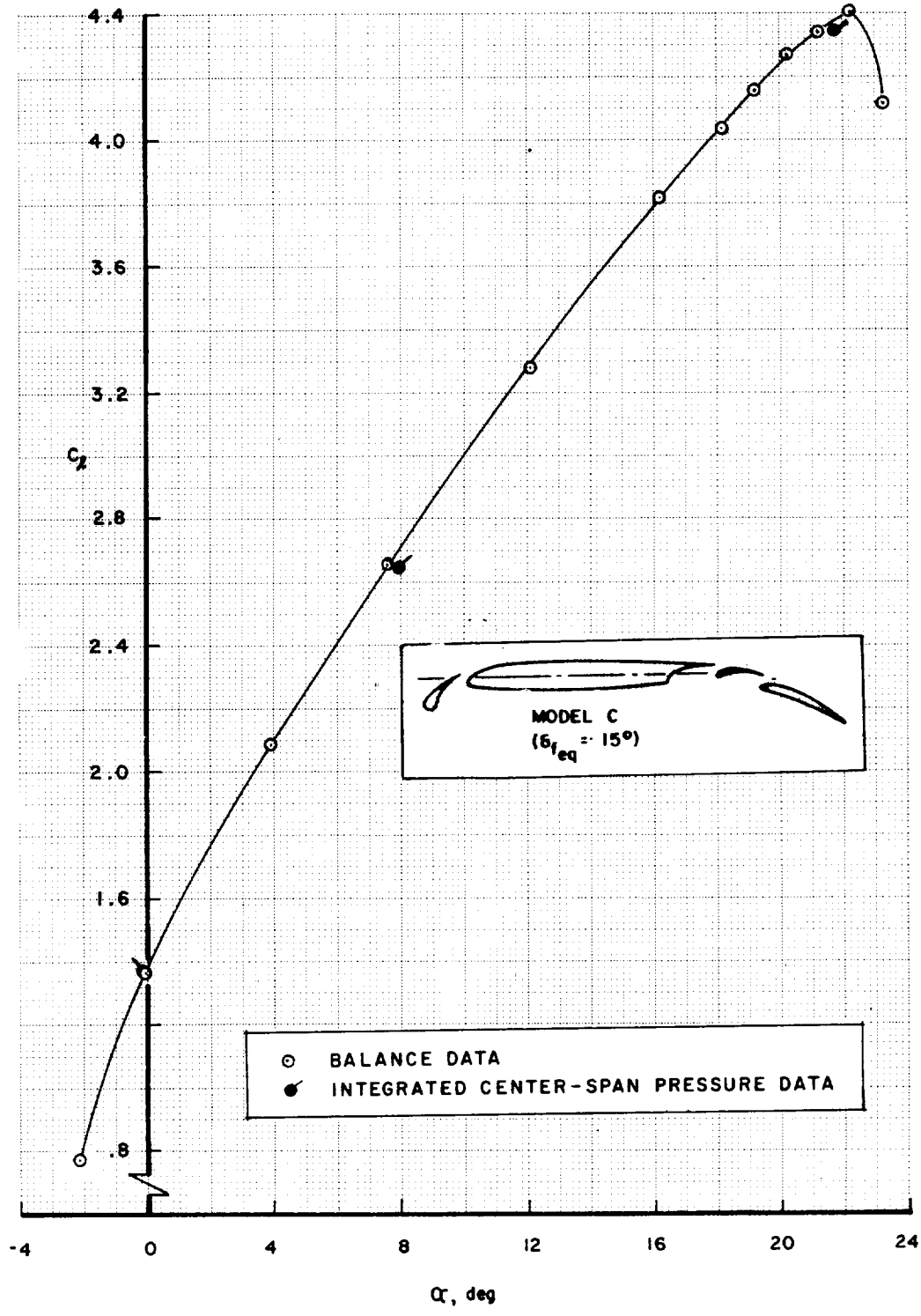

FIGURE 13.—COMPARISON OF CENTER-SPAN AND FULL-SPAN LIFTS OF MODEL C FOR 15° OF EQUIVALENT FLAP DEFLECTION

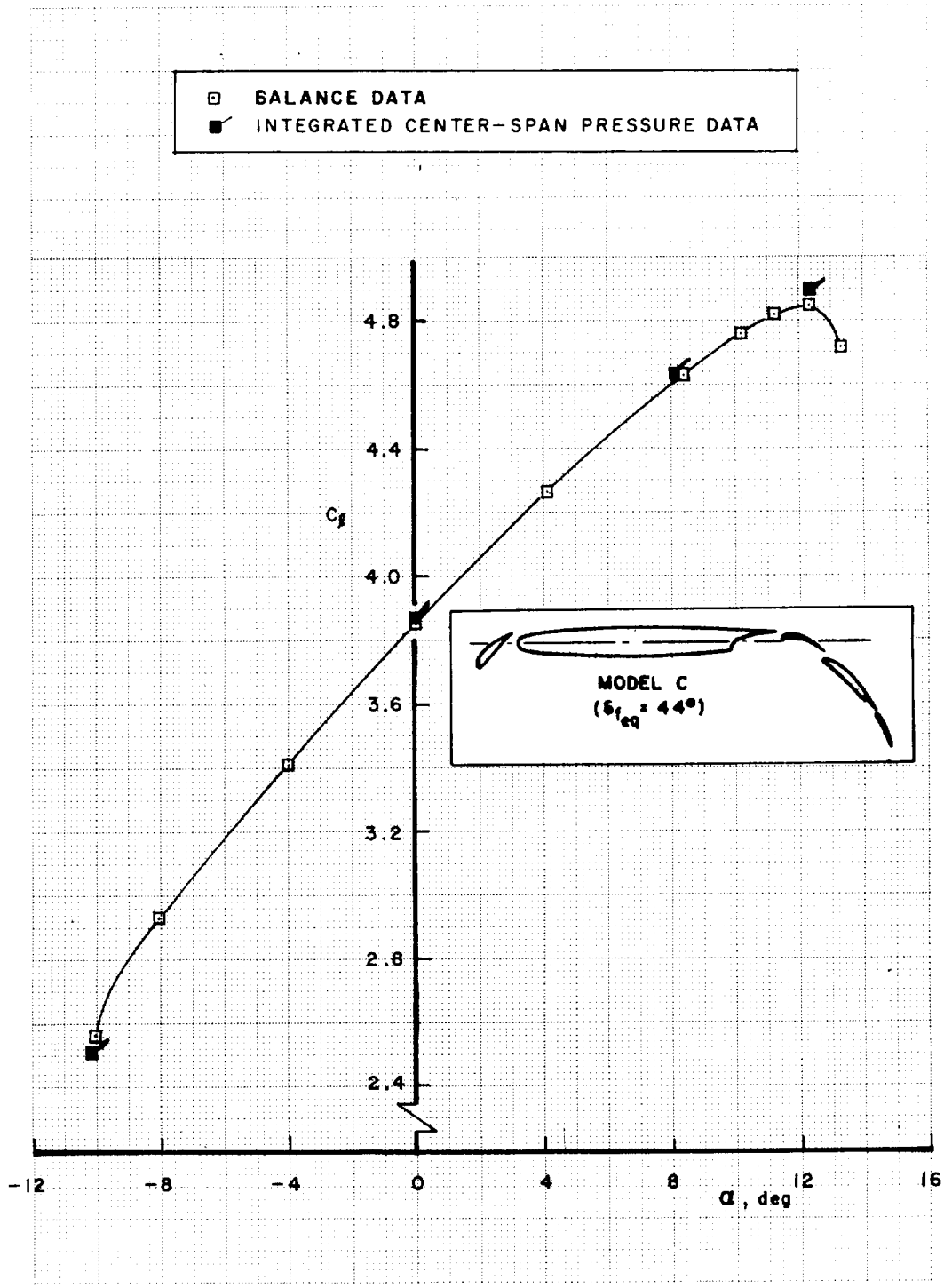

FIGURE 14.–COMPARISON OF CENTER-SPAN AND FULL-SPAN LIFTS OF MODEL C FOR 45° OF EQUIVALENT FLAP DEFLECTION

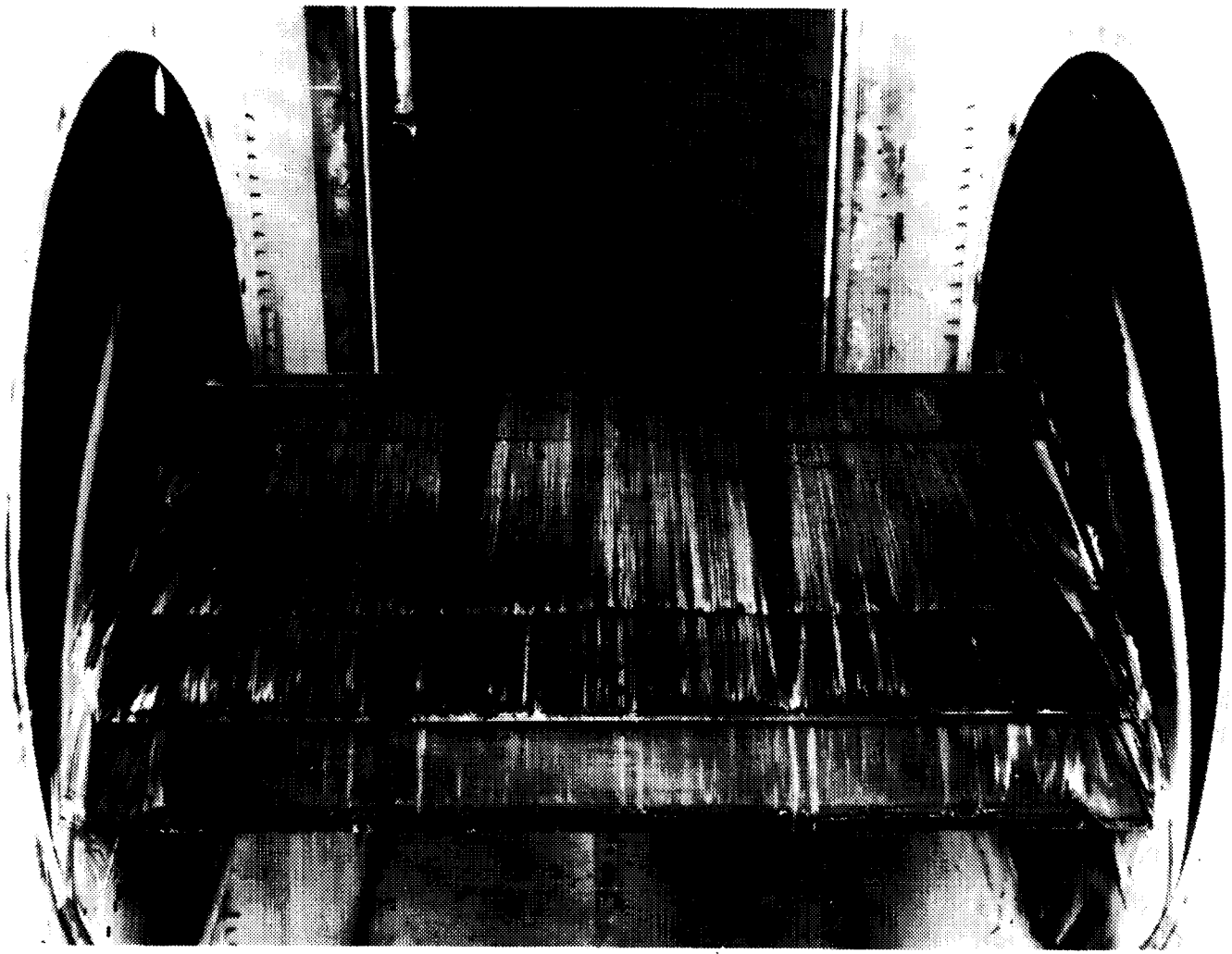

FIGURE 15.–FLOW VISUALIZATION OF UPPER SURFACES OF LEADING-EDGE FLAP AND WING OF MODEL D AT $C_{\ell_{max}}$ FOR $\delta_{f_{eq}} = 46°$

FIGURE 16.–CLOSEUP VIEW OF THE LEADING-EDGE TRANSITIONS OF MODEL D AT $C_{\ell_{max}}$ FOR $\delta_{f_{eq}} = 46°$

FIGURE 17.—FLOW VISUALIZATION OF UPPER SURFACES OF WING AND TRAILING-EDGE FLAPS OF MODEL D AT $C_{\ell_{max}}$ FOR $\delta_{f_{eq}} = 46°$

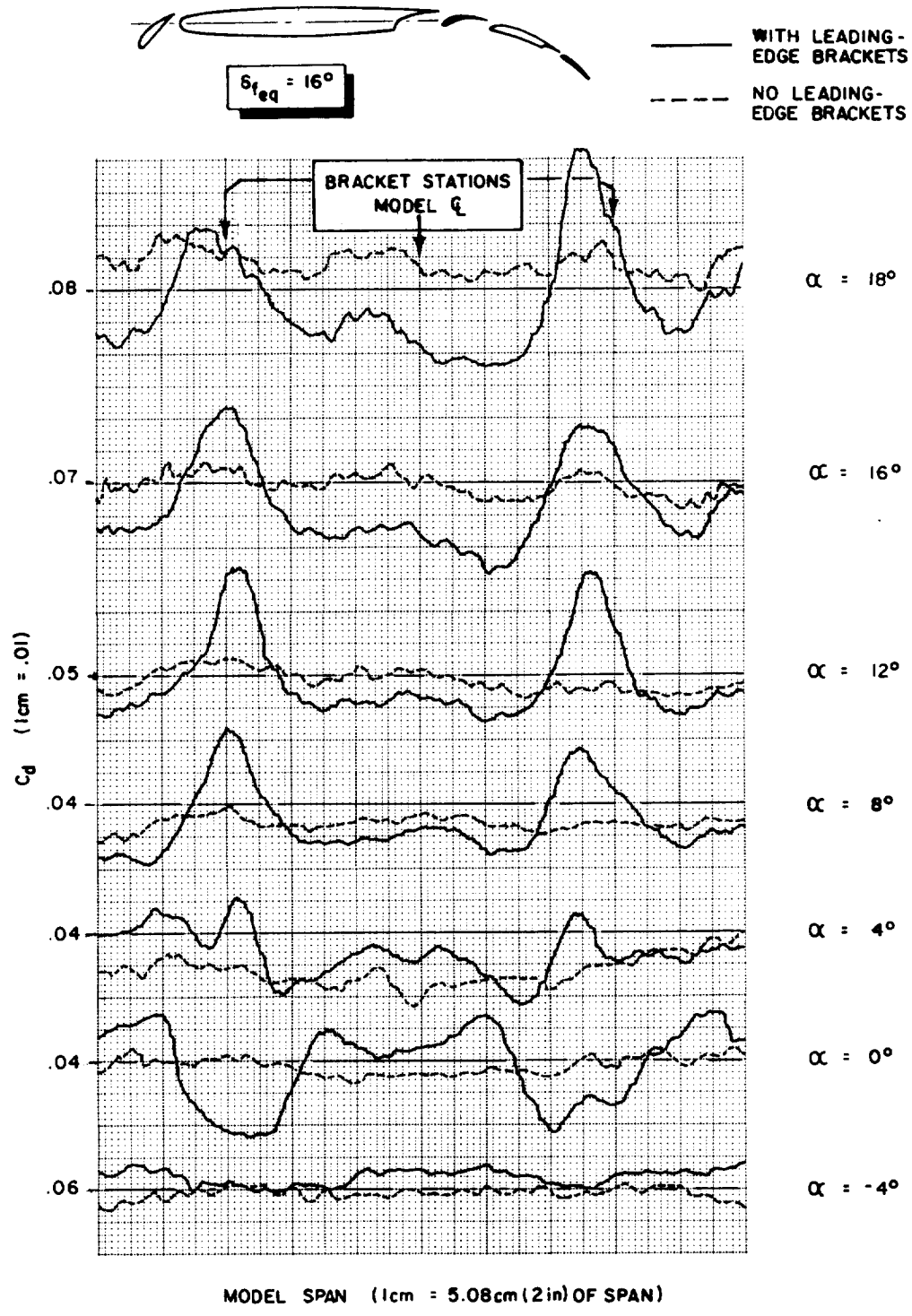

FIGURE 18.–EFFECTS OF LEADING-EDGE SUPPORT BRACKETS ON WAKE DRAG MEASUREMENTS ACROSS THE SPAN OF MODEL D FOR $\delta_{f_{eq}} = 16°$

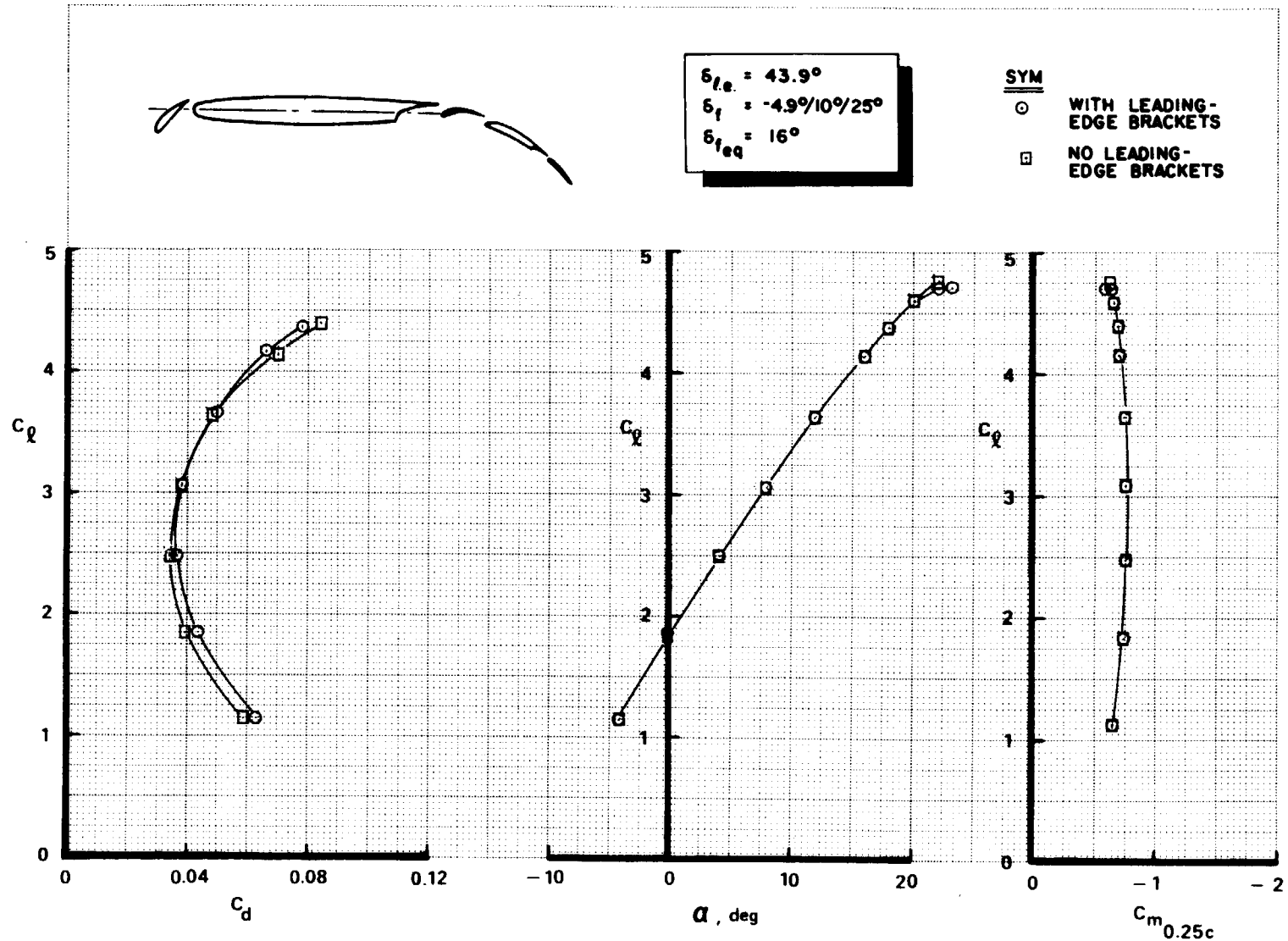

FIGURE 19.—EFFECTS OF LEADING-EDGE SUPPORT BRACKETS ON THE AERODYNAMIC CHARACTERISTICS OF MODEL D FOR $\delta_{f_{eq}} = 16°$

APPENDIX A

AIRFOIL SECTION CHARACTERISTICS

TABLE A1.–FORCE AND MOMENT FIGURE DESCRIPTIONS

Model	Comments	Figure number
A (basic airfoil)	Mach number and Reynolds number variation	A1
	Transition strip effect	A2
	Slat 1 effect	A3
B (single-slotted flap)	Slot gap and overlap effect ($\delta_f = 20°$)	A4
	Flap deflection angle variation	A5
	Boundary-layer study configuration	A6
C (double-slotted flap with slat 1)	Slat 1 deflection angle variation	A7
	Slat 1 slot optimization	A8
	Flap angle combination at constant $\delta_{f_{eq}}$ (44°)	A9
	Wing/vane-slot gap and overlap effects ($\delta_{f_{eq}} = 44°$)	A10
	Vane/flap-slot gap and overlap effects ($\delta_{f_{eq}} = 44°$)	A11
	Flap deflection angle variation	A12
	Flap angle combination at constant $\delta_{f_{eq}}$ (49°)	A13
	Wing/vane-slot gap and overlap effects ($\delta_{f_{eq}} = 49°$)	A14
	Low flap deflection angle study ($\delta_{f_{eq}} = 15°$)	A15
	Low flap deflection without leading edge device ($\delta_{f_{eq}} = 13°$)	A16
D (triple-slotted flap with slat 2)	Slat 2 deflection angle variation	A17
	Slat 2 slot optimization	A18
	Flap angle combination at constant $\delta_{f_{eq}}$ (46°)	A19
	Wing/vane-slot gap and overlap effects ($\delta_{f_{eq}} = 46°$)	A20
	Vane/main-slot gap and overlap effects ($\delta_{f_{eq}} = 46°$)	A21
	Main/aft-slot gap and overlap effects ($\delta_{f_{eq}} = 46°$)	A22
	Flap angle combination at constant $\delta_{f_{eq}}$ (53°)	A23
	Leading-edge device bracket effect ($\delta_{f_{eq}} = 16°$)	A24
	Flap deflection angle variation with slat 1	A25
	Low flap deflection without leading-edge device ($\delta_{f_{eq}} = 16°$)	A26

[redacted]

TABLE A2.–BOUNDARY-LAYER TRANSITION LOCATIONS

Configuration	Pressure figure number	α, deg	Transition location, % of wing chord (see figs. 3.2-3.7)				
			L_1 or L_2	Wing	$F_{2.1}$	$F_{2.2}$ or $F_{3.2}$	$F_{3.3}$
N_1WT	C1c	0	–	18.8	–	–	–
↓	↓	14	–	0.7 [b]64.2	–	–	–
$N_1WC_1F_1$	C5a	0	–	NA	–	14.1	–
$N_1WC_1F_1$	C5i	-6.5	–	Laminar [b]25.4	–	13.2	–
↓	↓	-4	–	10.0 [b]60.0	–	13.2	–
↓	↓	8	–	0.8 [b]60.0	–	8.2	–
$N_1WC_1F_1$	C6a	0	–	NA	–	3.6	–
$N_1WC_1F_1$	C6c	0	–	NA	–	5.2	–
$L_2N_2WC_1F_2$	C15b	0	NA	NA	2.5	6.6	–
$L_2N_2WC_3F_2$	C17b	0	NA	NA	Laminar	15.3	–
$N_1WC_1F_2$	C18	0	–	1.7	12.6	14.9	–
$L_1N_1WC_1F_3$	C23a	0	NA	NA	6.7	8.5	3.7
↓	↓	15	1.1	2.1	5.0	6.0	3.7
$L_1N_1WC_1F_3$	C25b	0	NA	NA	3.3	8.1	3.2
$L_1N_1WC_1F_3$	C26a	0	NA	NA	4.2	5.2	NA
$L_1N_1WC_1F_3$	C26b	0	NA	NA	9.6	11.8	4.1
↓	↓	22	1.0	2.1	9.6	11.8	4.1
$L_2N_2WC_1F_3$	C27a	17.5	1.2	10.8	10.3	12.2	3.7
L_2N_2WT	C27b	20	1.4	11.7	–	–	–
↓	↓	26	1.2	10.8	–	–	–
$N_1WC_3F_3$	C28	0	–	1.7	12.6	15.6	6.6

[a]All transition locations on upper surface unless otherwise noted. NA = not available.

[b]Lower surface.

[redacted]

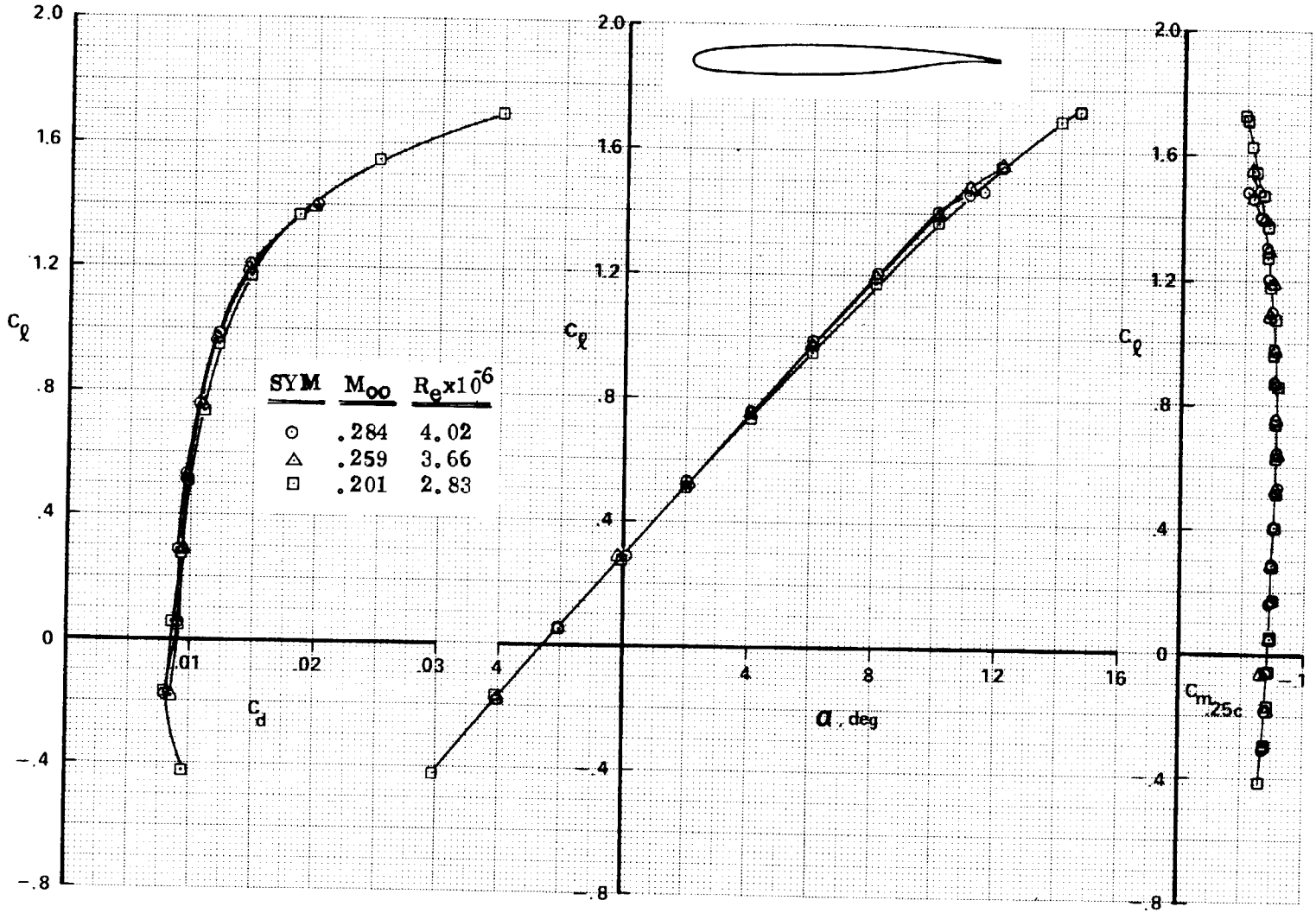

(a)

FIGURE A1.—EFFECT OF MACH NUMBER AND REYNOLDS NUMBER VARIATION—MODEL A

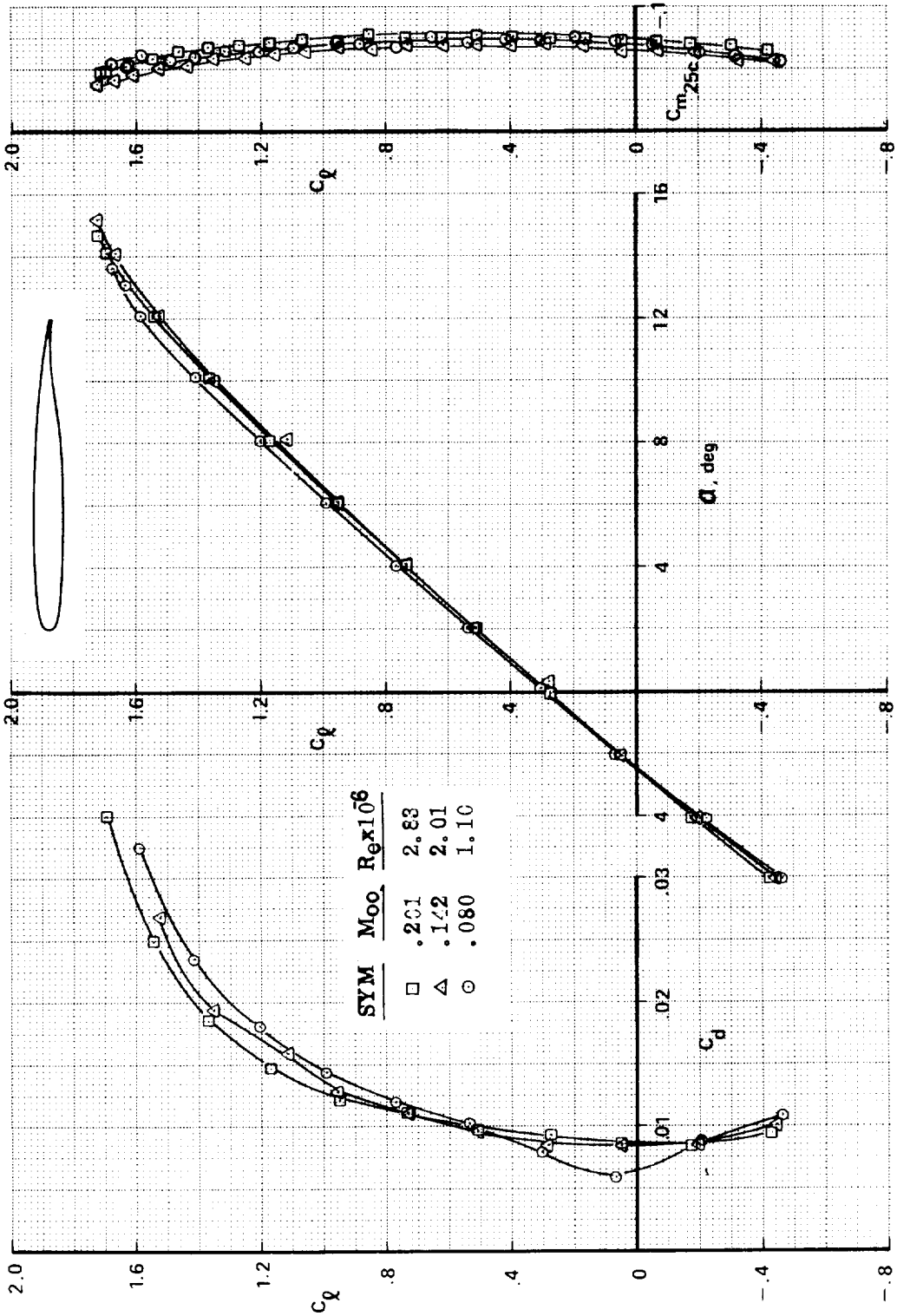

(b)

FIGURE A1.—Concluded

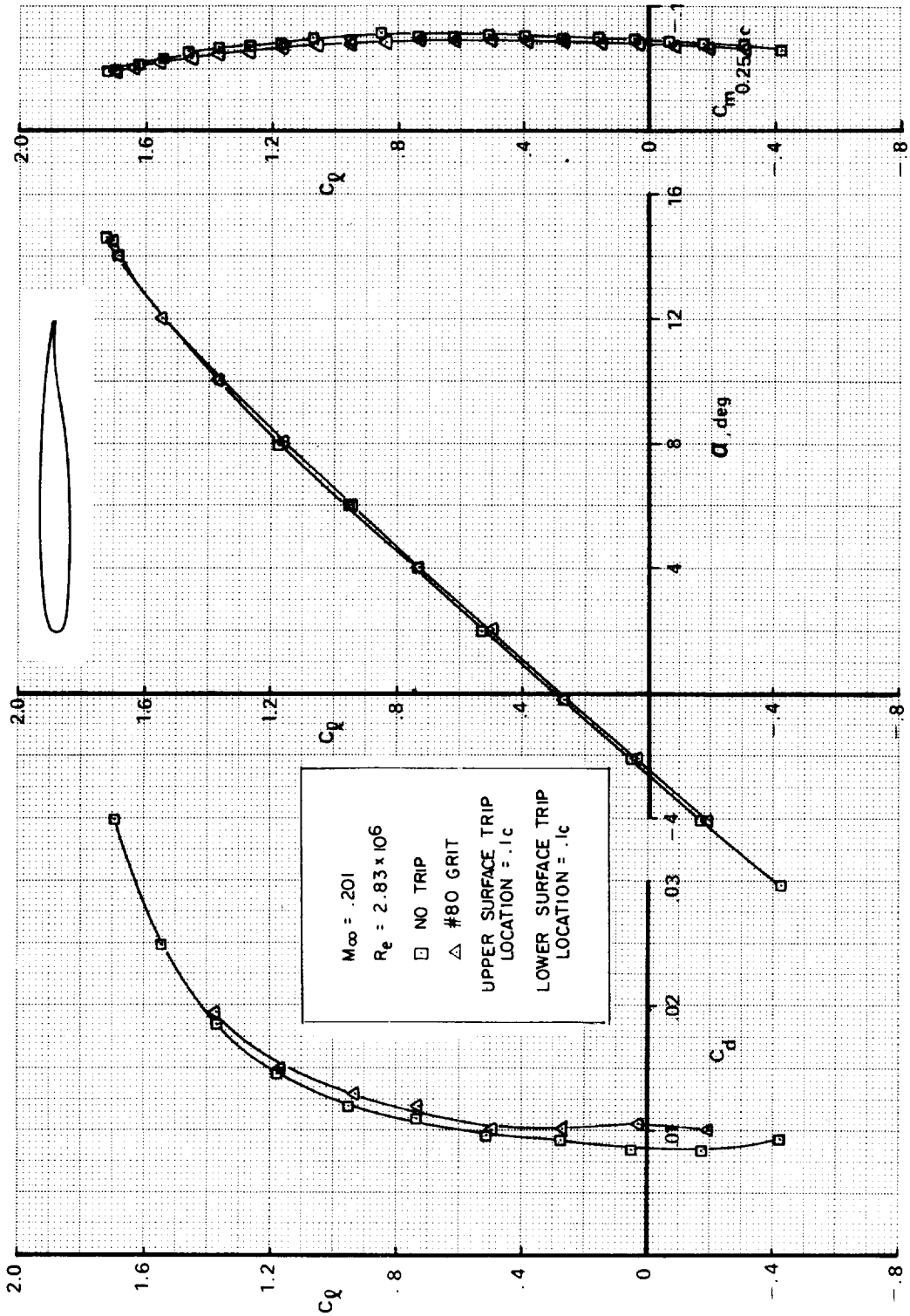

FIGURE A2.–TRANSITION STRIP EFFECT–MODEL A

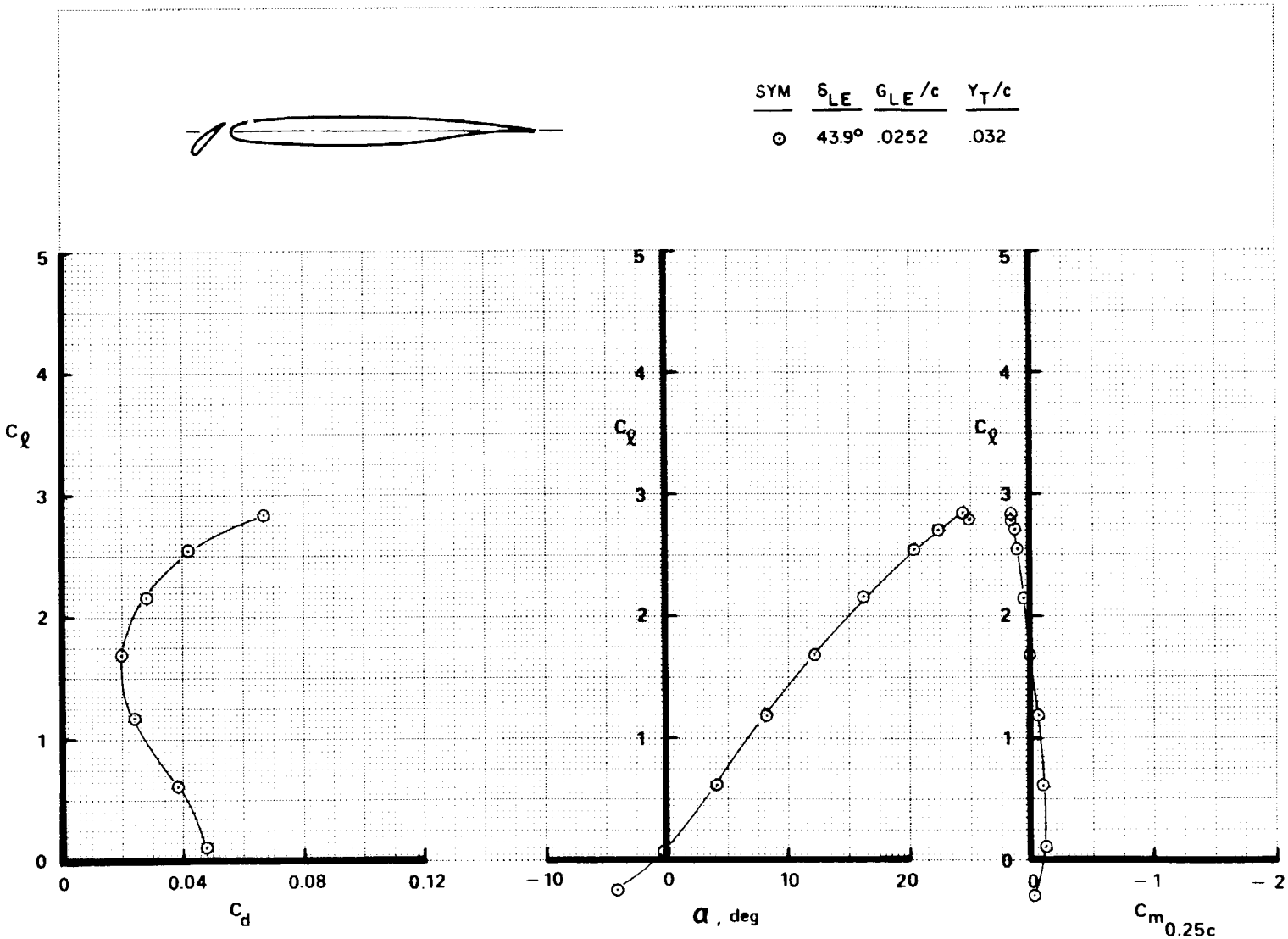

FIGURE A3.—EFFECT OF SLAT 2—MODEL A

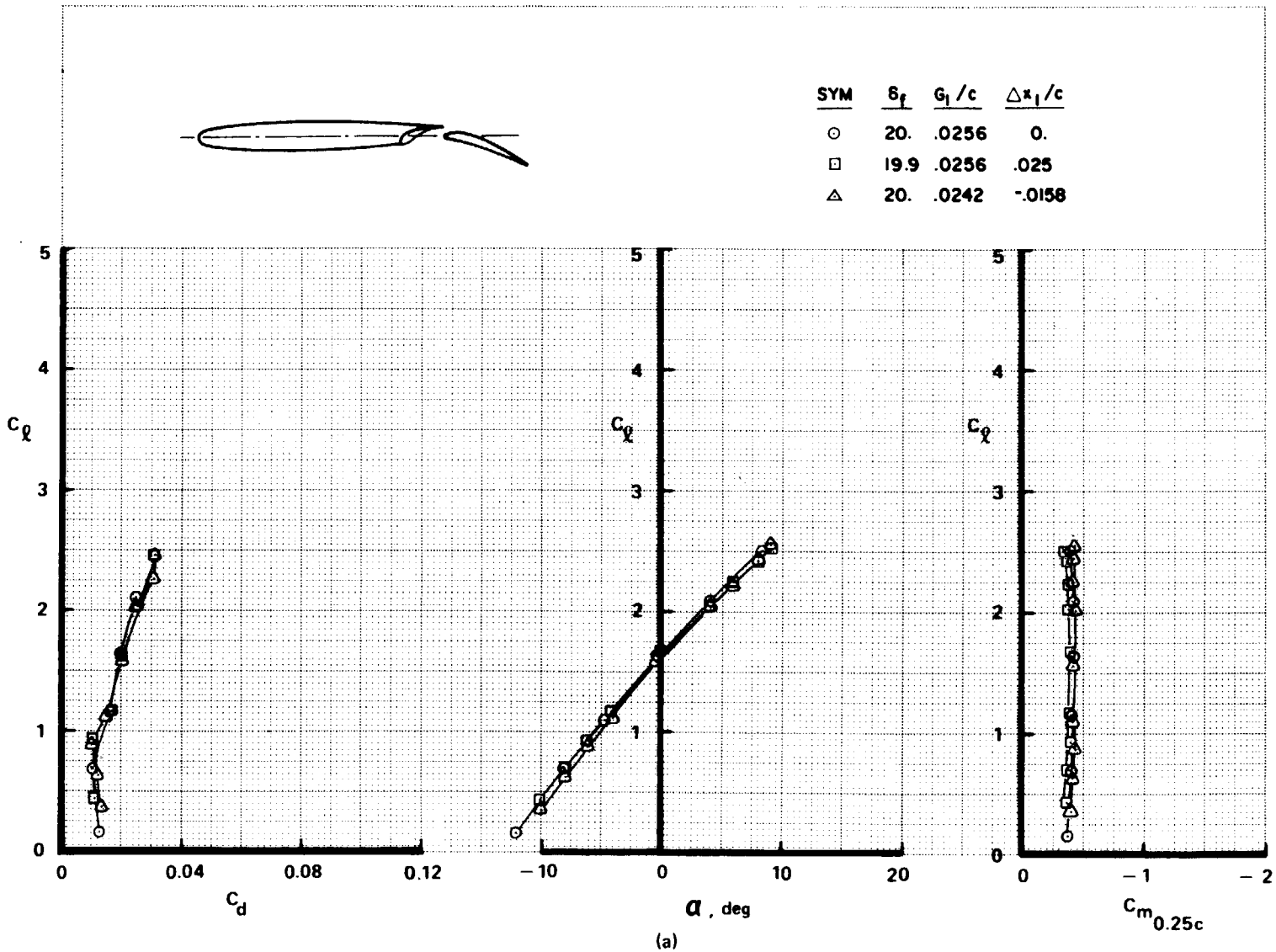

(a)

FIGURE A4.–EFFECT OF FLAP SLOT GAP AND OVERLAP–MODEL B ($\delta_{f_{eq}} = 20°$)

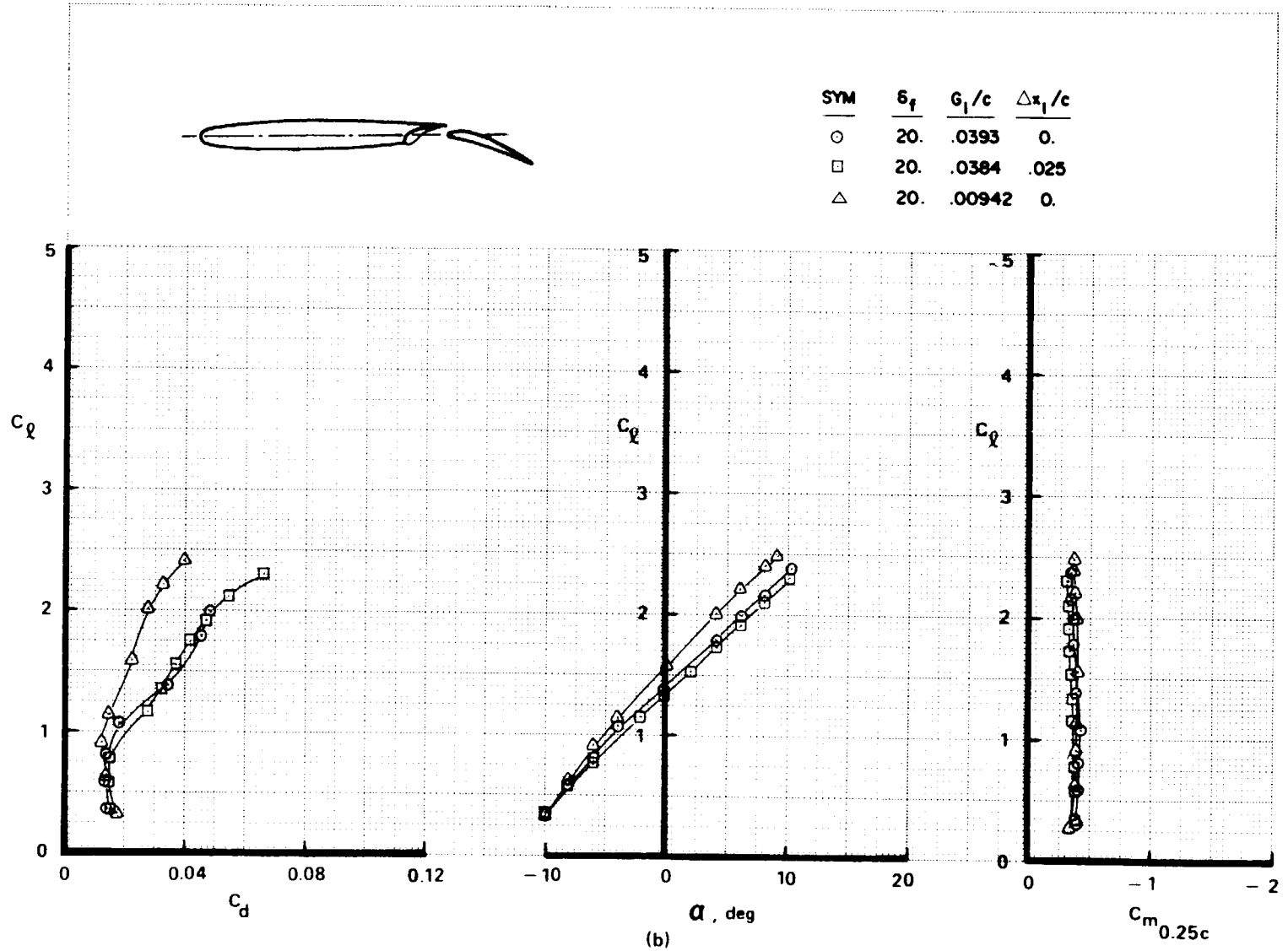

FIGURE A4.—Continued

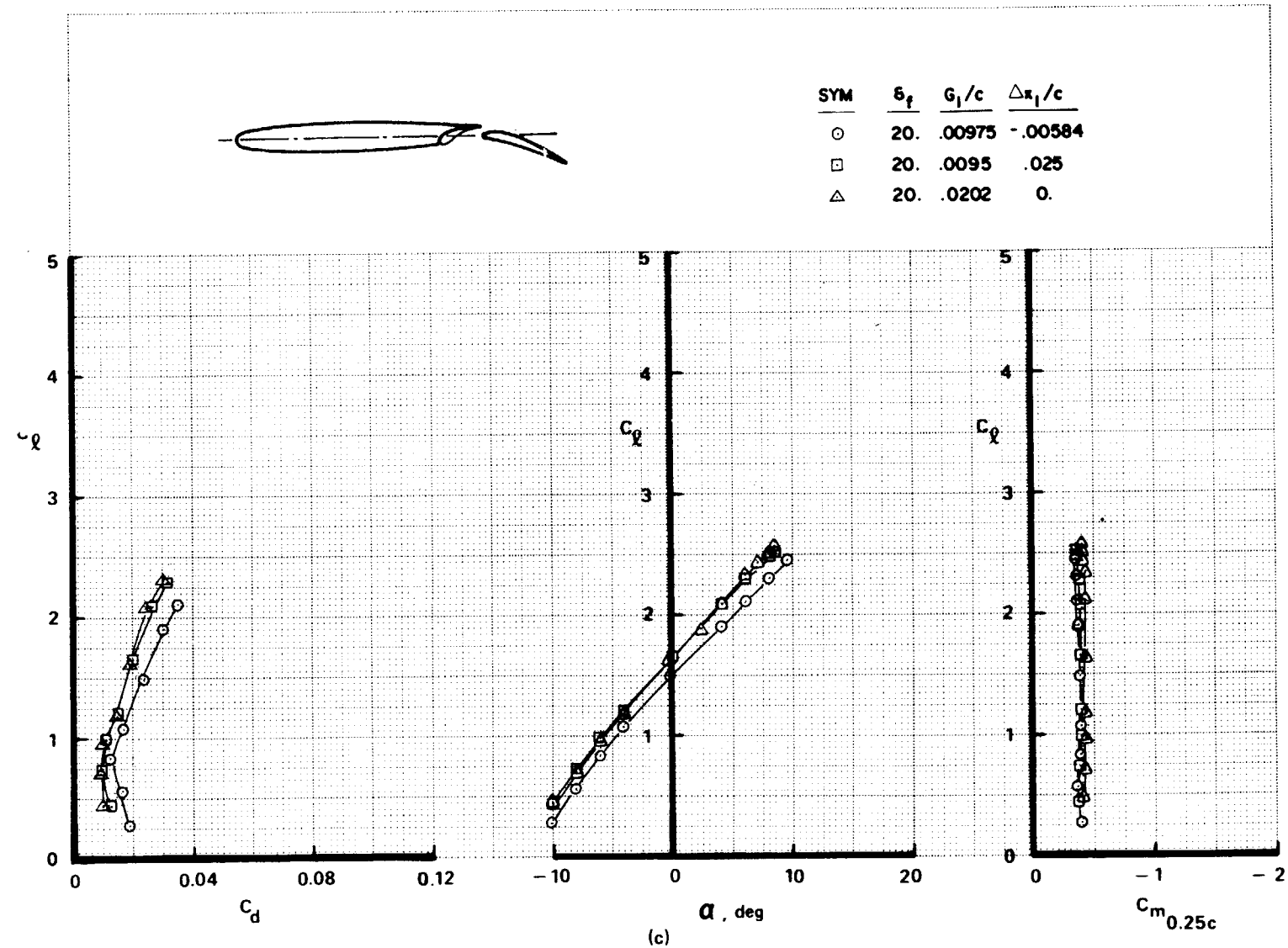

(c)

FIGURE A4.—Concluded

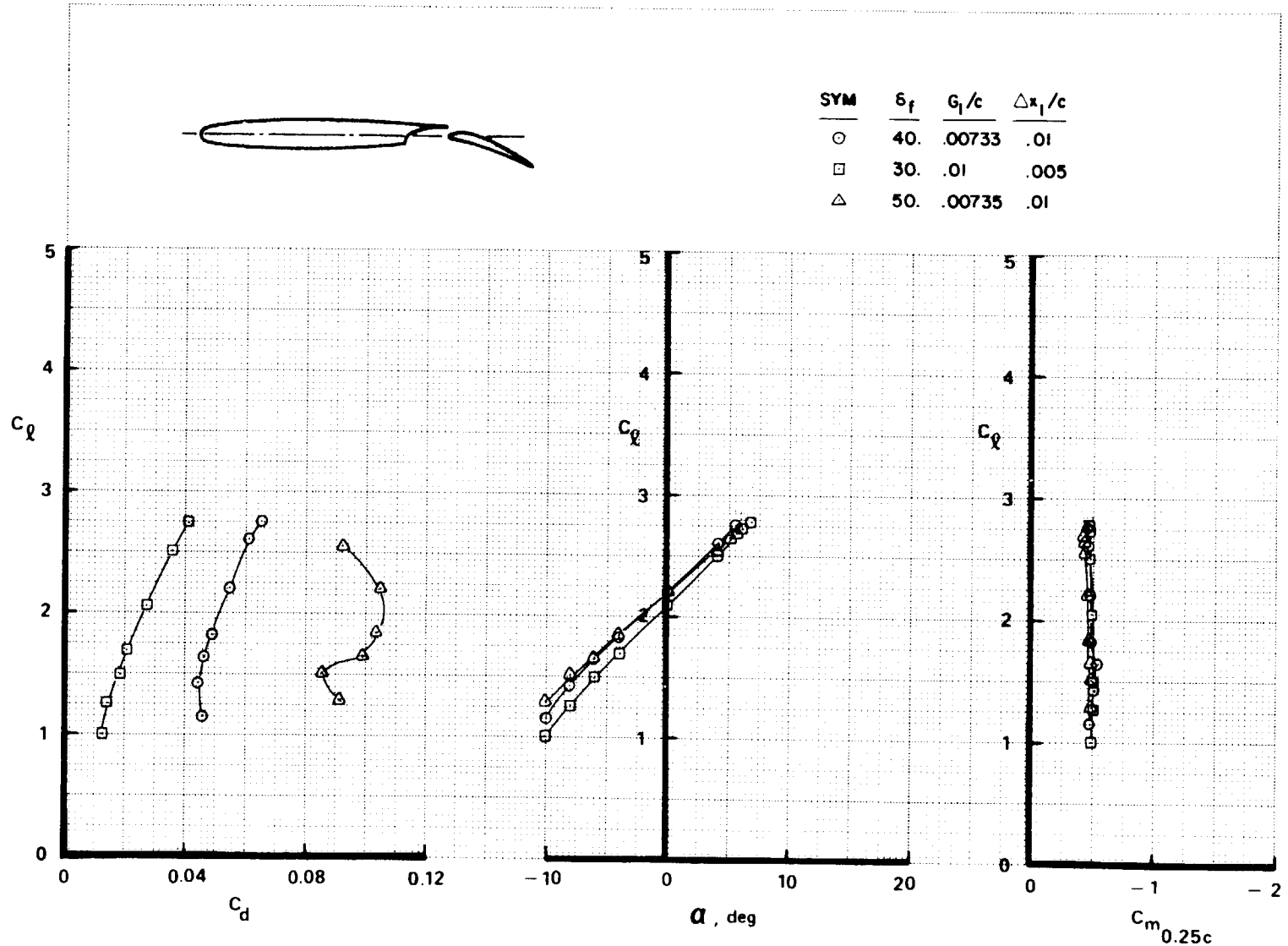

FIGURE A5.–EFFECT OF FLAP DEFLECTION ANGLE VARIATION–MODEL B

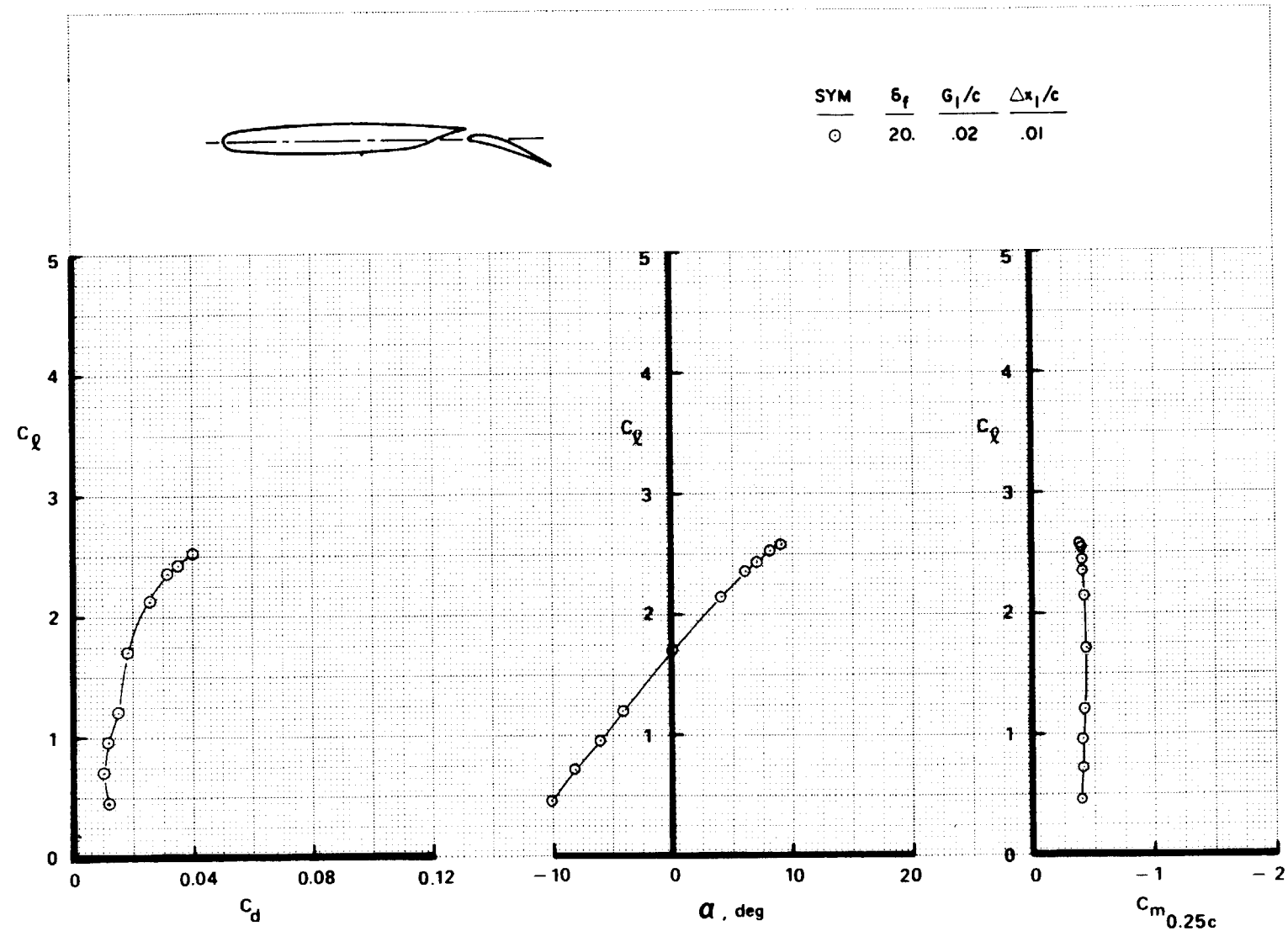

FIGURE A6.—BOUNDARY-LAYER STUDY CONFIGURATION—MODEL B ($\delta_{f_{eq}} = 20°$)

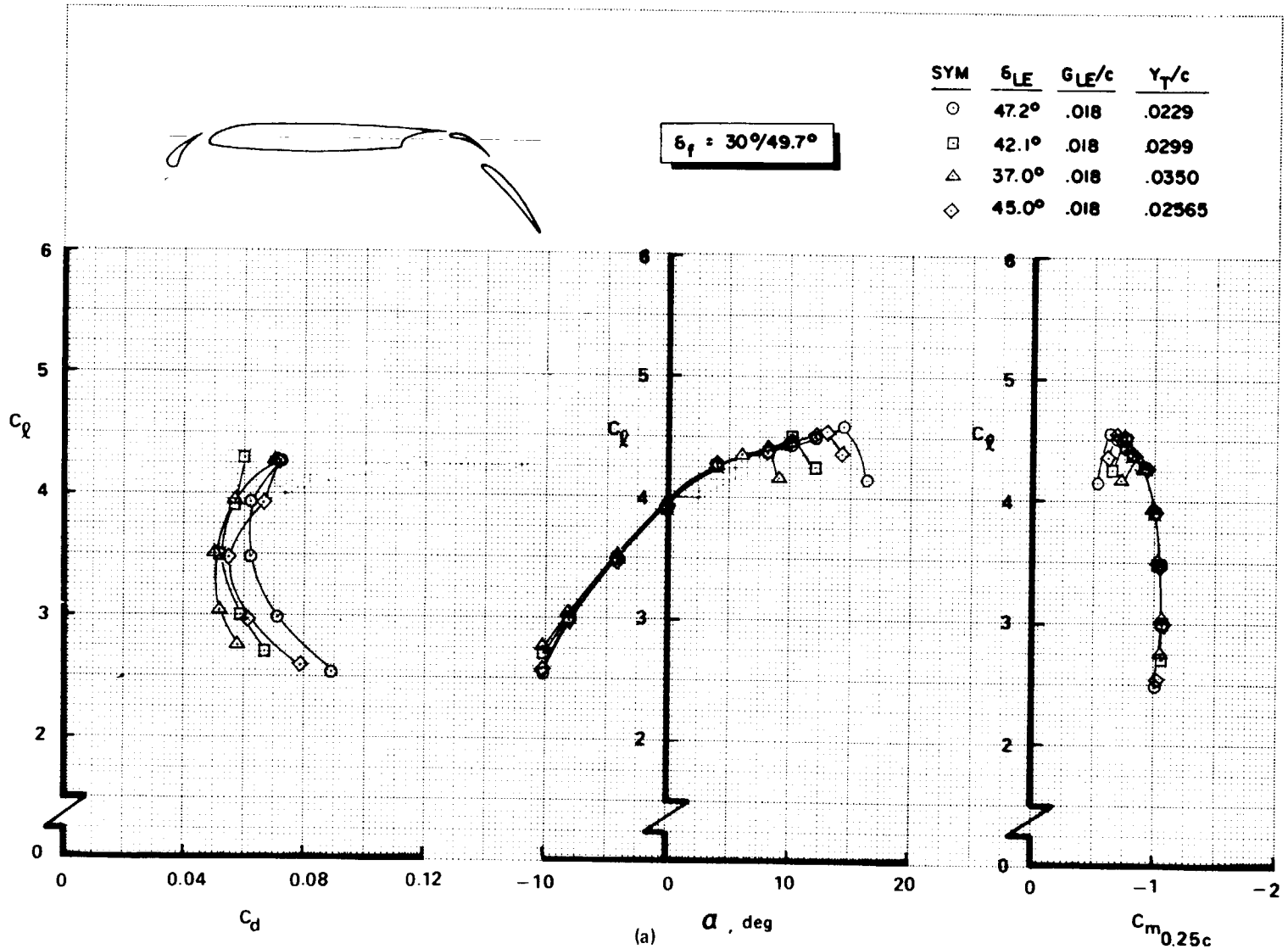

FIGURE A7.–EFFECT OF SLAT 1 DEFLECTION ANGLE VARIATION–MODEL C ($\delta_{f_{eq}} = 44°$)

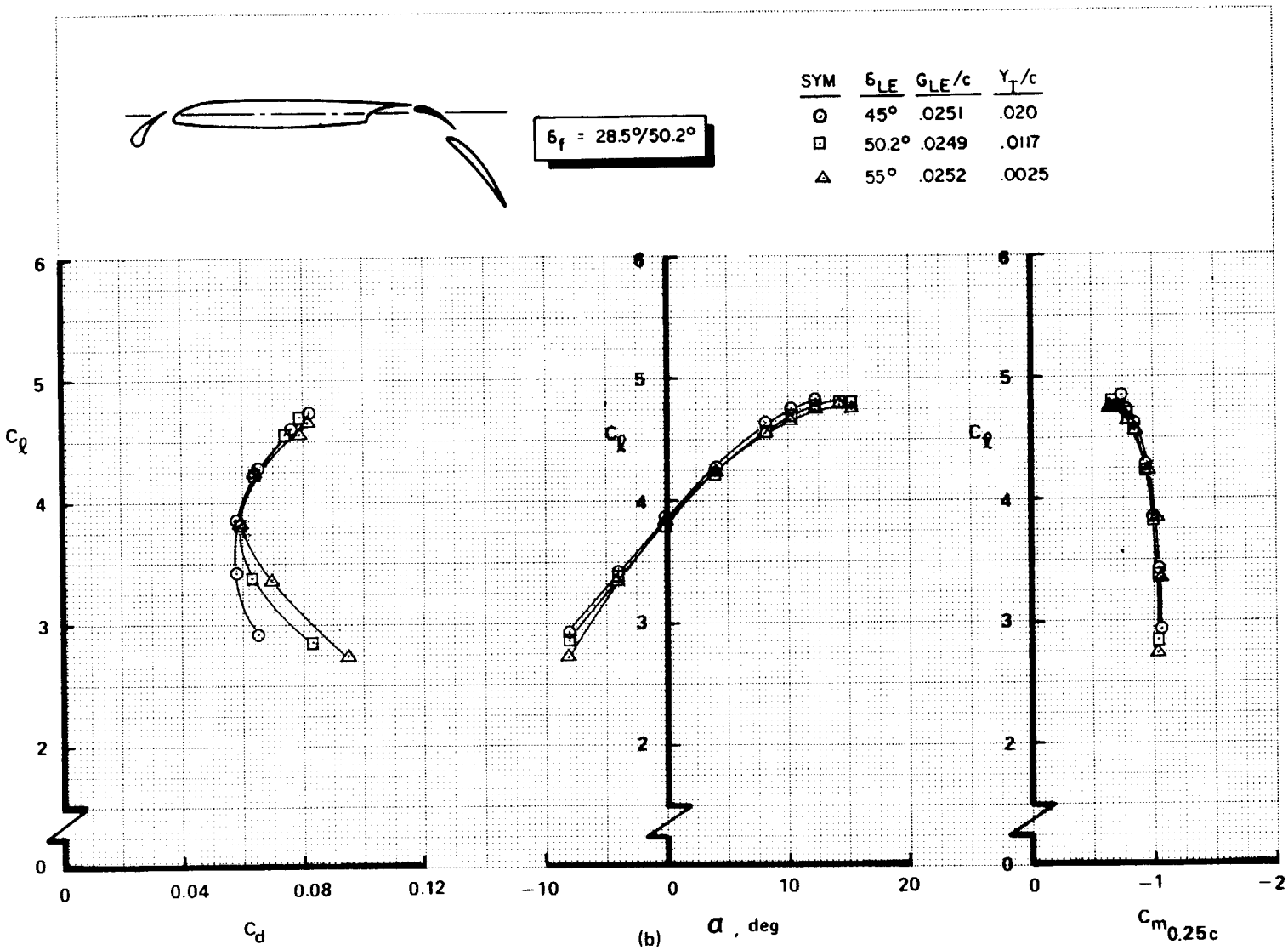

FIGURE A7.—Concluded

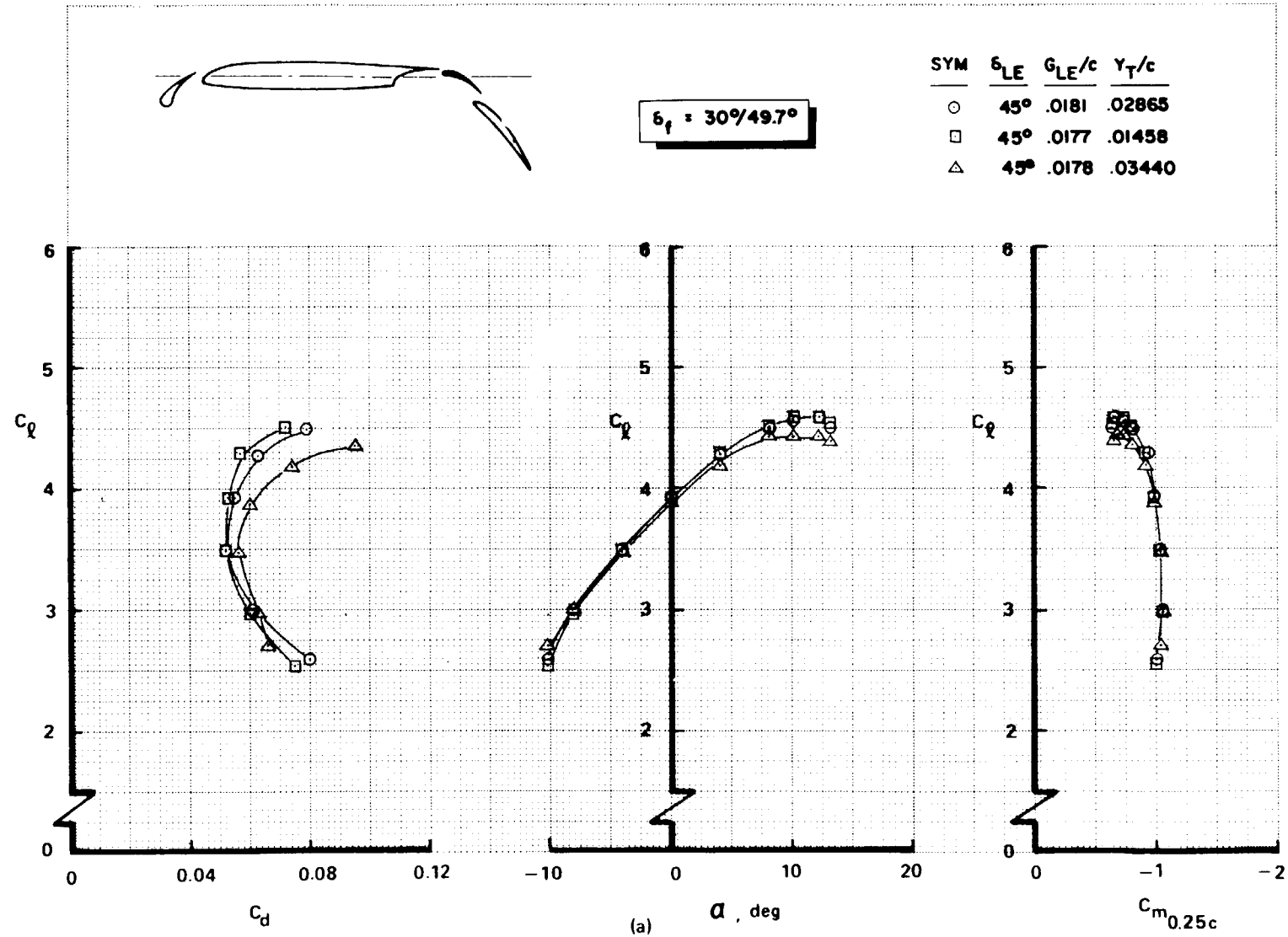

FIGURE A8.–SLAT 1 SLOT GAP AND HEIGHT OPTIMIZATION–MODEL C ($\delta_{f_{eq}} = 44°$)

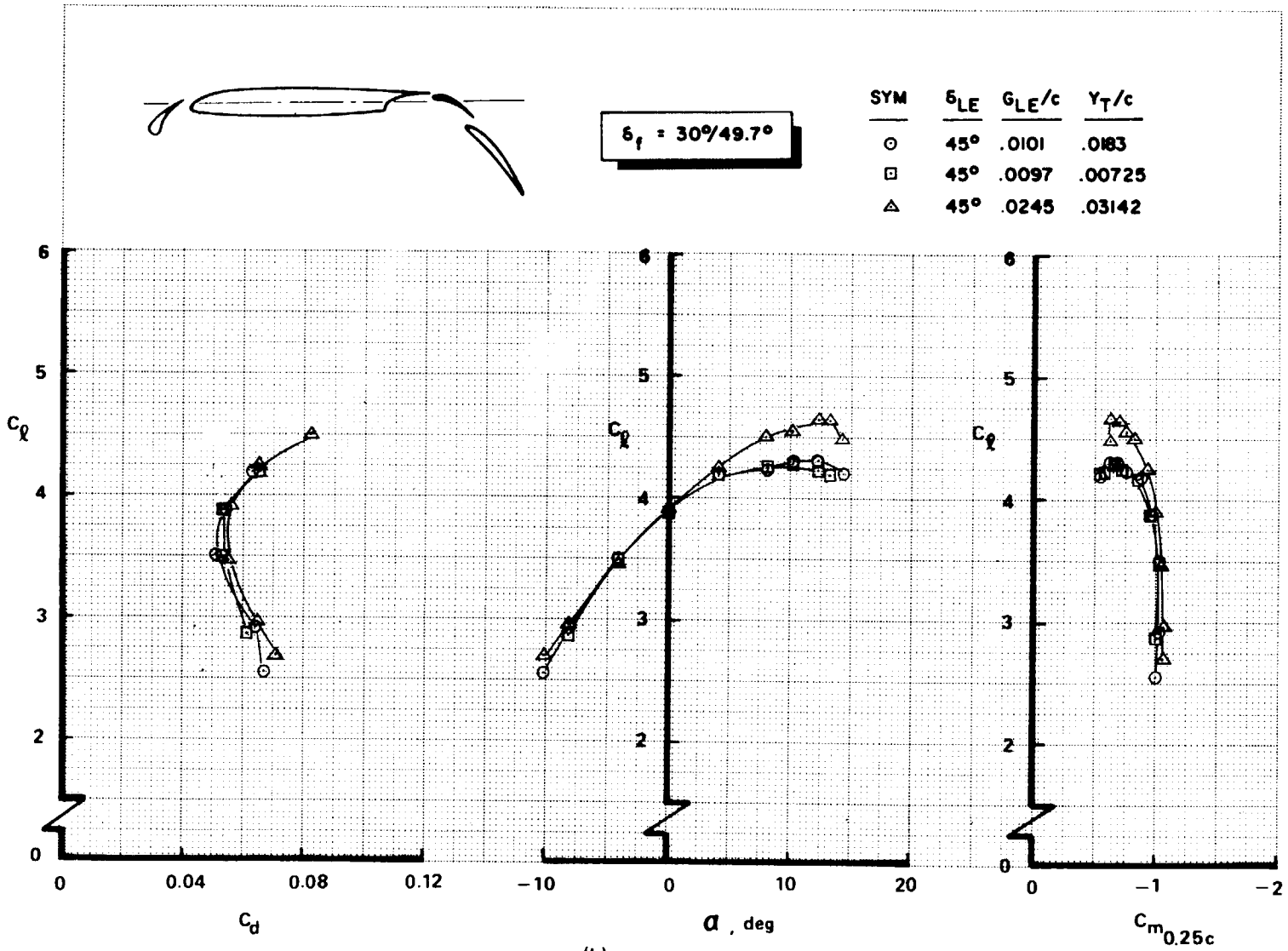

(b)

FIGURE A8.—Continued

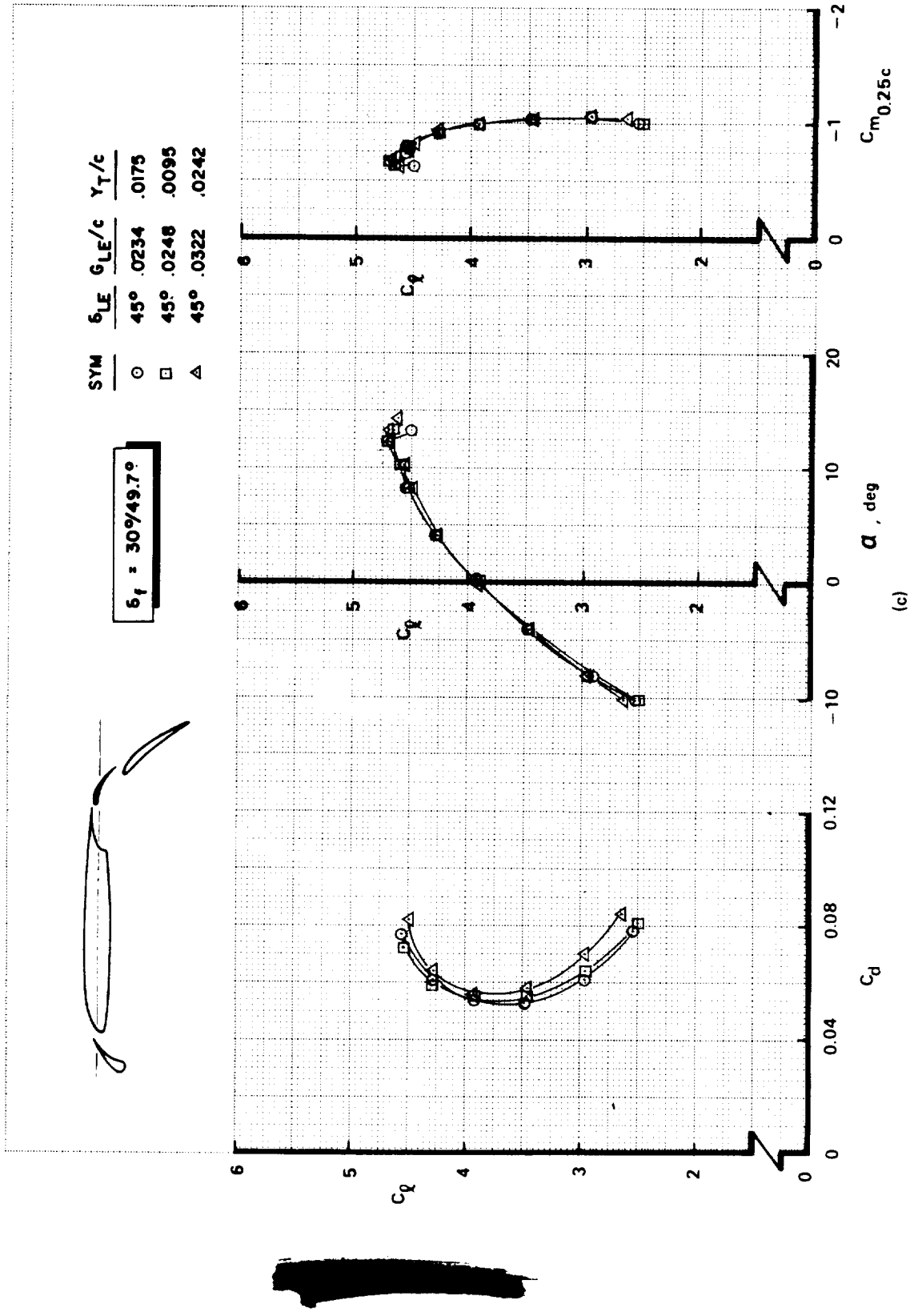

(c)

FIGURE A8.—Continued

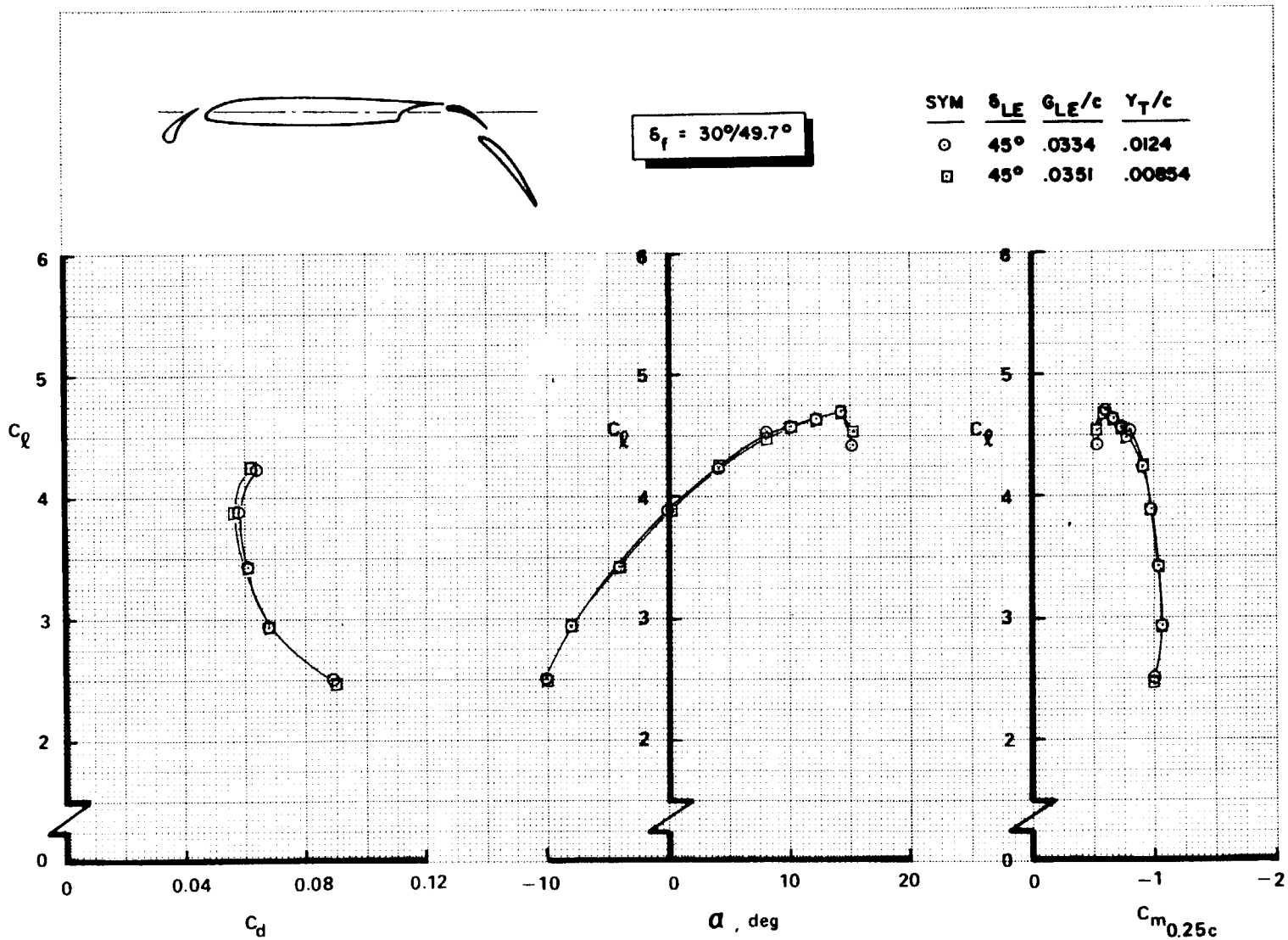

(d)

FIGURE A8.—Continued

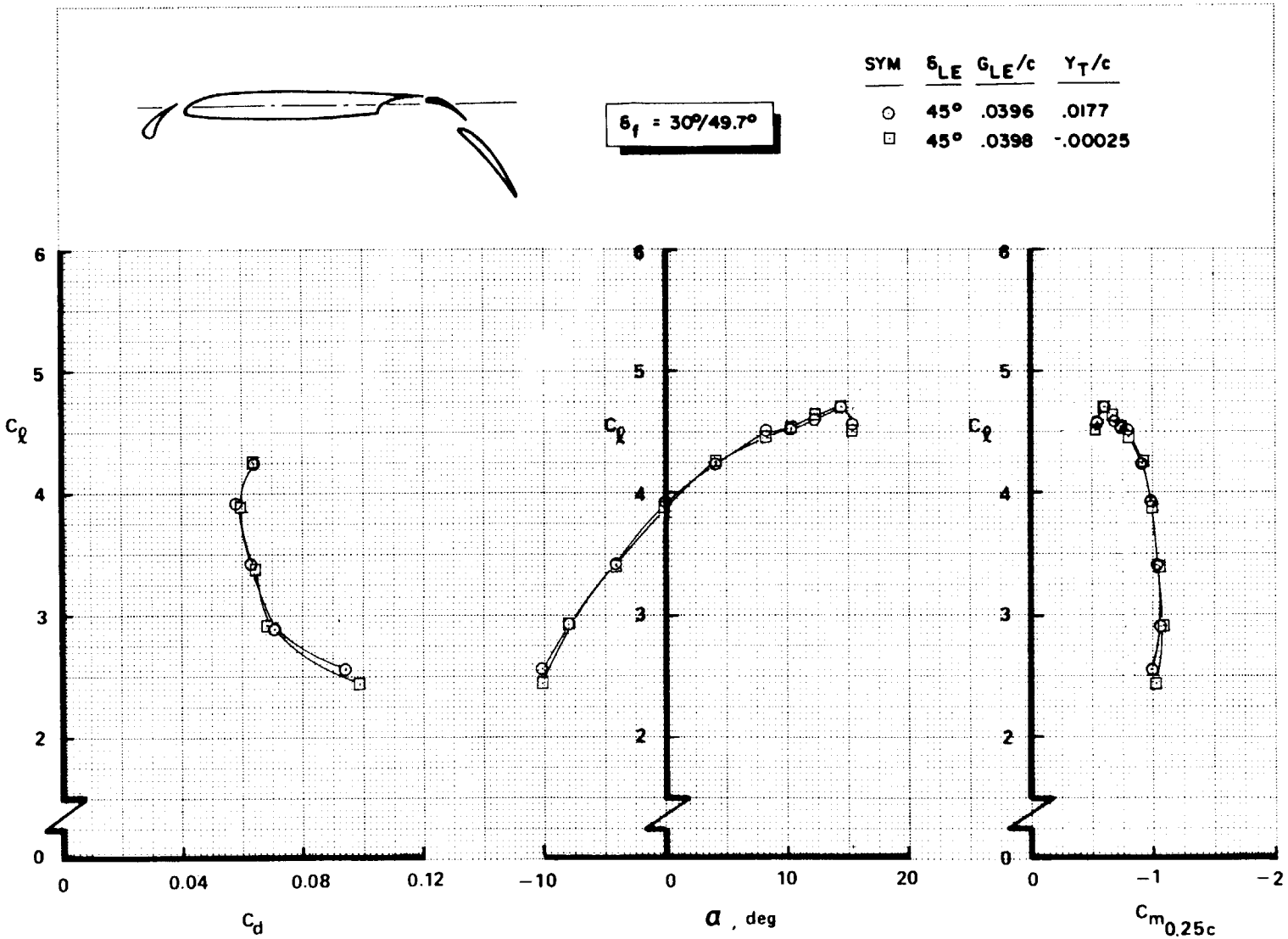

(e)

FIGURE A8.—Continued

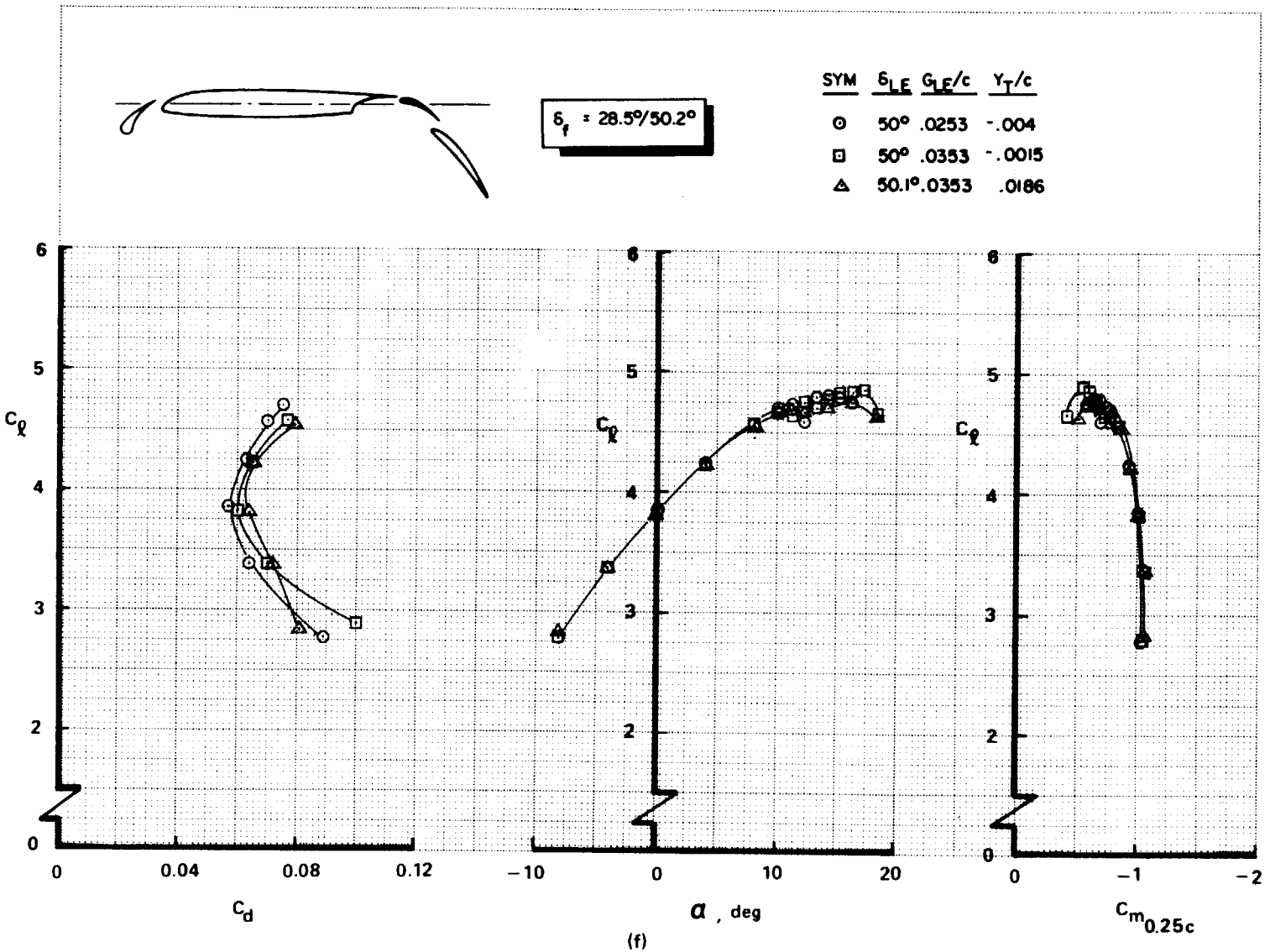

(f)

FIGURE A8.—Continued

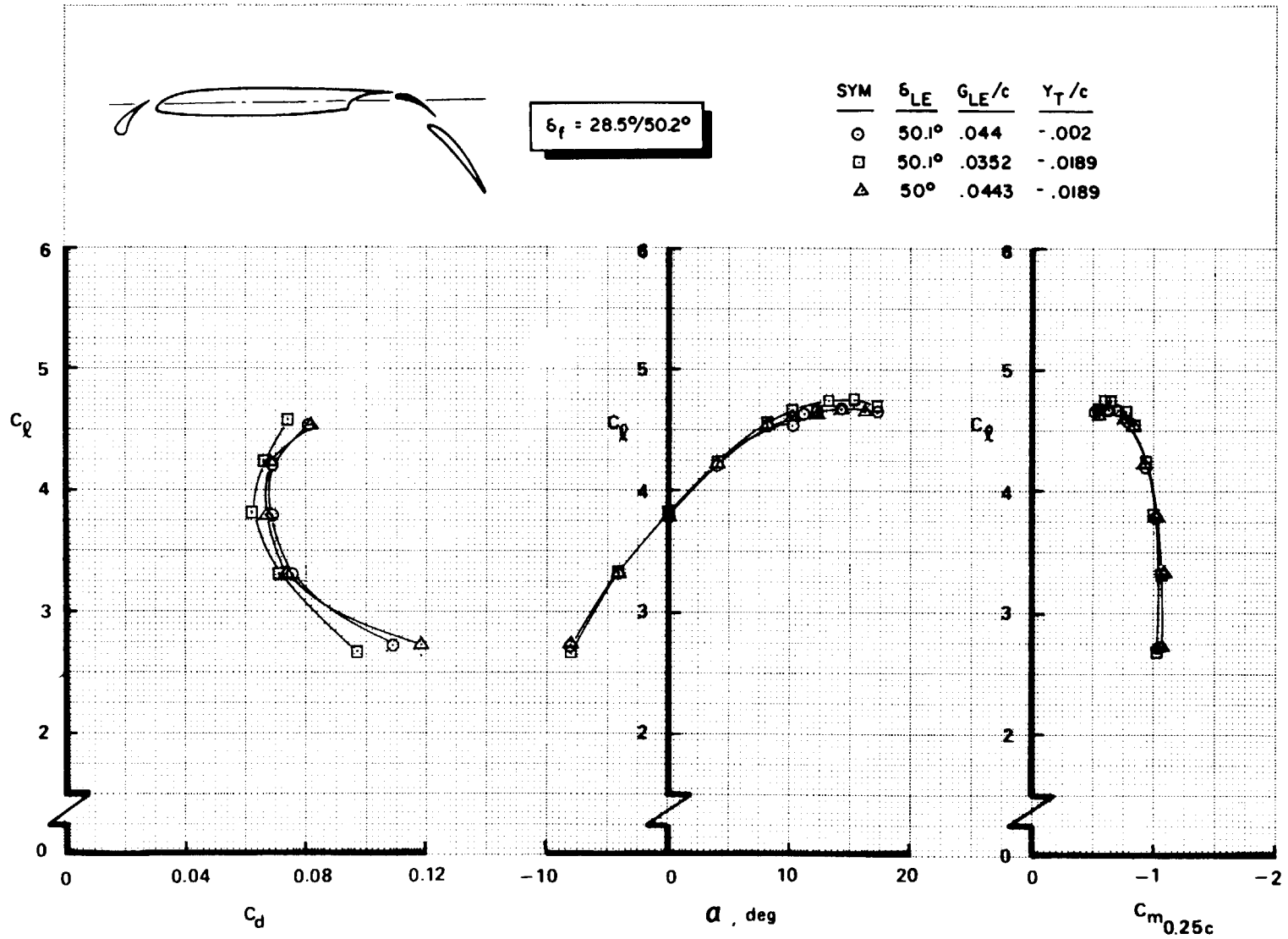

(g)

FIGURE A8.—Concluded

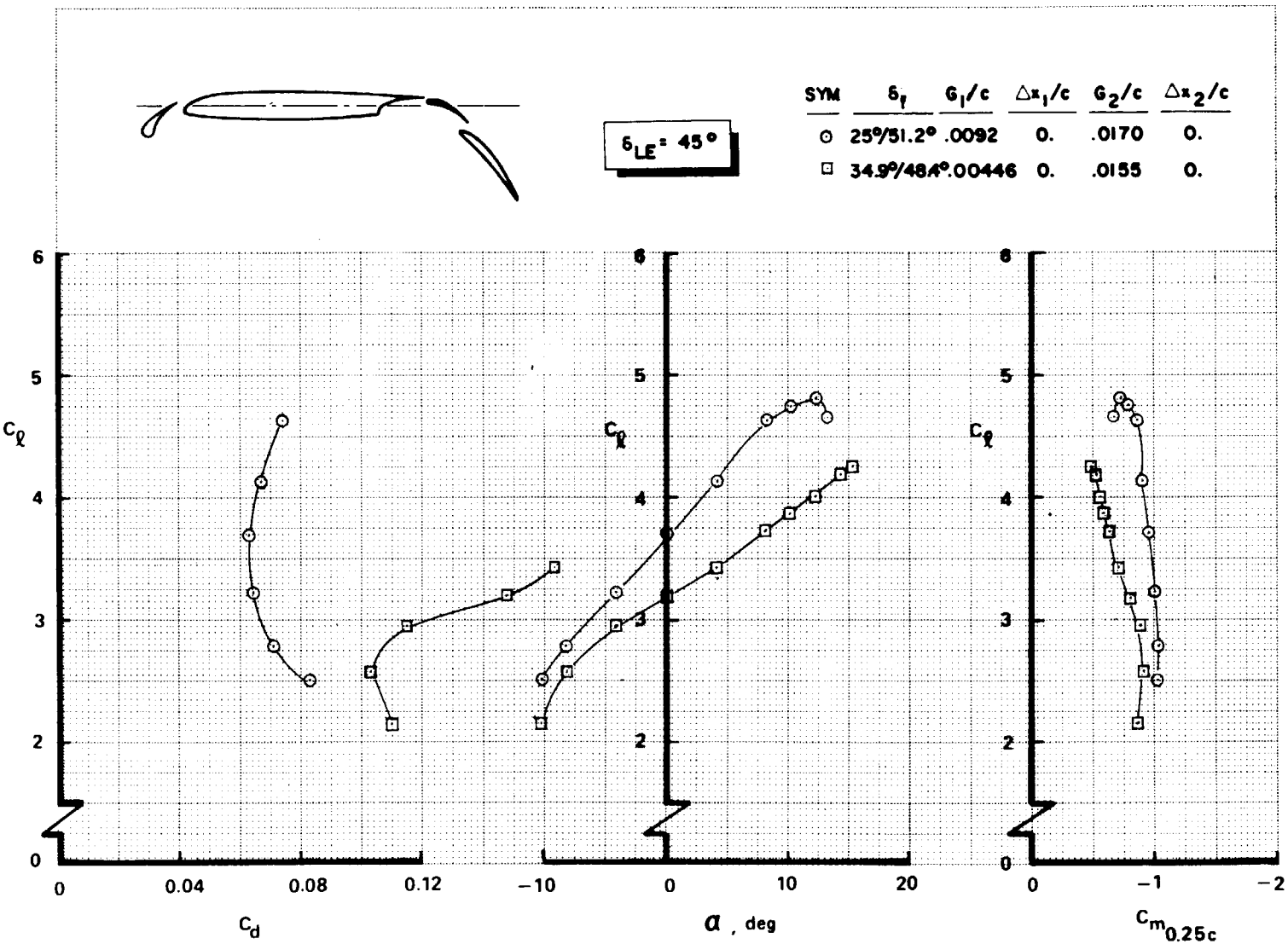

FIGURE A9.–EFFECT OF FLAP COMPONENT ANGLE COMBINATION AT CONSTANT $\delta_{f_{eq}}$ (44°)–MODEL C

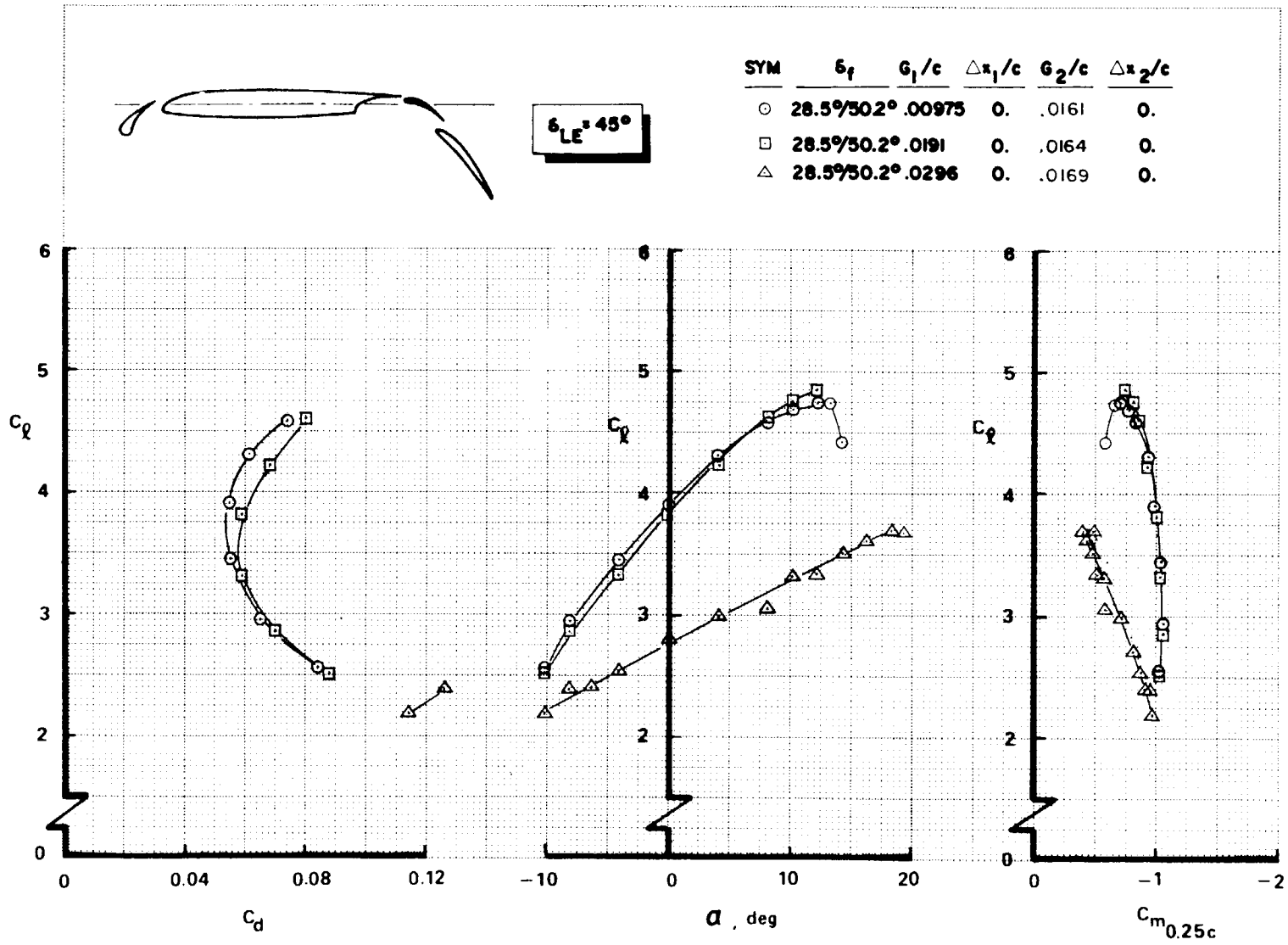

(a)

FIGURE A10.–EFFECT OF WING-VANE SLOT GAP AND OVERLAP–MODEL C ($\delta_{f_{eq}} = 44°$)

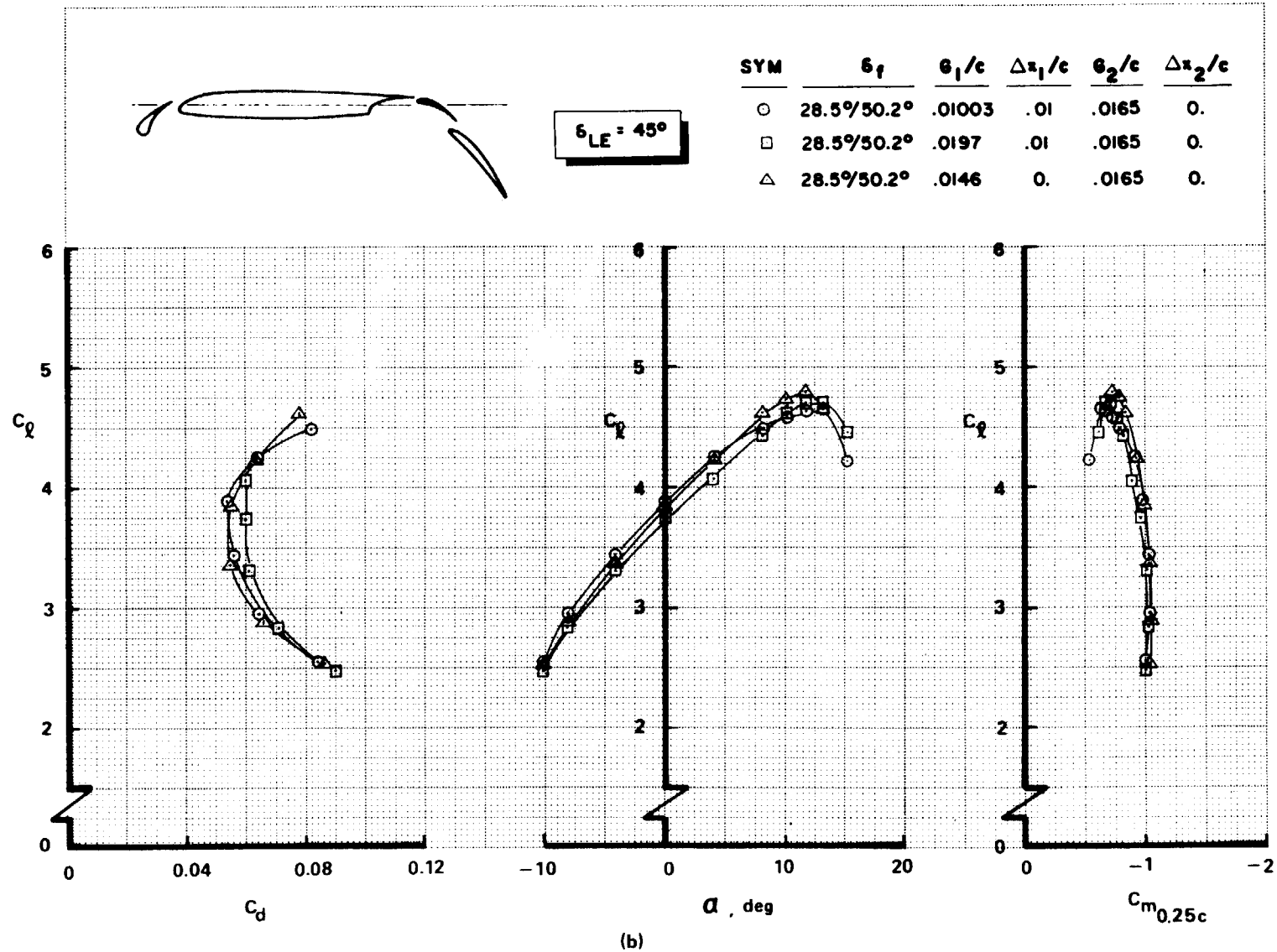

(b)

FIGURE A10.—Continued

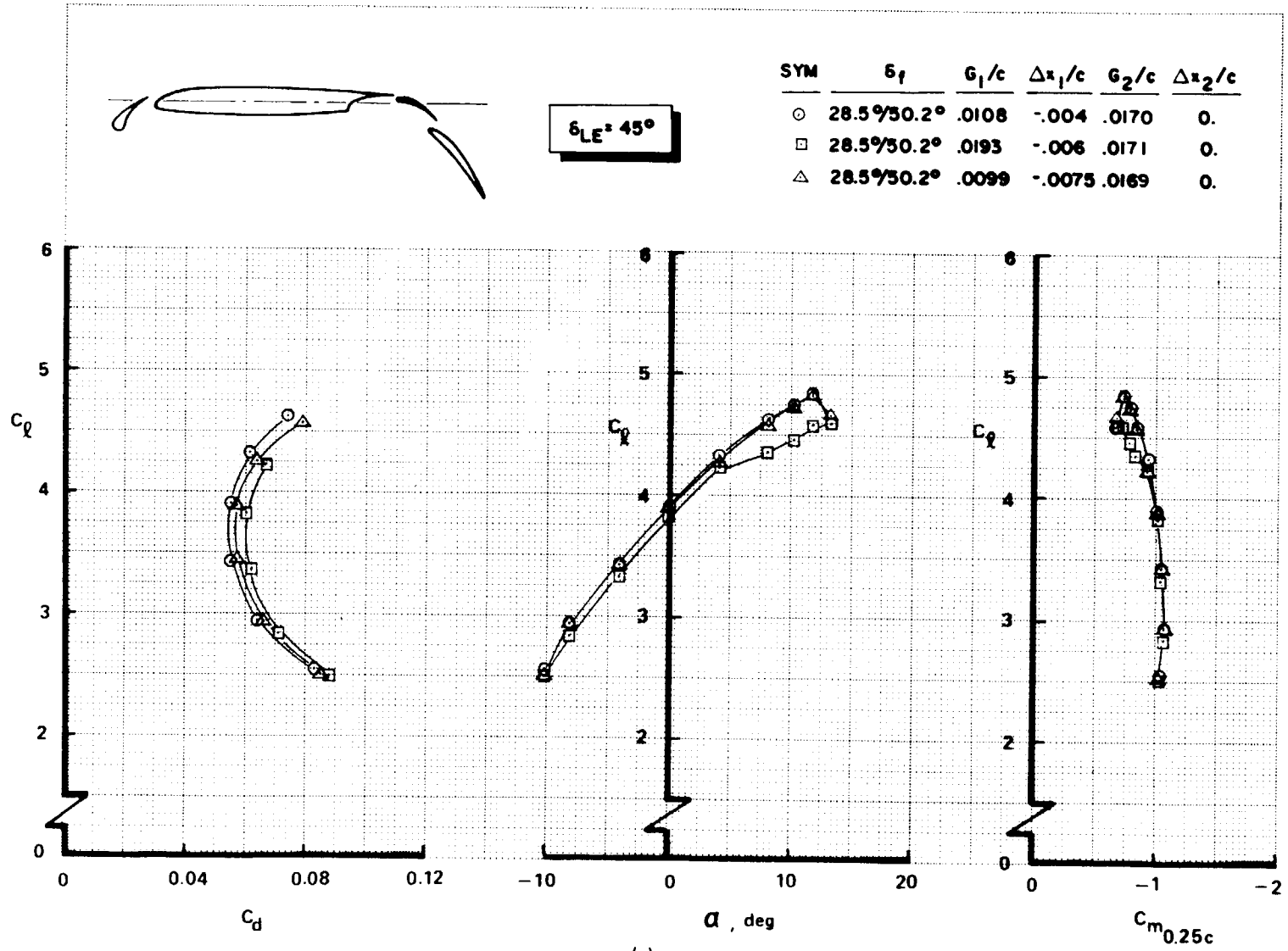

(c)

FIGURE A10.—Continued

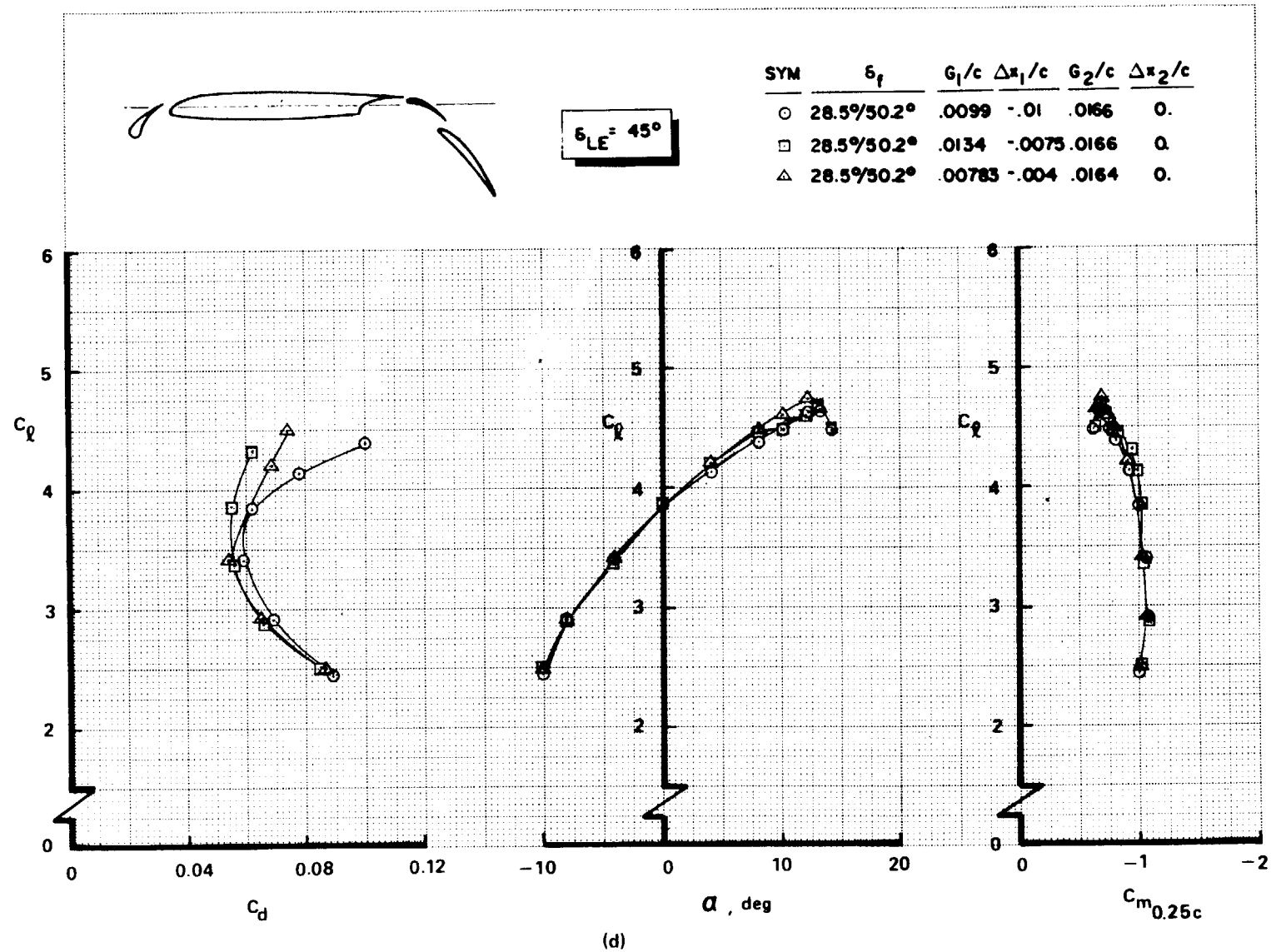

(d)

FIGURE A10.—Concluded

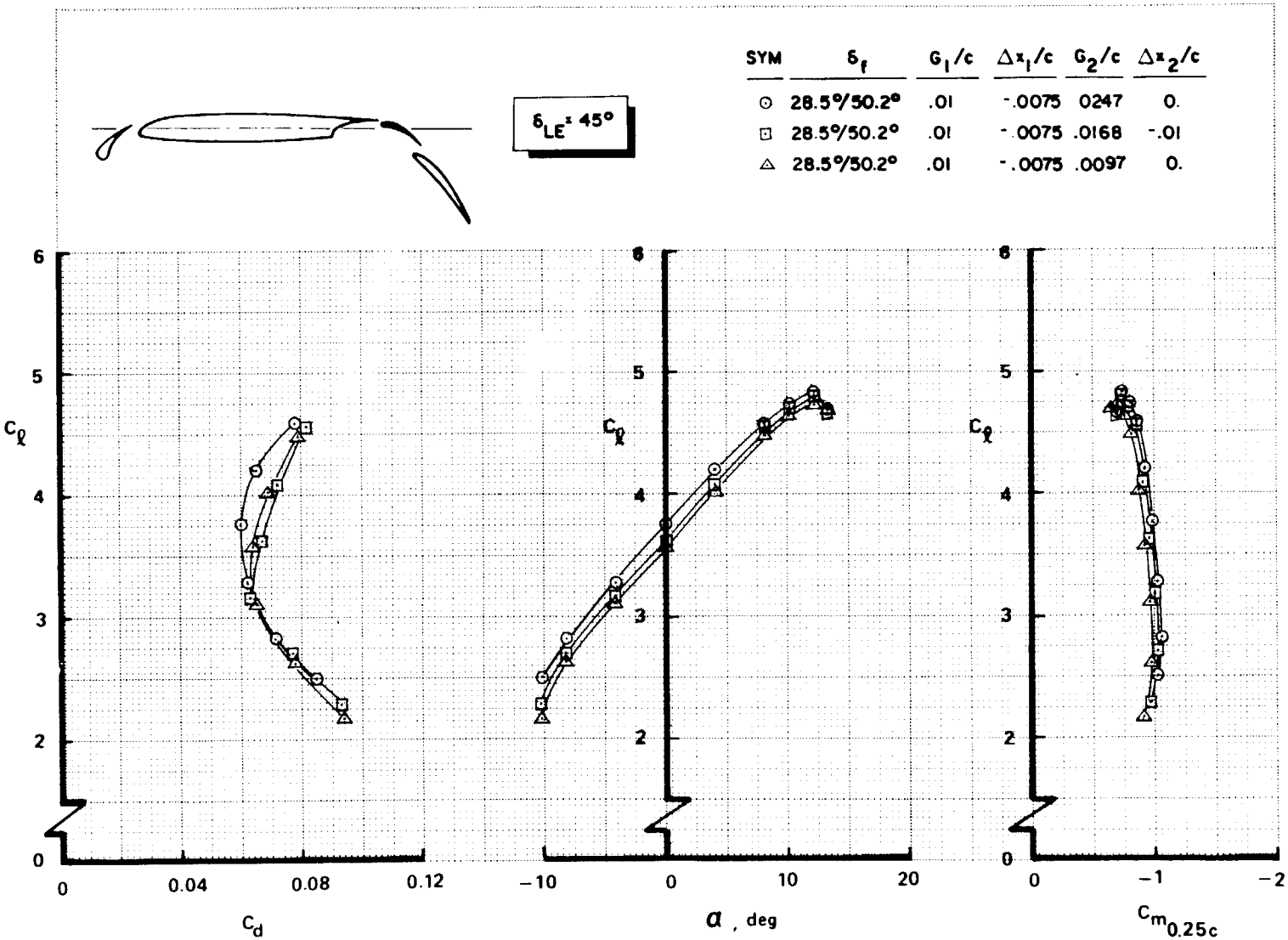

(a)

FIGURE A11.–EFFECT OF VANE-FLAP SLOT GAP AND OVERLAP–MODEL C ($\delta_{f_{eq}}$ = 44°)

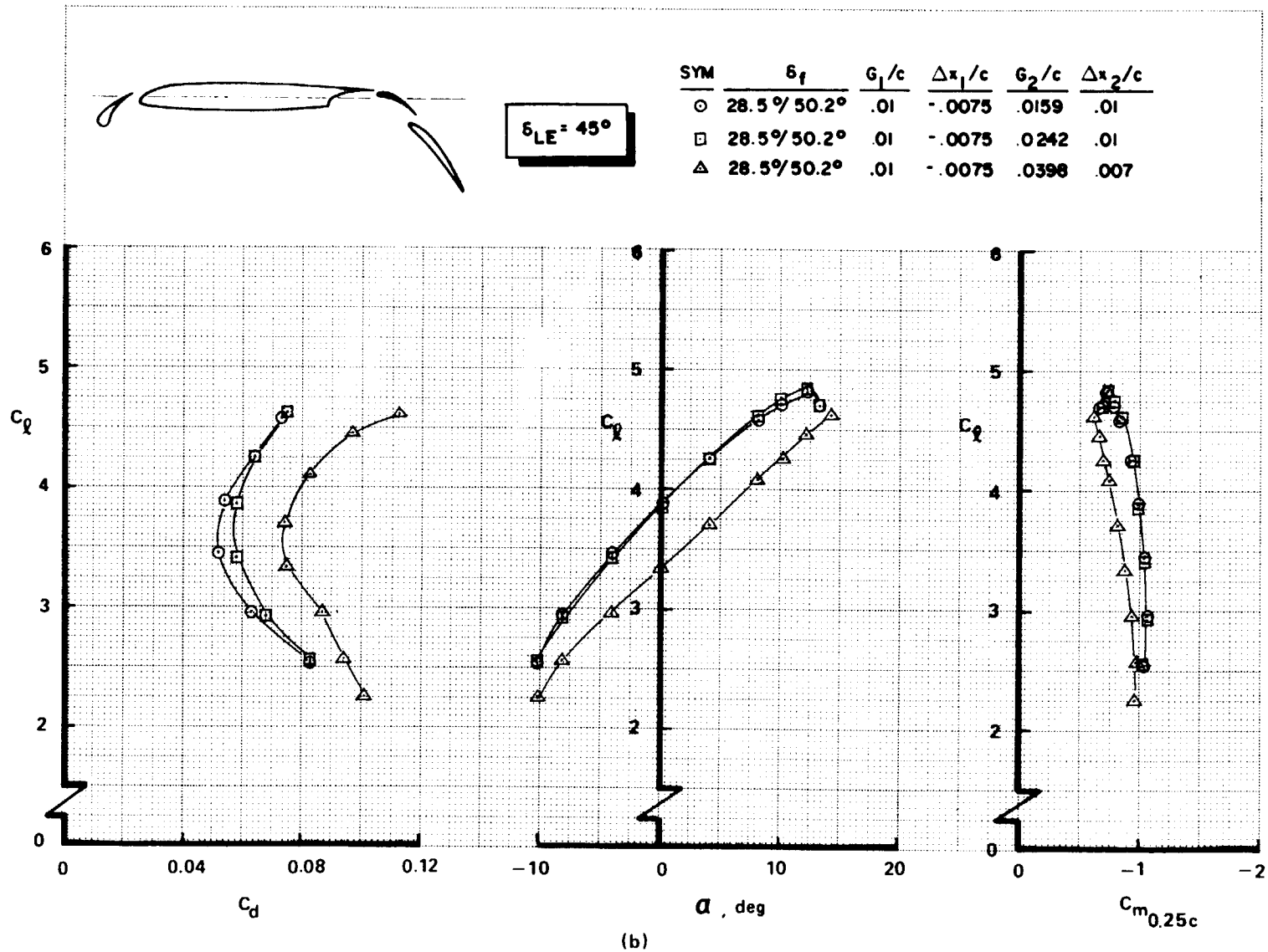

(b)

FIGURE A11.—Continued

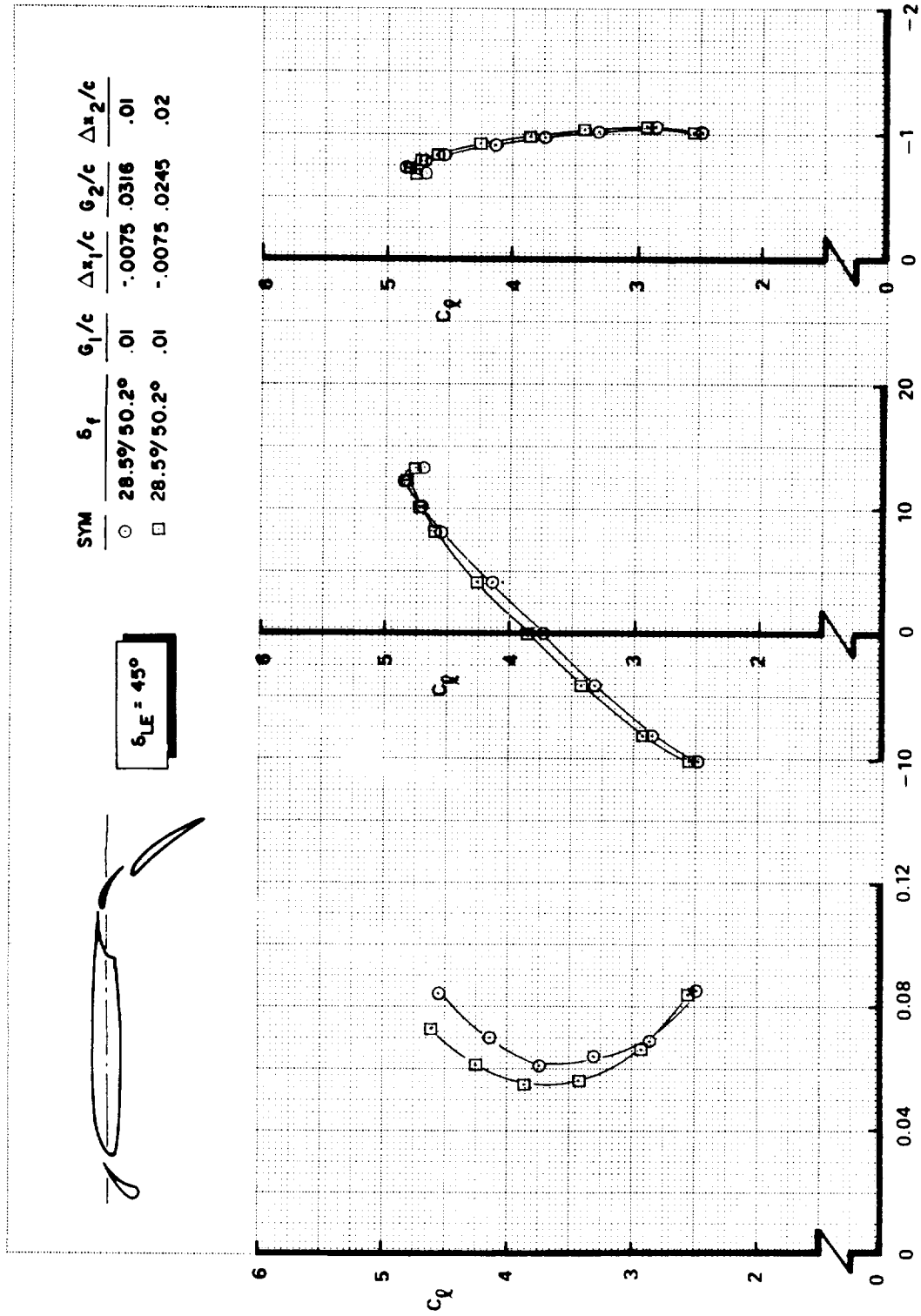

FIGURE A11.–Continued

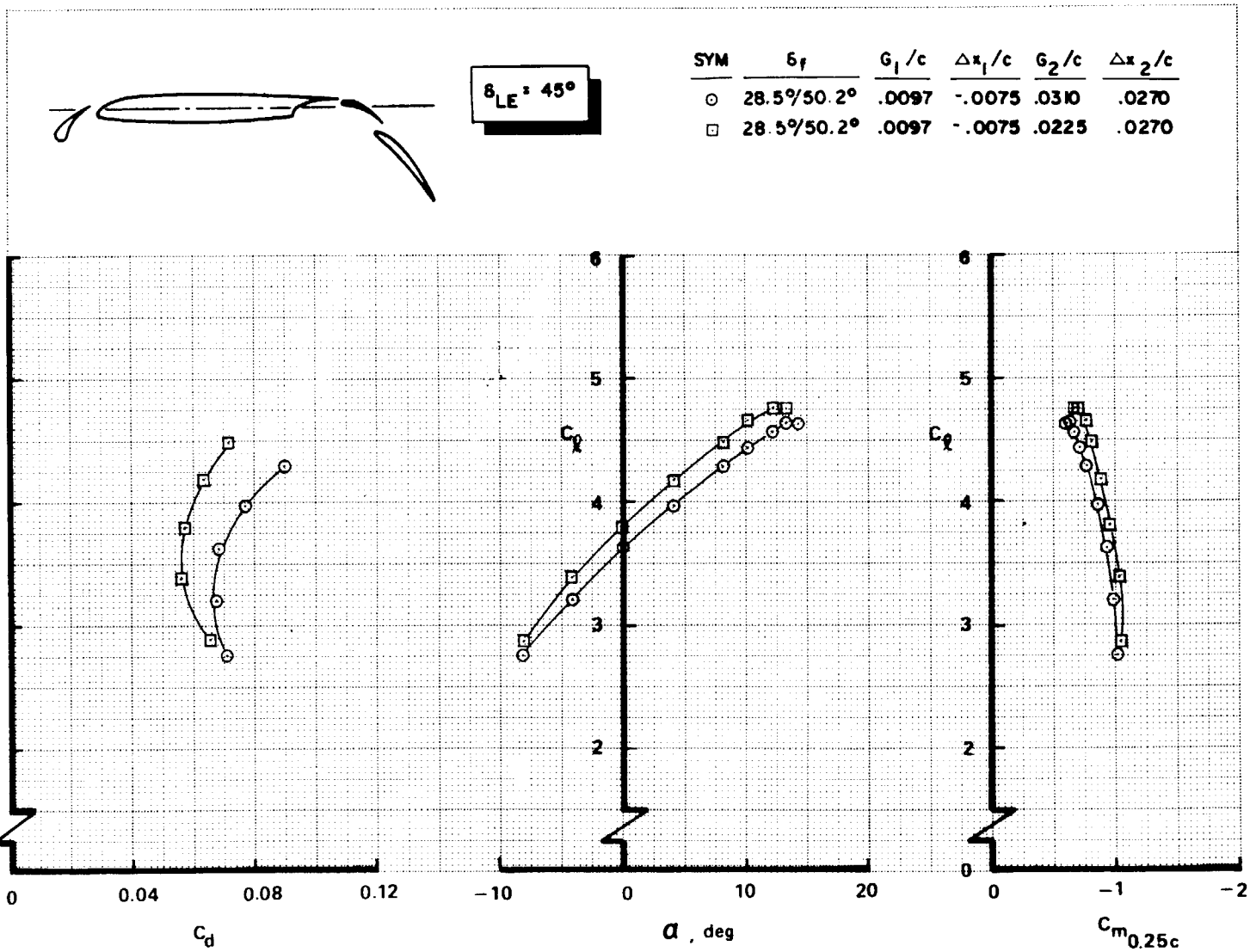

(d)

FIGURE A11.—Concluded

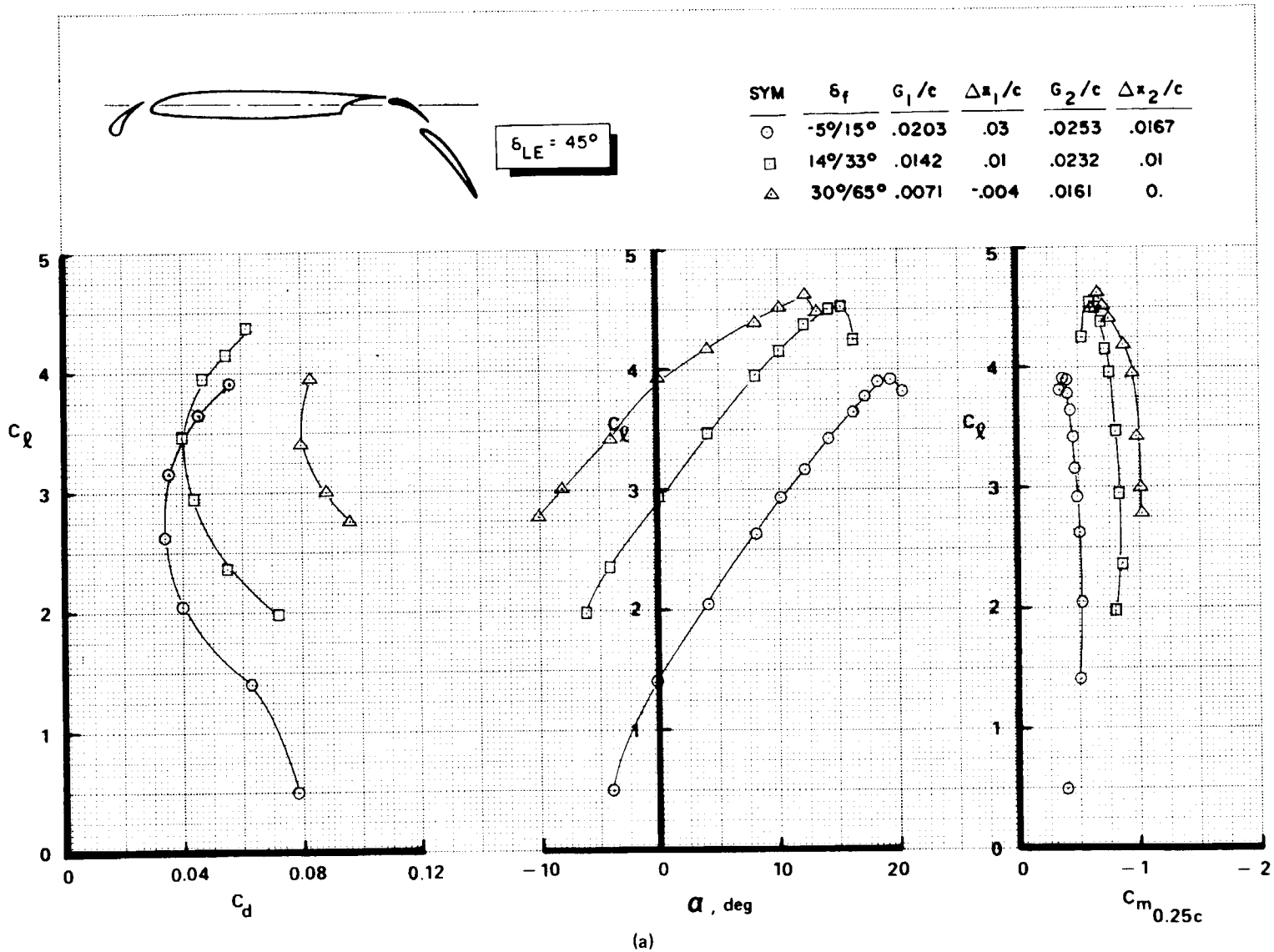

(a)

FIGURE A12.—EFFECT OF FLAP DEFLECTION ANGLE VARIATION—MODEL C

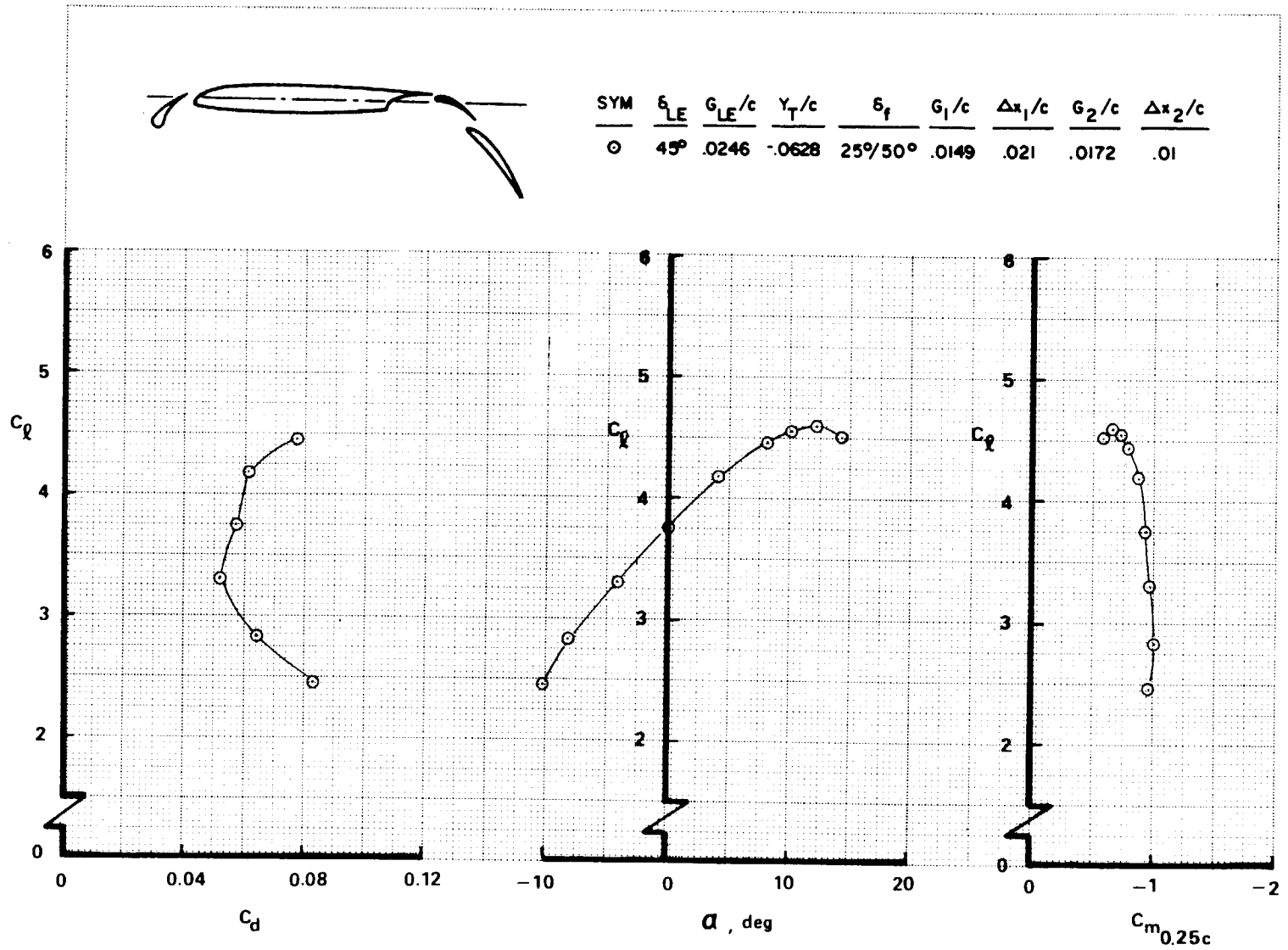

(b)

FIGURE A12.—CONCLUDED

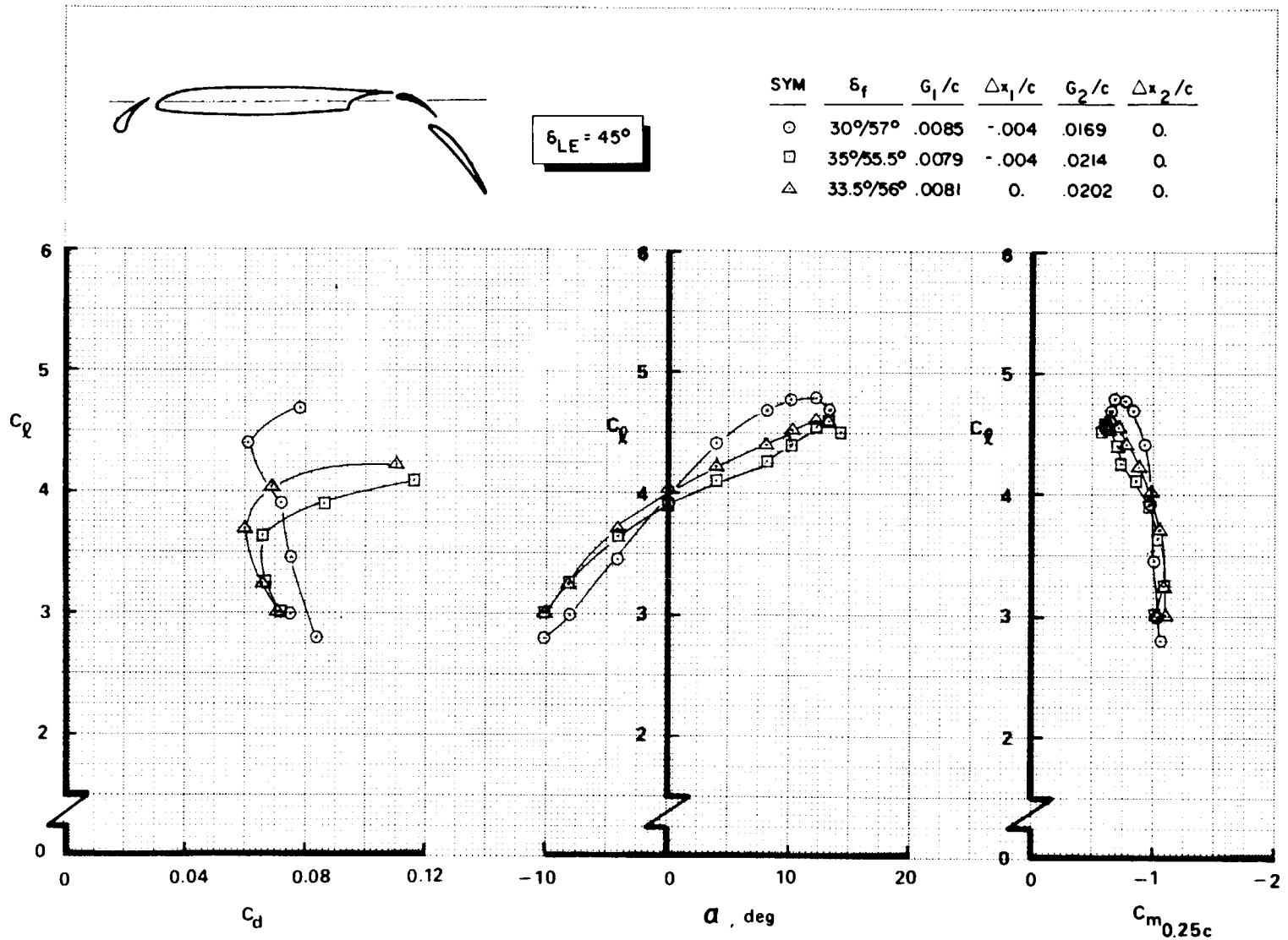

FIGURE A13.–EFFECT OF FLAP COMPONENT ANGLE COMBINATION AT CONSTANT $\delta_{f_{eq}}$ (49°)–MODEL C

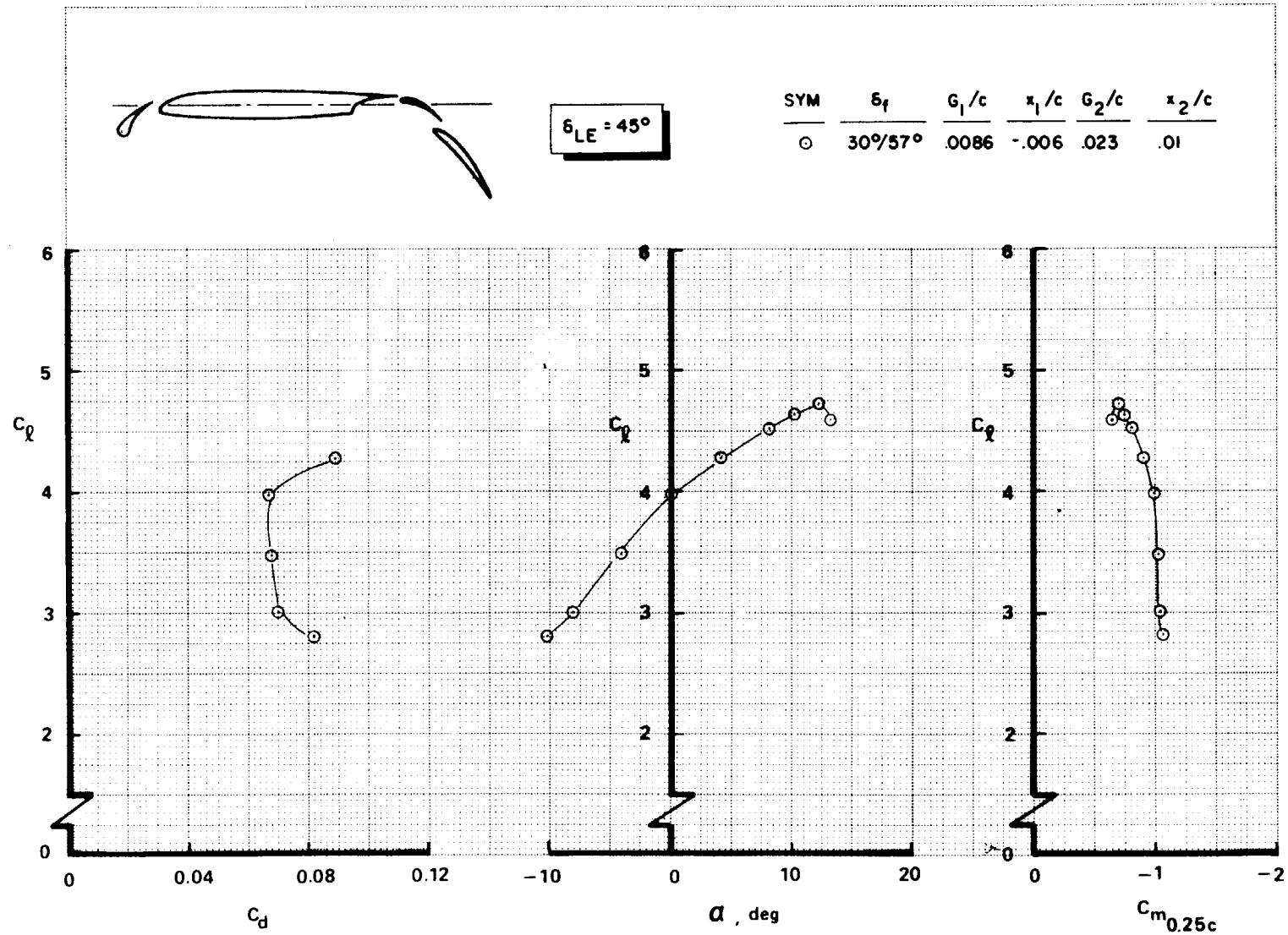

FIGURE A14.—EFFECT OF WING-VANE SLOT GAP AND OVERLAP—MODEL C ($\delta_{f_{eq}}$ = 49°)

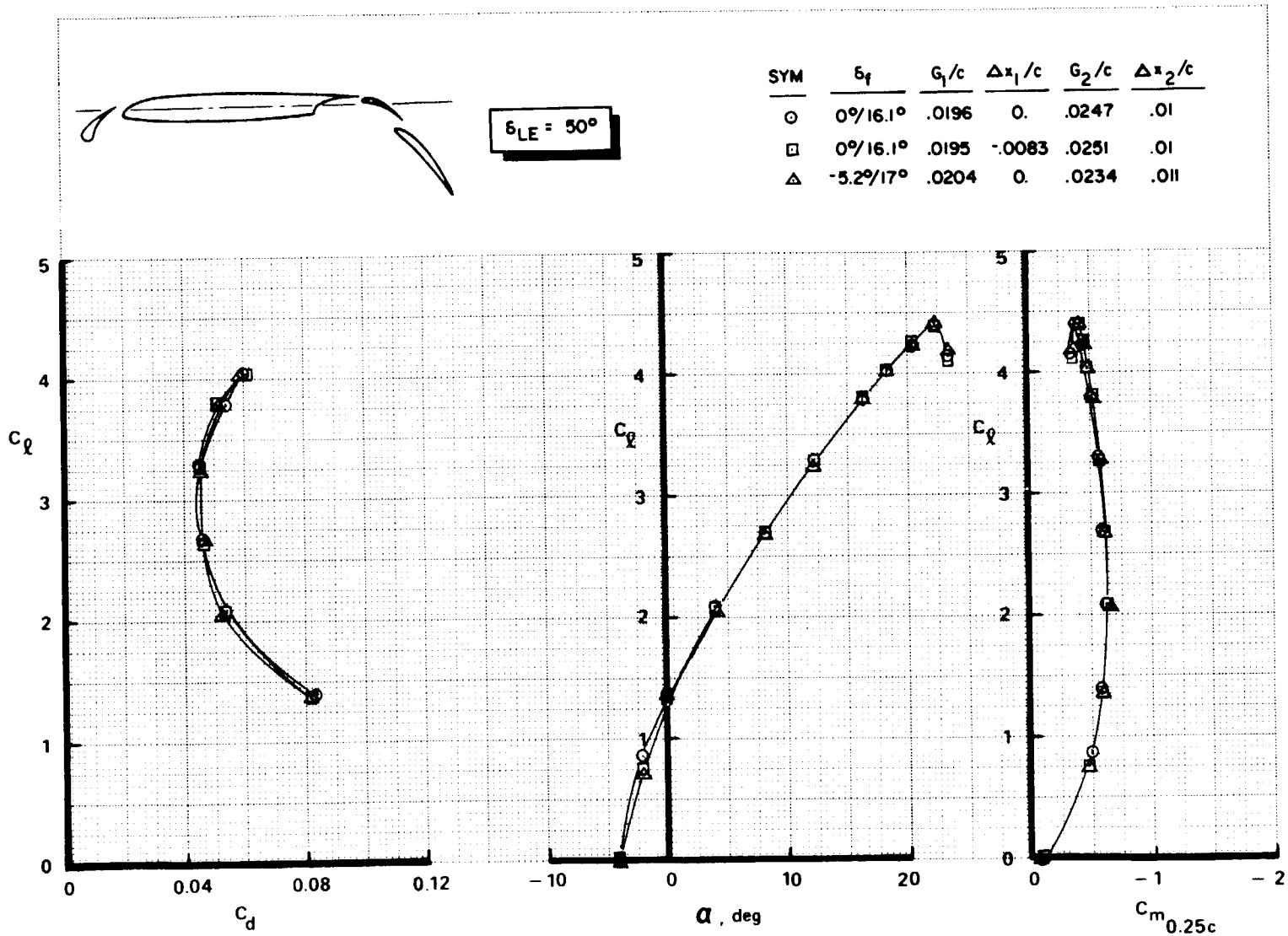

FIGURE A15.—FLAP DEFLECTION ANGLE STUDY AT $\delta_{f_{eq}} = 15°$—MODEL C

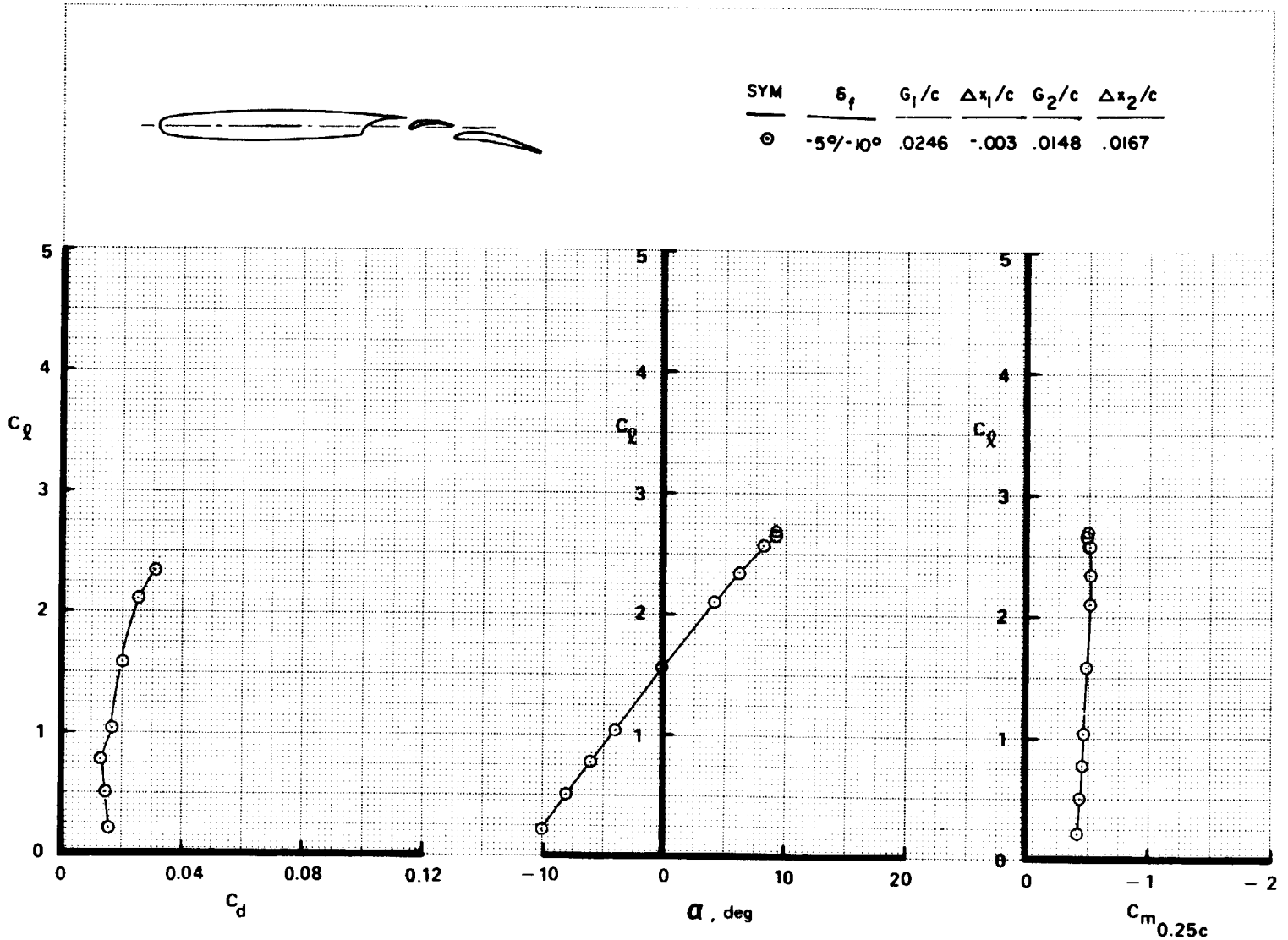

FIGURE A16.–EFFECT OF FLAP WITHOUT LEADING-EDGE DEVICE–MODEL C ($\delta_{f_{eq}} = 13°$)

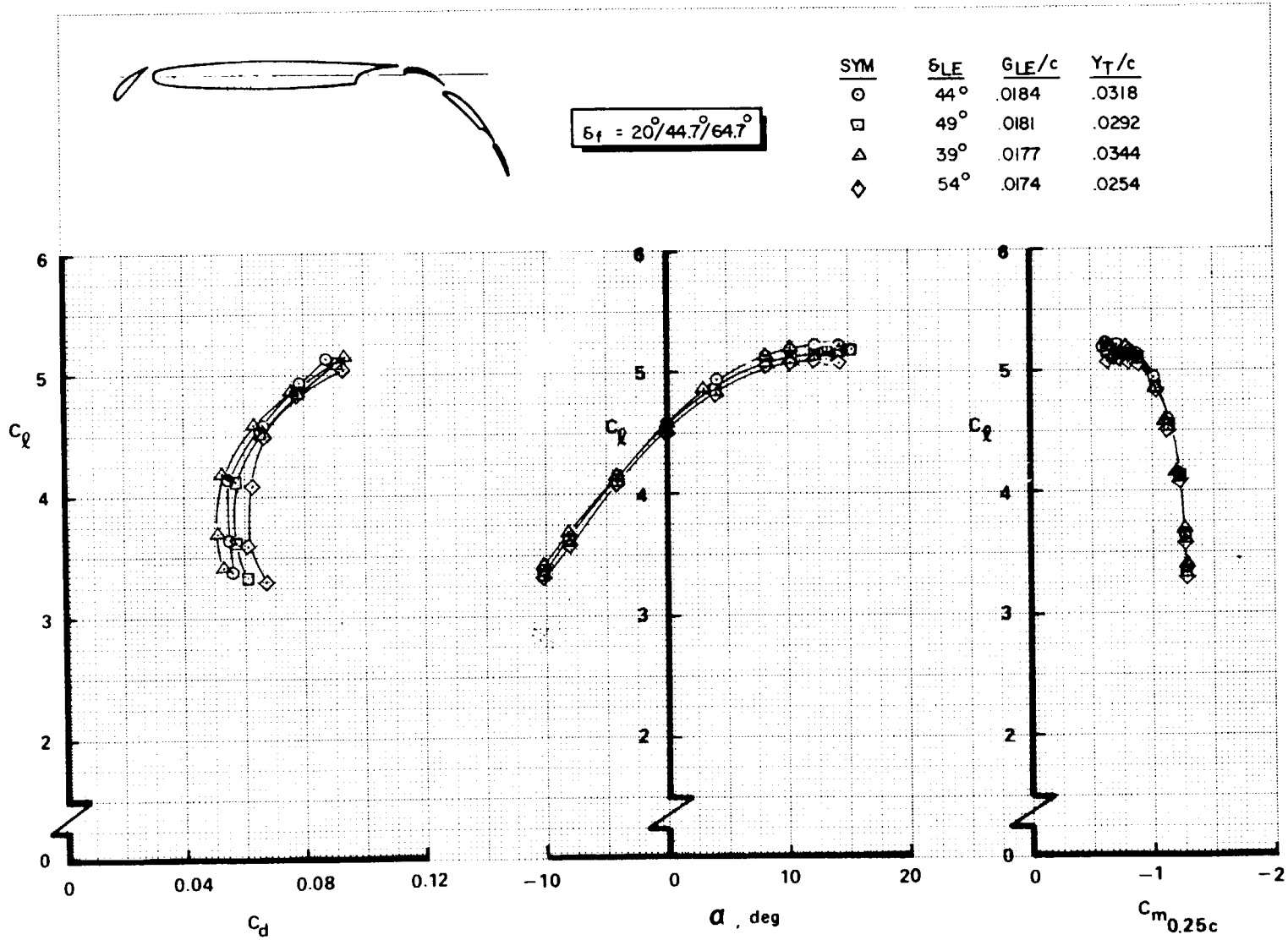

FIGURE A17.–EFFECT OF SLAT 2 DEFLECTION ANGLE VARIATION–MODEL D ($\delta_{f_{eq}} = 46°$)

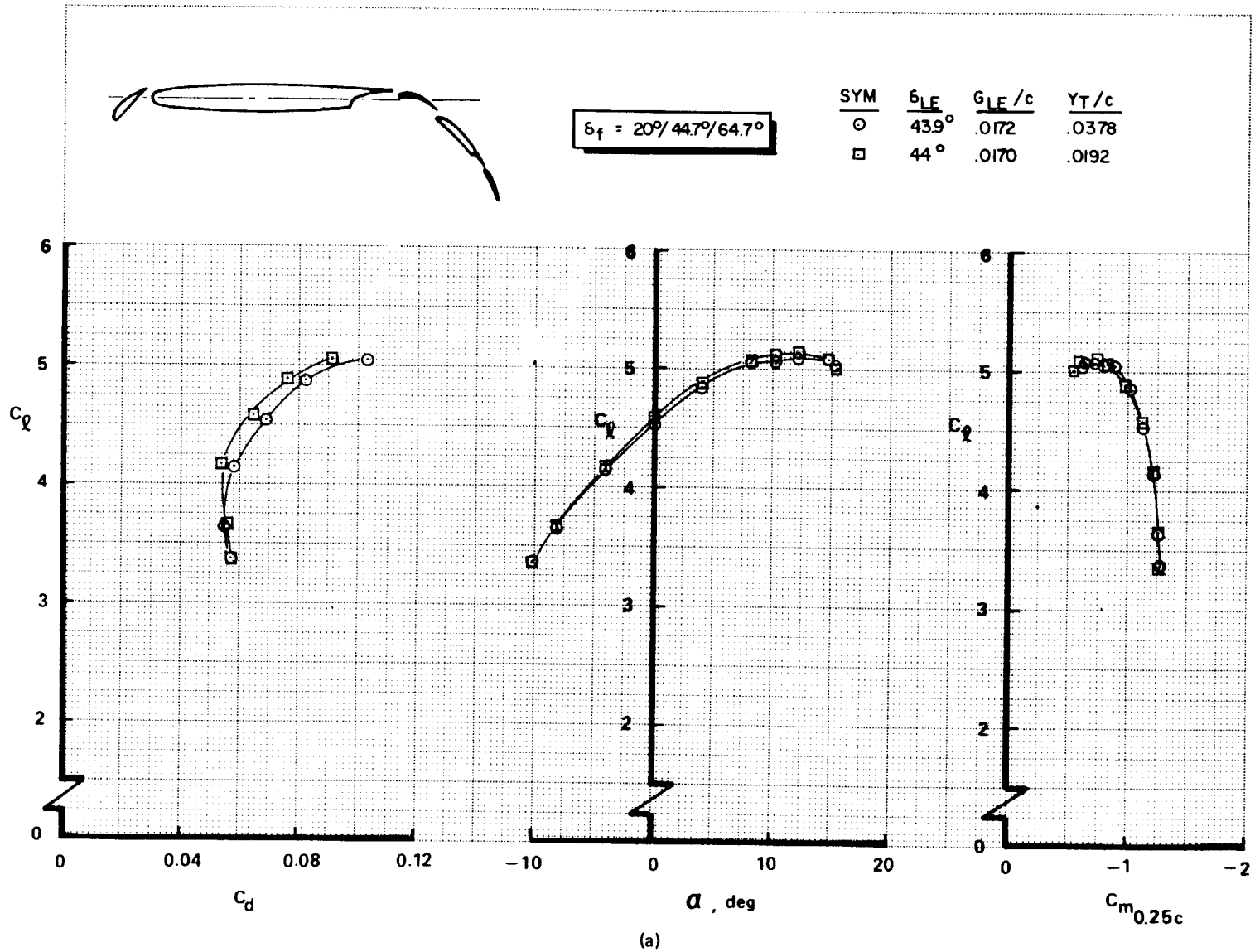

(a)

FIGURE A18.–SLAT 2 SLOT GAP AND HEIGHT OPTIMIZATION–MODEL D ($\delta_{f_{eq}}$ = 46°) (U)

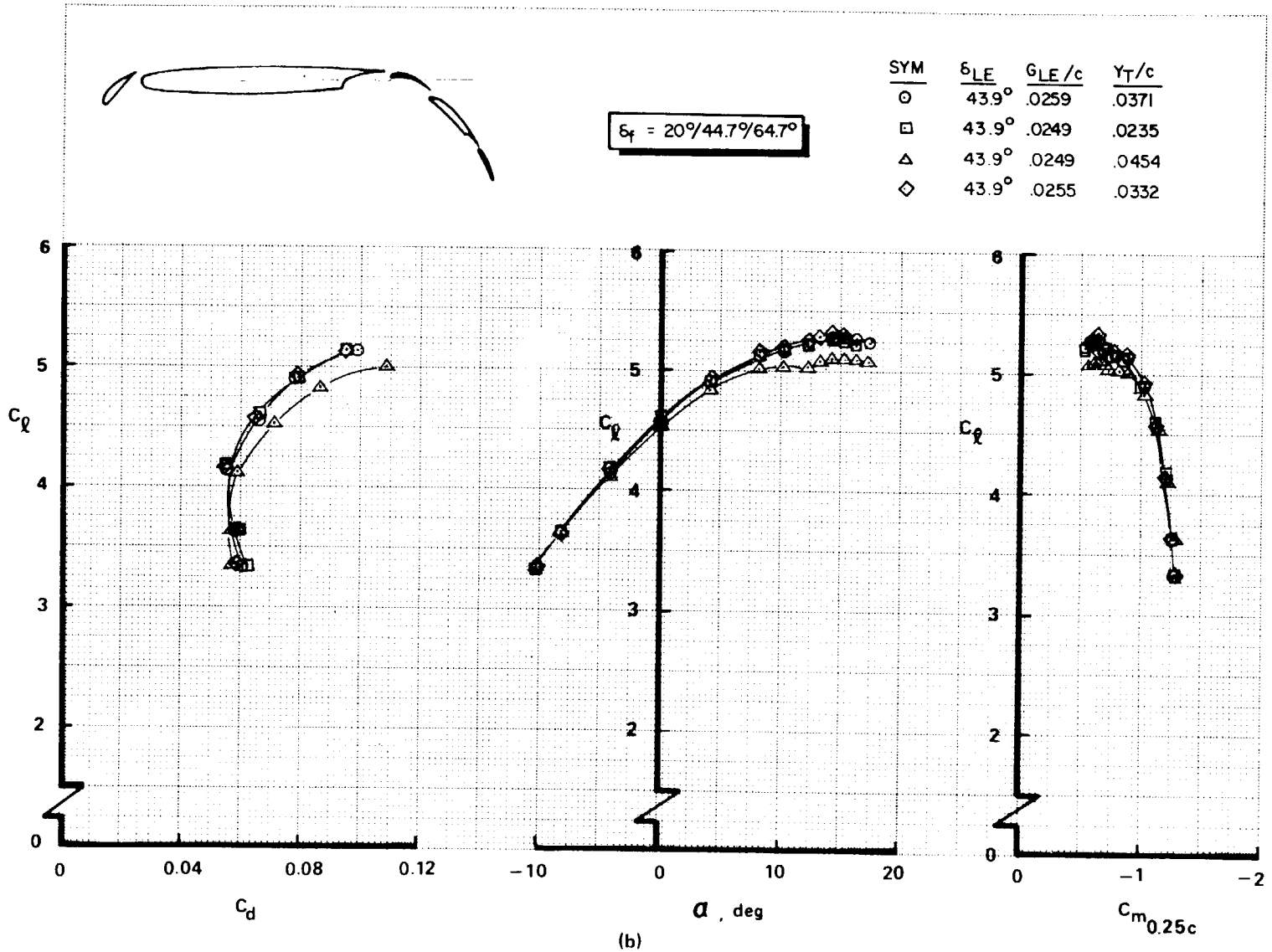

(b)

FIGURE A18.—Continued

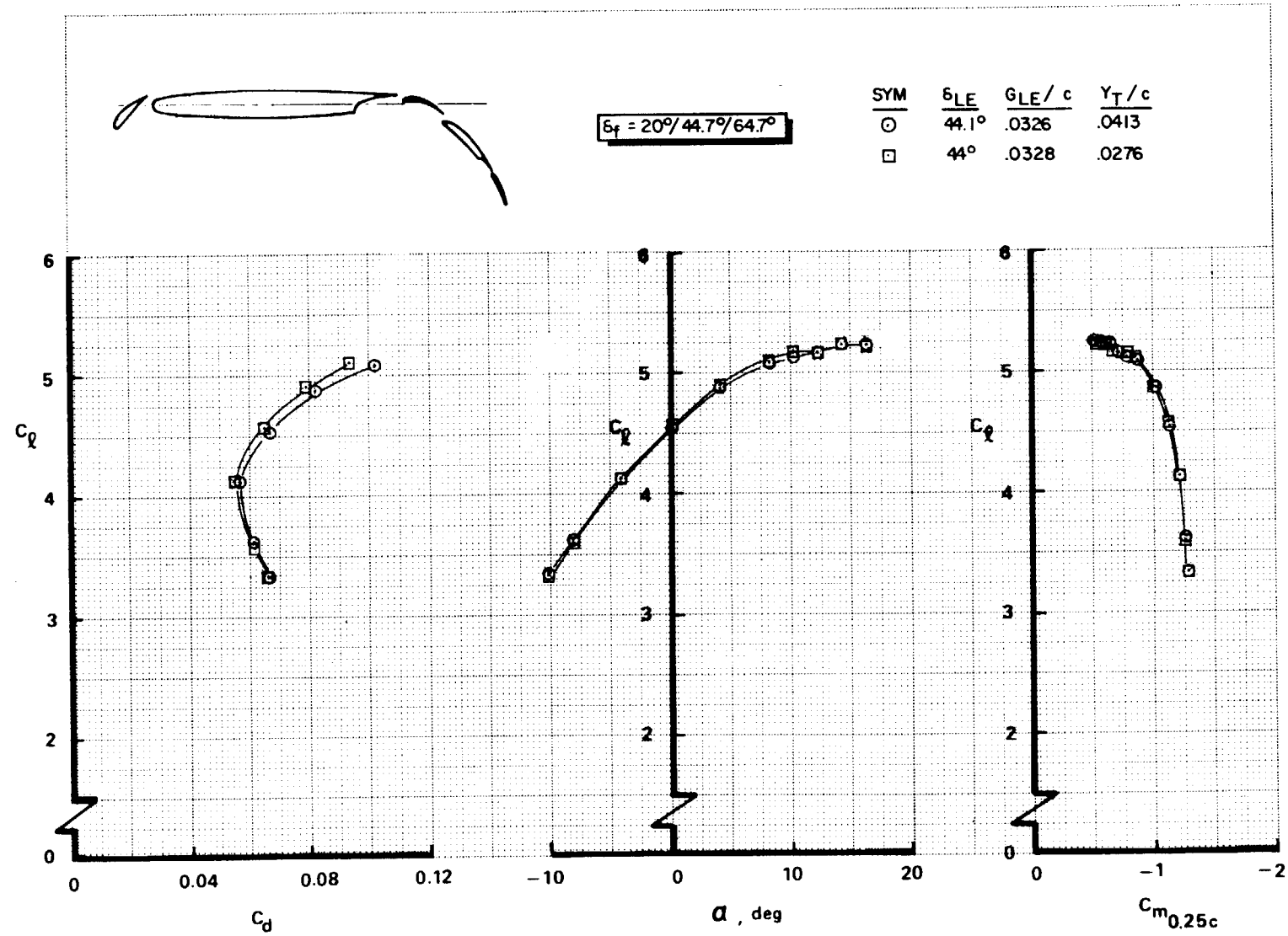

(c)

FIGURE A18.—Concluded

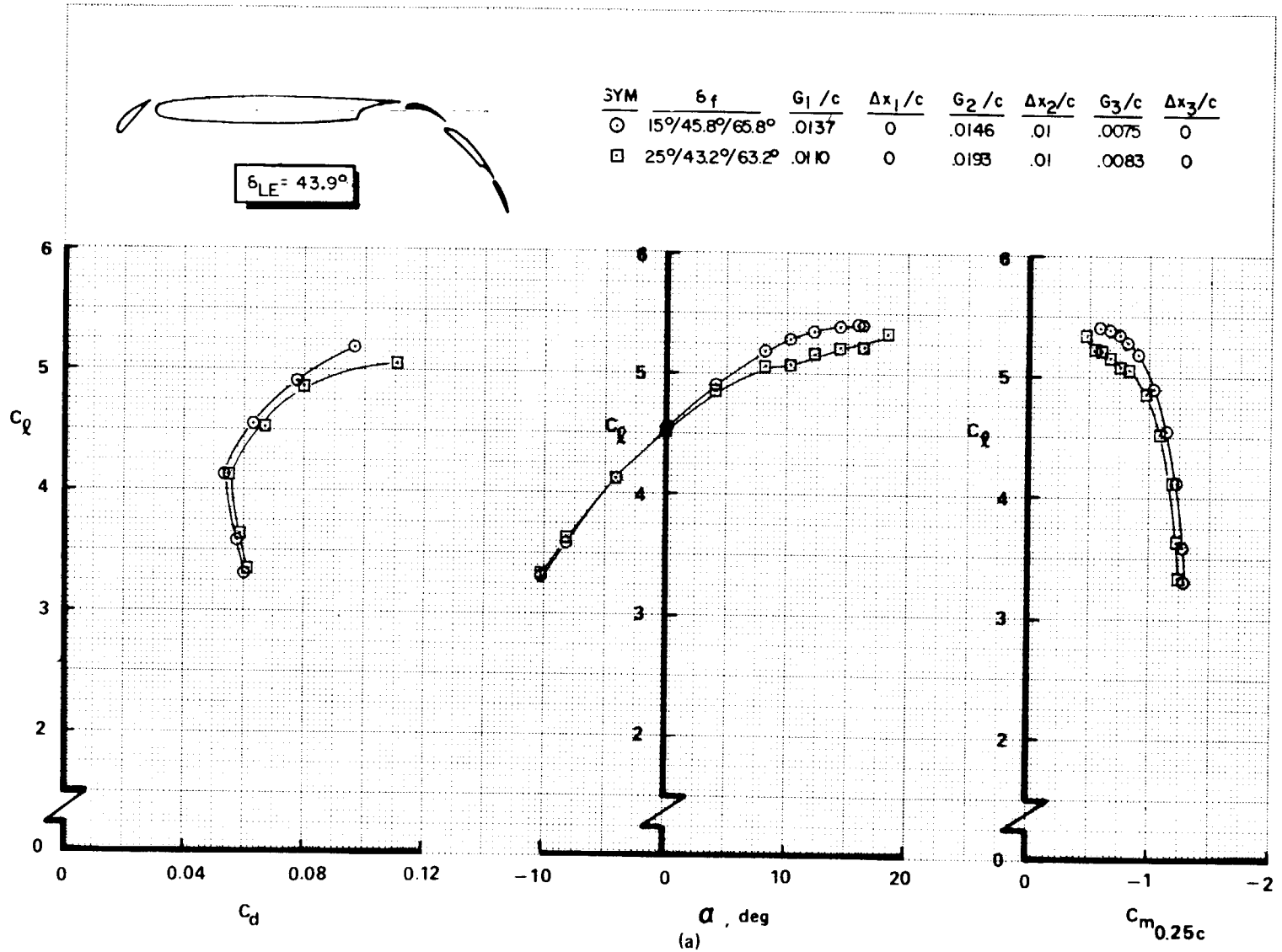

FIGURE A19.–EFFECT OF FLAP COMPONENT ANGLE COMBINATION AT CONSTANT $\delta_{f_{eq}}$ (46°)–MODEL D

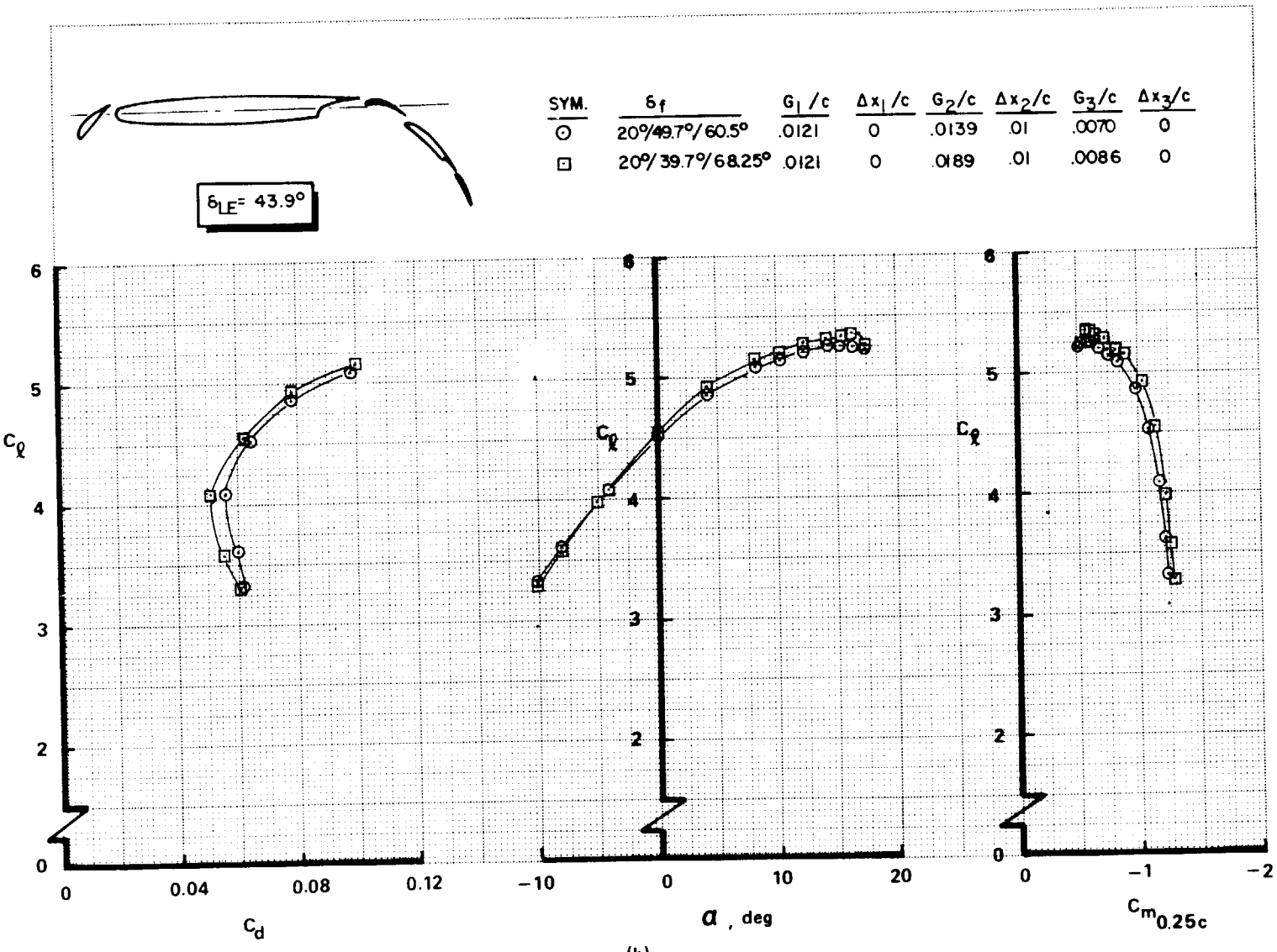

(b)

FIGURE A19.—Concluded

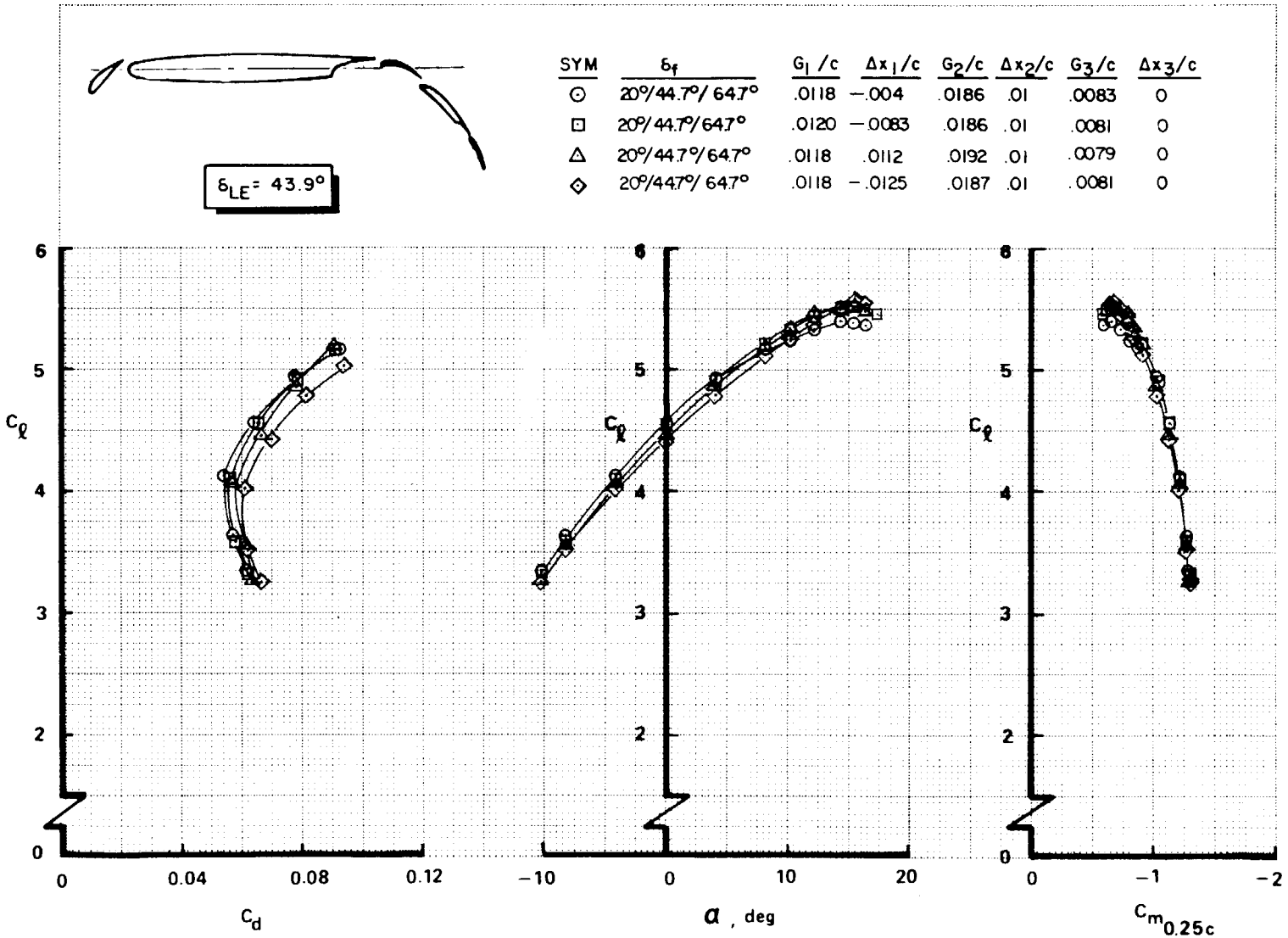

FIGURE A20.—EFFECT OF WING-VANE SLOT GAP AND OVERLAP—MODEL D ($\delta_{f_{eq}} = 46°$)

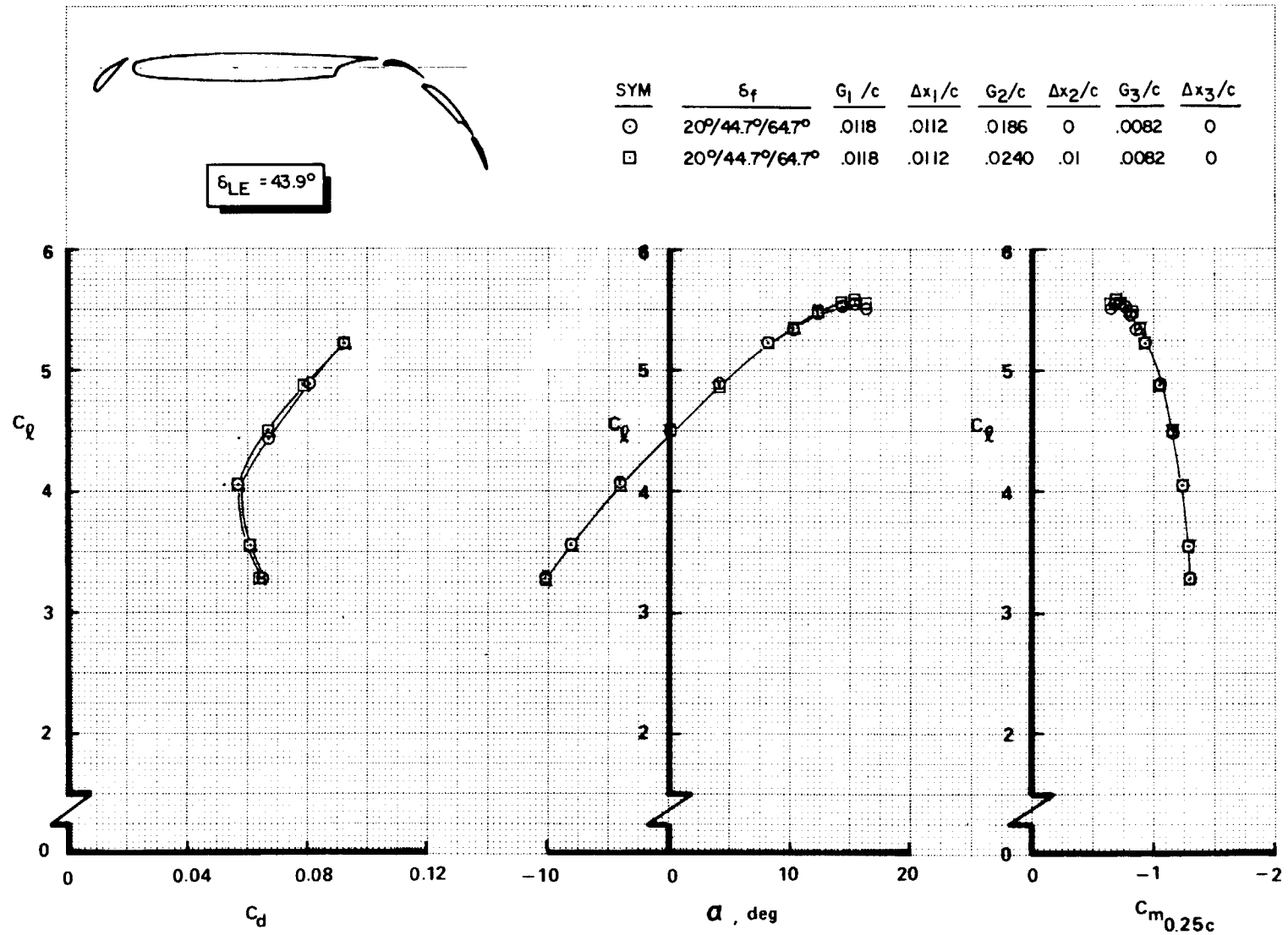

FIGURE A21.—EFFECT OF VANE/MAIN-FLAP SLOT GAP AND OVERLAP—MODEL D ($\delta_{f_{eq}}$ = 46°)

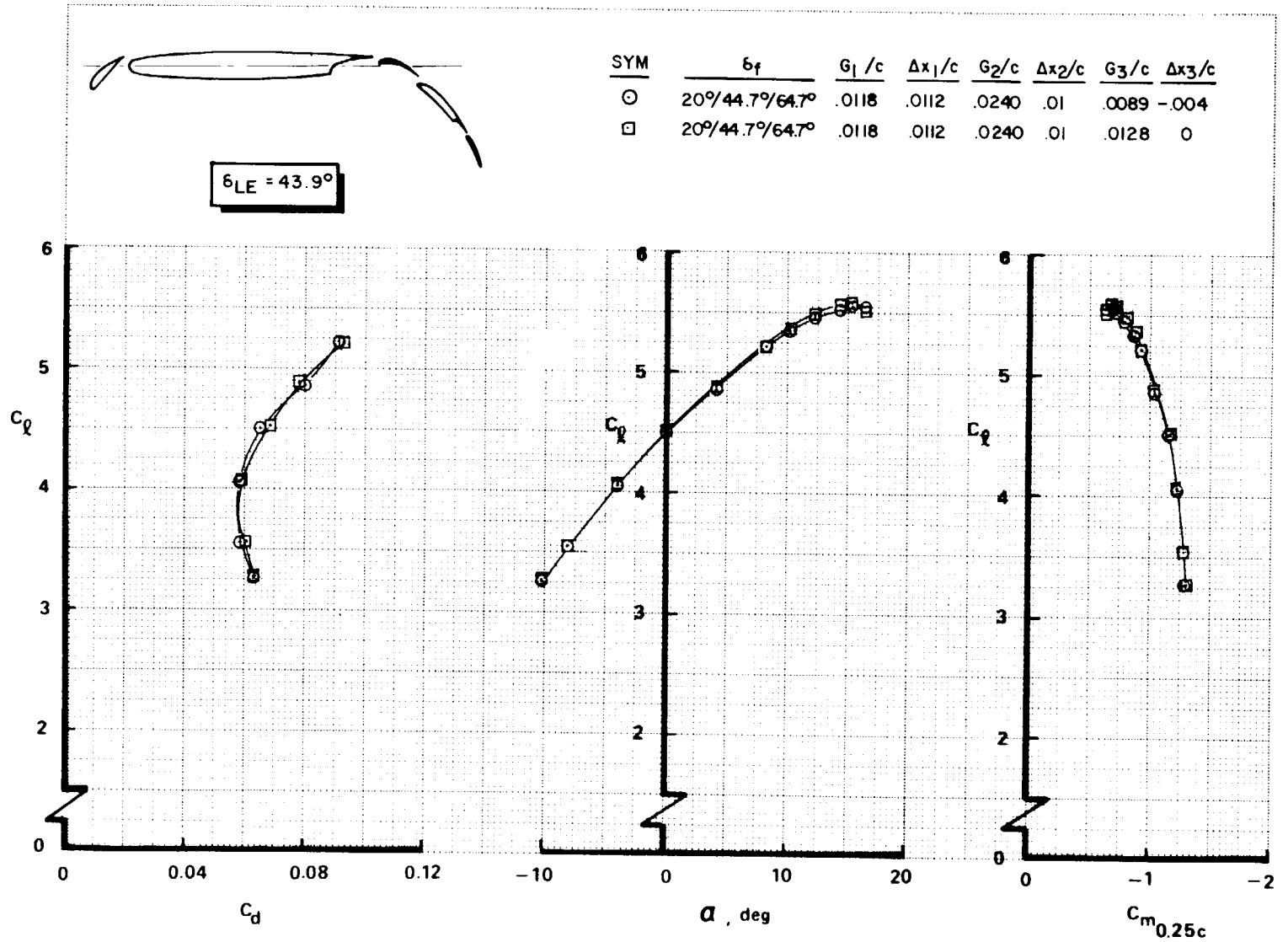

FIGURE A22.—EFFECT OF MAIN-FLAP/AFT-FLAP SLOT GAP AND OVERLAP—MODEL D ($\delta_{f_{eq}}$ = 46°)

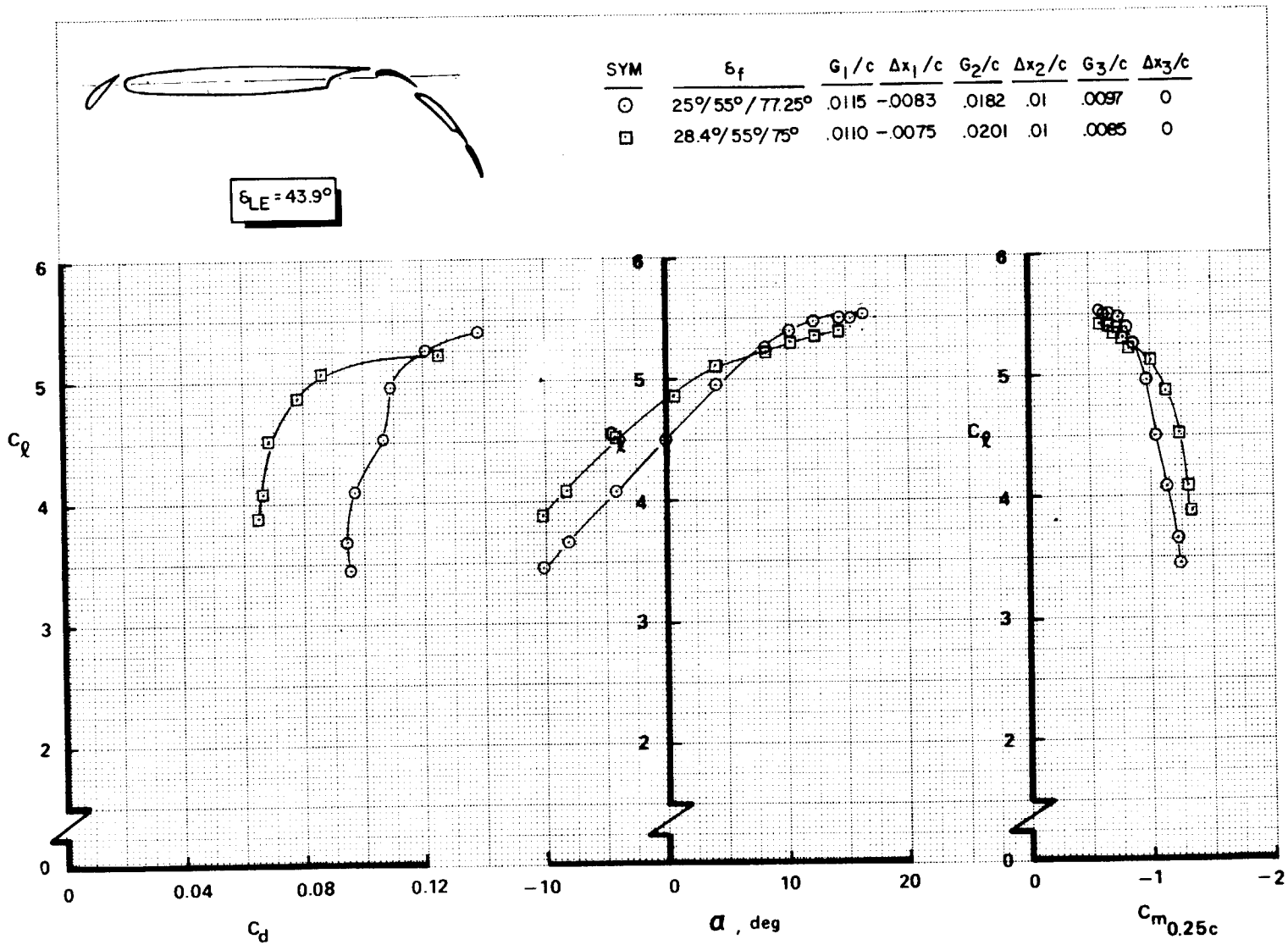

FIGURE A23.–EFFECT OF FLAP COMPONENT ANGLE COMBINATION AT CONSTANT $\delta_{f_{eq}}$ (53°)–MODEL D

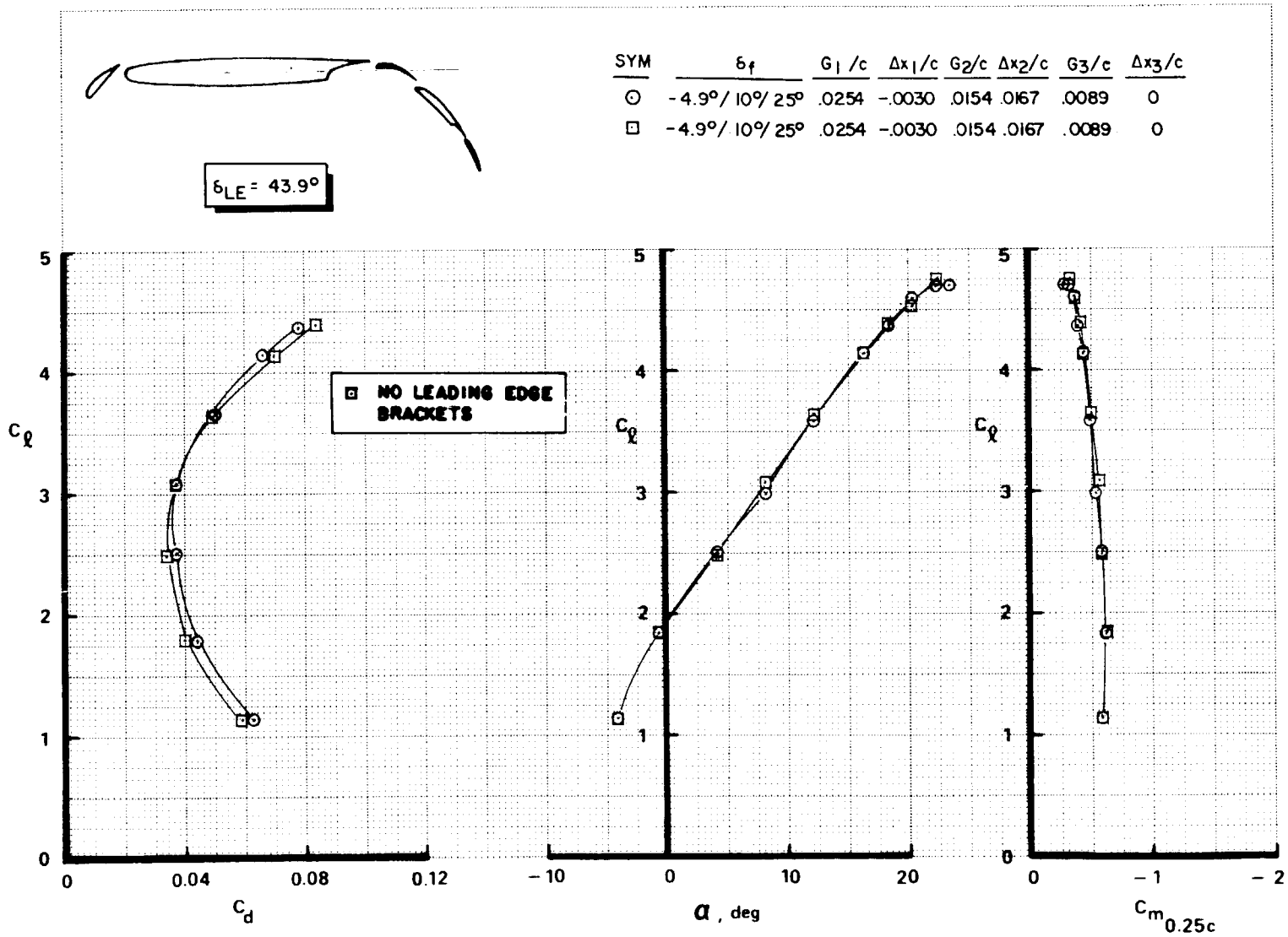

FIGURE A24.–EFFECT OF LEADING-EDGE DEVICE BRACKETS–MODEL D ($\delta_{f_{eq}}$ = 16°)

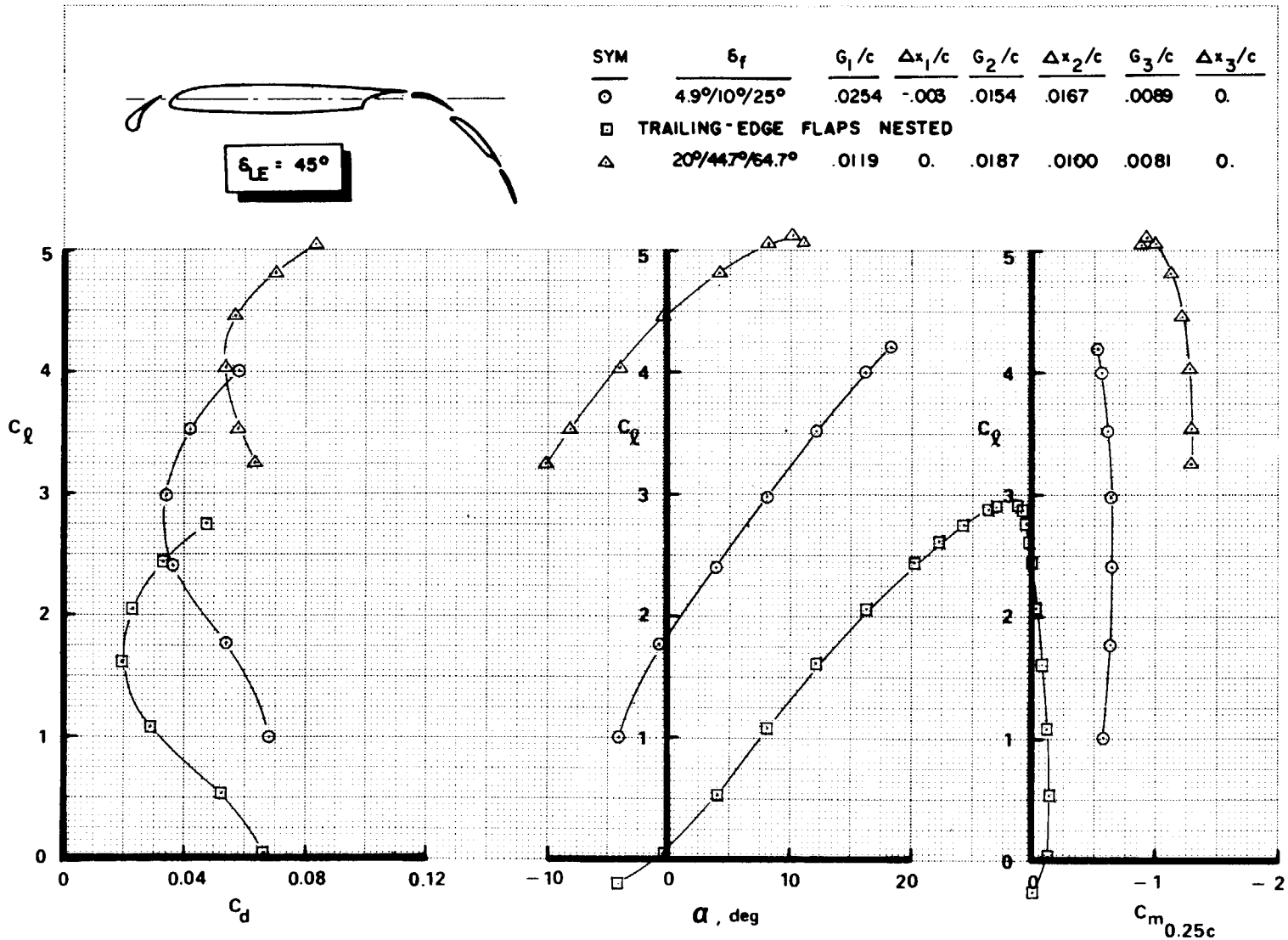

FIGURE A25.–EFFECT OF FLAP DEFLECTION ANGLE VARIATION WITH SLAT 1–MODEL D

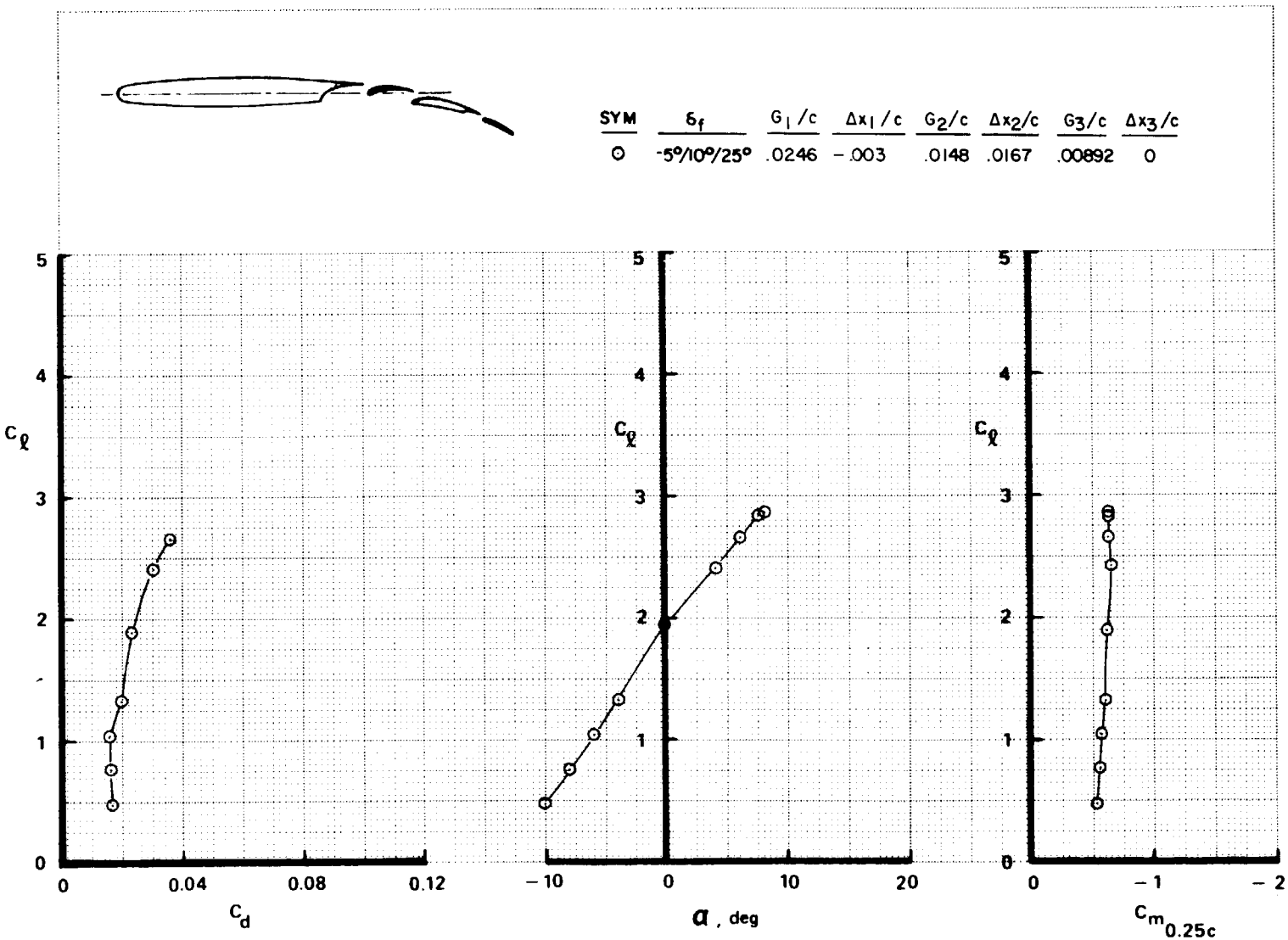

FIGURE A26.—EFFECT OF FLAP WITHOUT LEADING-EDGE DEVICE—MODEL D ($\delta_{f_{eq}} = 16°$)

APPENDIX B

WAKE/BOUNDARY-LAYER MEASUREMENTS–MODEL B

[redacted]

TABLE B1.—WAKE/BOUNDARY-LAYER TEST CONDITIONS

Configuration		$N_1WC_2F_{2.2}$	
(Basic nose and wing span with faired cove and single-slotted flap; $\delta_f = 20°$; $\Delta x/c = 0.01$; and $G/c = 0.02$)			
Tunnel conditions:			
$M_\infty = 0.201$ and $Re = 2.83 \times 10^6$			
Model flow conditions:			
α	=	$0°$ and $4°$	Boundary-layer transition at 43% chord on flap, no separation
α	=	$8°$	Boundary-layer transition at 42% chord on flap, no separation
α	=	$8.5°$	Flow separation on main wing

[redacted]

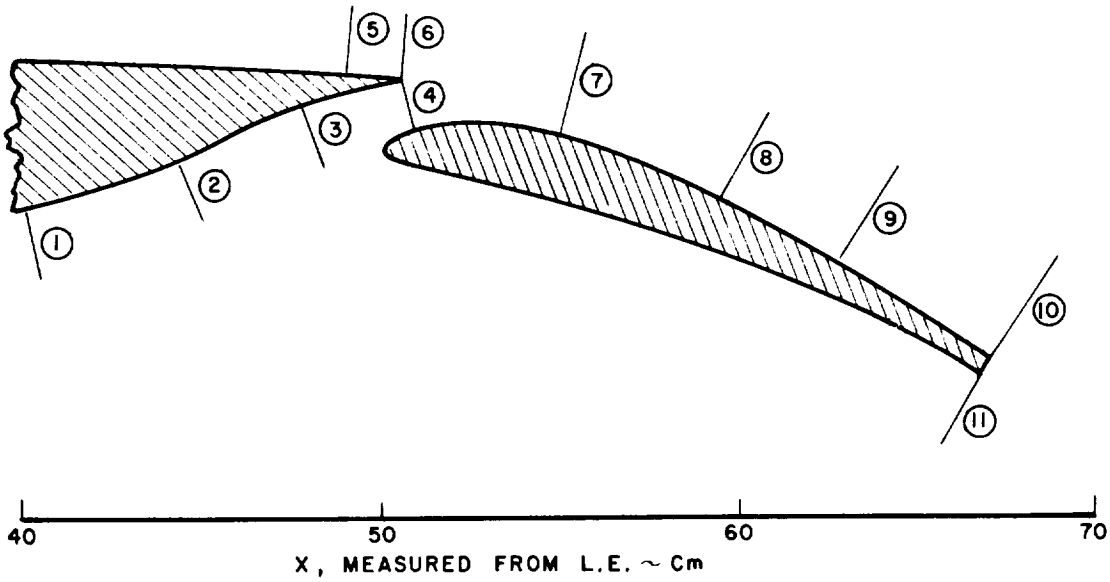

FIGURE B1.– WAKE/BOUNDRY-LAYER SURVEY STATIONS

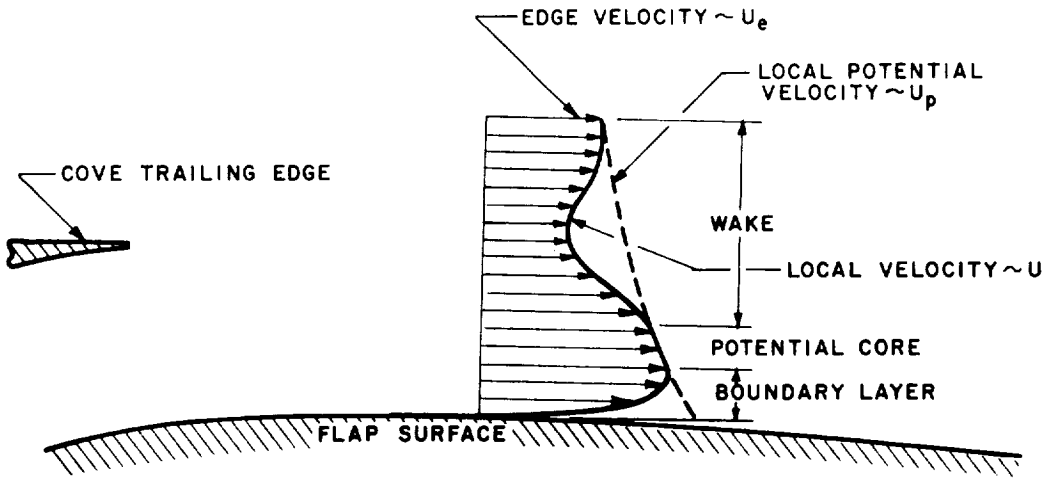

FIGURE B2.–WAKE/BOUNDARY-LAYER COMPONENTS

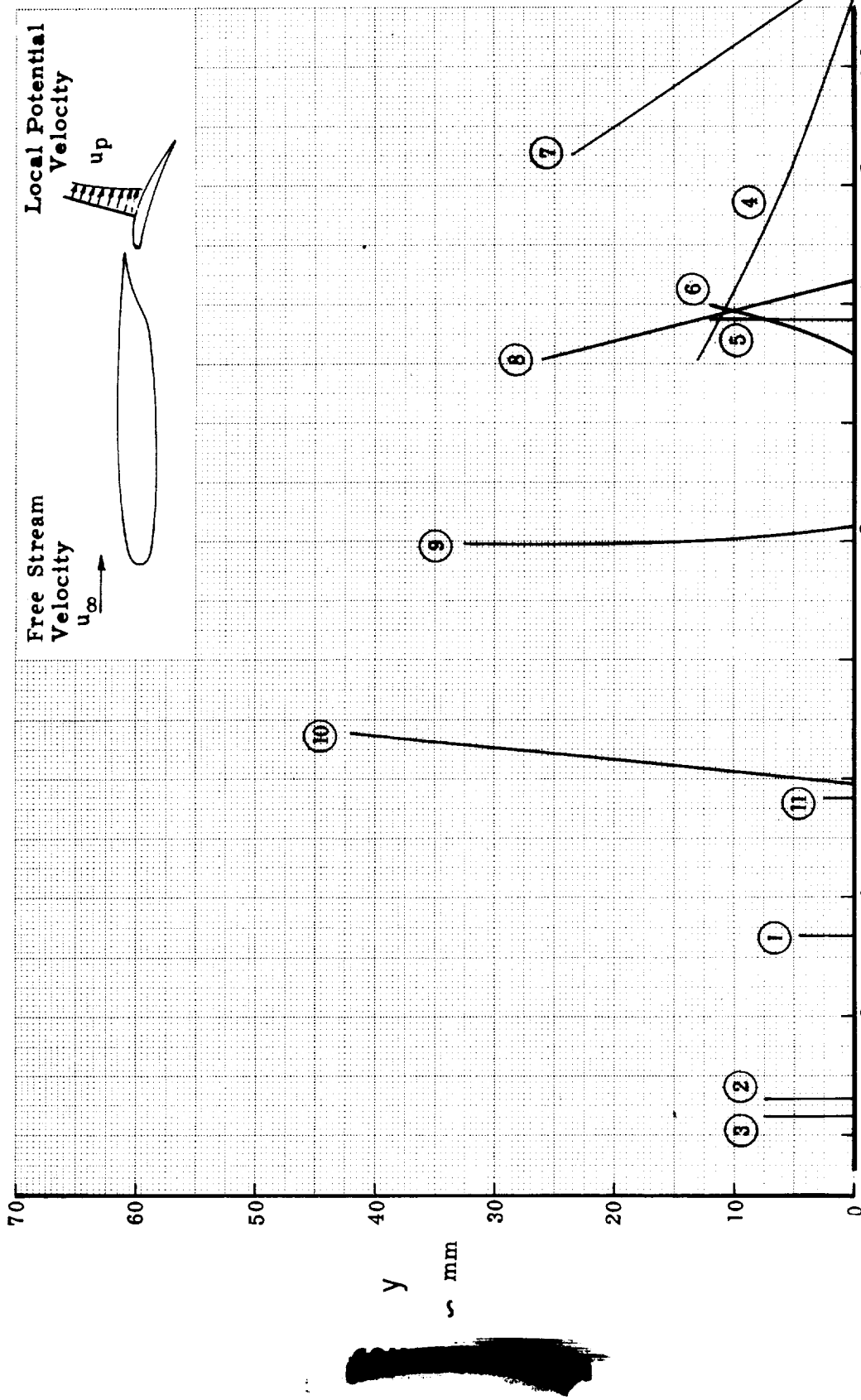

FIGURE B3.–POTENTIAL VELOCITY DISTRIBUTION, $\alpha = 0°$

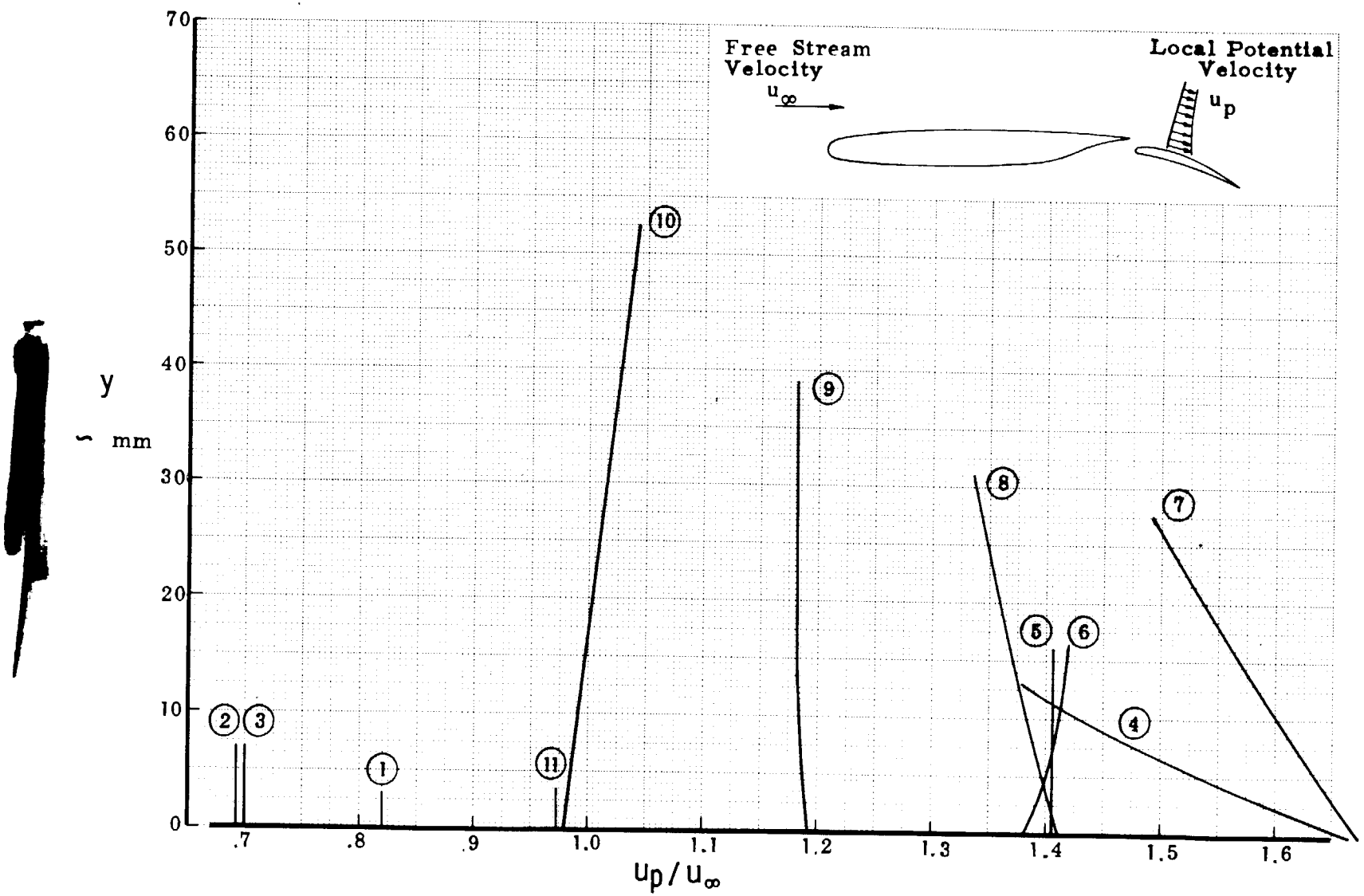

FIGURE B4.—POTENTIAL VELOCITY DISTRIBUTION, $\alpha = 4°$

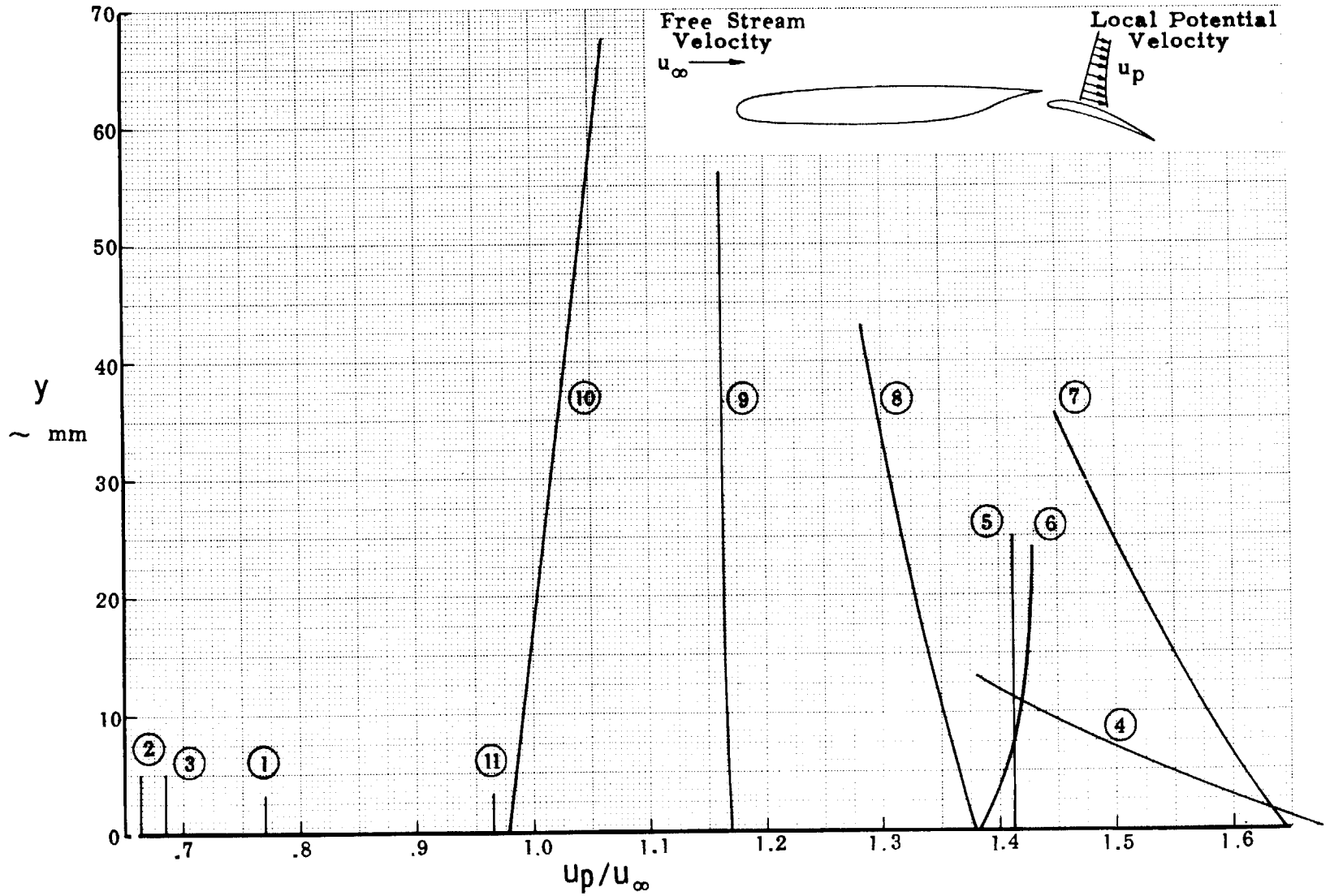

FIGURE B5.–POTENTIAL VELOCITY DISTRIBUTION, $\alpha = 8°$

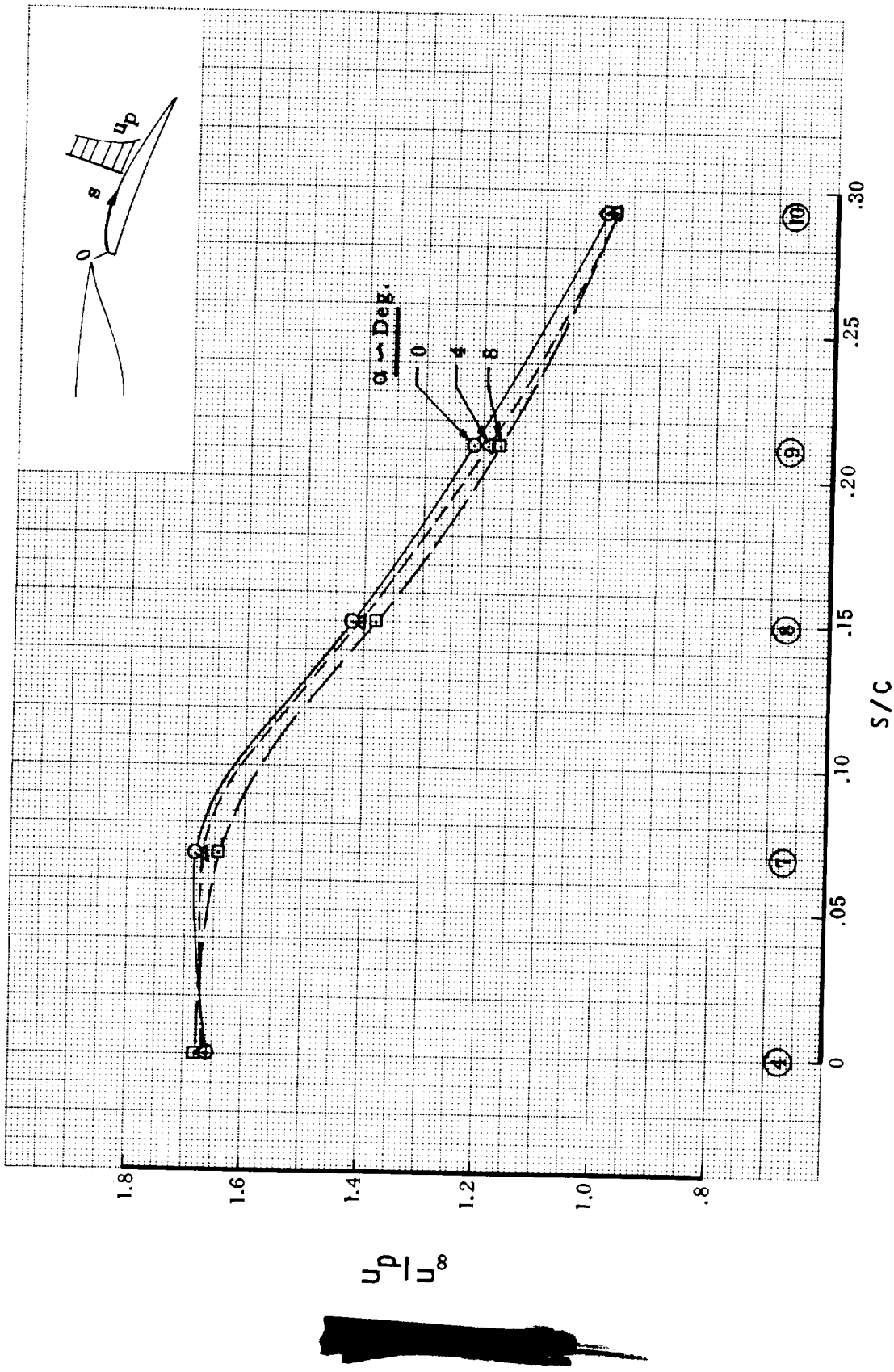

FIGURE B6.–VELOCITY DISTRIBUTION ALONG FLAP SURFACE

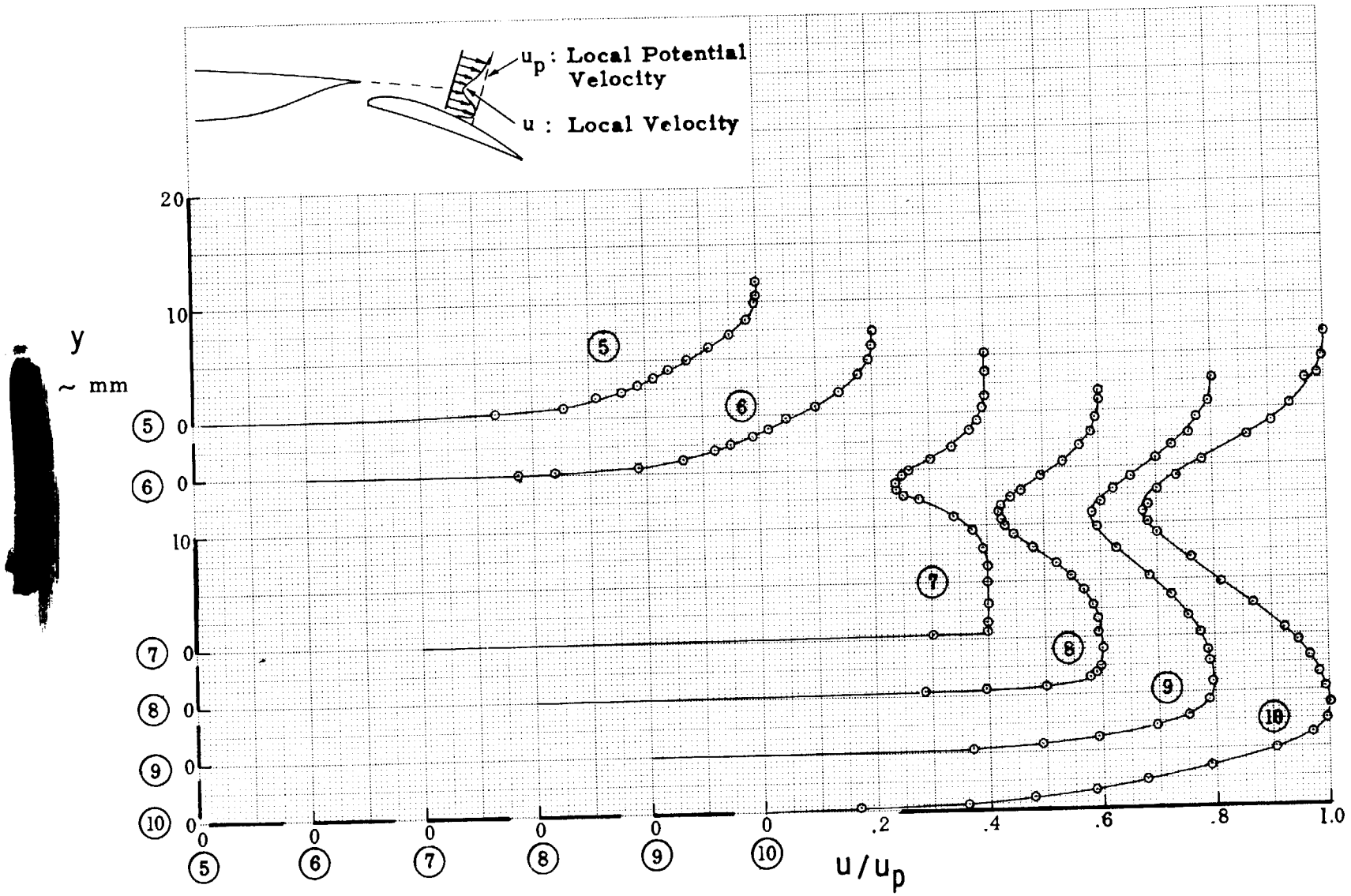

(a)

FIGURE B7.—LOCAL VELOCITY PROFILES, $\alpha = 0°$

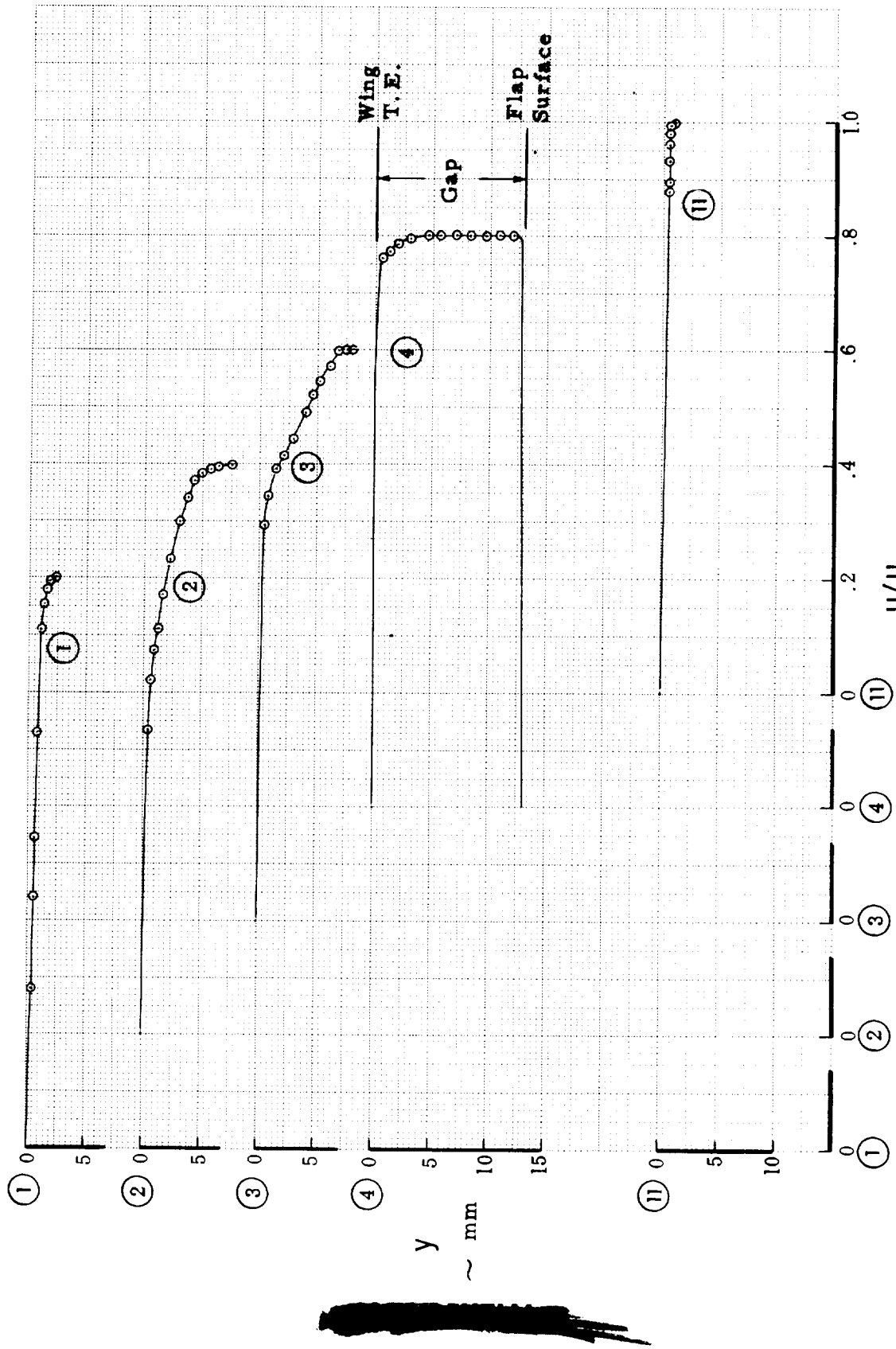

(b)

FIGURE B7.–Concluded

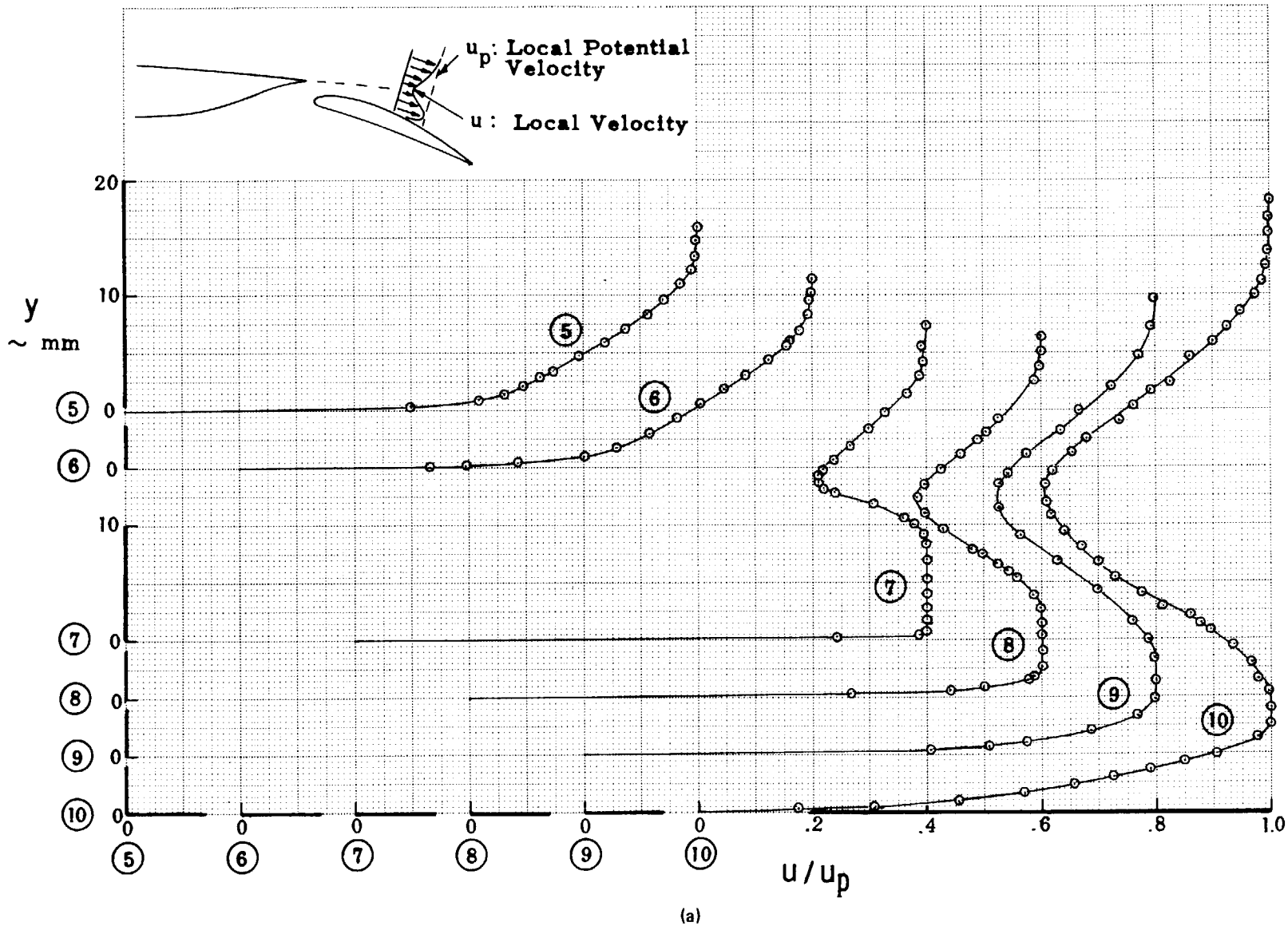

(a)

FIGURE B8.—LOCAL VELOCITY PROFILES, $\alpha = 4°$

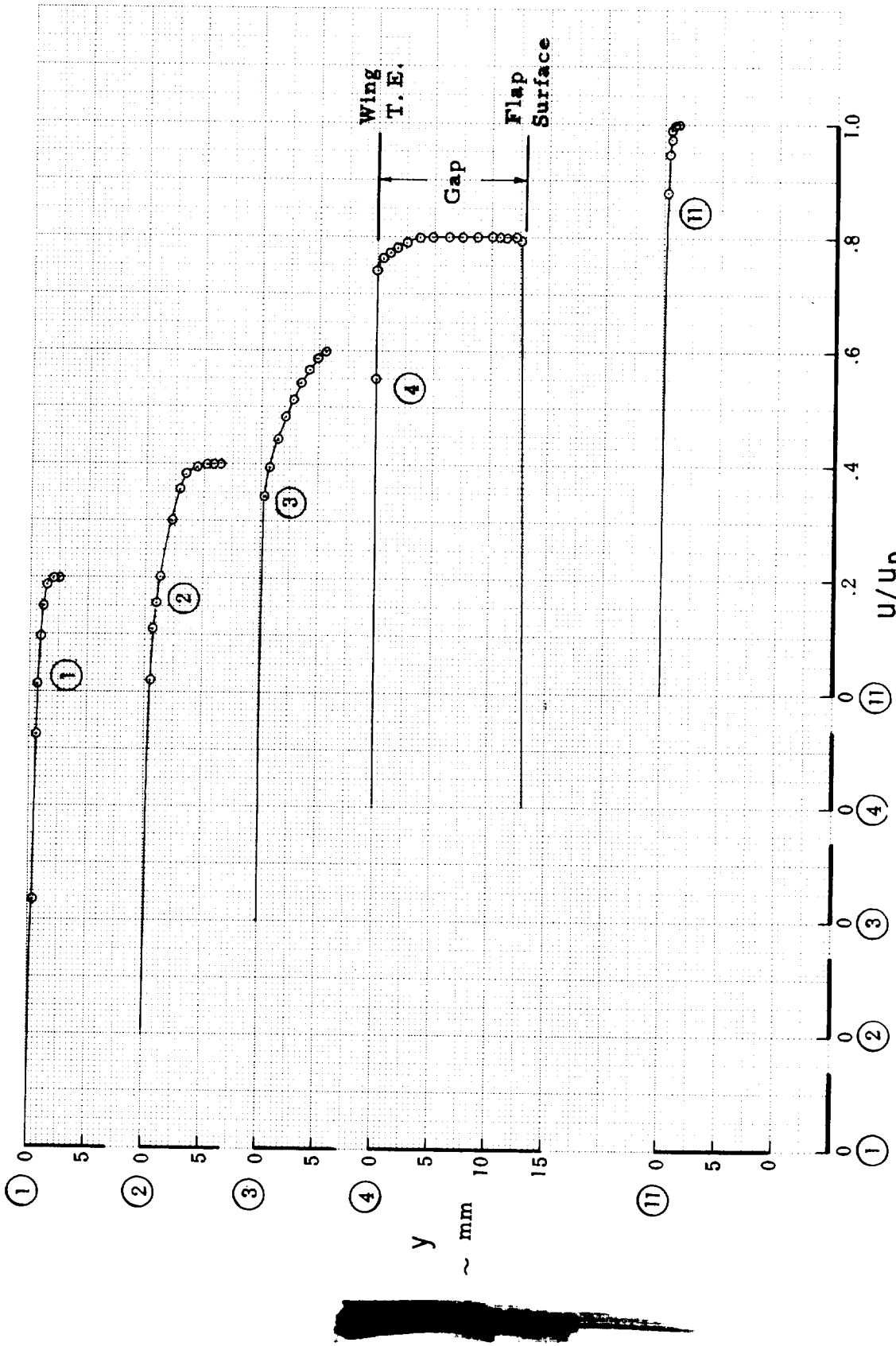

(b)

FIGURE B8.—Concluded

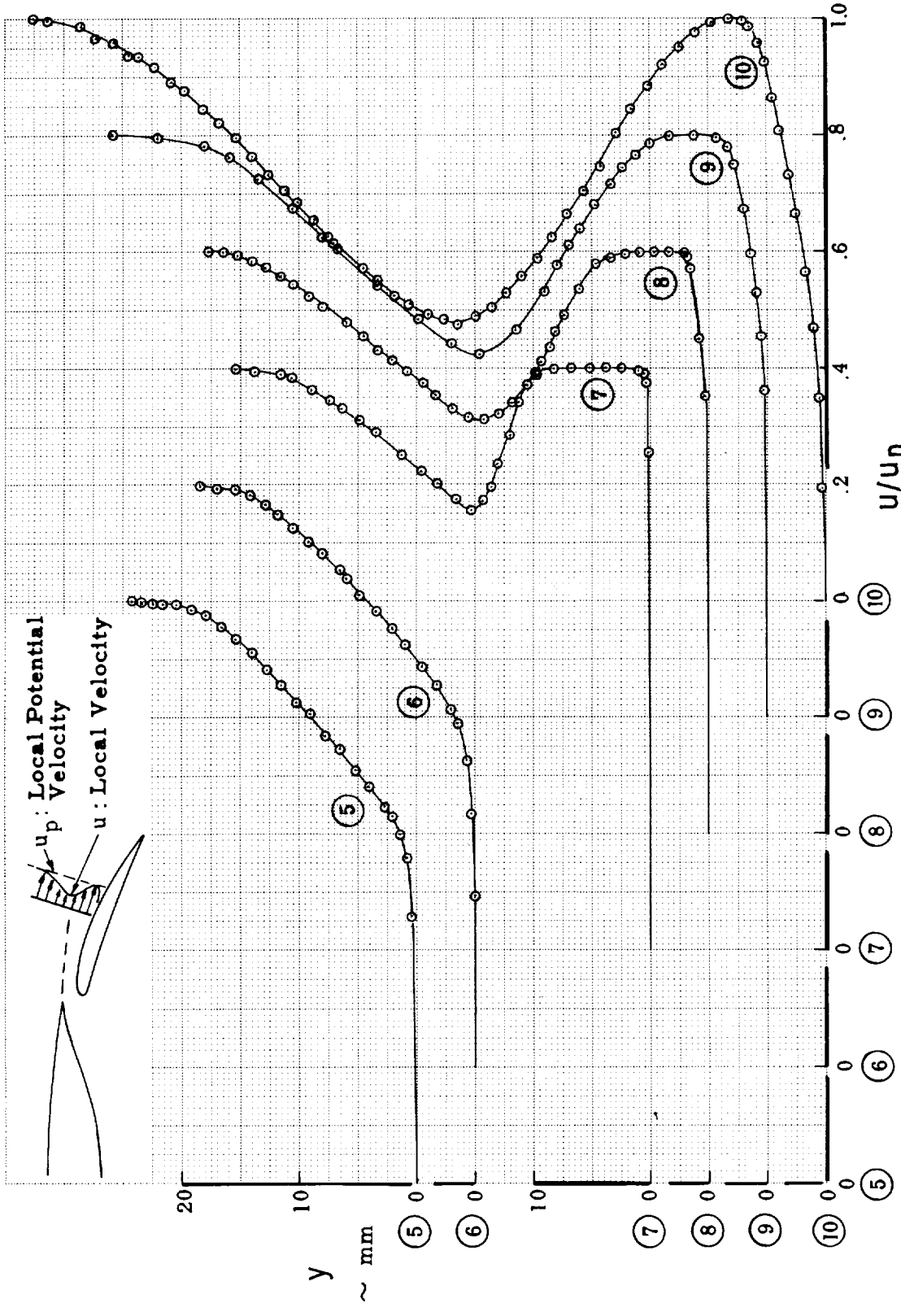

(a)

FIGURE B9.—LOCAL VELOCITY PROFILES, $\alpha = 8°$

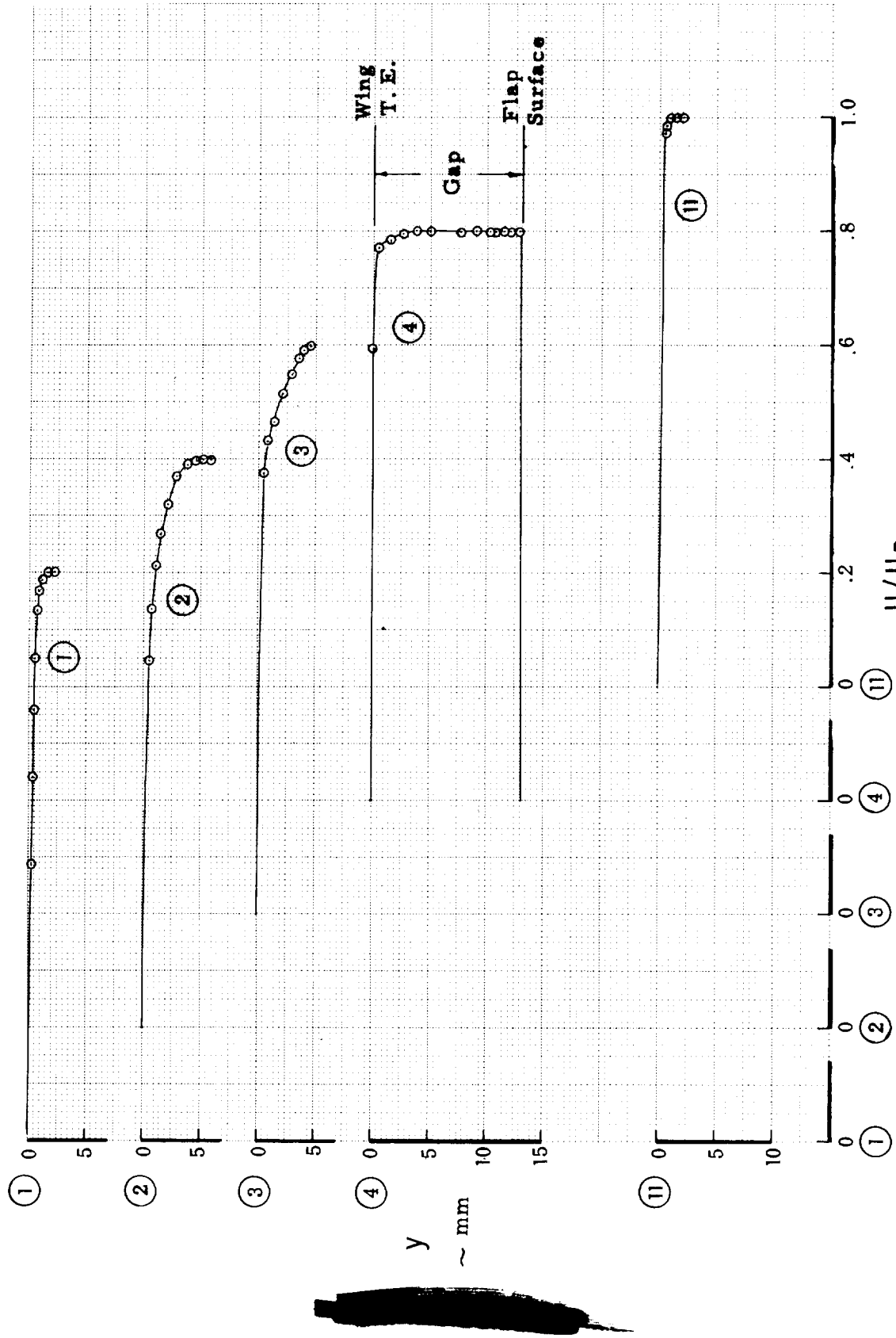

FIGURE B9.—Concluded

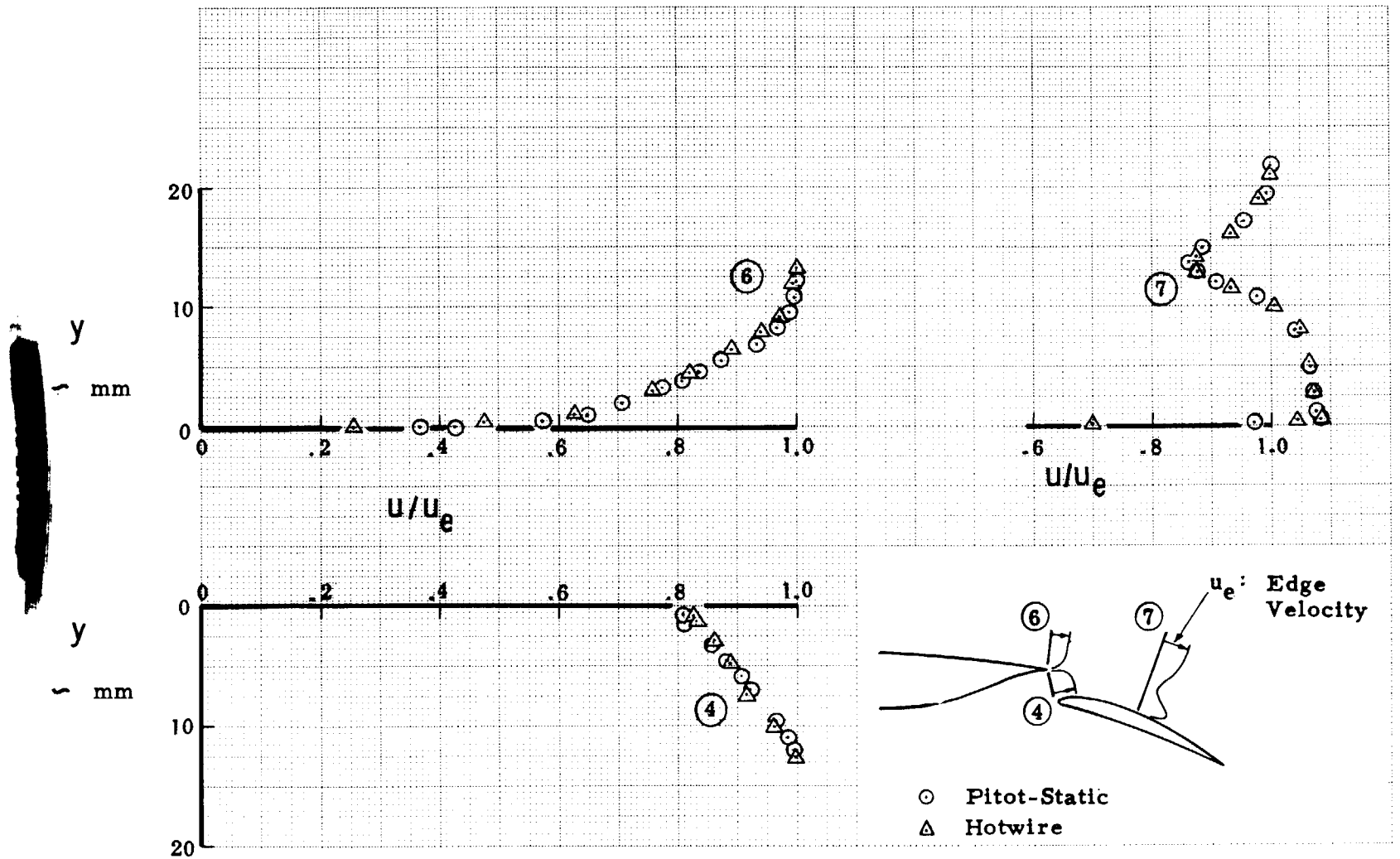

FIGURE B10.—COMPARISON OF HOT-WIRE AND PITOT-STATIC MEASUREMENTS, $\alpha = 0°$

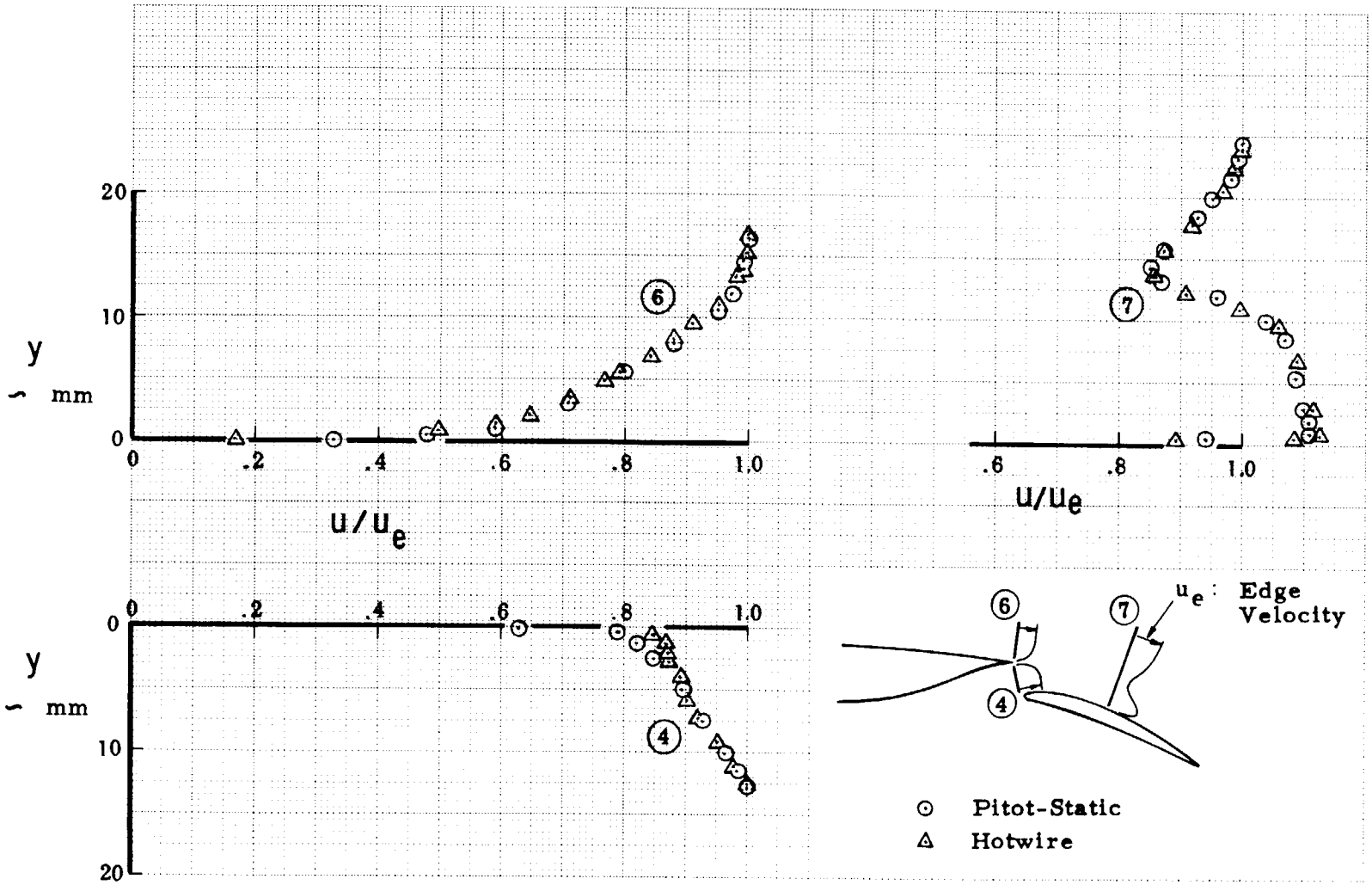

FIGURE B11.–COMPARISON OF HOT-WIRE AND PITOT-STATIC MEASUREMENTS, $\alpha = 4°$

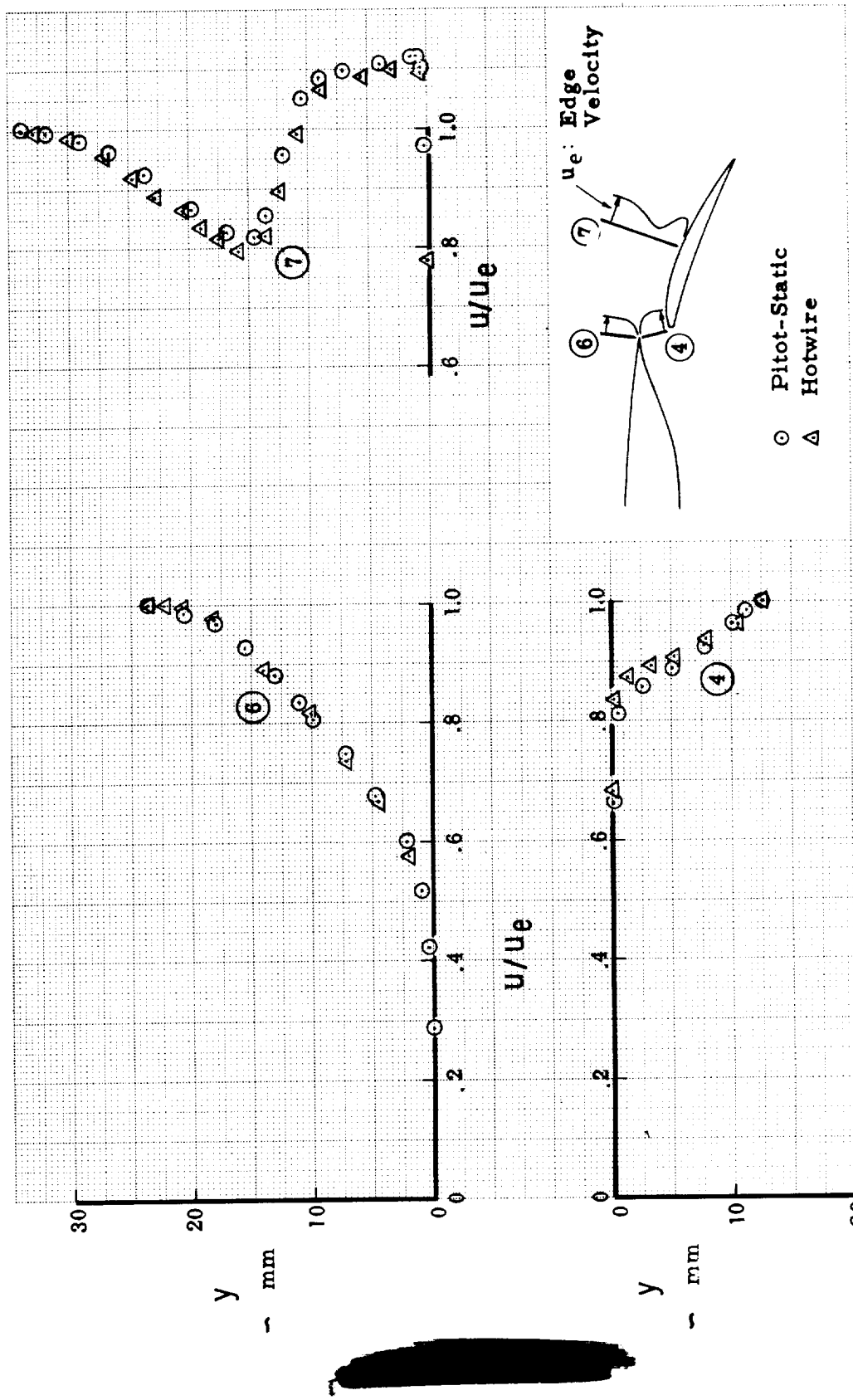

FIGURE B12.–COMPARISON OF HOT-WIRE AND PITOT-STATIC MEASUREMENT, $\alpha = 8°$

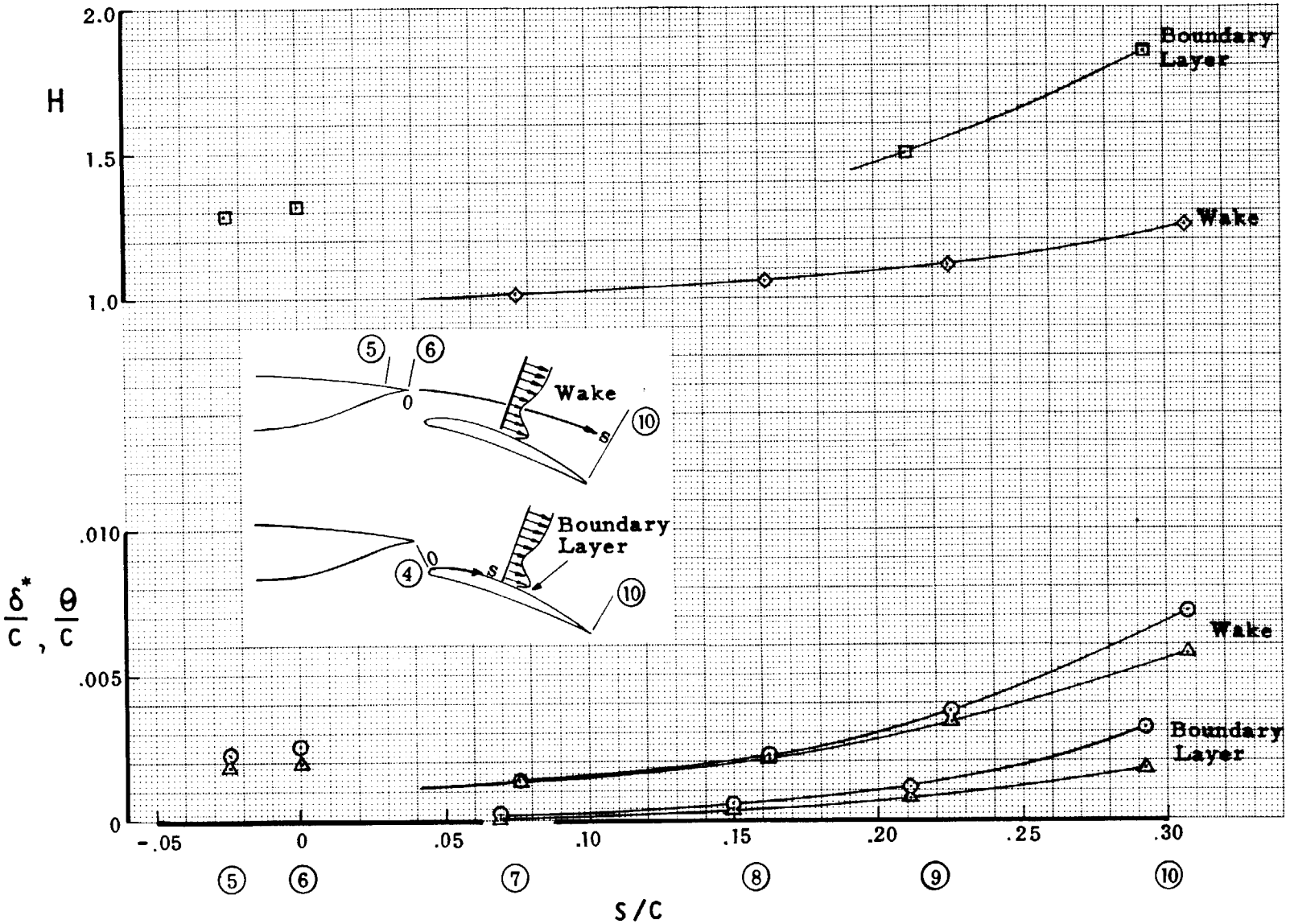

FIGURE B13.– VARIATIONS OF DISPLACEMENT, MOMENTUM THICKNESS, AND SHAPE FACTOR, $\alpha = 0°$

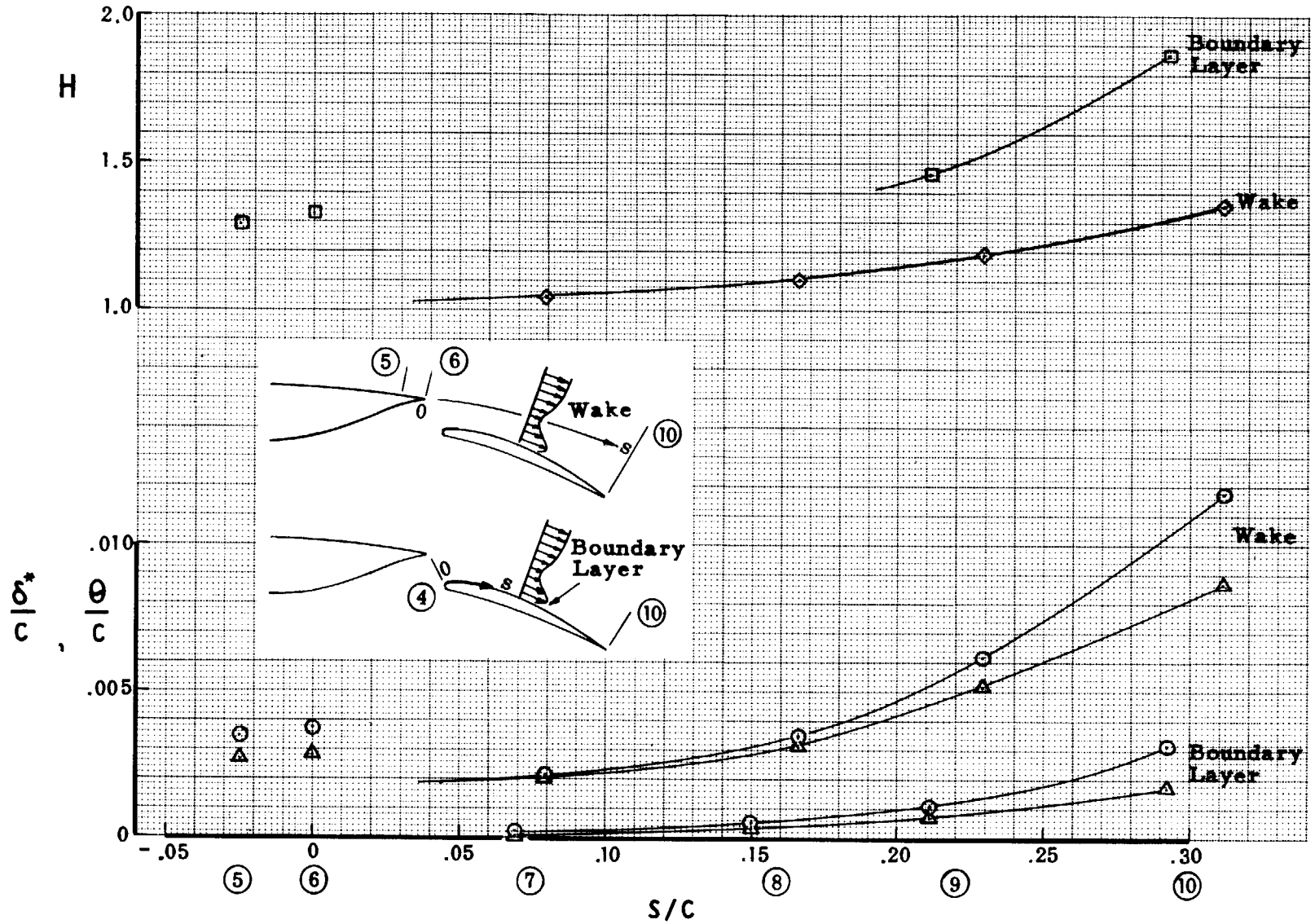

FIGURE B14.—VARIATIONS OF DISPLACEMENT, MOMENTUM THICKNESS, AND SHAPE FACTOR, $\alpha = 4°$

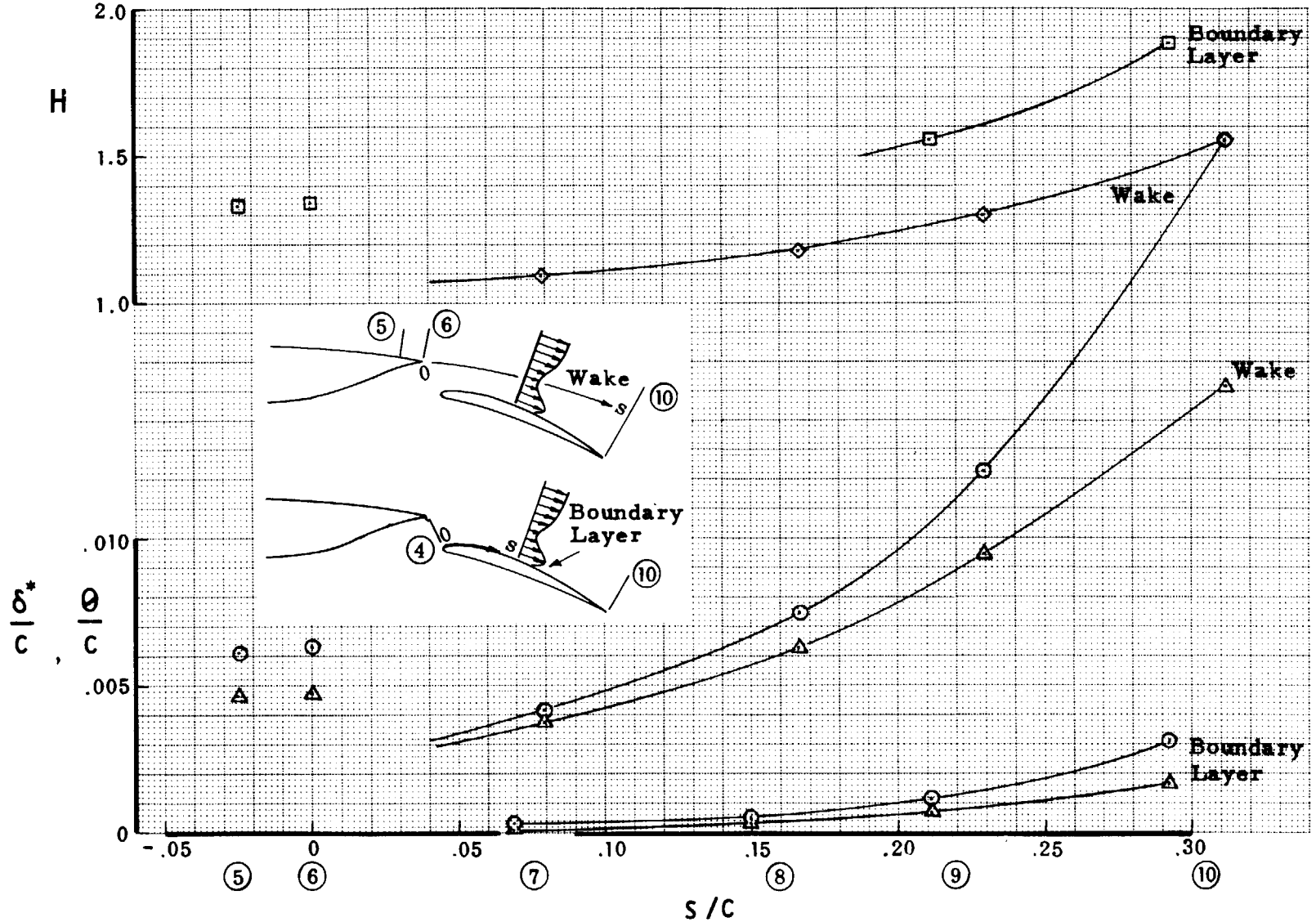

FIGURE B15.–VARIATIONS OF DISPLACEMENT, MOMENTUM THICKNESS, AND SHAPE FACTOR, $\alpha = 8°$

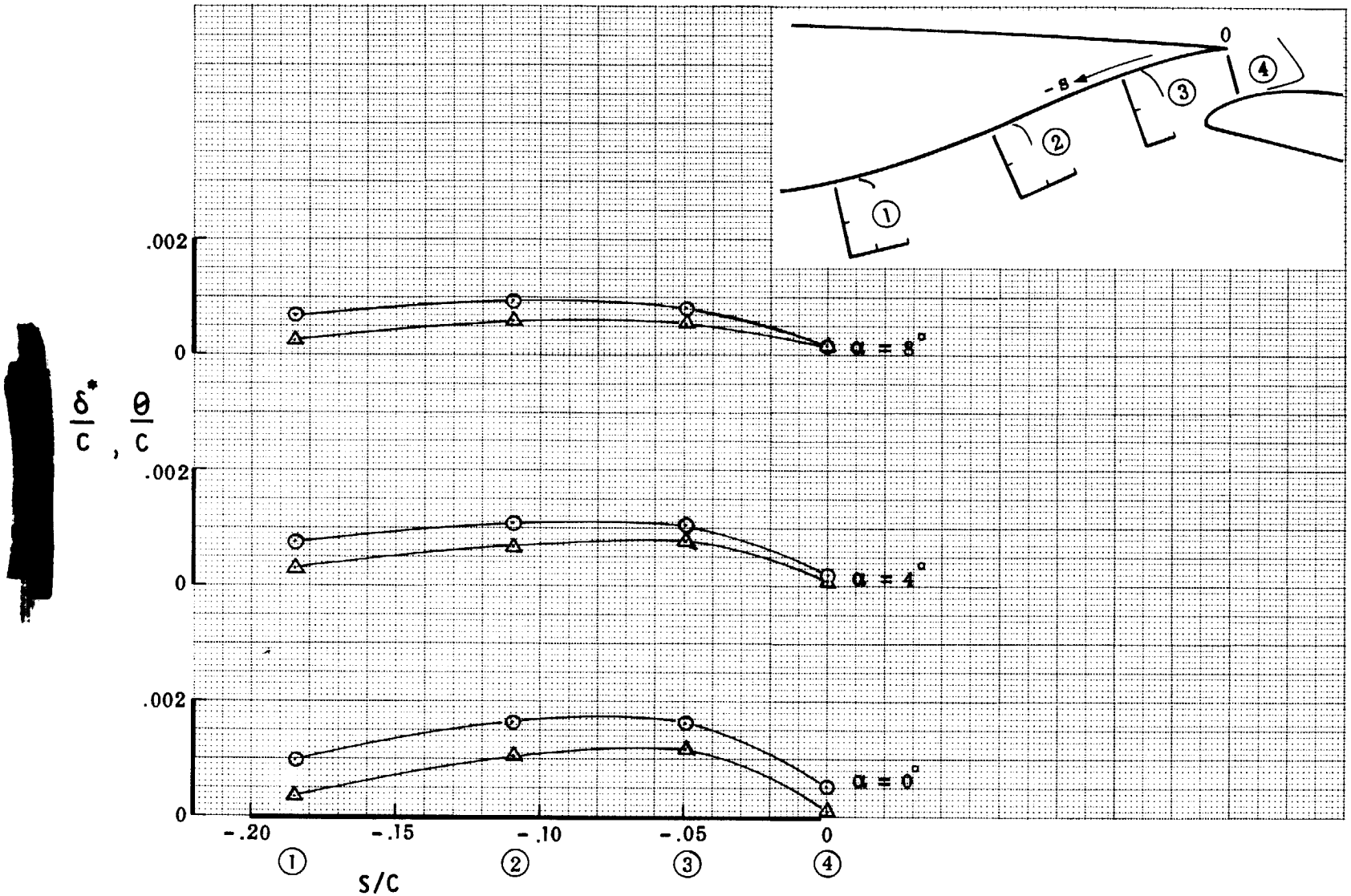

FIGURE B16.—VARIATIONS OF DISPLACEMENT AND MOMENTUM THICKNESS ON THE COVE

APPENDIX C

PRESSURE DISTRIBUTIONS

TABLE C1.–PRESSURE DISTRIBUTION FIGURE DESCRIPTIONS

Model	Comments	Figure number
A (basic airfoil)	Mach number and Reynolds number variation	C1
	Transition strip effect	C2
	Slat 1 effect	C3
	Slat 2 effect	C4
B (single-slotted flap)	Slot gap and overlap effect (δ_f = 20°)	C5
	Flap deflection angle variation	C6
	Boundary-layer study configuration	C7
C (double-slotted flap with slat 1)	Optimized configuration ($\delta_{f_{eq}}$ = 44°)	C8
	Slat 1 deflection angle variation	C9
	Slat 1 slot optimization	C10
	Flap angle combination at constant $\delta_{f_{eq}}$ (44°)	C11
	Wing/vane-slot gap and overlap effects ($\delta_{f_{eq}}$ = 44°)	C12
	Vane/flap-slot gap and overlap effects ($\delta_{f_{eq}}$ = 44°)	C13
	Flap deflection angle variation	C14
	Flap angle combination at constant $\delta_{f_{eq}}$ (49°)	C15
	Wing/vane-slot gap and overlap effects ($\delta_{f_{eq}}$ = 49°)	C16
	Low flap deflection angle study ($\delta_{f_{eq}}$ = 15°)	C17
	Low flap deflection without leading-edge device ($\delta_{f_{eq}}$ = 13°)	C18
D (triple-slotted flap with slat 2)	Optimized configuration	C19
	Slat 2 deflection angle variation	C20
	Slat 2 slot optimization	C21
	Flap angle combination at constant $\delta_{f_{eq}}$ (46°)	C22
	Wing/vane slot gap and overlap effects ($\delta_{f_{eq}}$ = 46°)	C23
	Vane/main-slot gap and overlap effects ($\delta_{f_{eq}}$ = 46°)	C24
	Main/aft-slot gap and overlap effects ($\delta_{f_{eq}}$ = 46°)	C25
	Flap angle combination at constant $\delta_{f_{eq}}$ (53°)	C26
	Leading-edge device bracket effects ($\delta_{f_{eq}}$ = 16°)	C27
	Flap deflection angle variation with slat 1	C28
	Low flap deflection without leading edge device ($\delta_{f_{eq}}$ = 16°)	C29

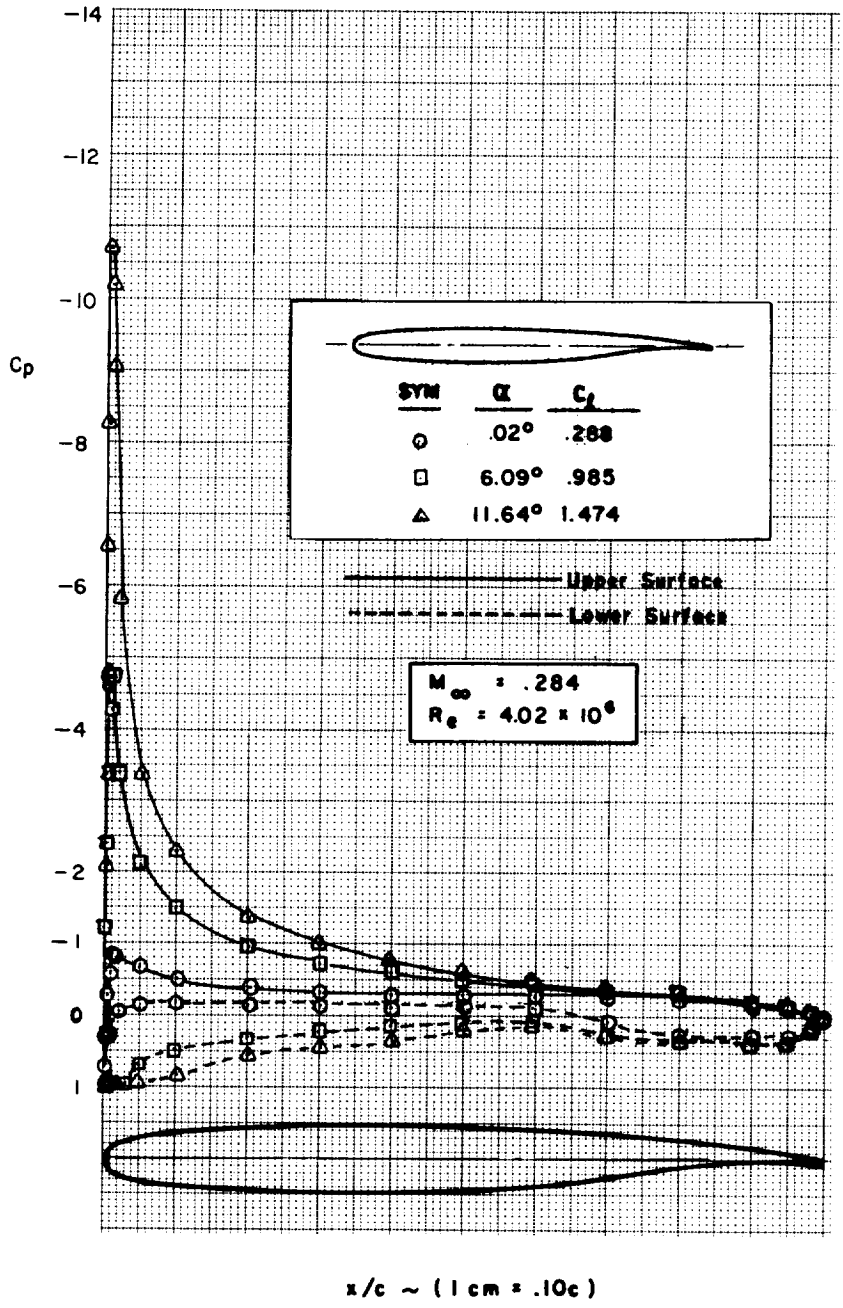

FIGURE C1.–EFFECT OF MACH NUMBER AND REYNOLDS NUMBER–MODEL A

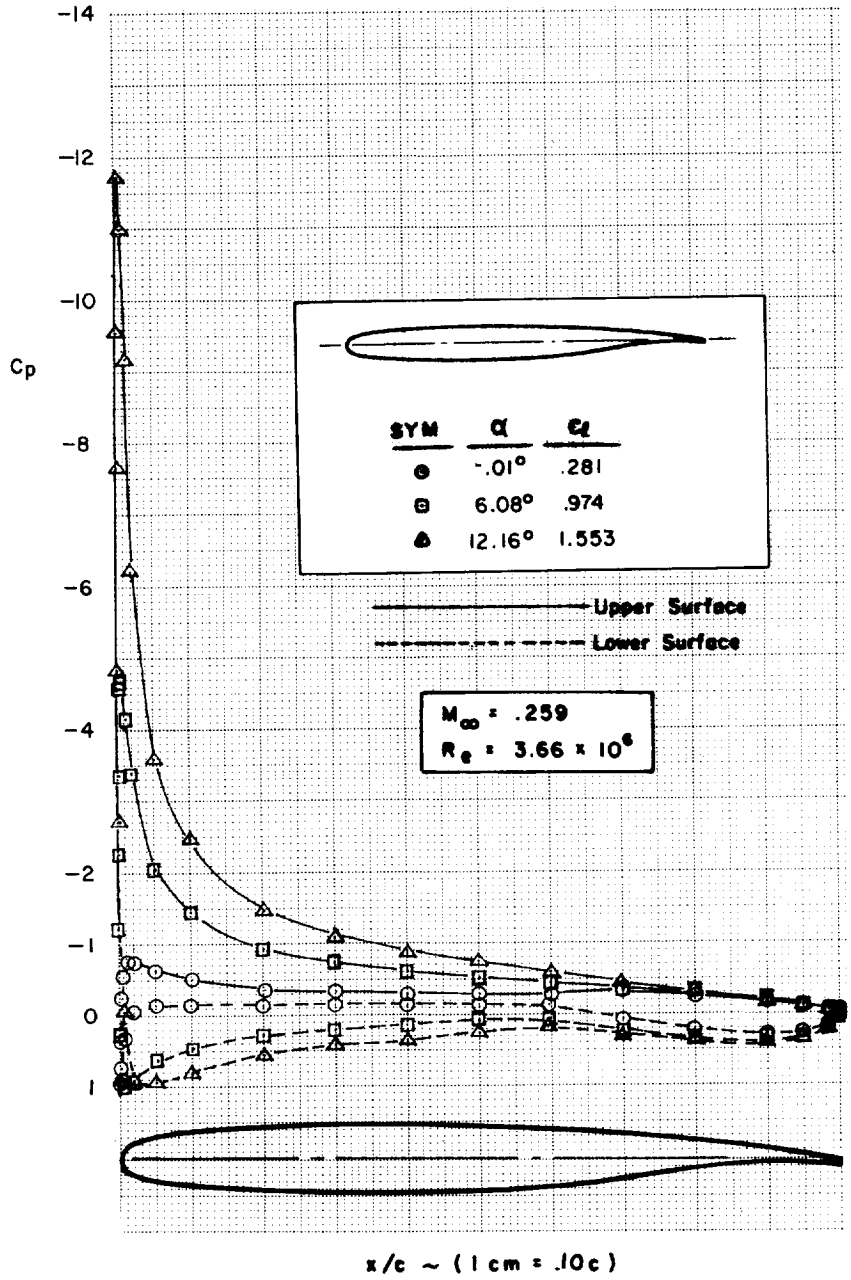

(b)

FIGURE C1.—Continued

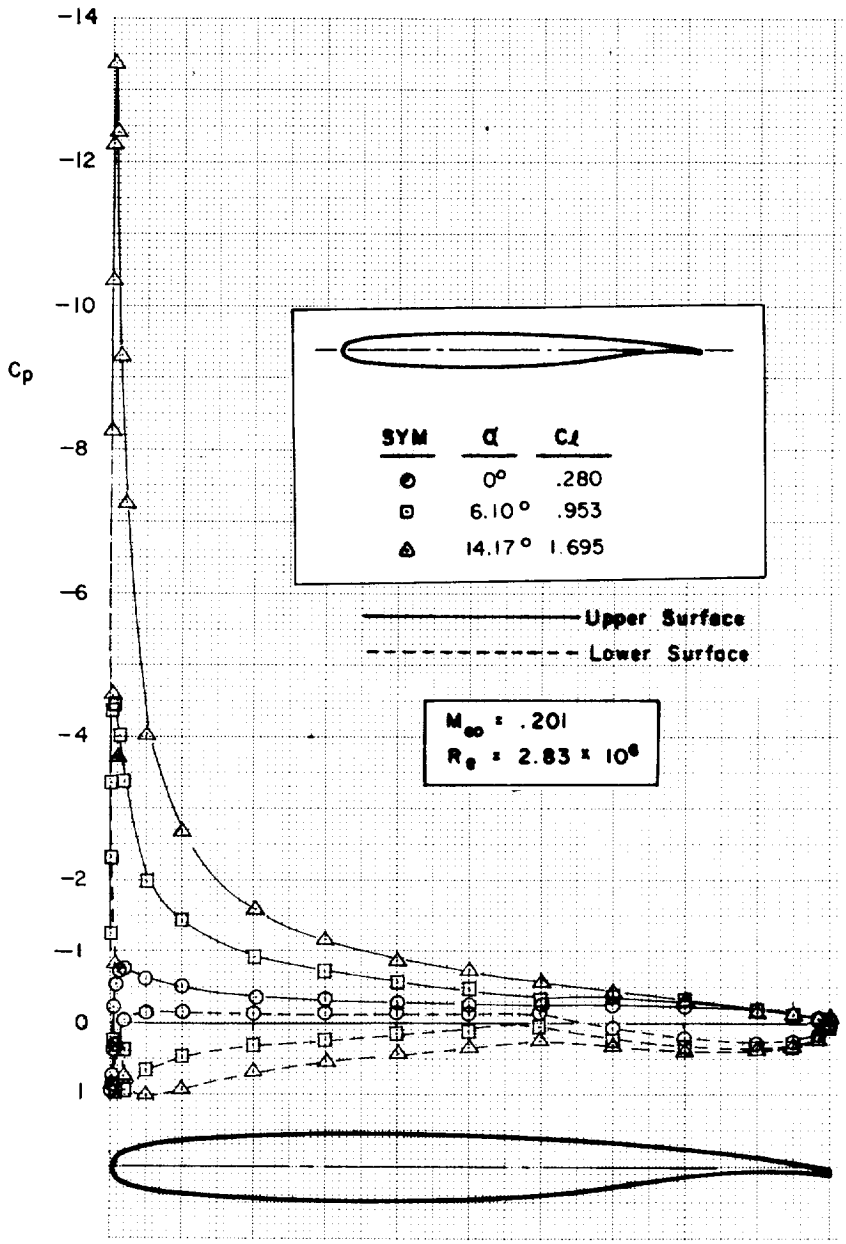

(c)

FIGURE C1.—Continued

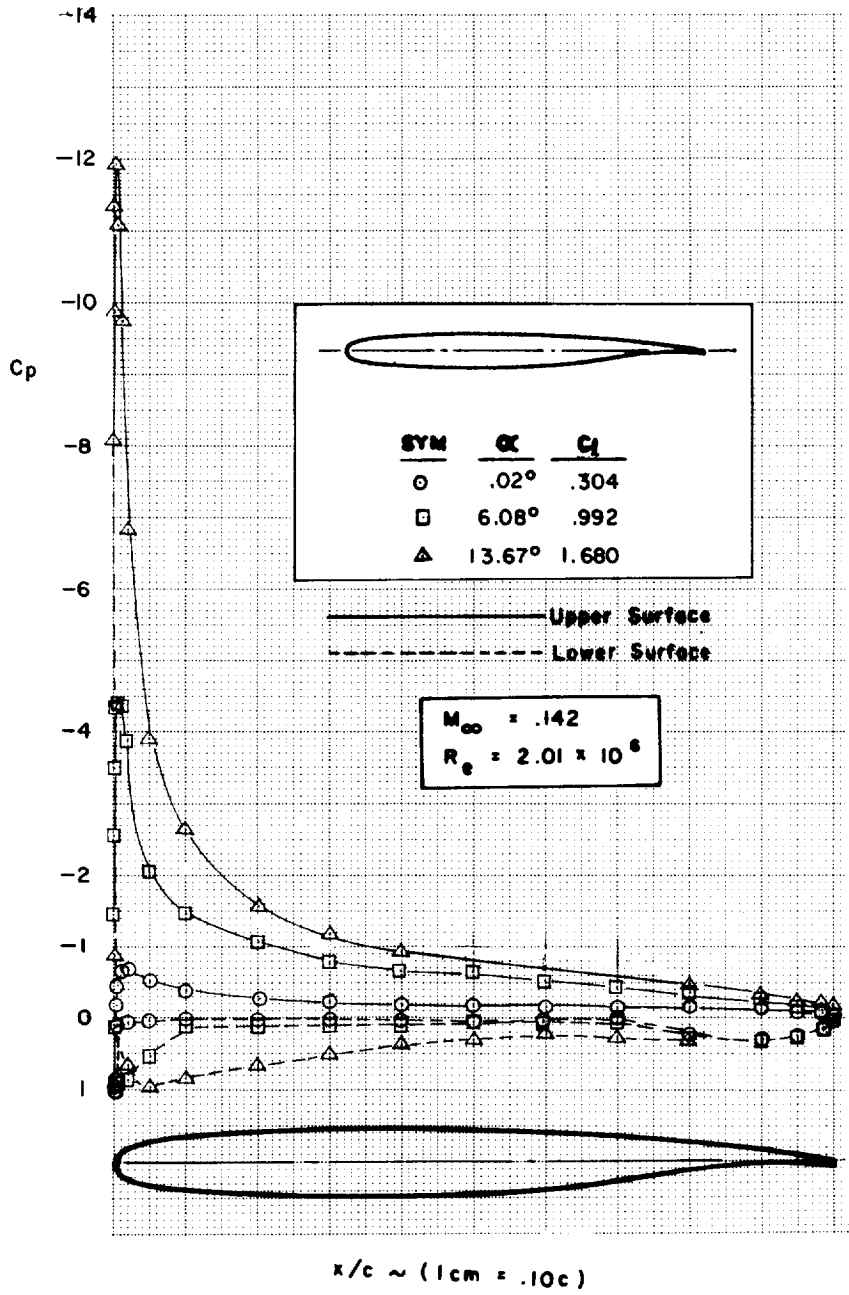

(d)

FIGURE C1.—Continued

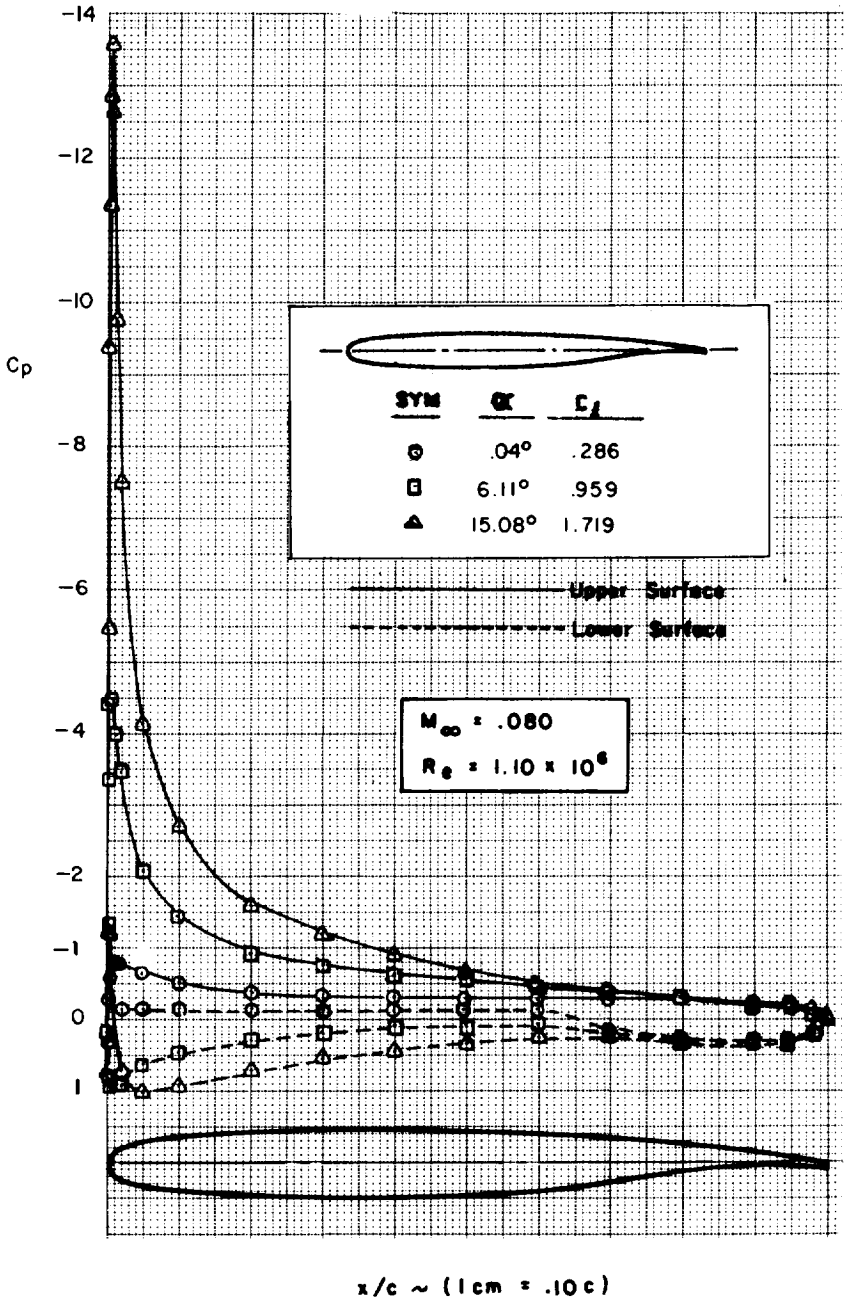

(e)

FIGURE C1.—Concluded

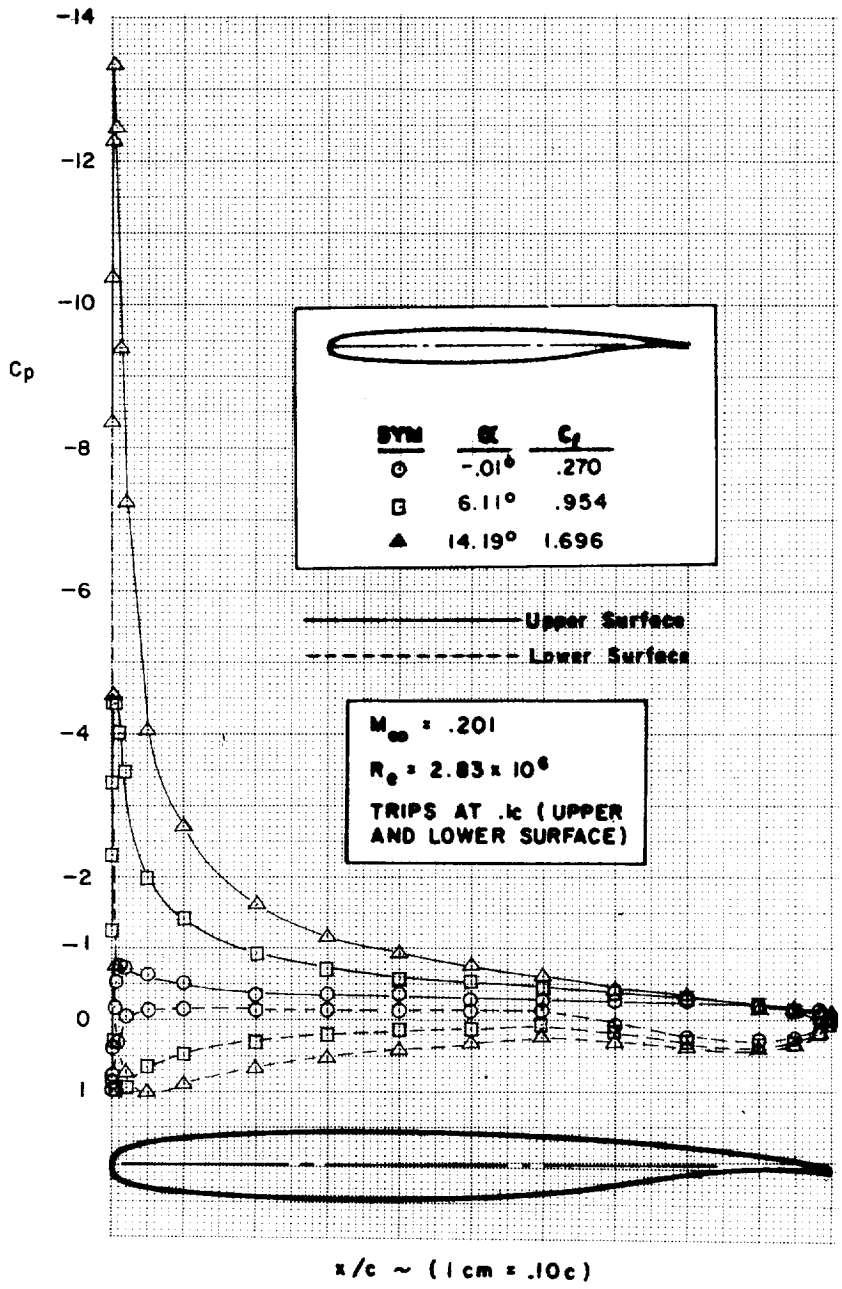

FIGURE C2.—TRANSITION STRIP EFFECT—MODEL A

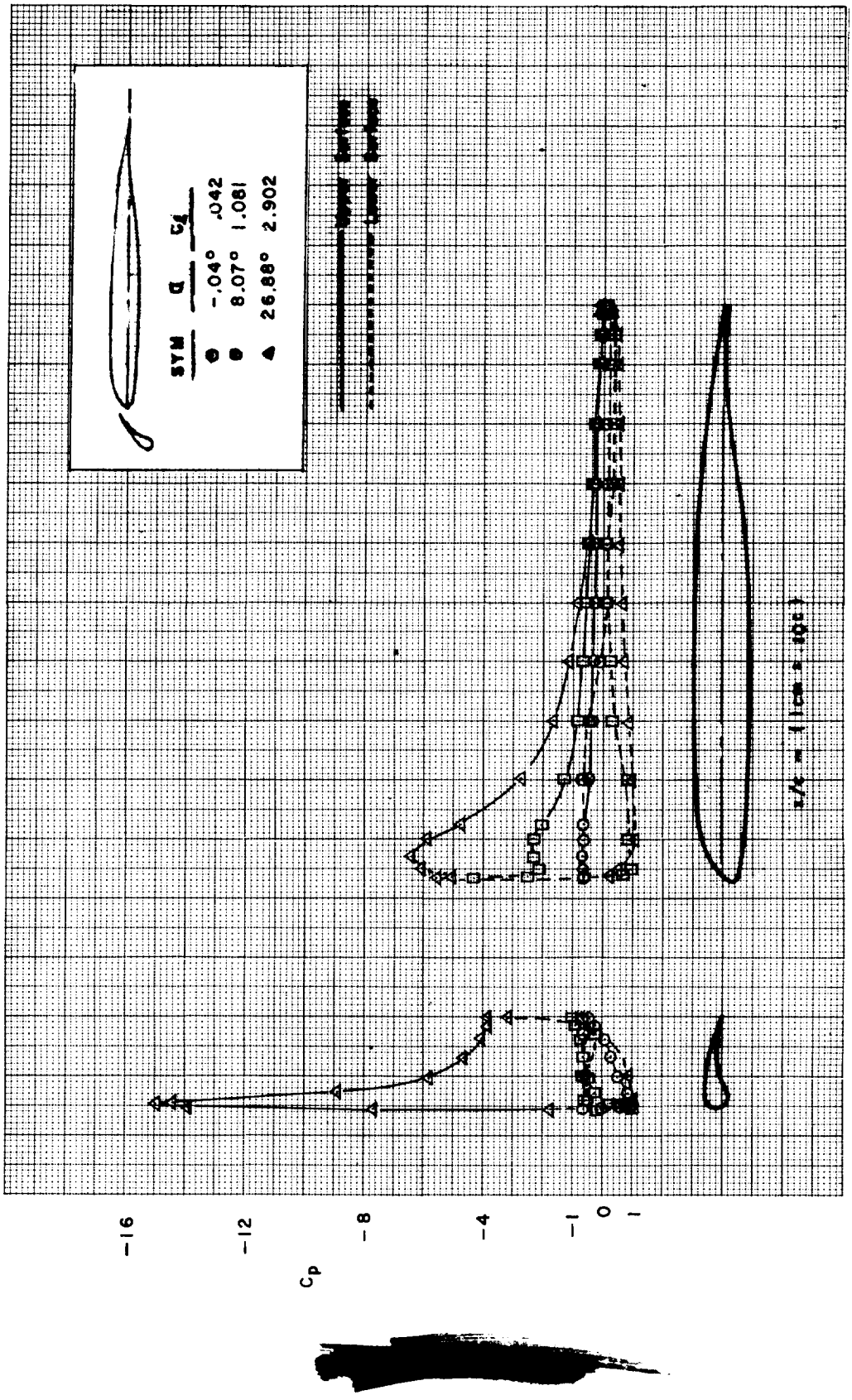

FIGURE C3.–EFFECT OF SLAT I– [illegible] A

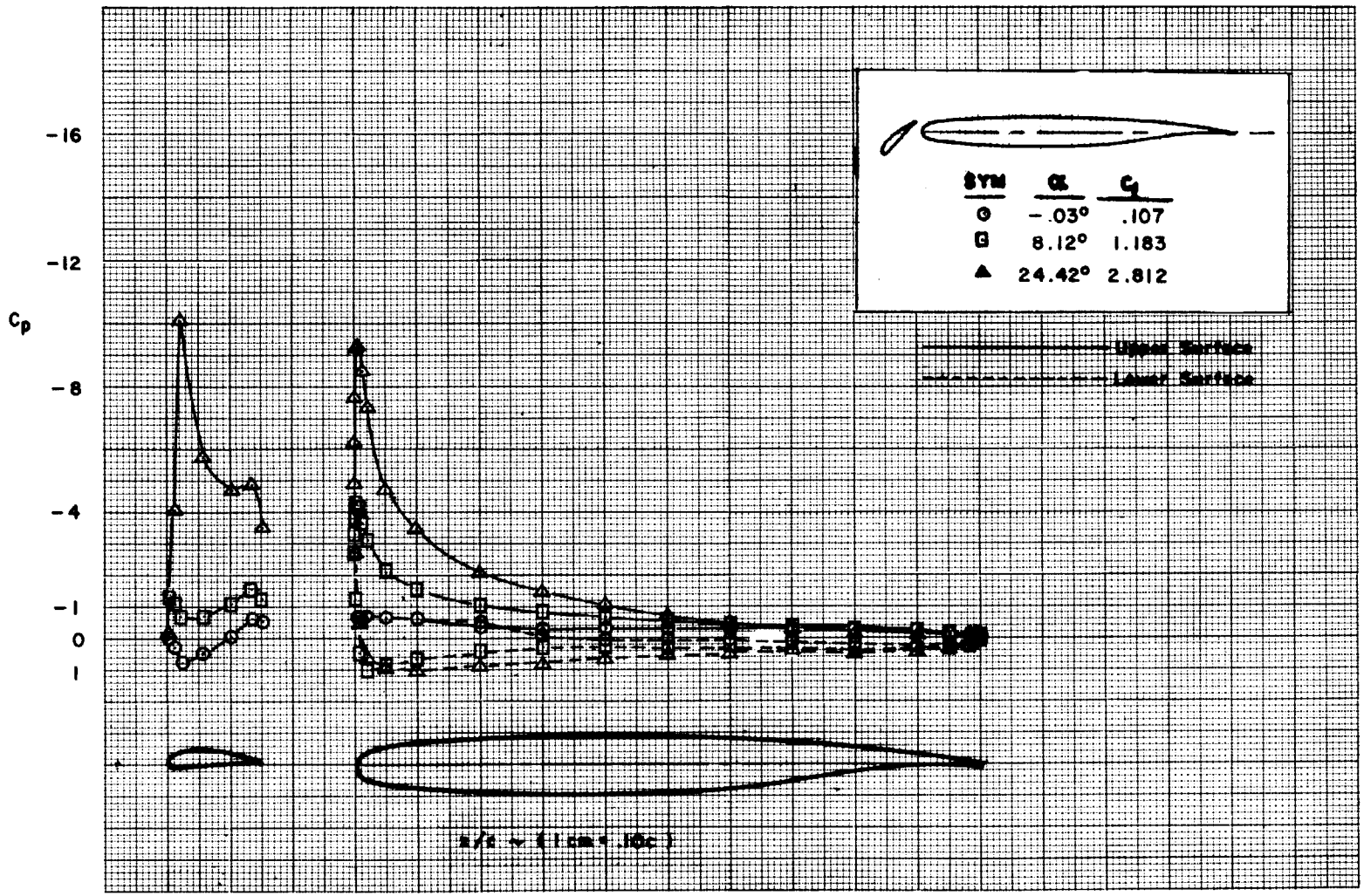

FIGURE C4.–EFFECT OF SLAT 2–MODEL A

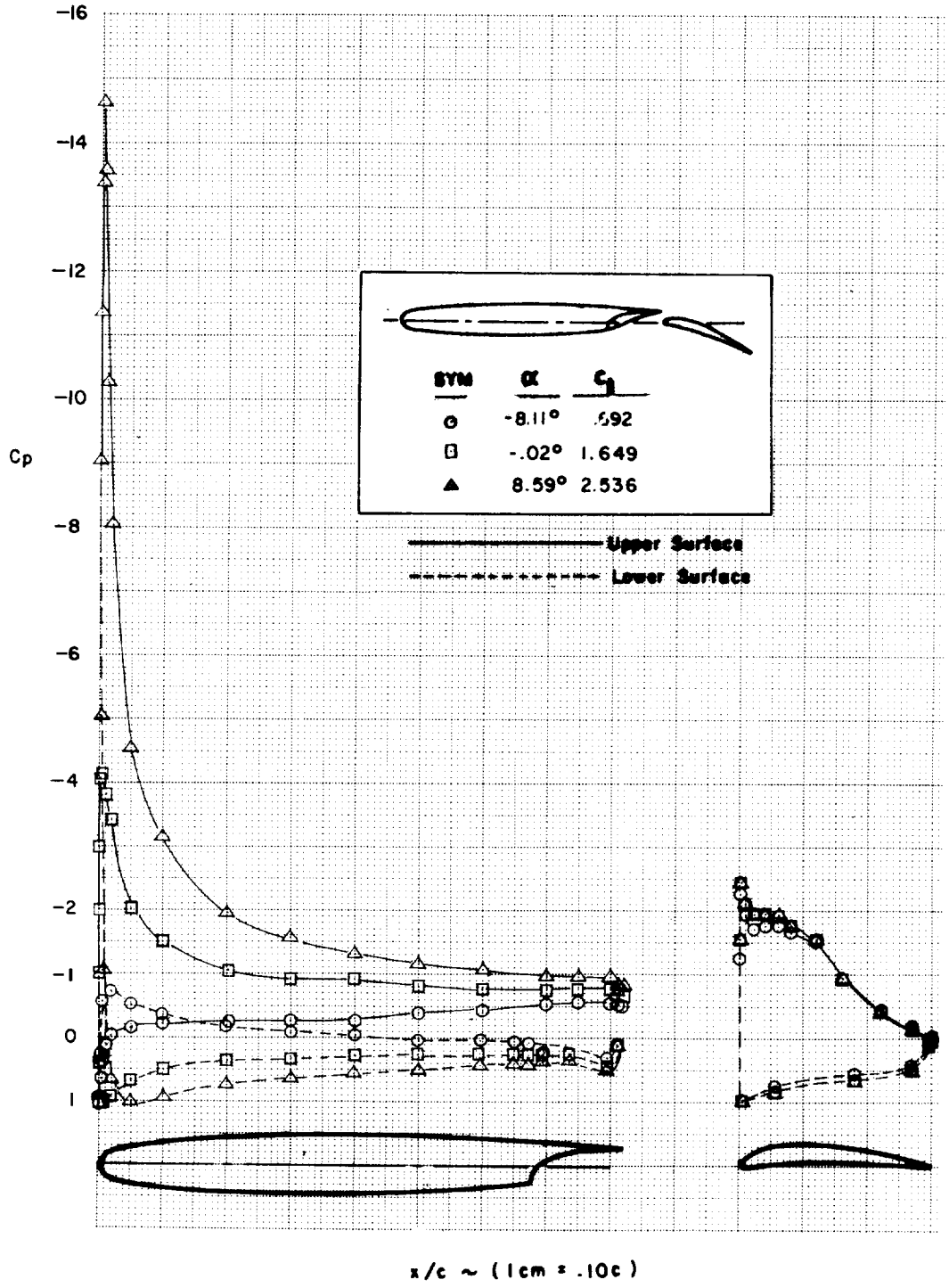

(a)

FIGURE C5.–EFFECT OF FLAP SLOT GAP AND OVERLAP–MODEL B ($\delta_{f_{eq}} = 20°$)

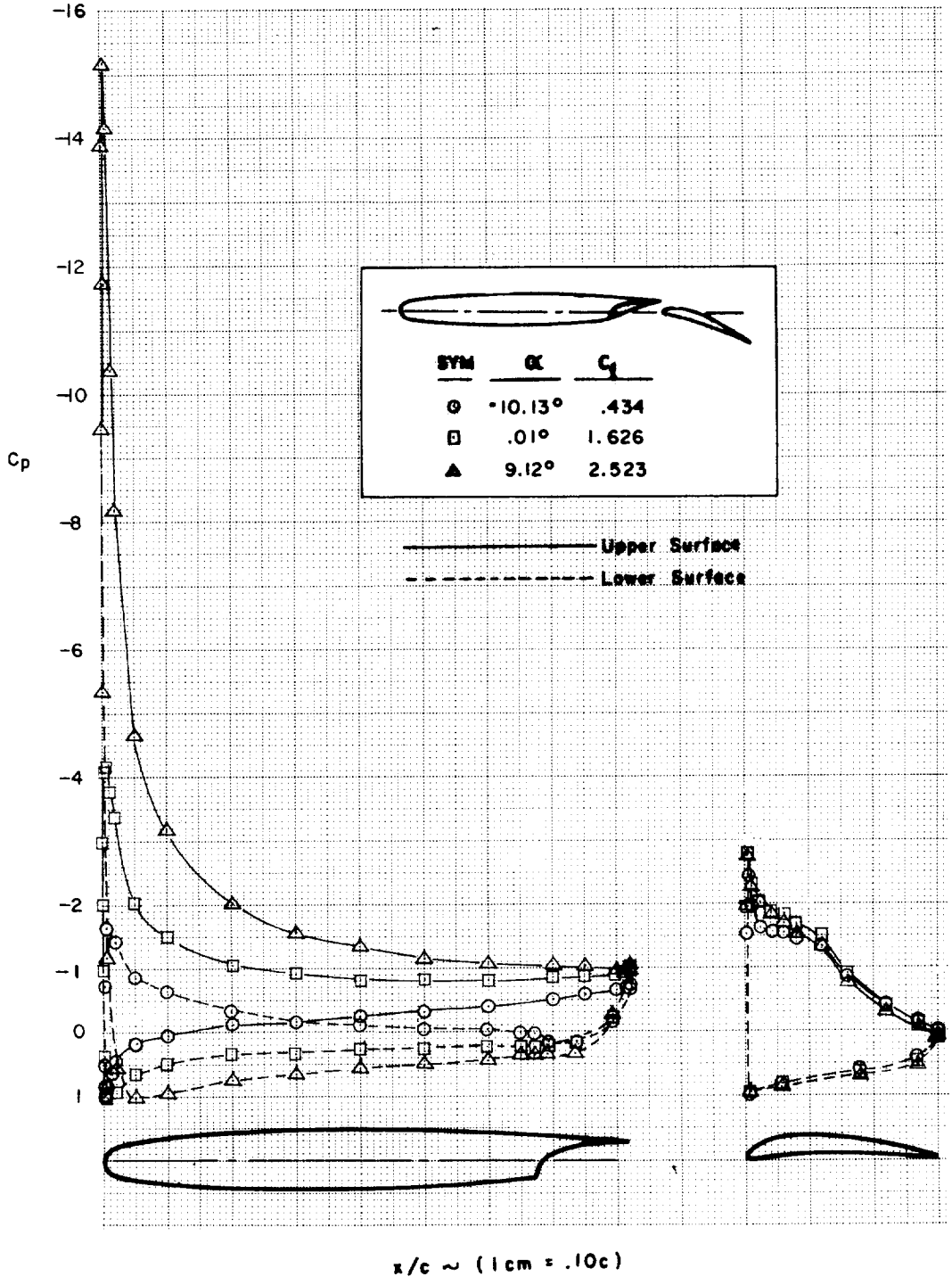

(b)

FIGURE C5.—Continued

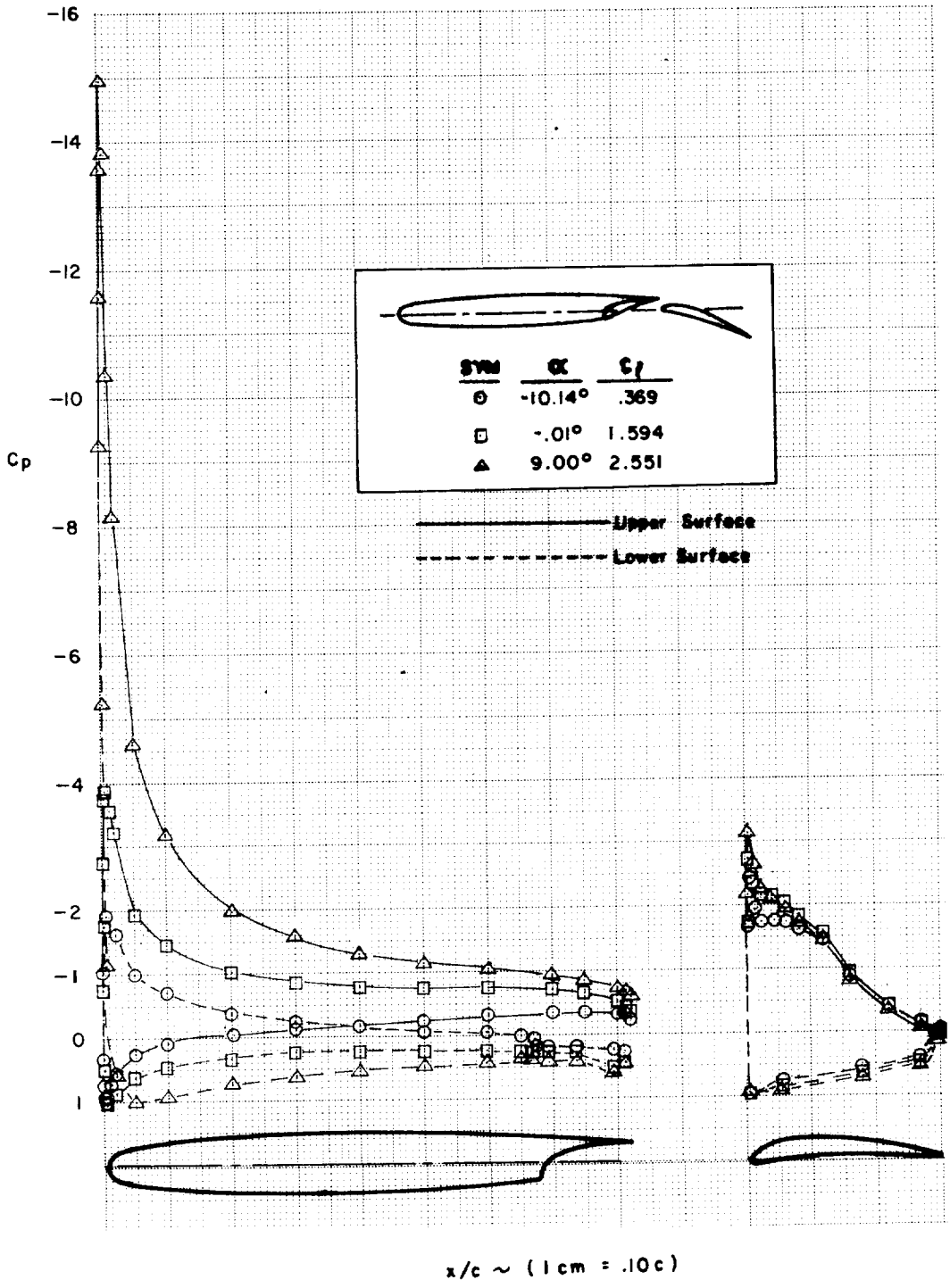

(c)

FIGURE C5.—Continued

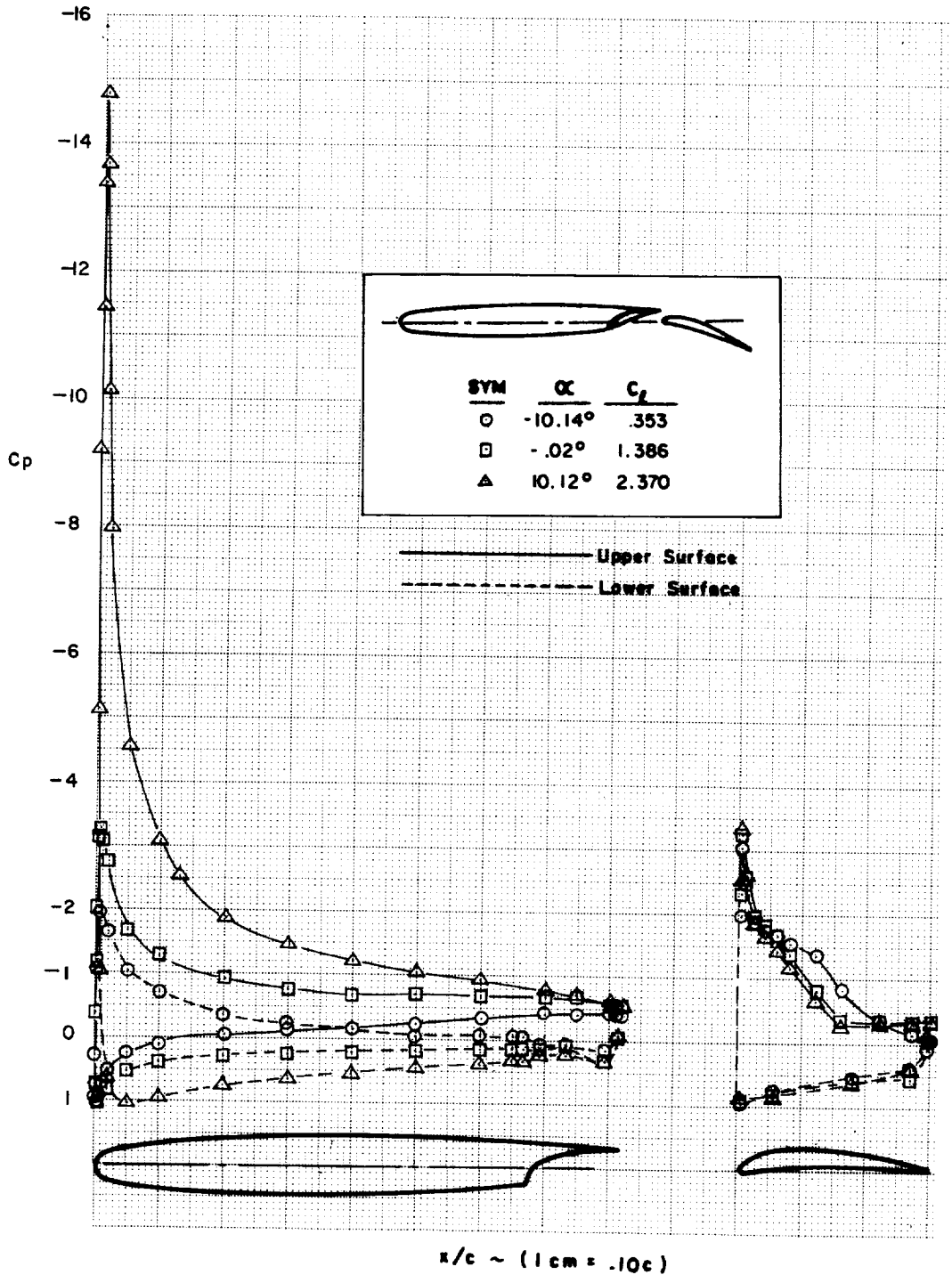

(d)

FIGURE C5.—Continued

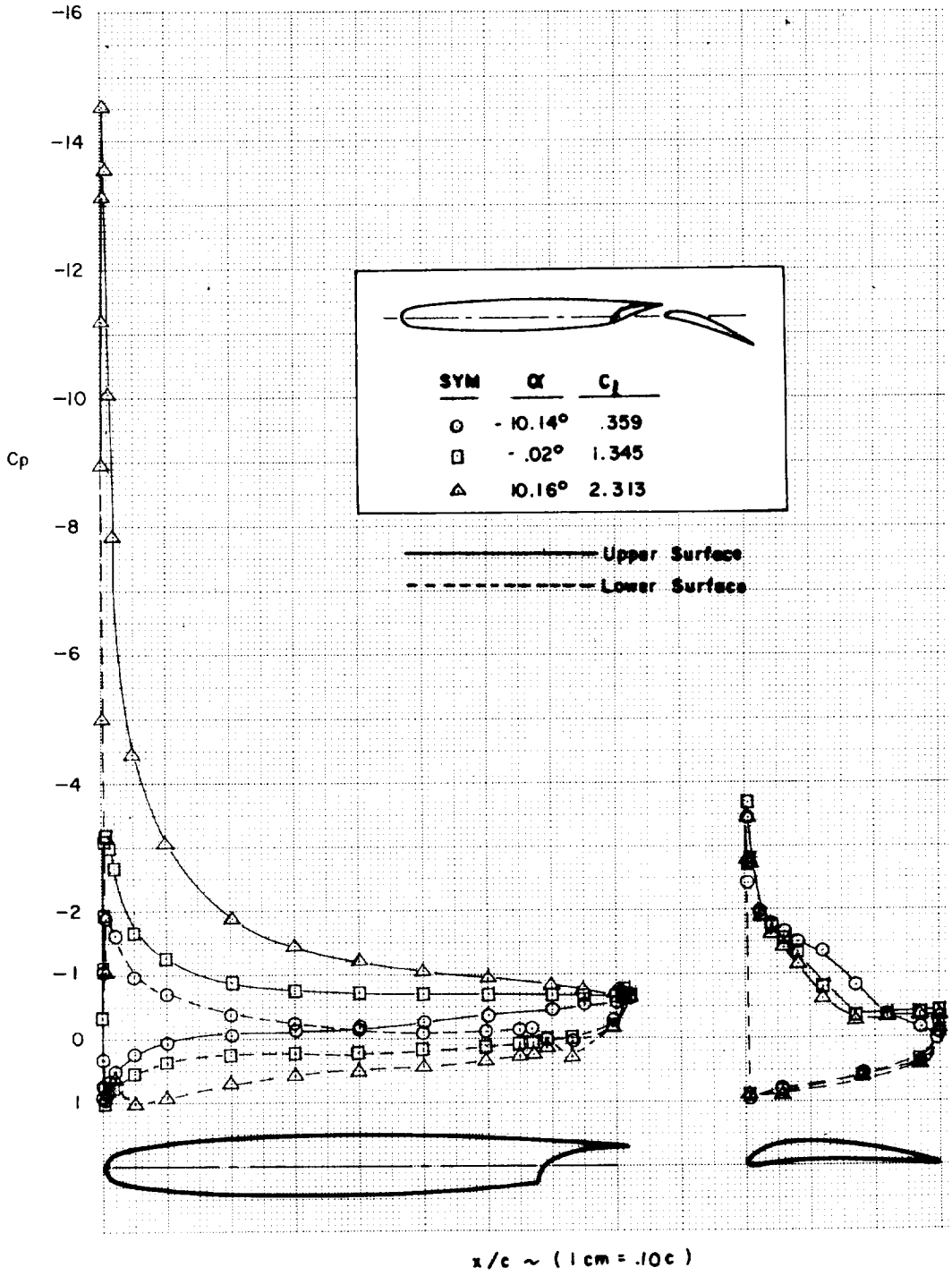

(e)

FIGURE C5.—Continued

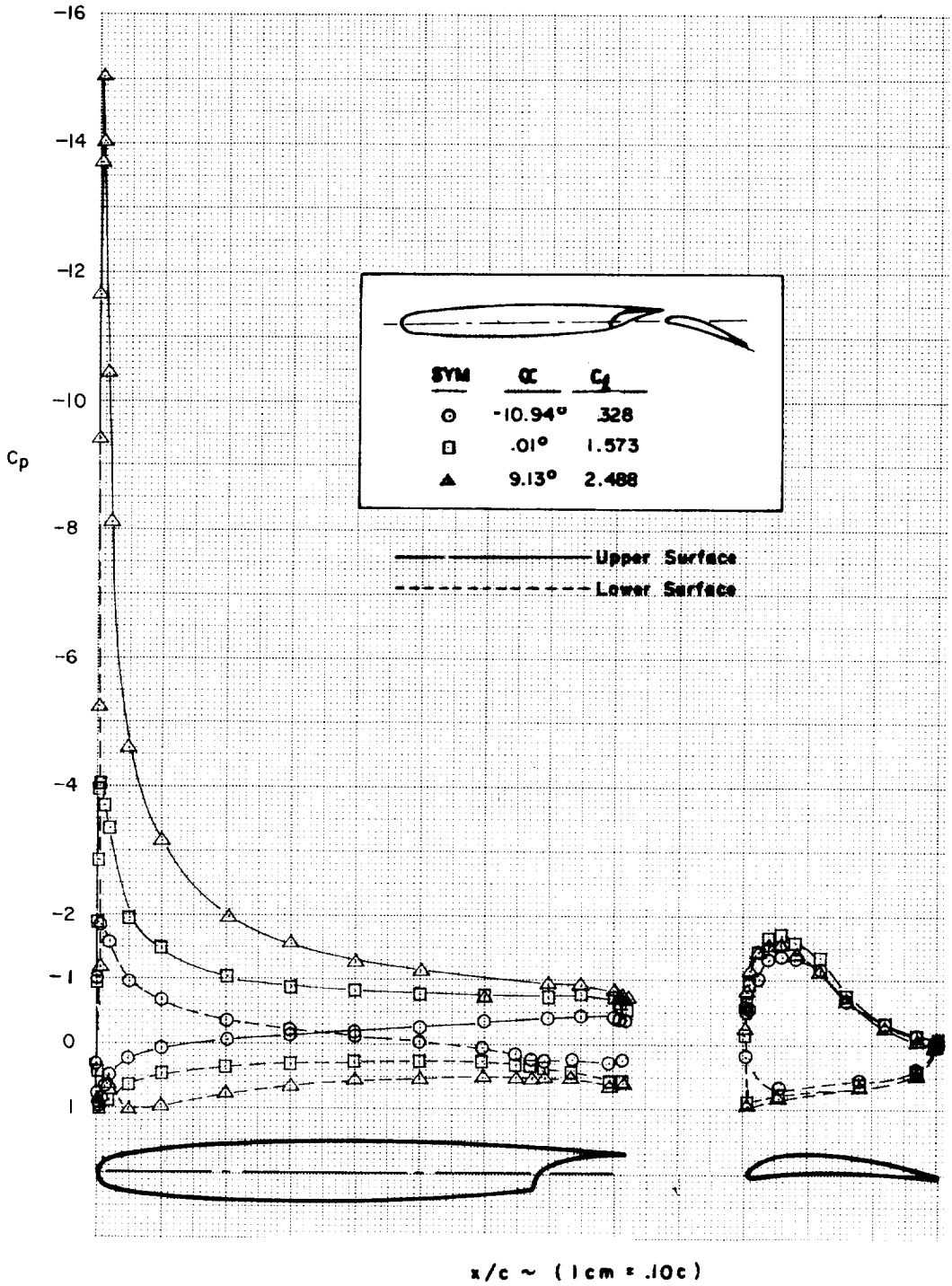

(f)

FIGURE C5.—Continued

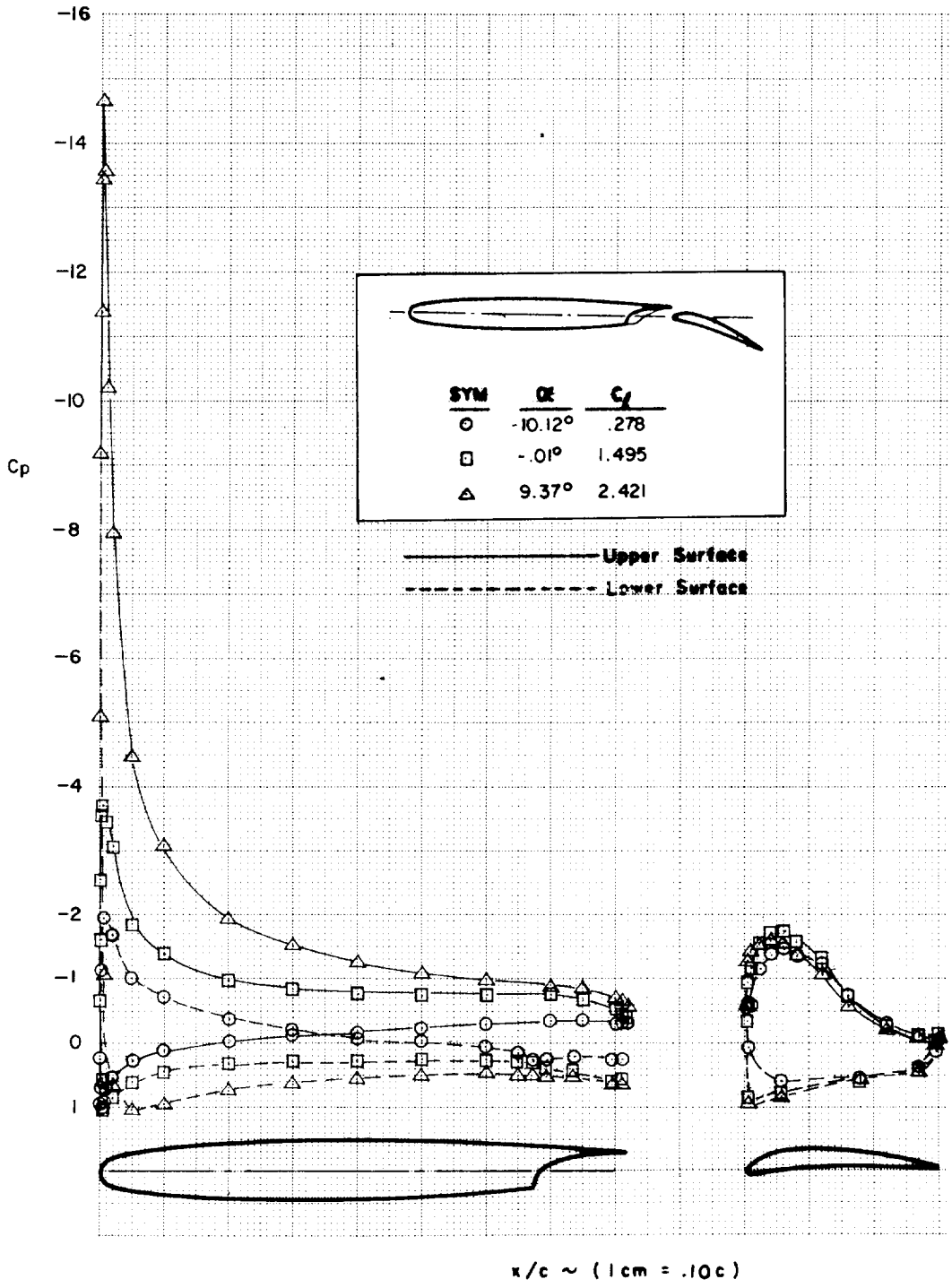

(g)

FIGURE C5.—Continued

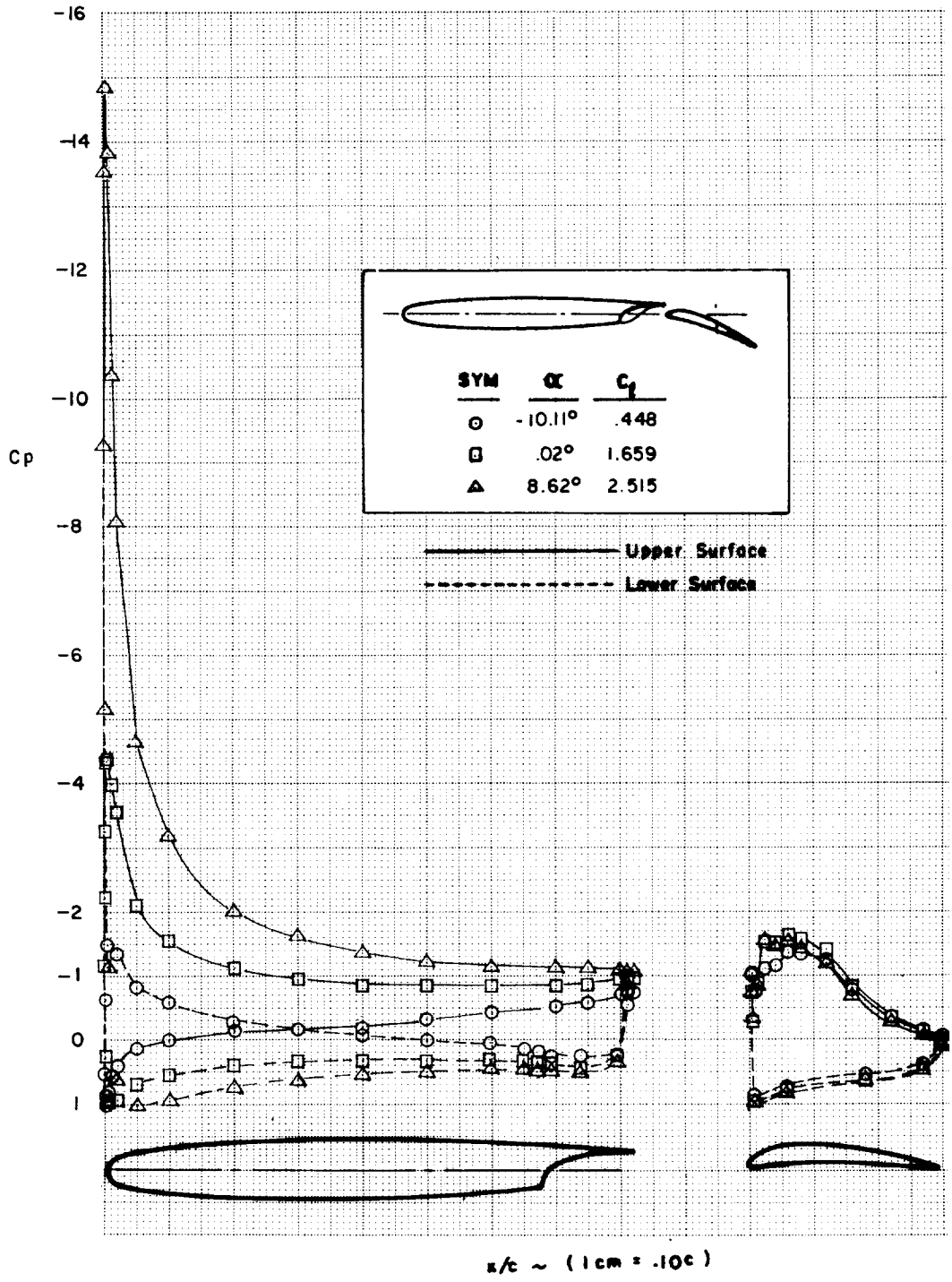

(h)

FIGURE C5.—Continued

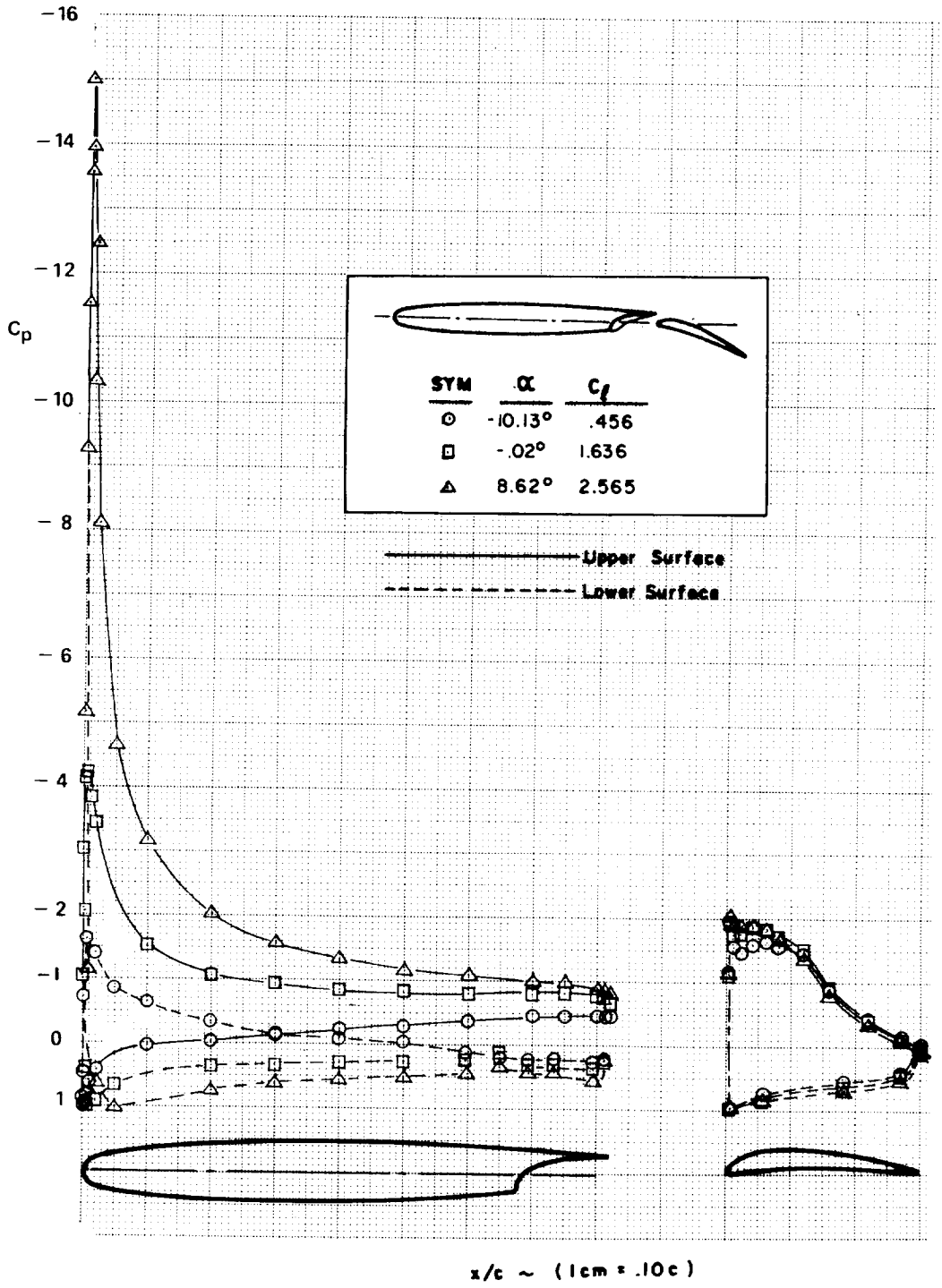

(i)

FIGURE C5.—Concluded

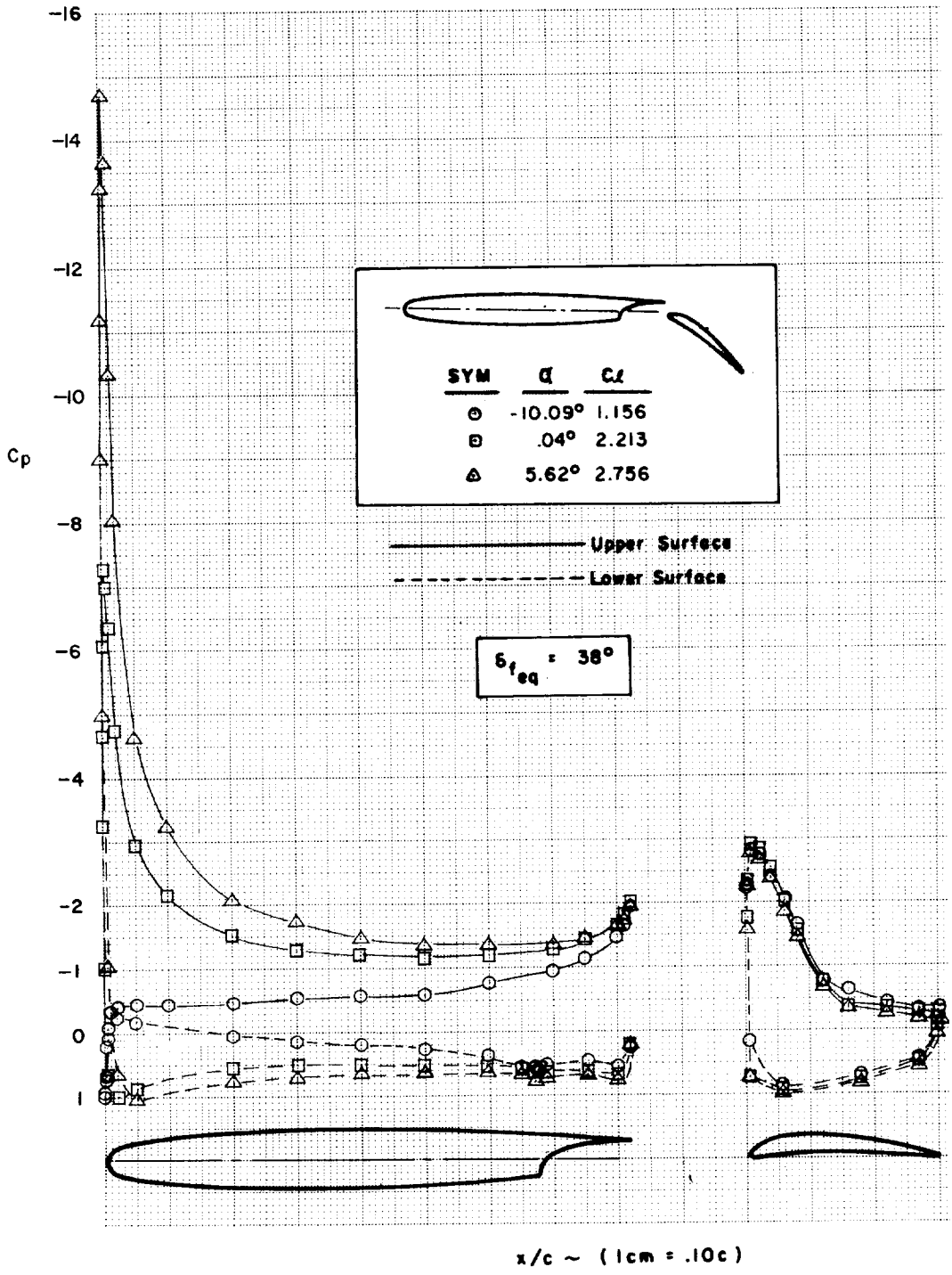

(a)

FIGURE C6.–EFFECT OF FLAP DEFLECTION ANGLE VARIATION–MODEL B

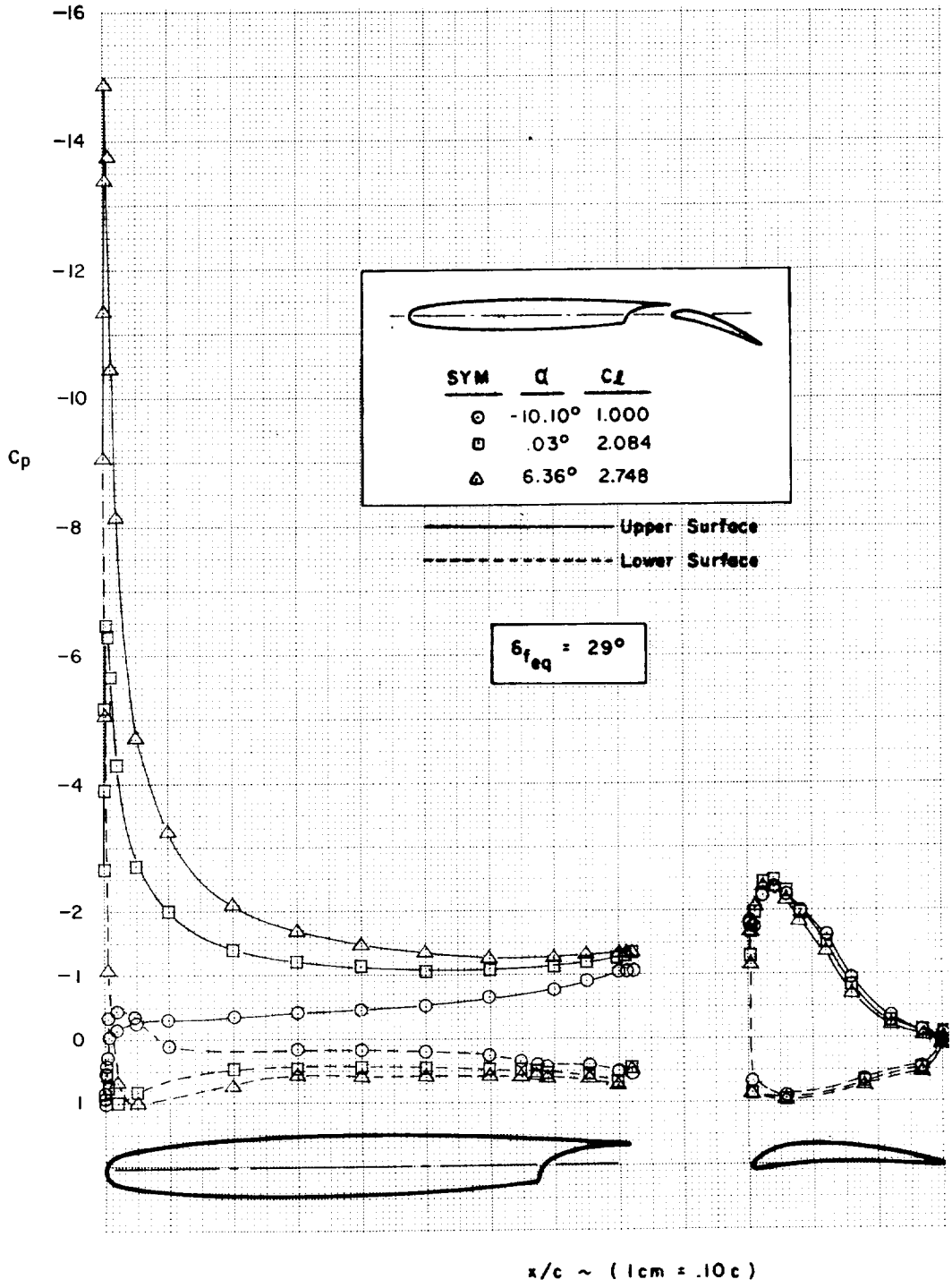

(b)

FIGURE C6.—Continued

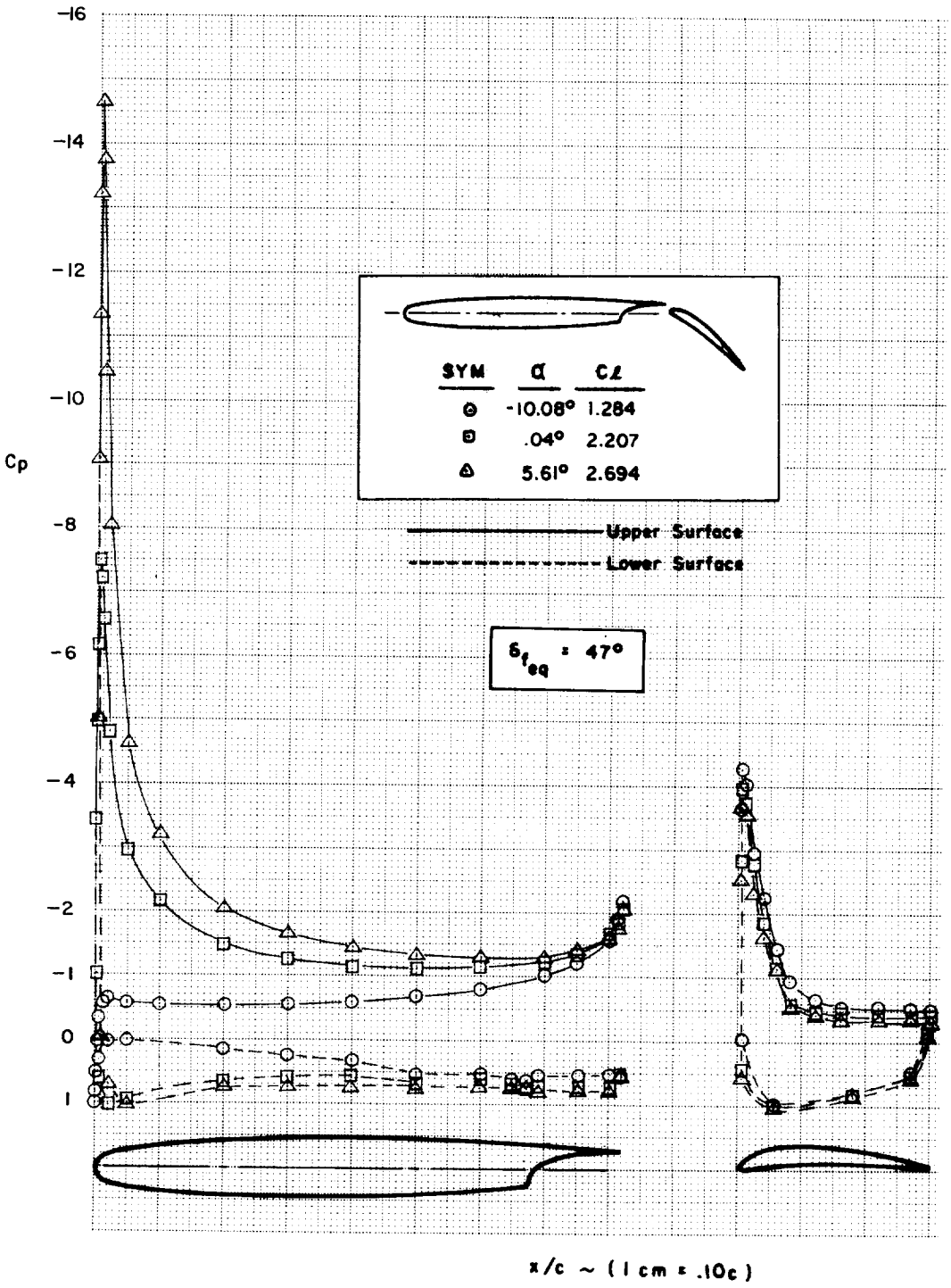

(c)

FIGURE C6.—Concluded

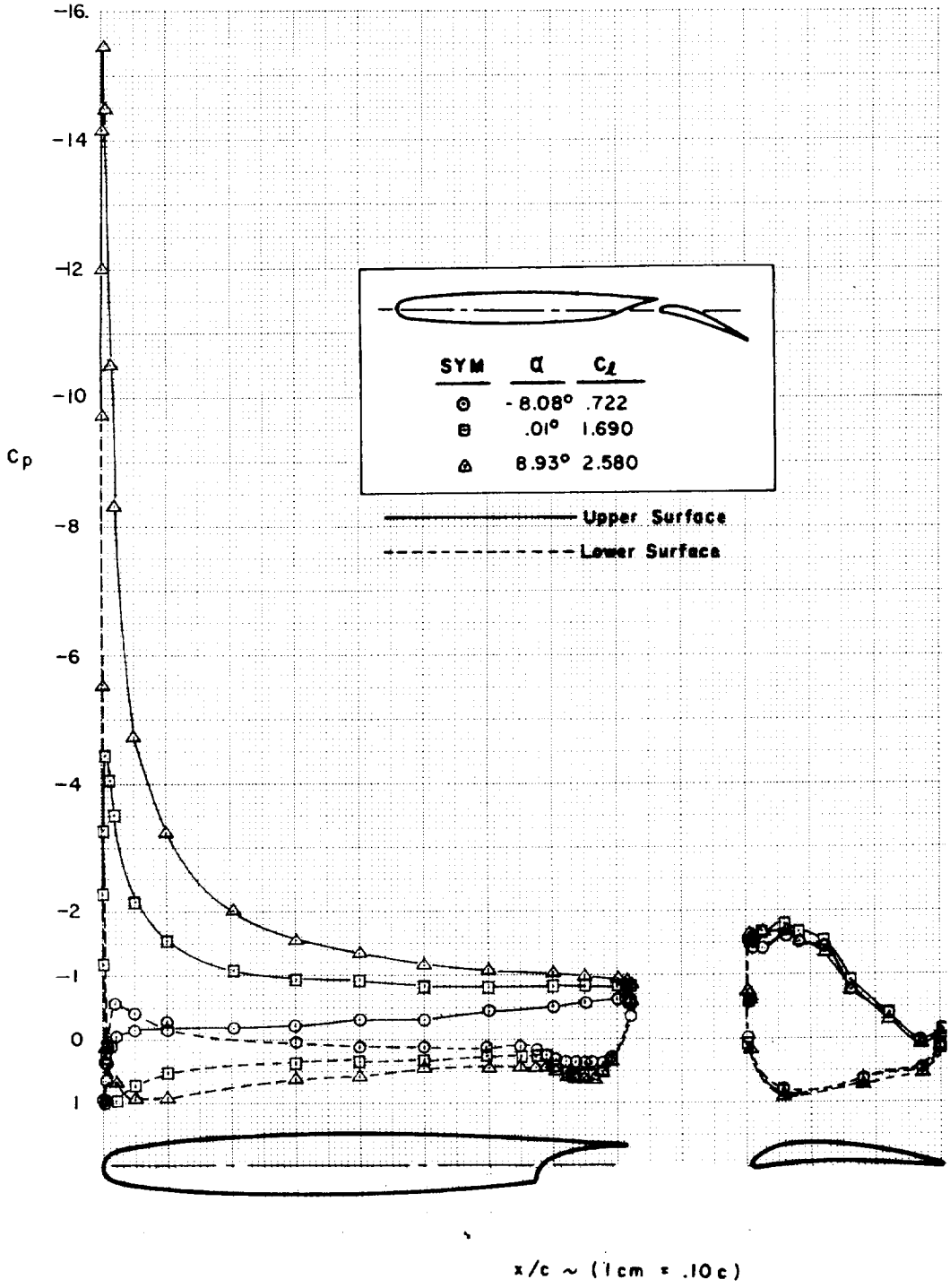

FIGURE C7.–BOUNDARY-LAYER STUDY CONFIGURATION–MODEL B ($\delta_f = 20°$)

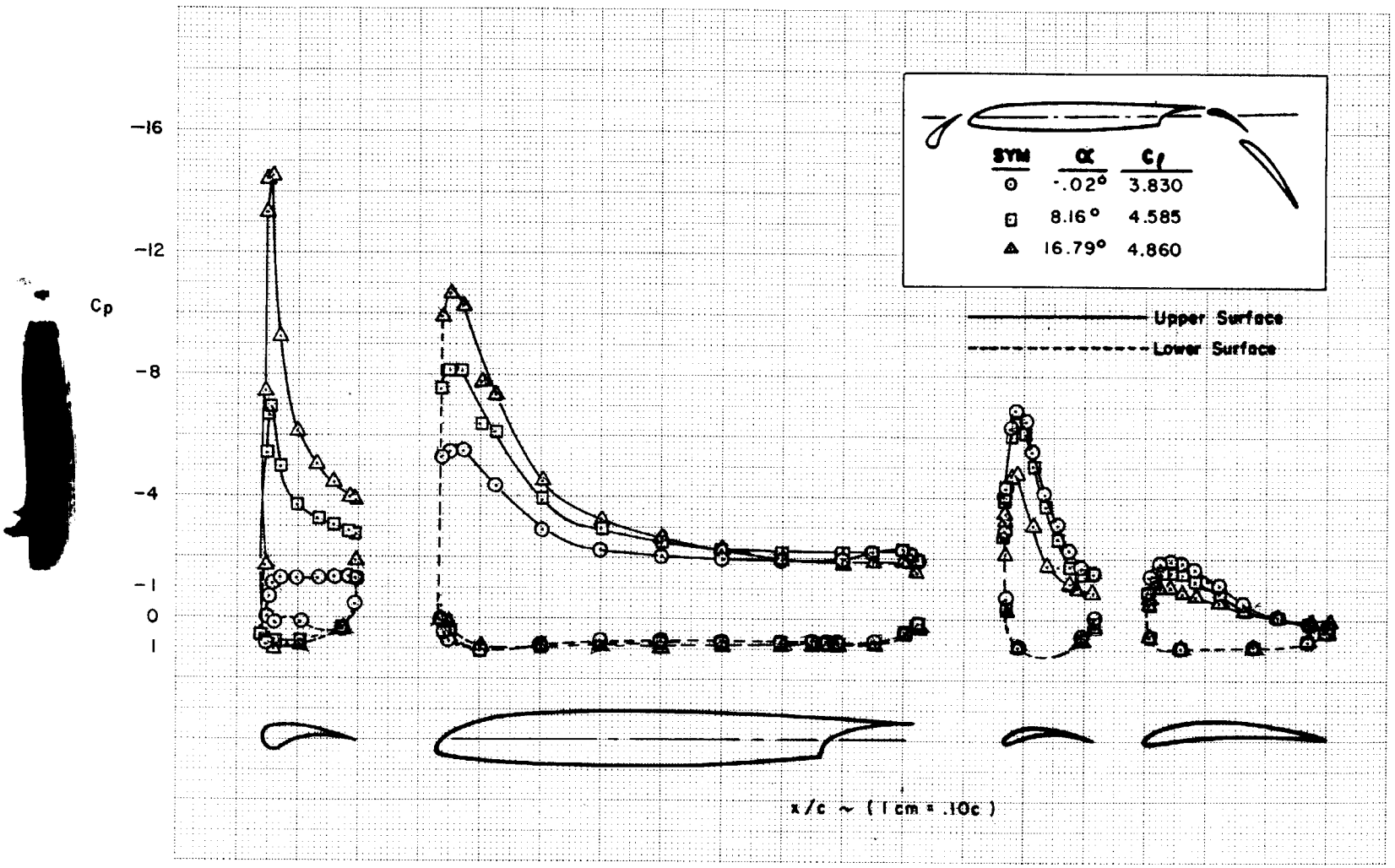

FIGURE C8.—OPTIMIZED CONFIGURATION—MODEL C ($\delta_{f_{eq}} = 44°$)

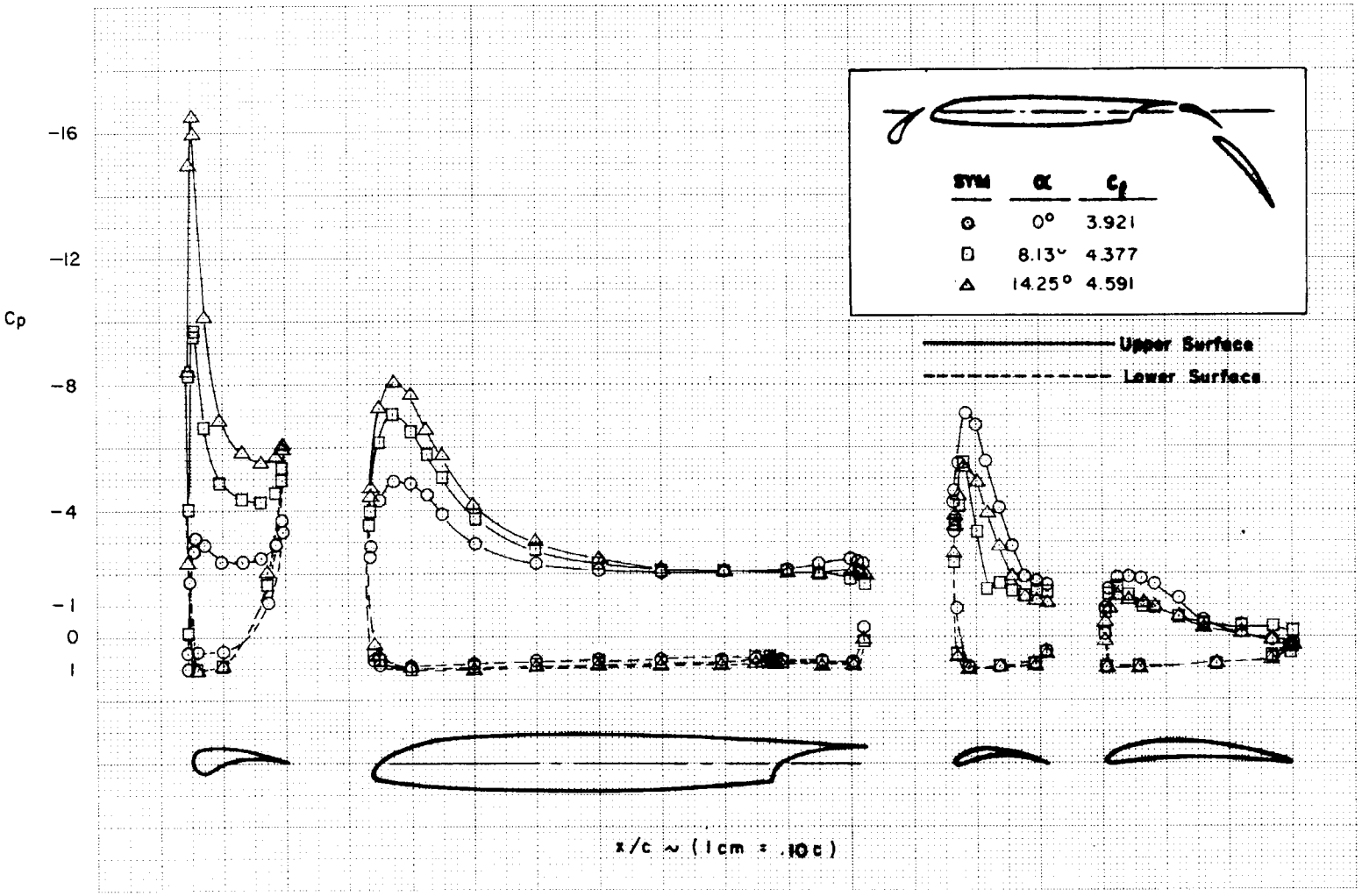

(a)

FIGURE C9.–EFFECT OF SLAT 1 DEFLECTION ANGLE VARIATION–MODEL C ($\delta_{f_{eq}} = 44°$)

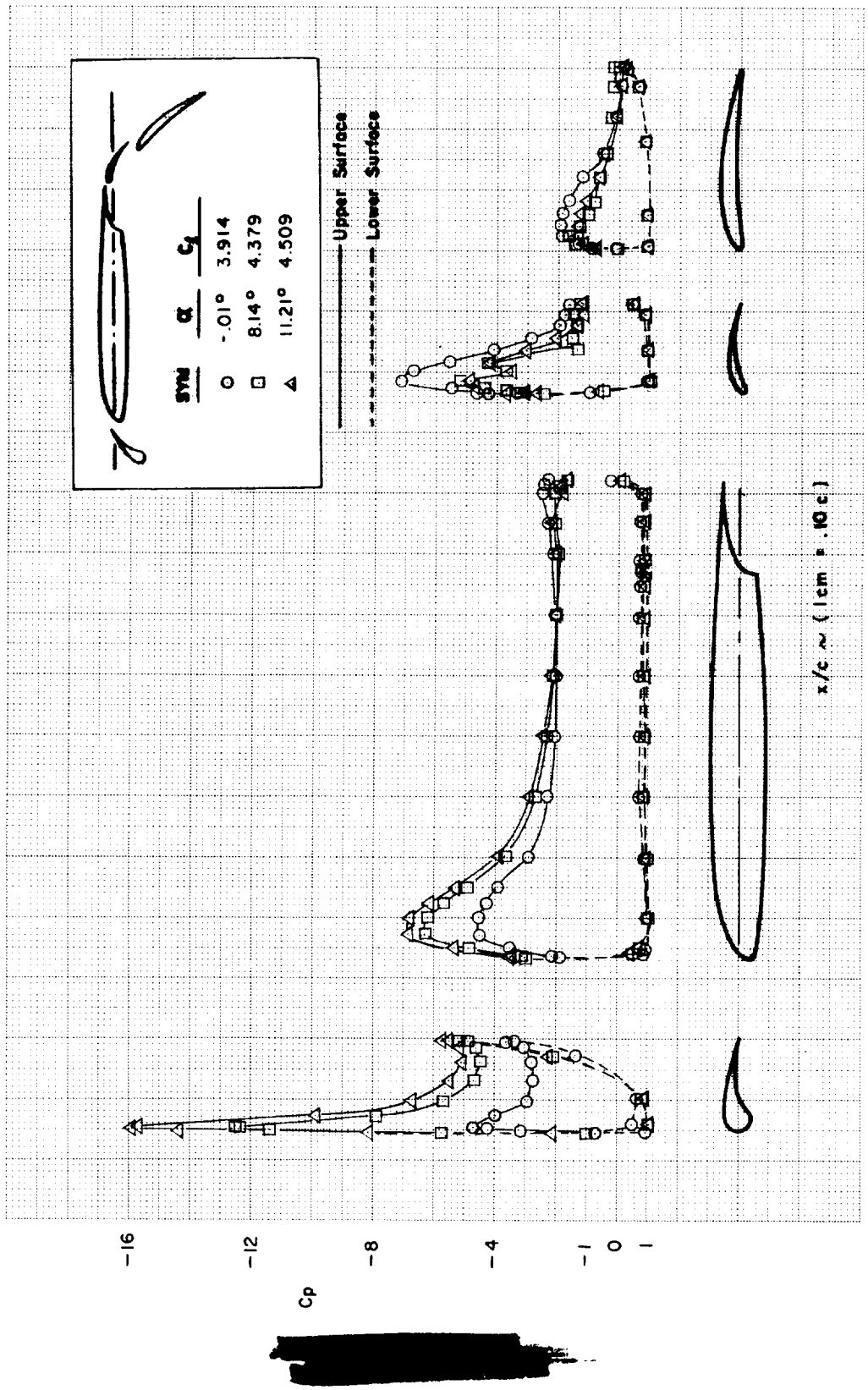

(b)

FIGURE C9.—Continued

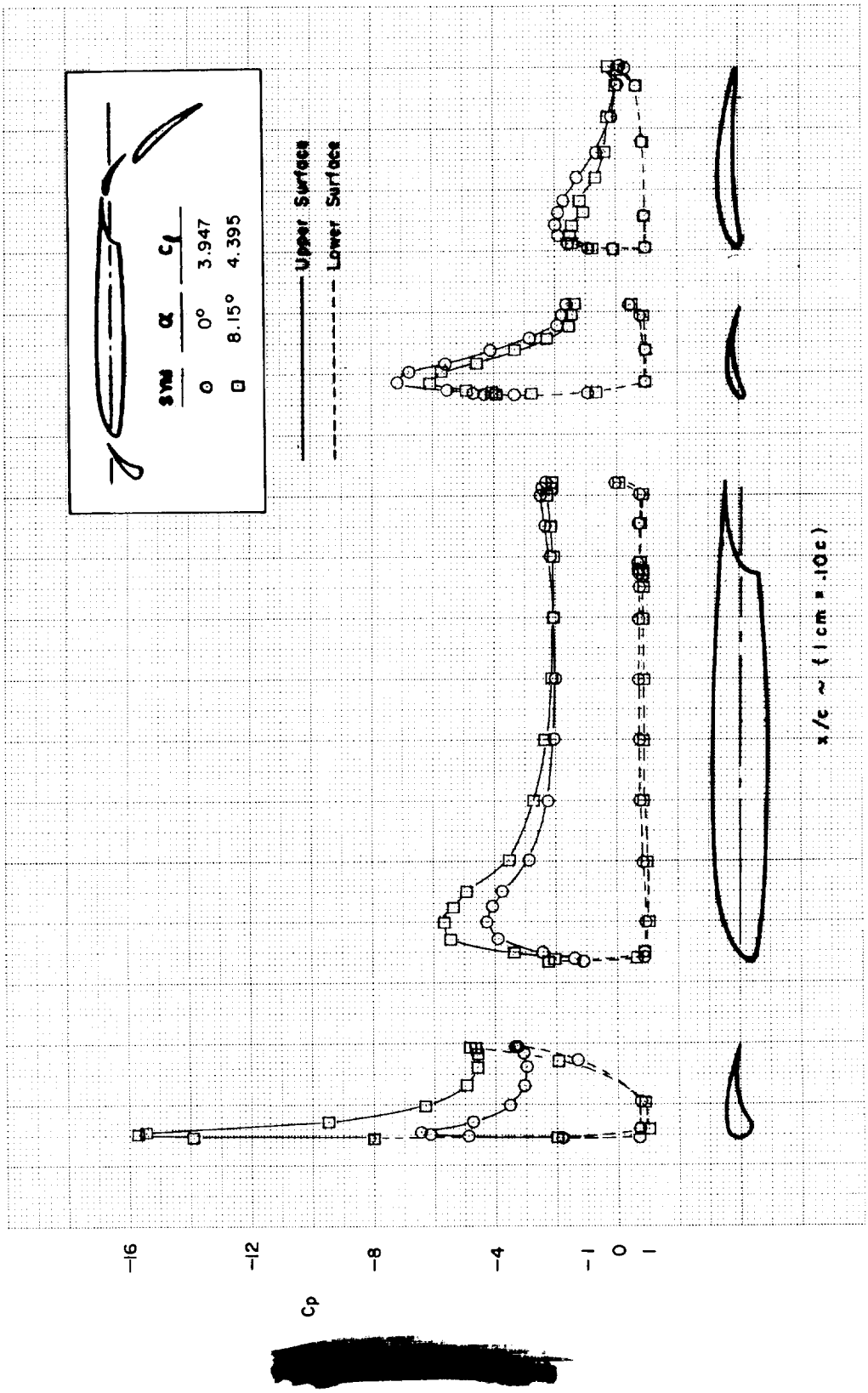

(c)

FIGURE C9.—Continued

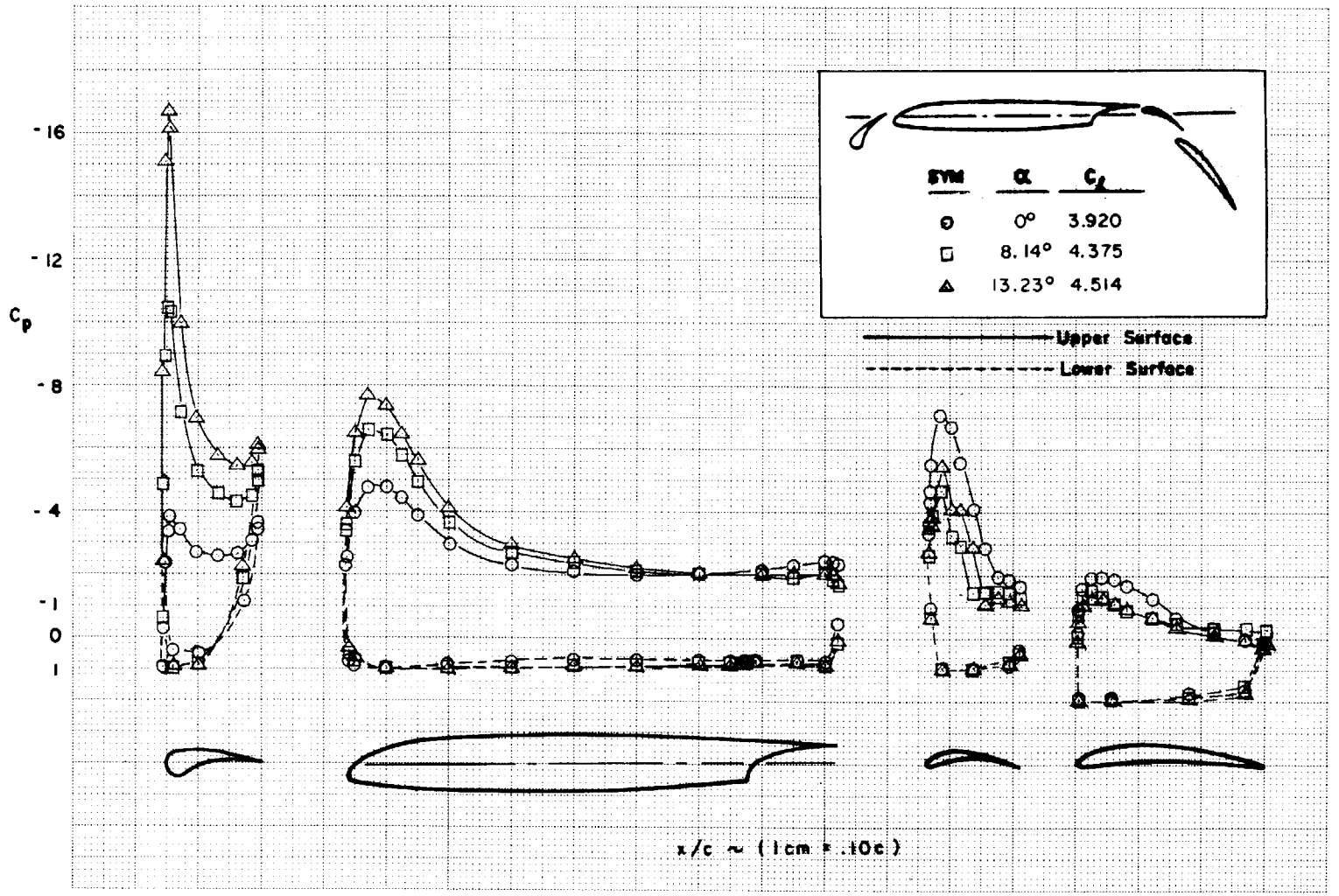

(d)

FIGURE C9.—Continued

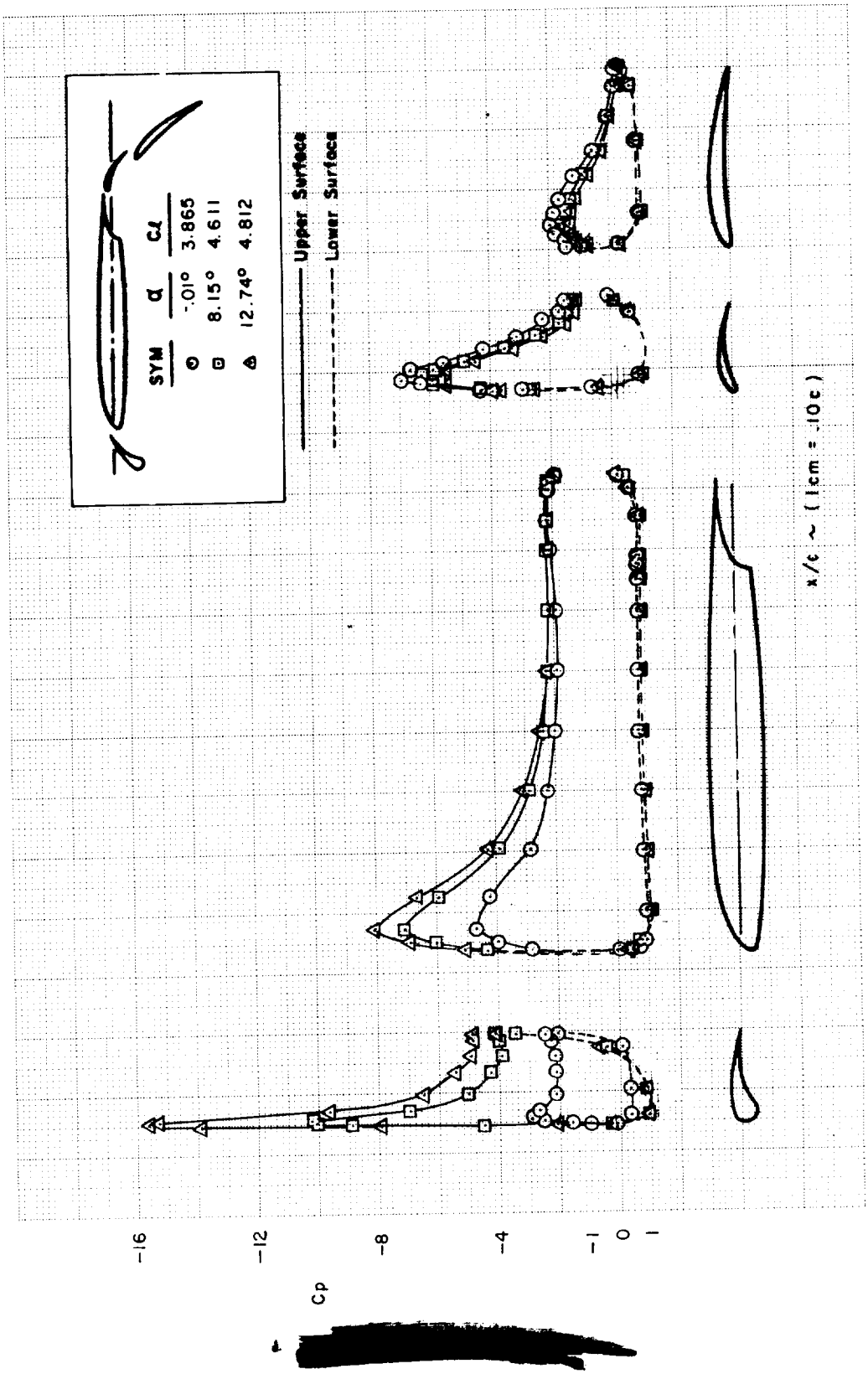

(e)

FIGURE C9.—Continued

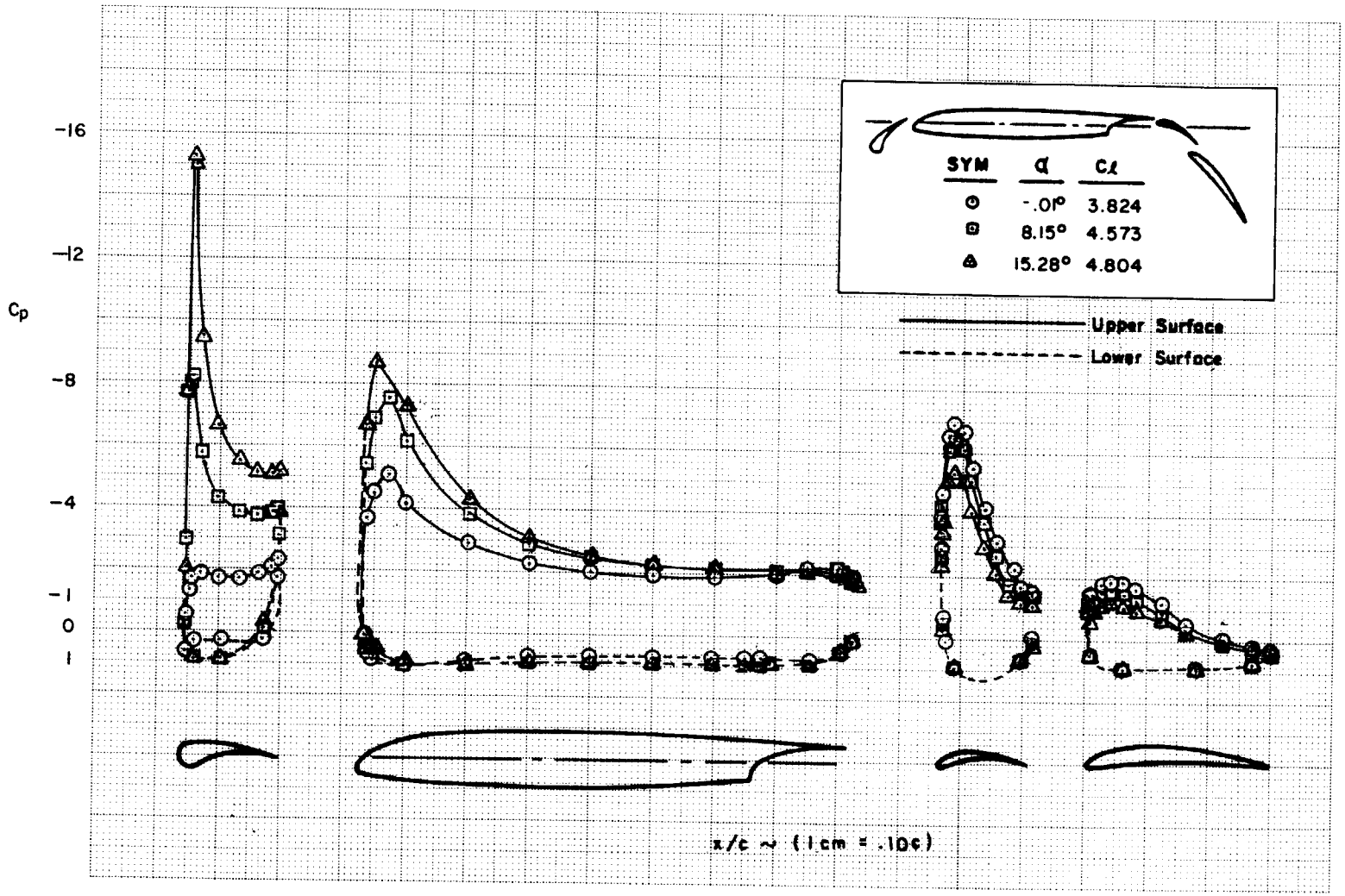

(f)

FIGURE C9.—Continued

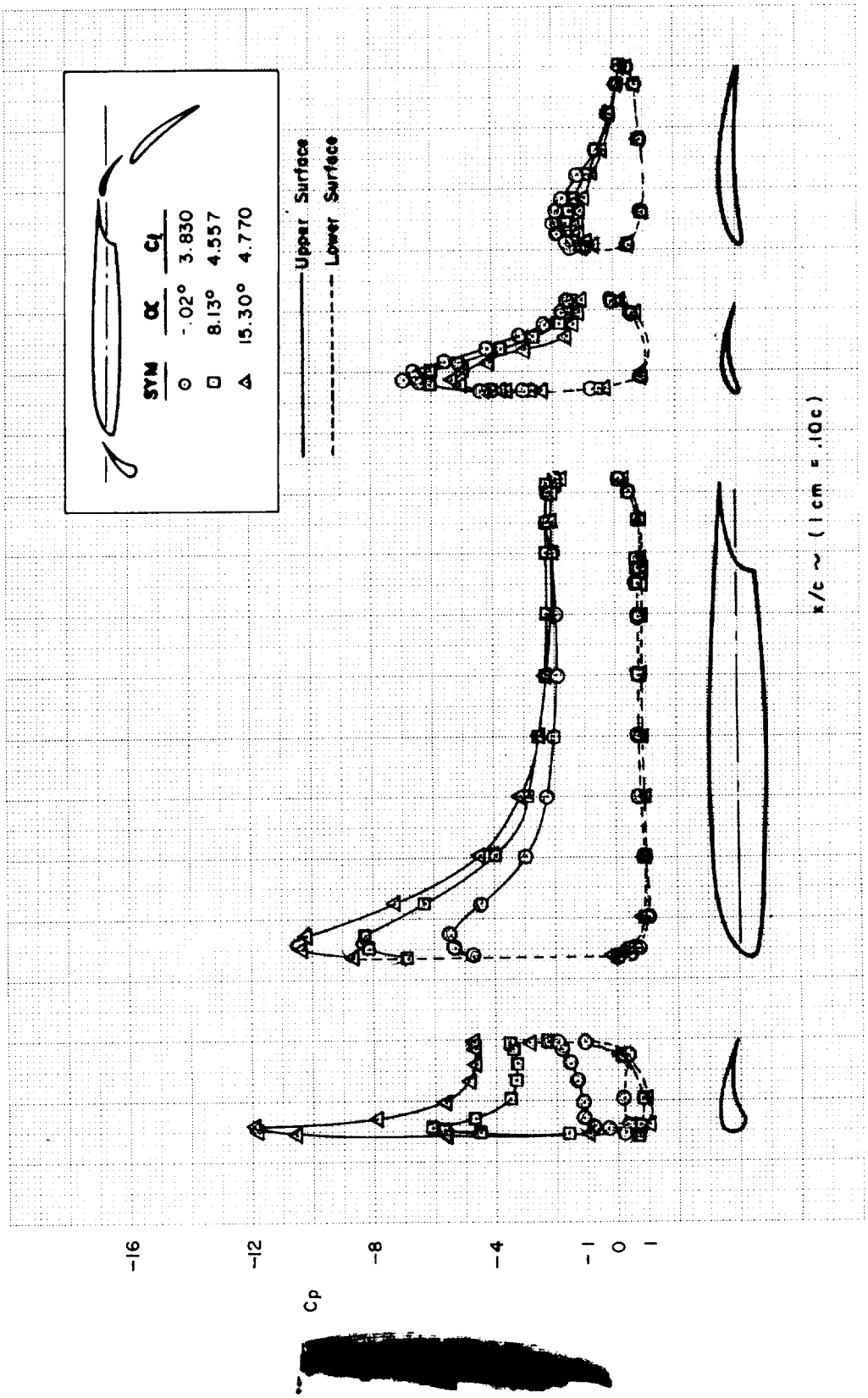

(g)

FIGURE C9.—Concluded

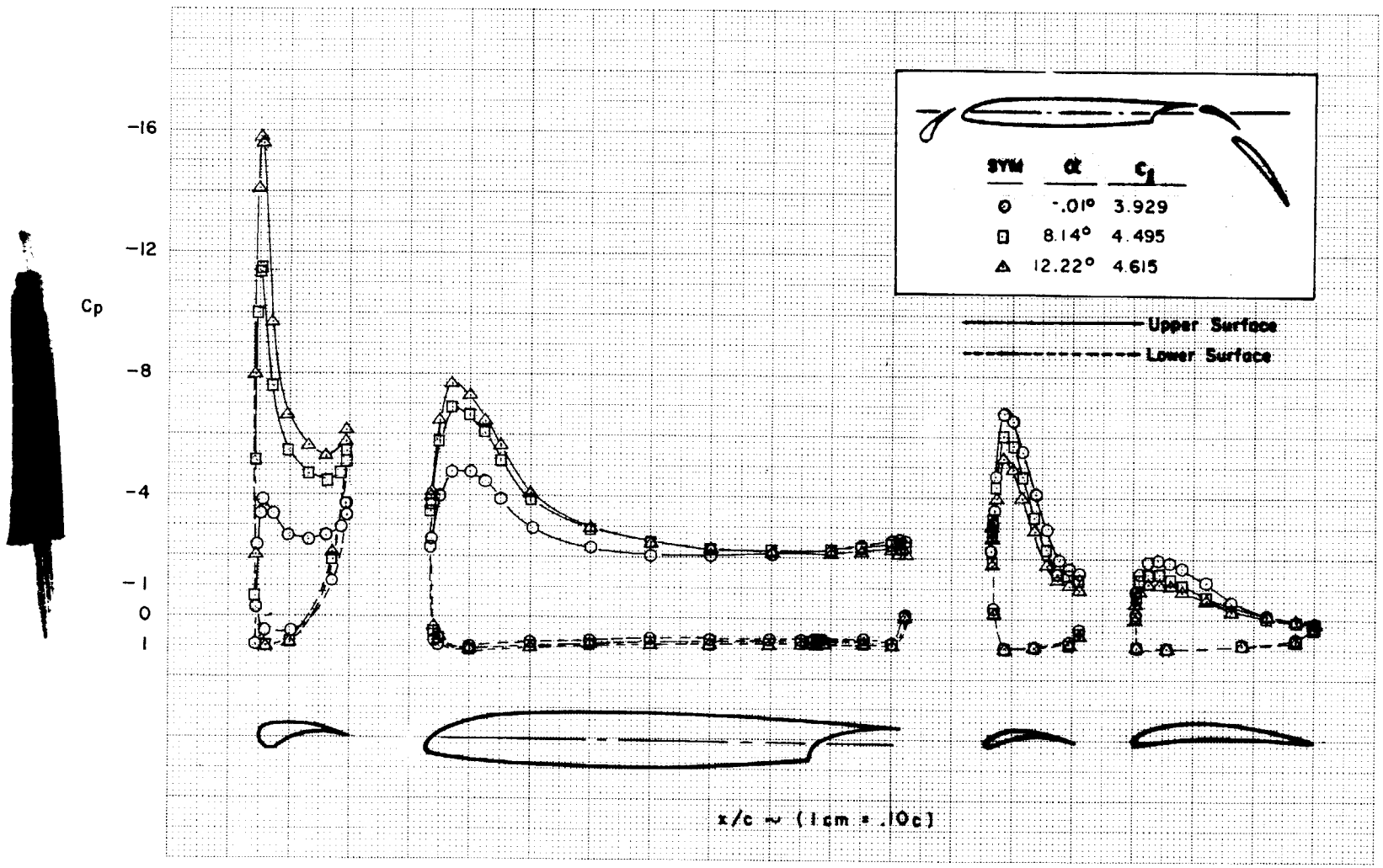

(a)

FIGURE C10.—SLAT 1 SLOT GAP AND HEIGHT OPTIMIZATION—MODEL C ($\delta_{f_{eq}} = 44°$)

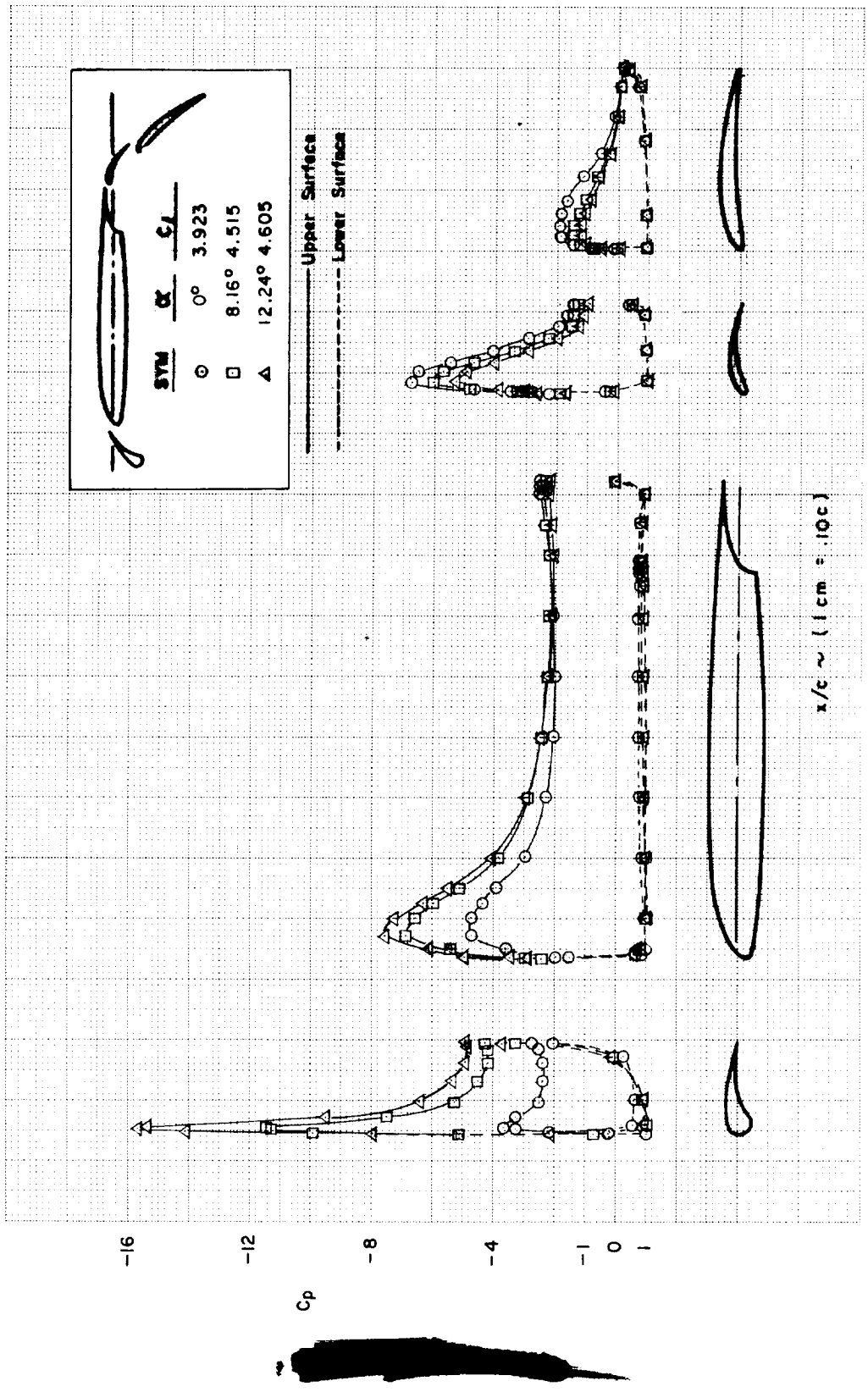

(b)

FIGURE C10.—Continued

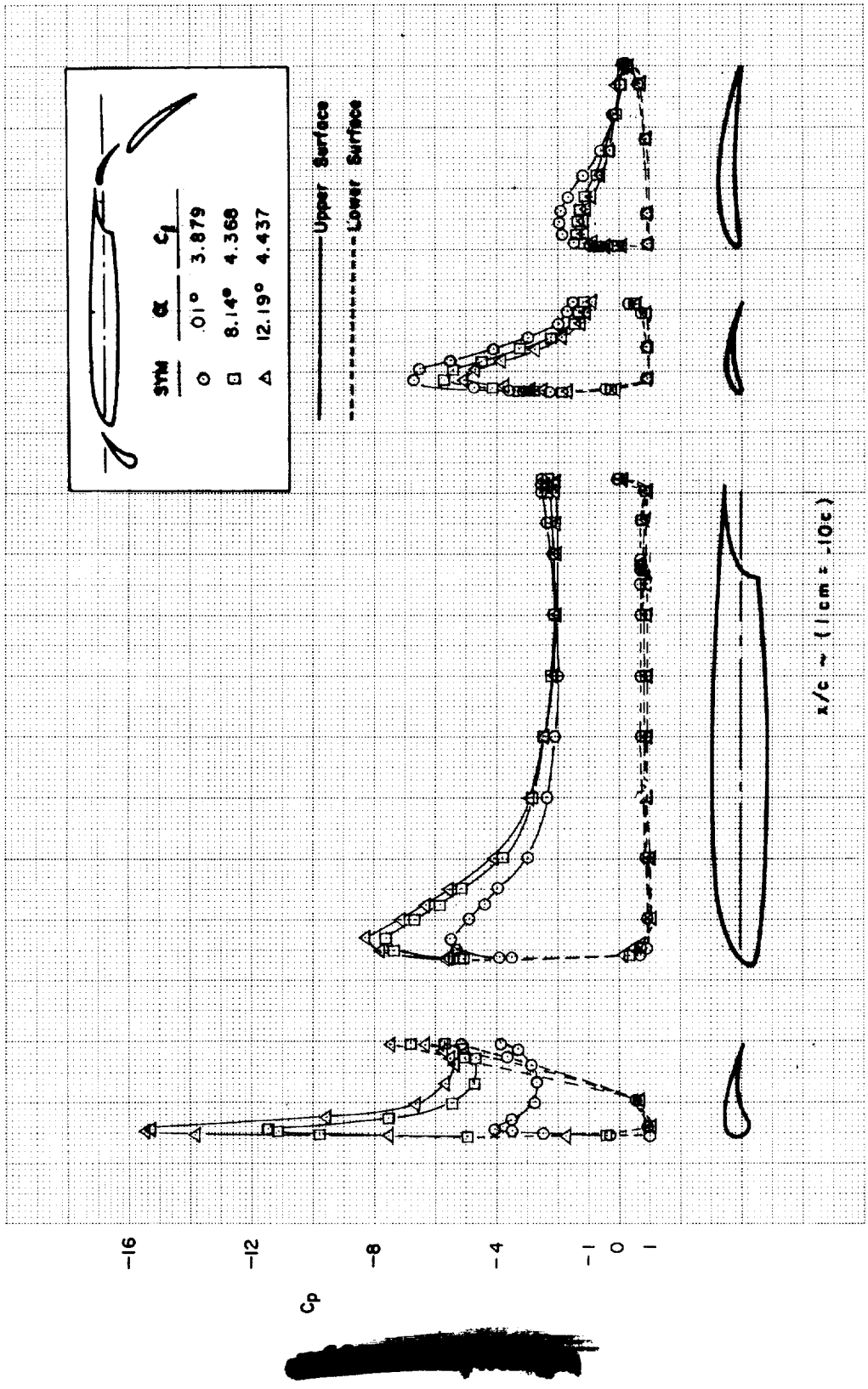

(c)

FIGURE C10.—Continued

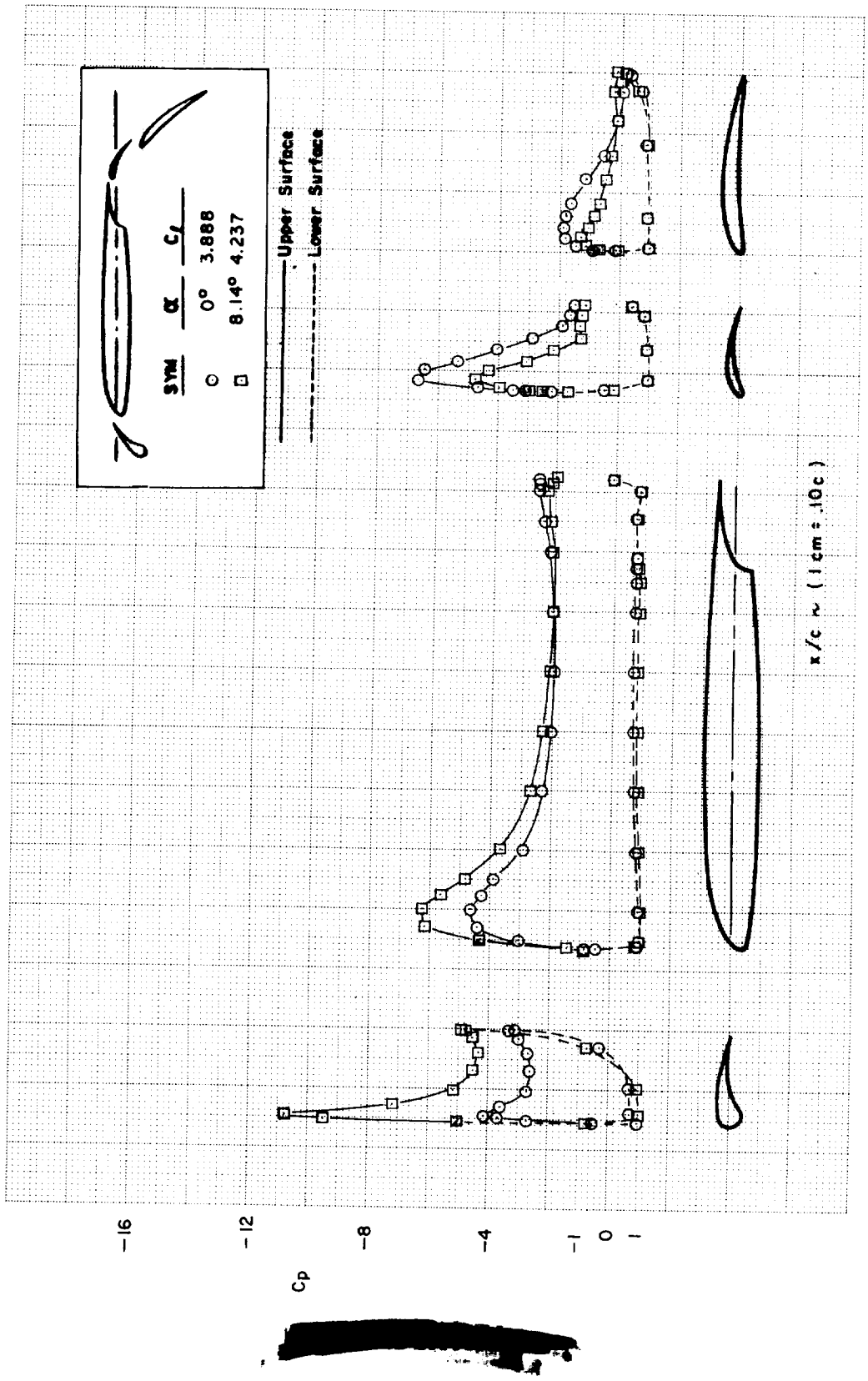

(d)

FIGURE C10.—Continued

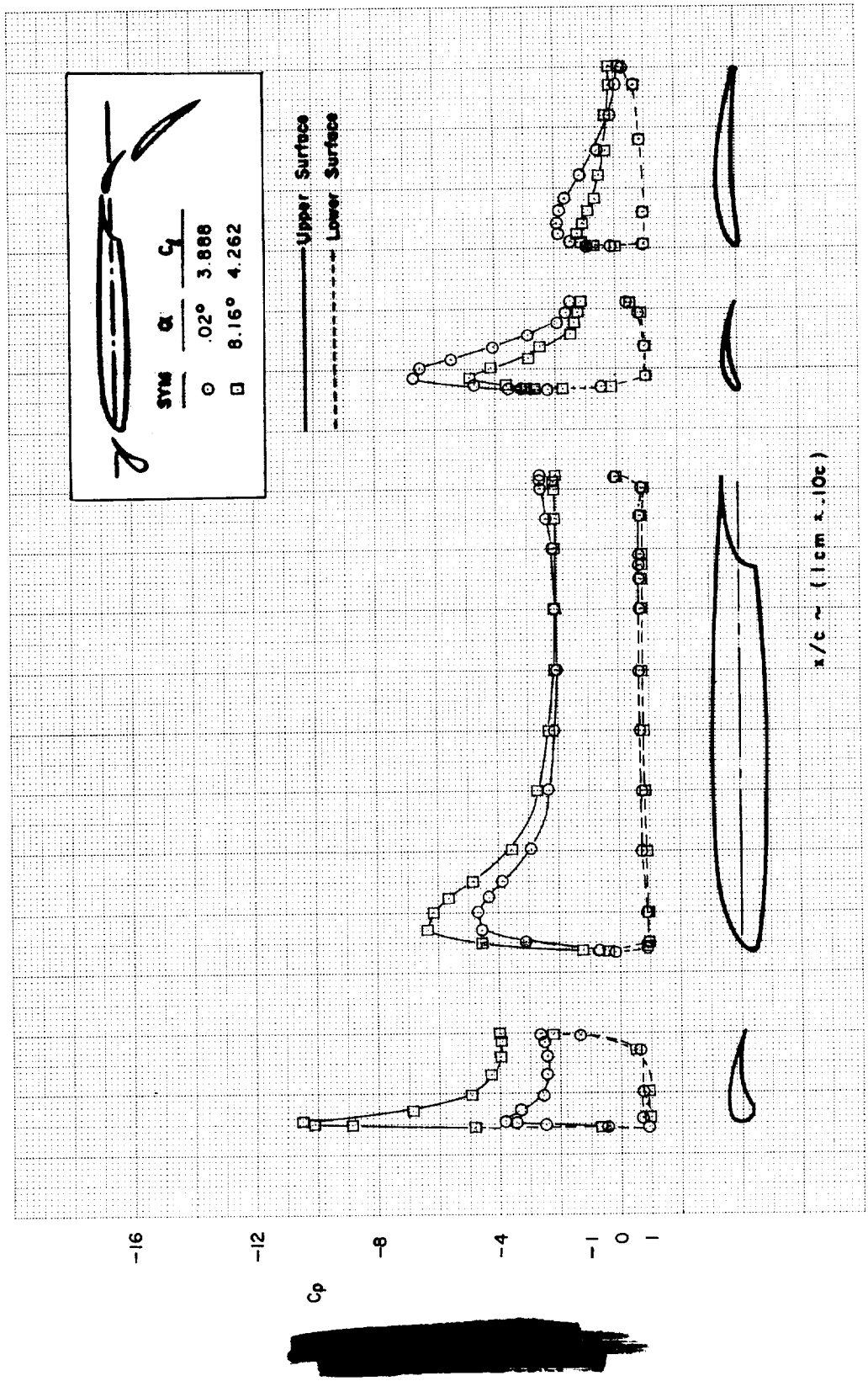

(e)

FIGURE C10.—Continued

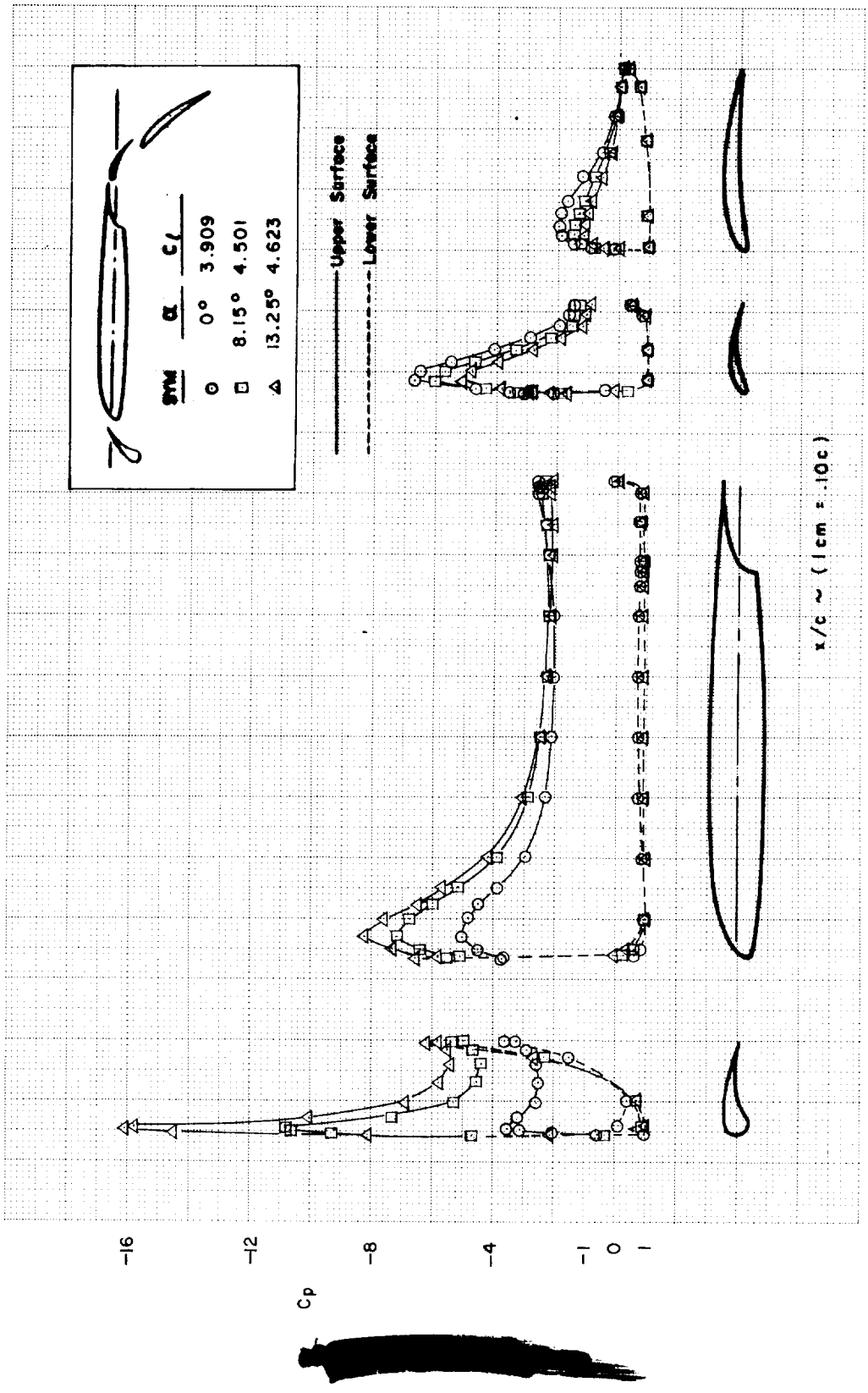

(f)

FIGURE C10.—Continued

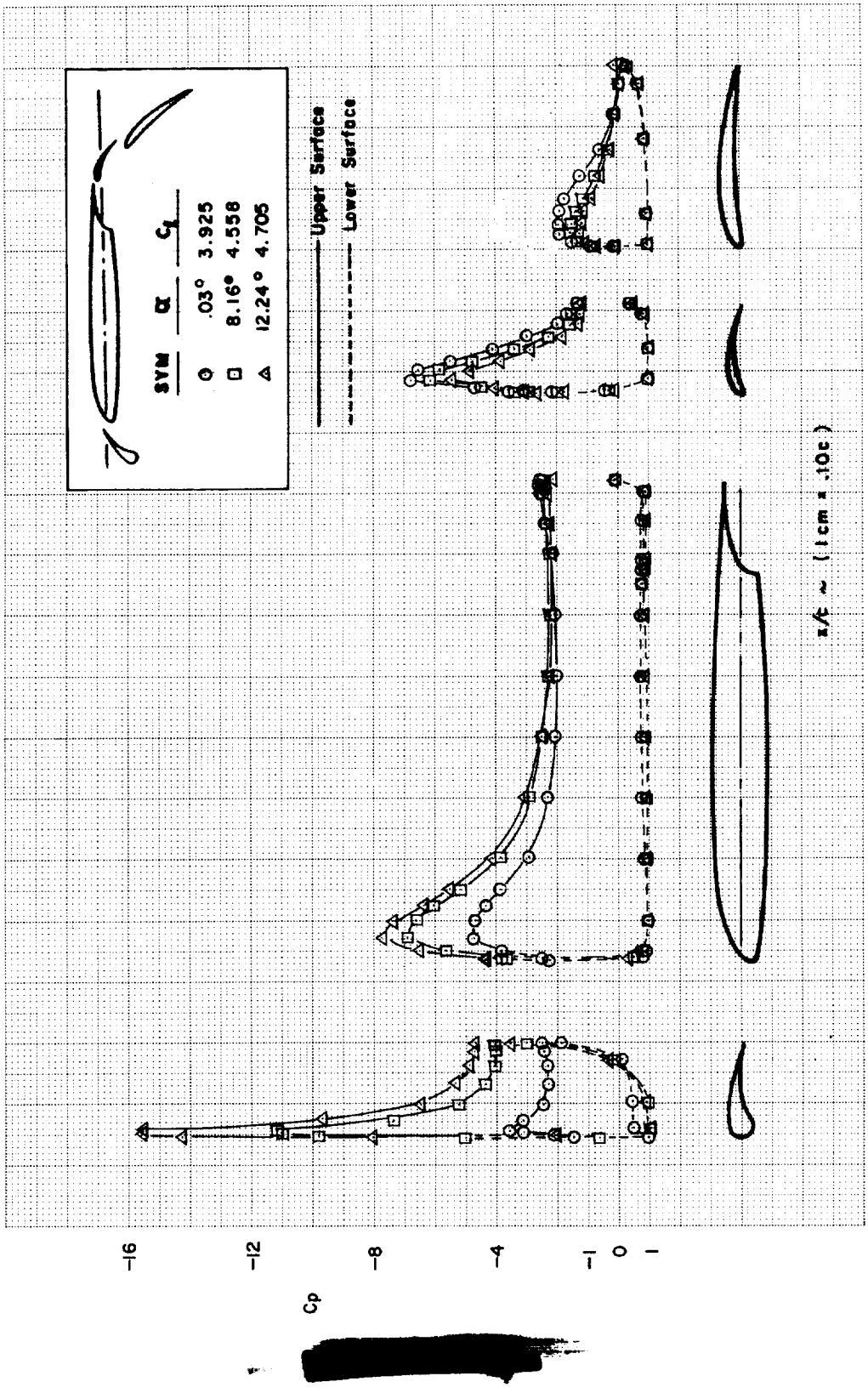

(g)

FIGURE C10.—Continued

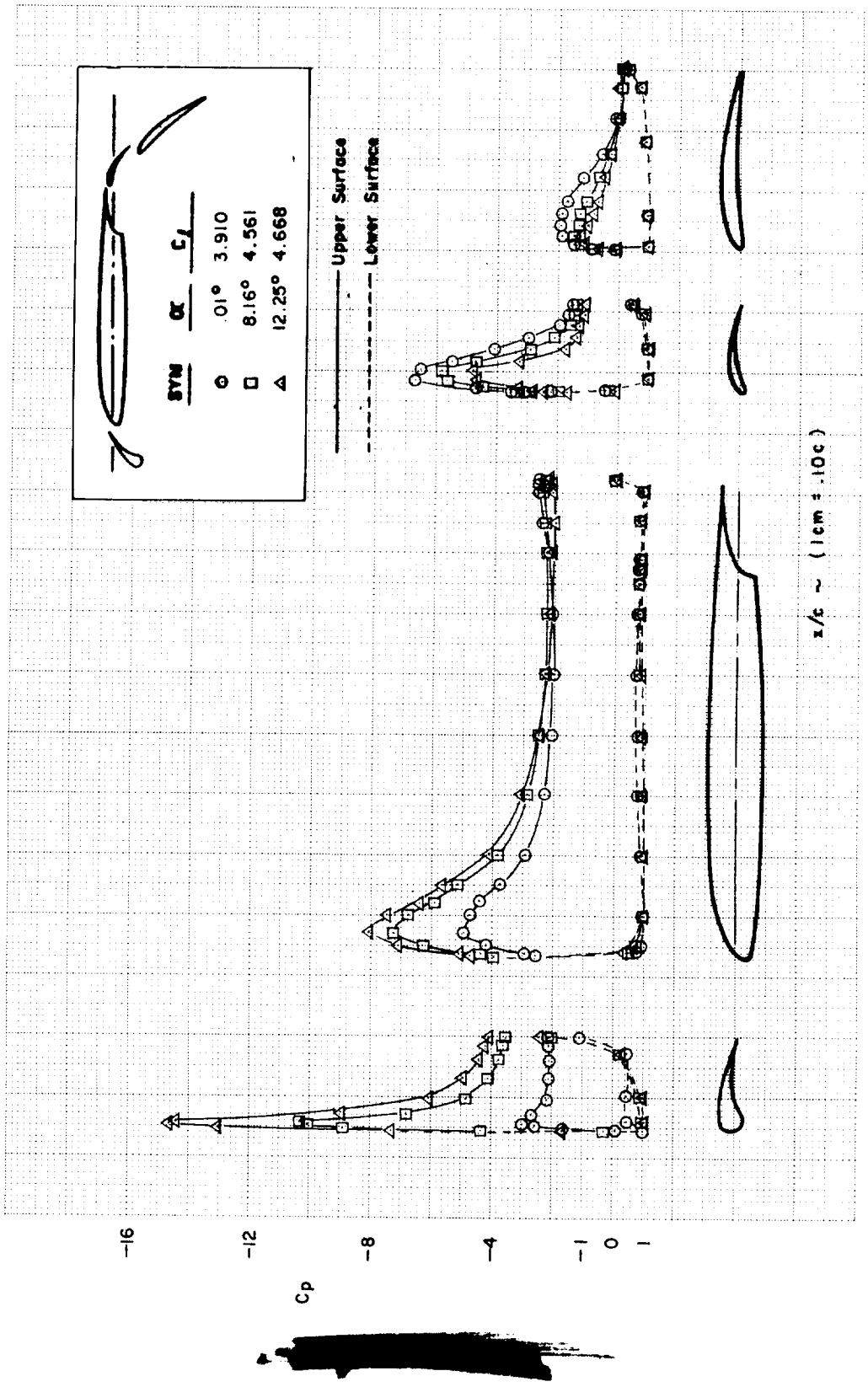

(h)

FIGURE C10.—Continued

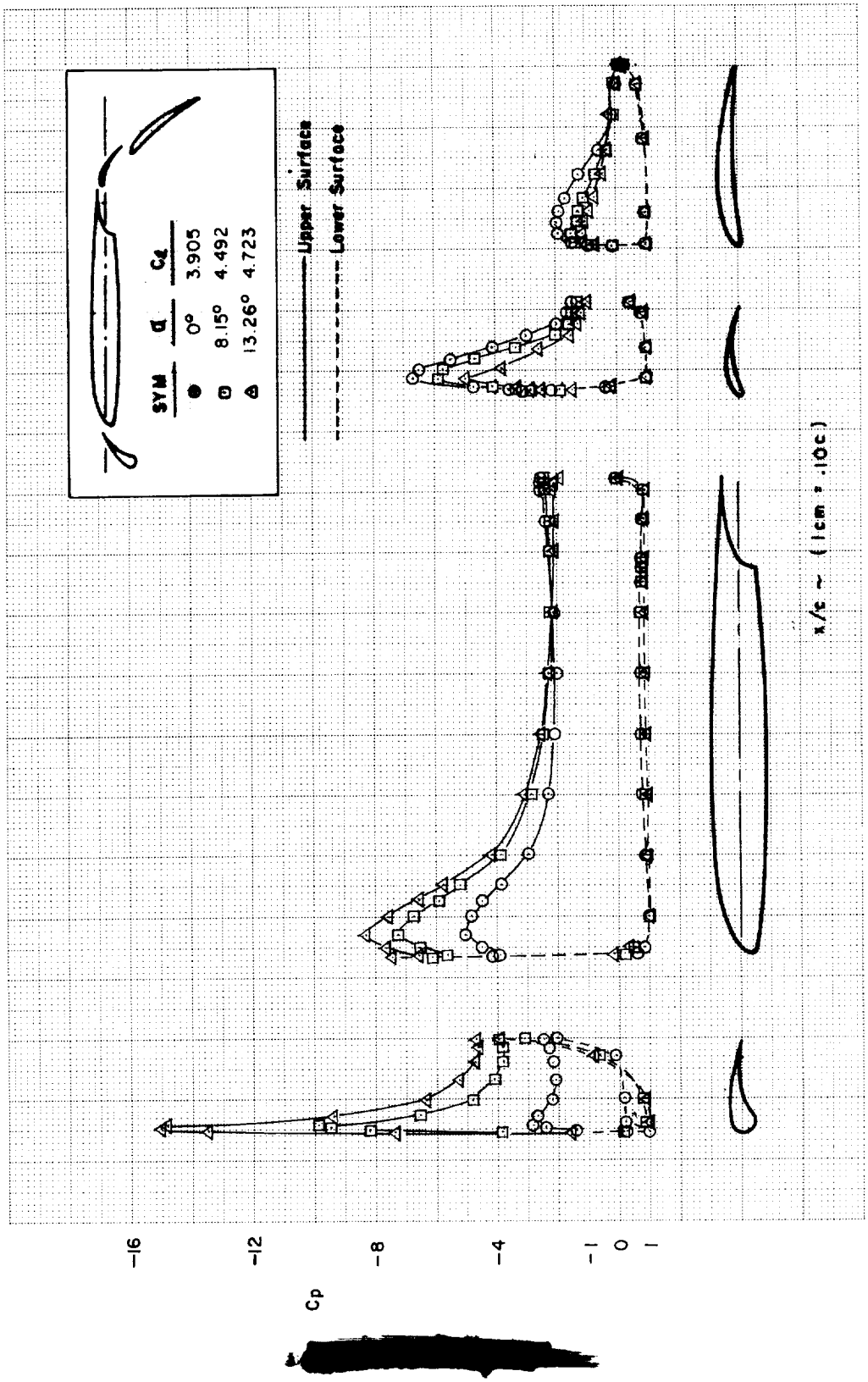

(i)

FIGURE C10.–Continued

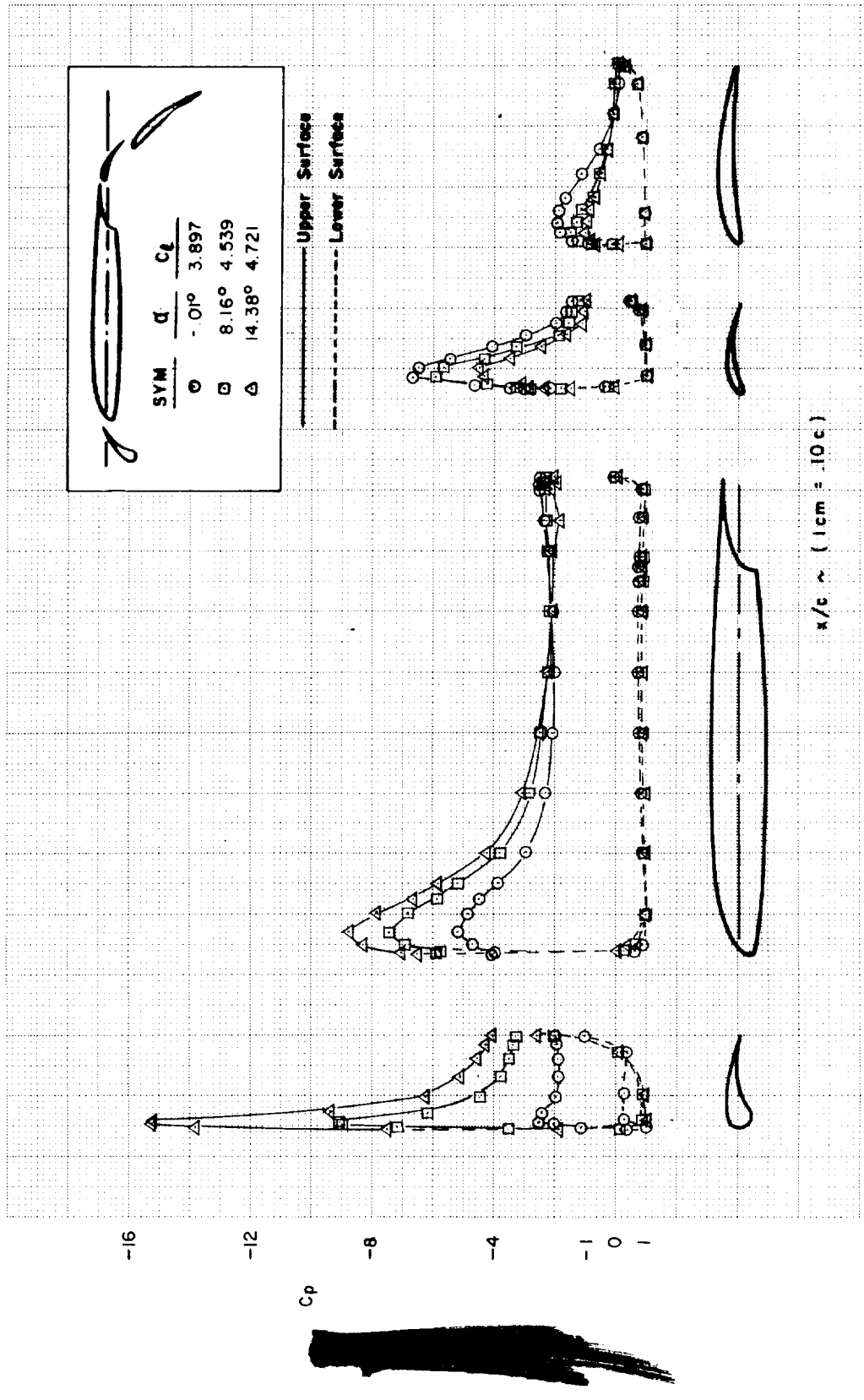

(i)

FIGURE C10.—Continued

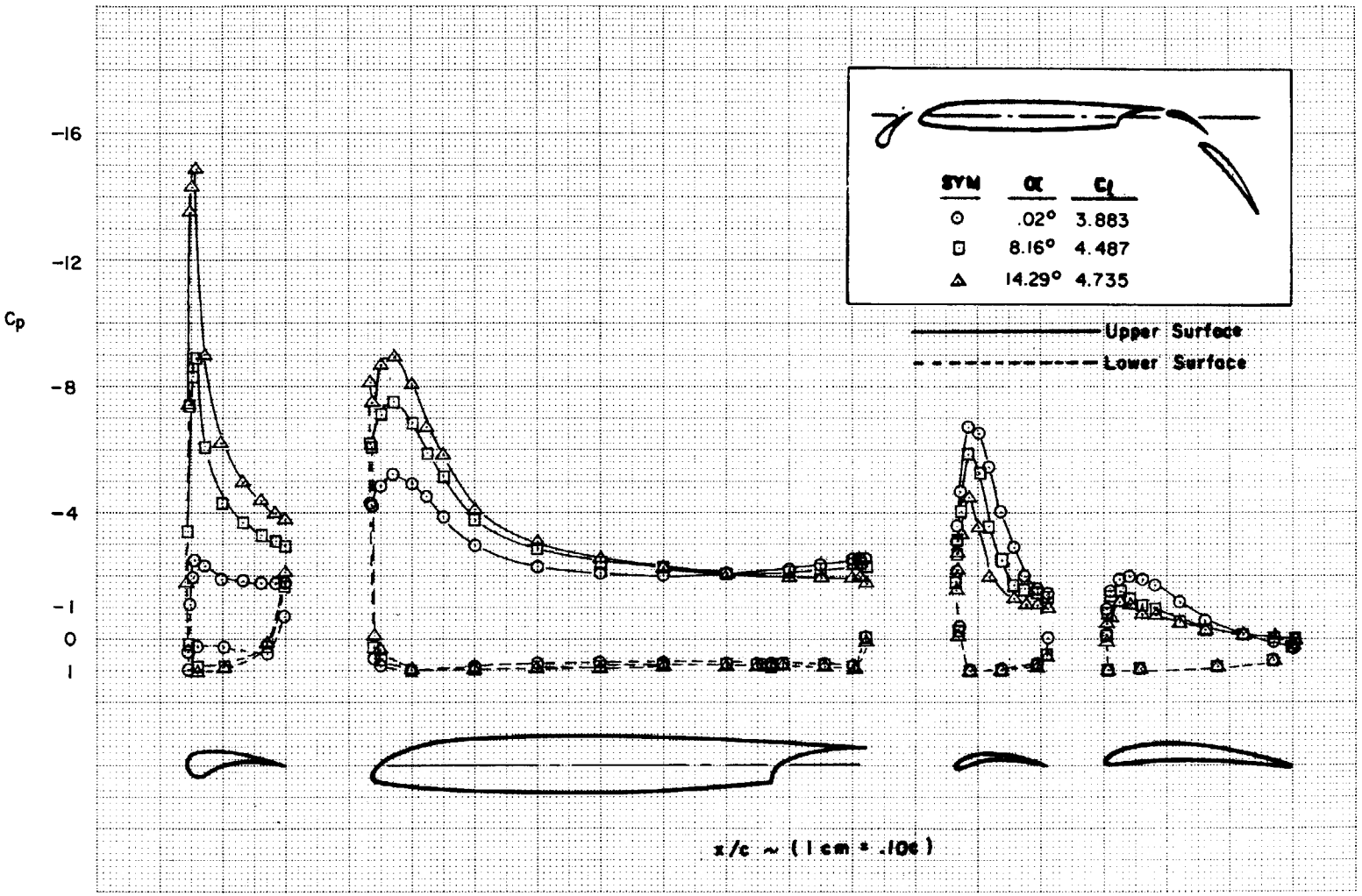

(k)

FIGURE C10.—Continued

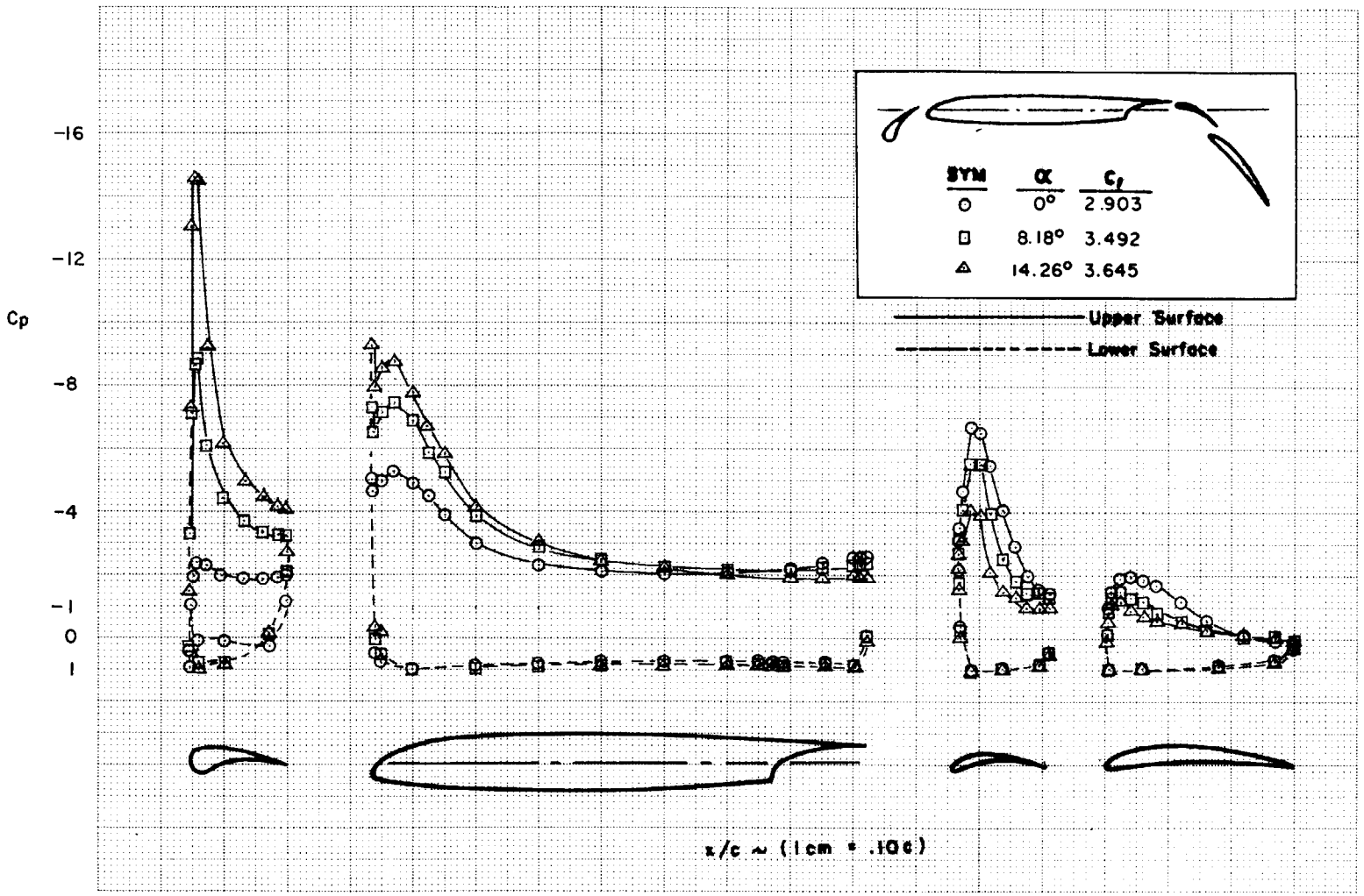

(l)

FIGURE C10.—Continued

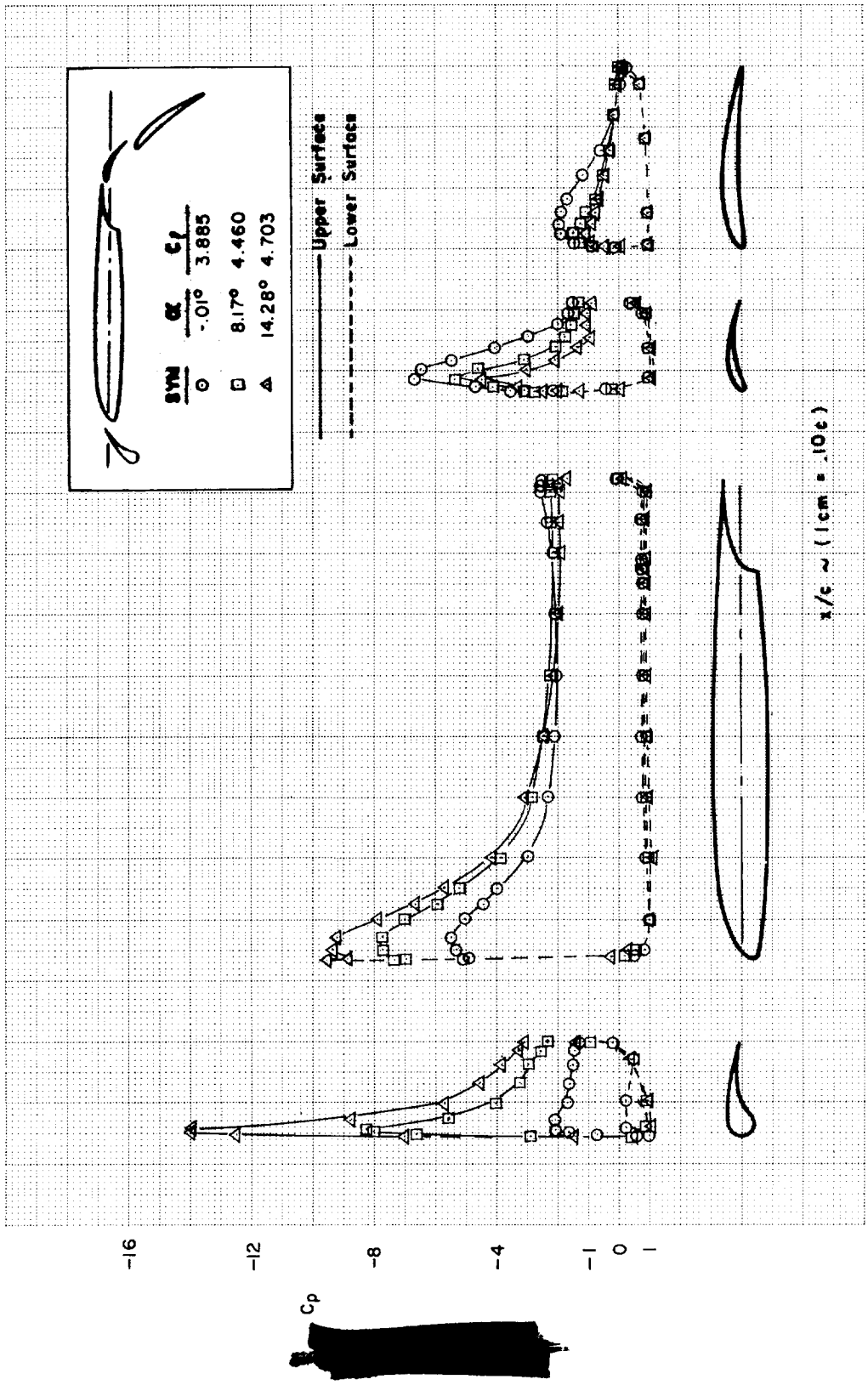

FIGURE C10.—Continued

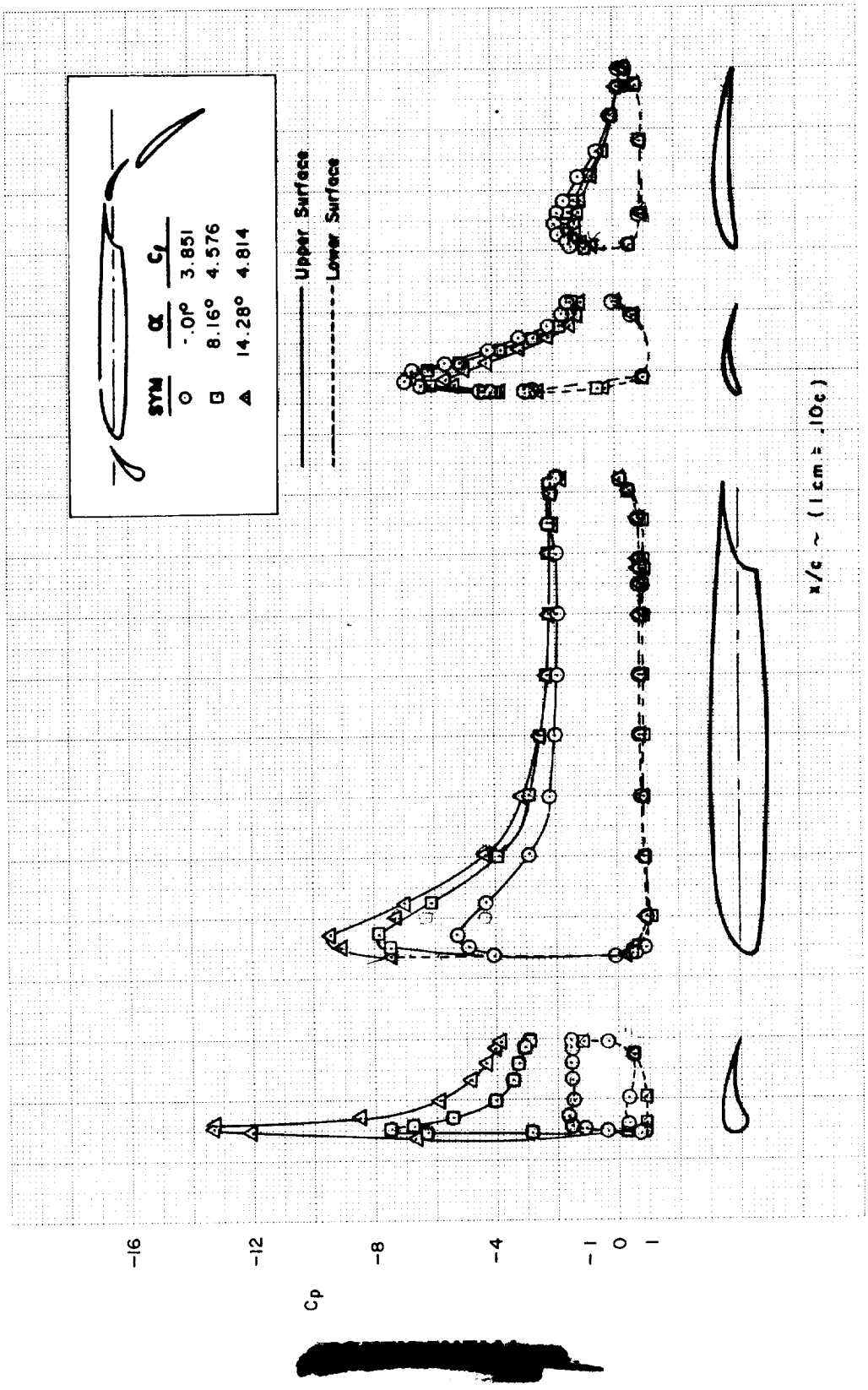

(n)

FIGURE C10.–Continued

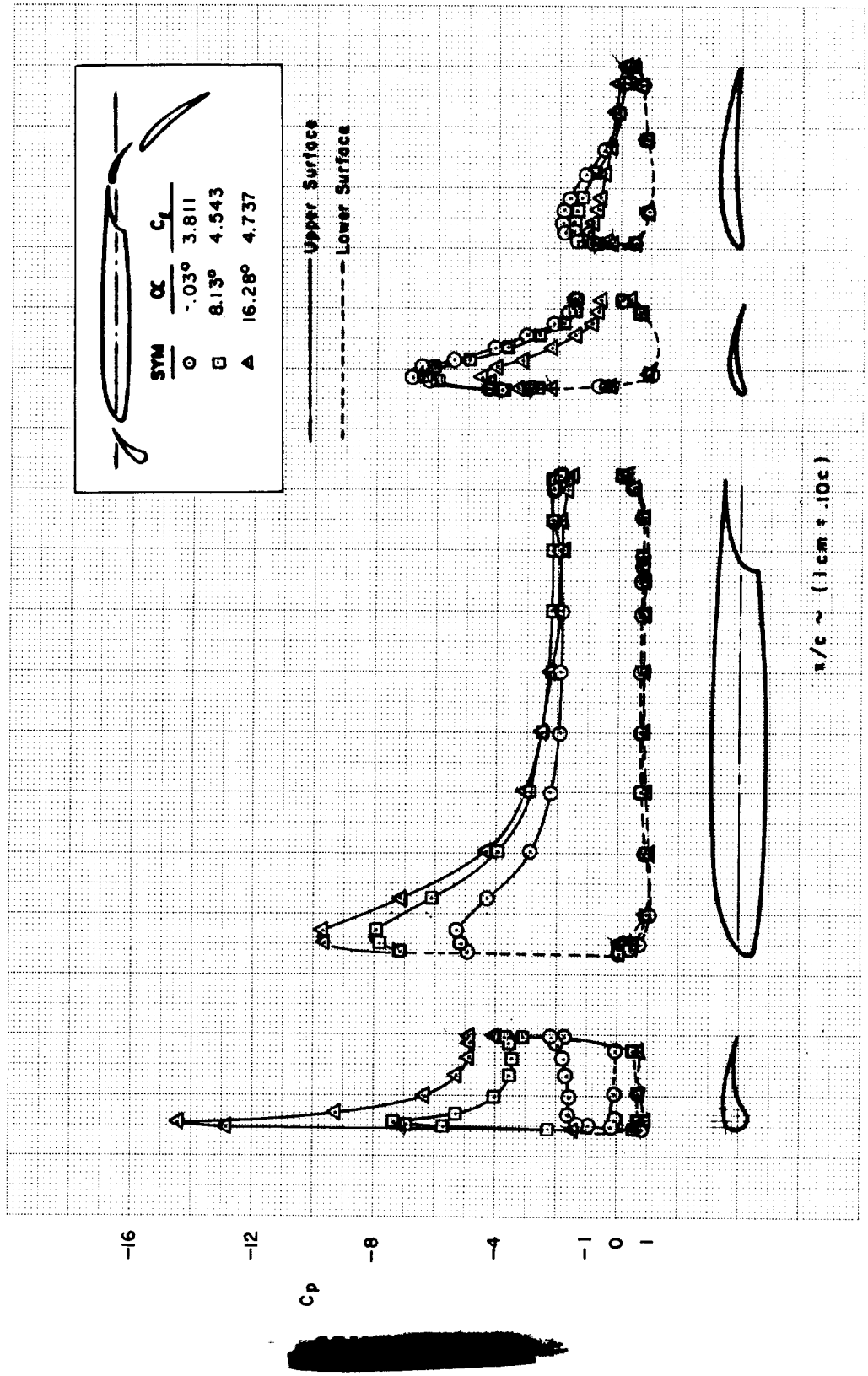

(o)

FIGURE C10.—Continued

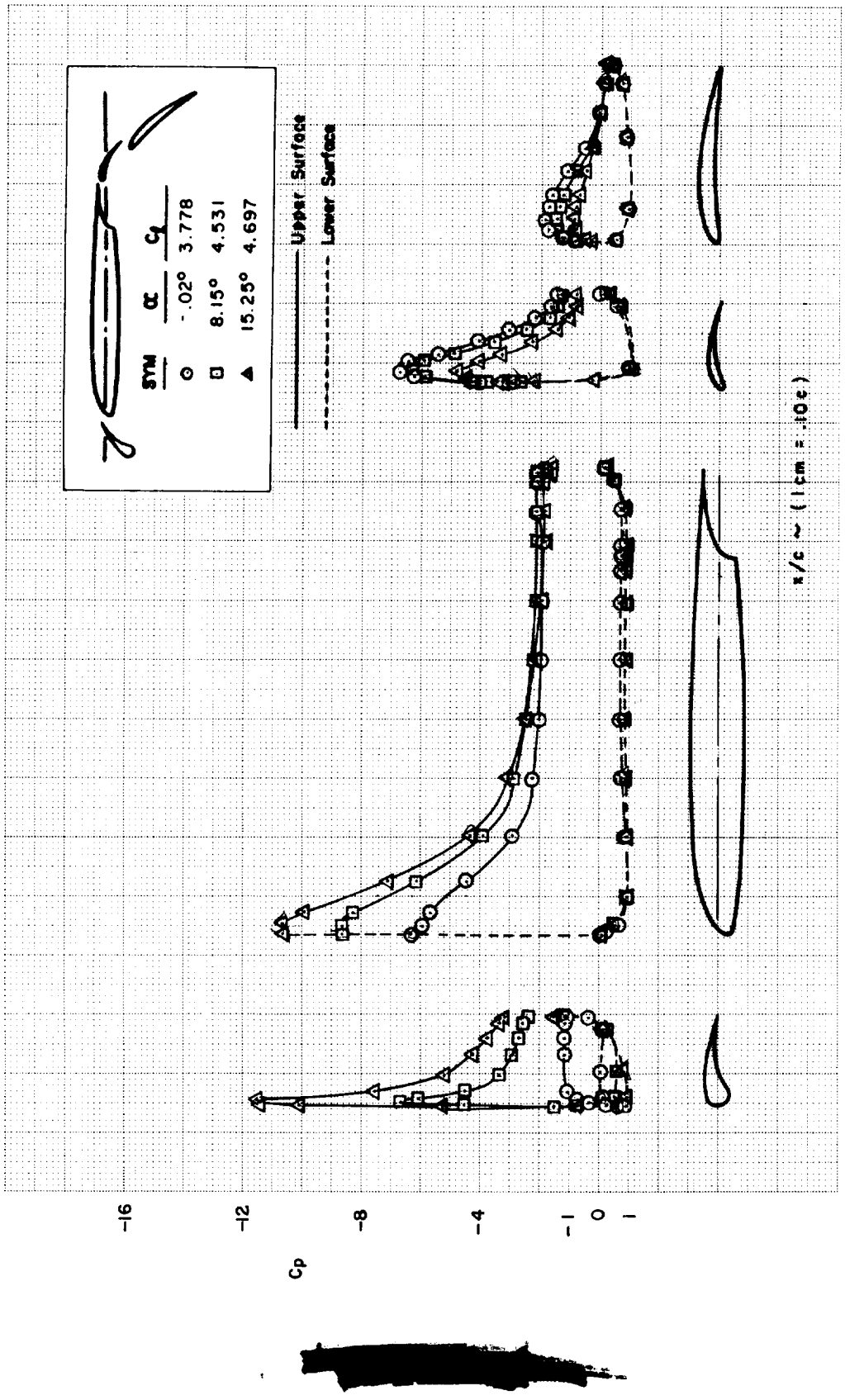

(p)

FIGURE C10.–Continued

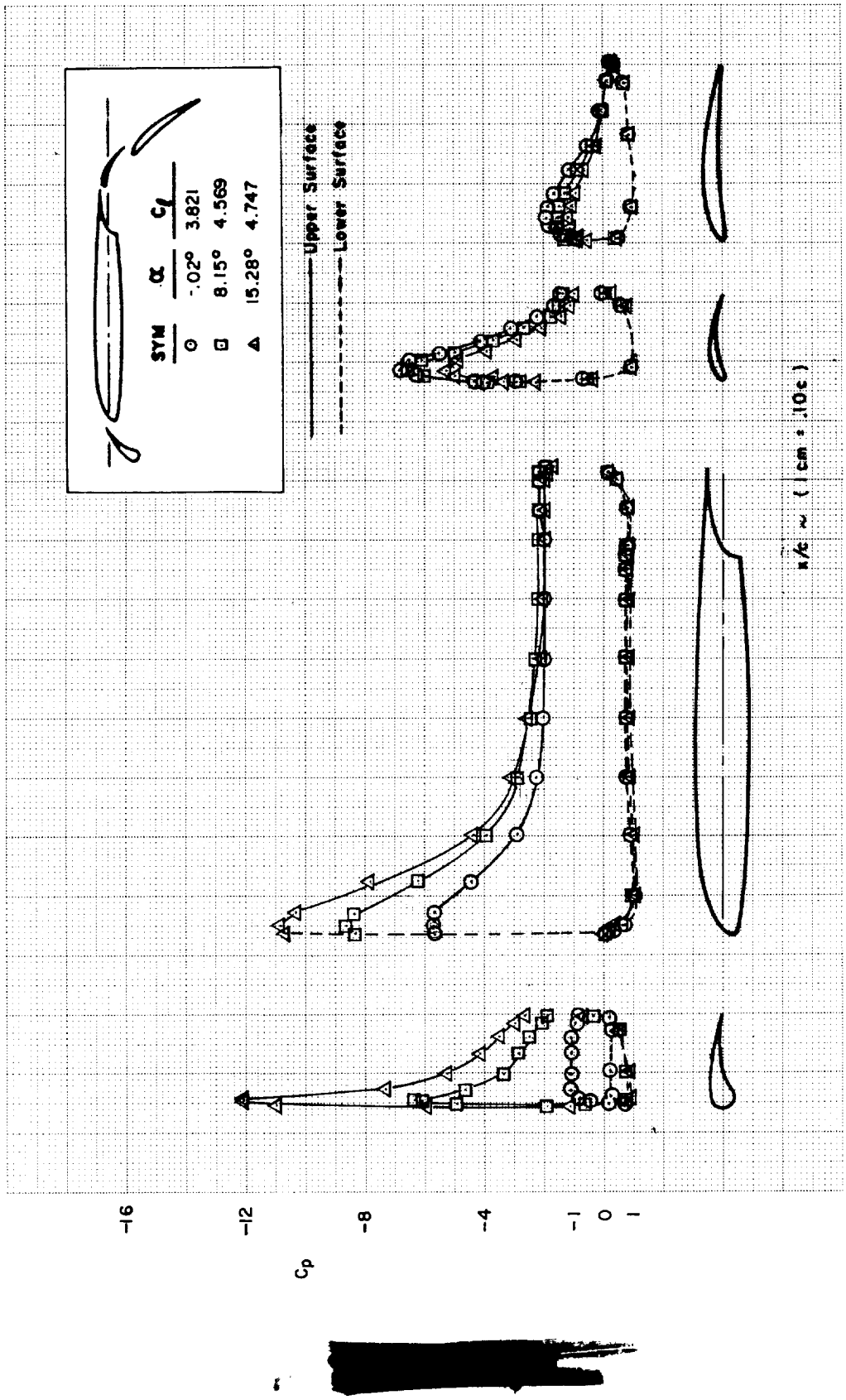

(q)

FIGURE C10.—Continued

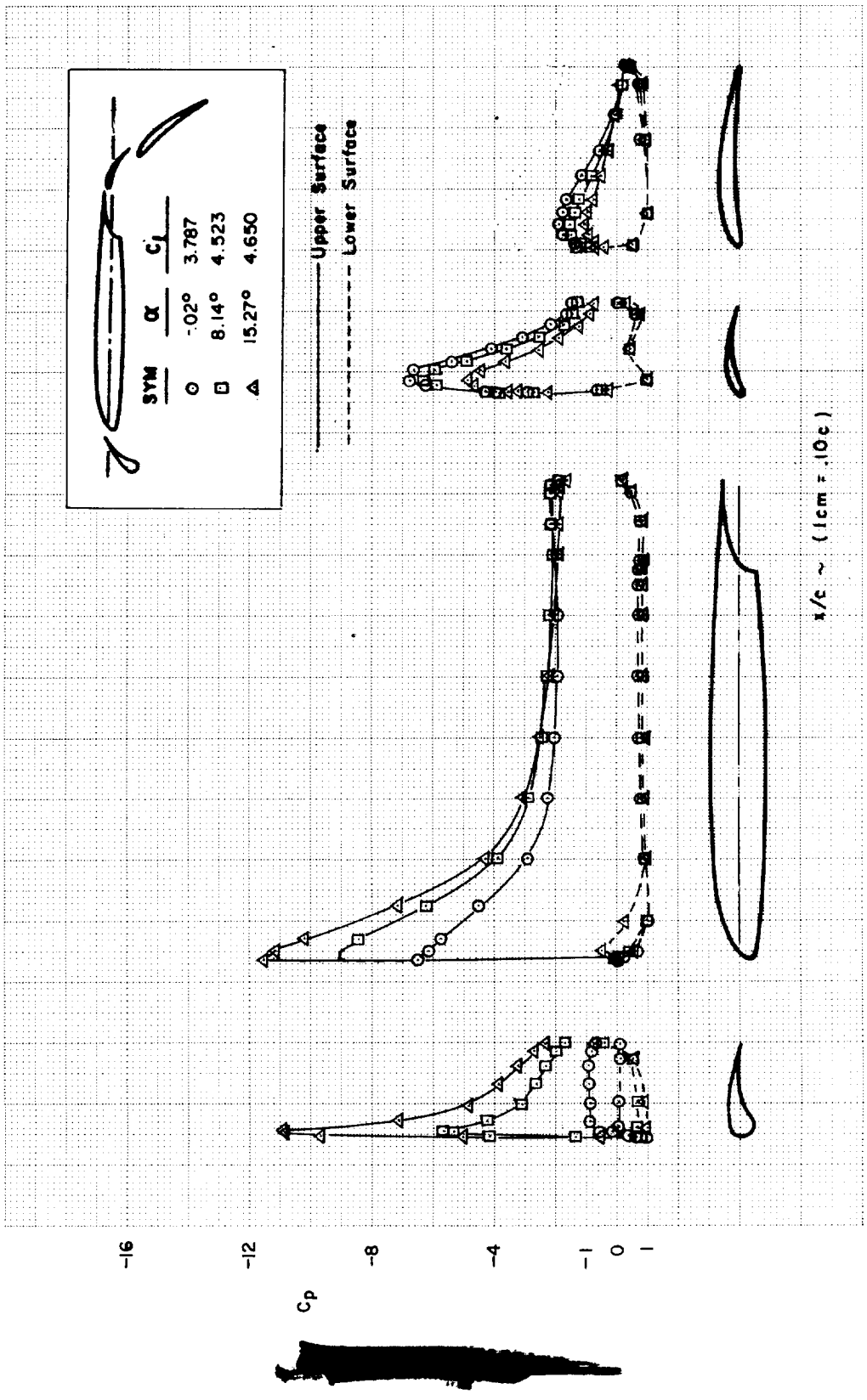

(r)

FIGURE C10.—Concluded

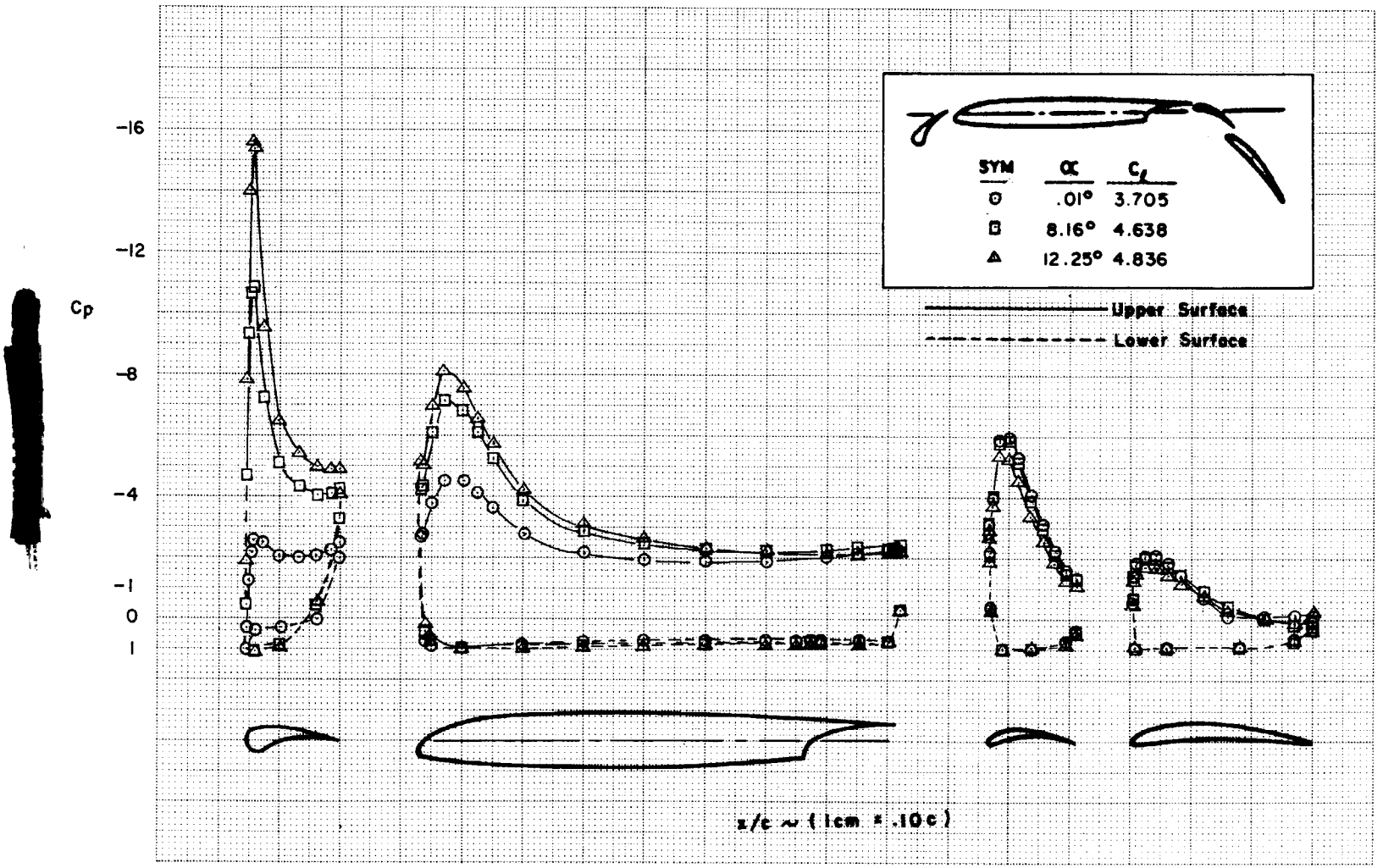

(a)

FIGURE C11.–EFFECT OF FLAP COMPONENT ANGLE COMBINATION AT CONSTANT $\delta_{f_{eq}}$ (44°)–MODEL C

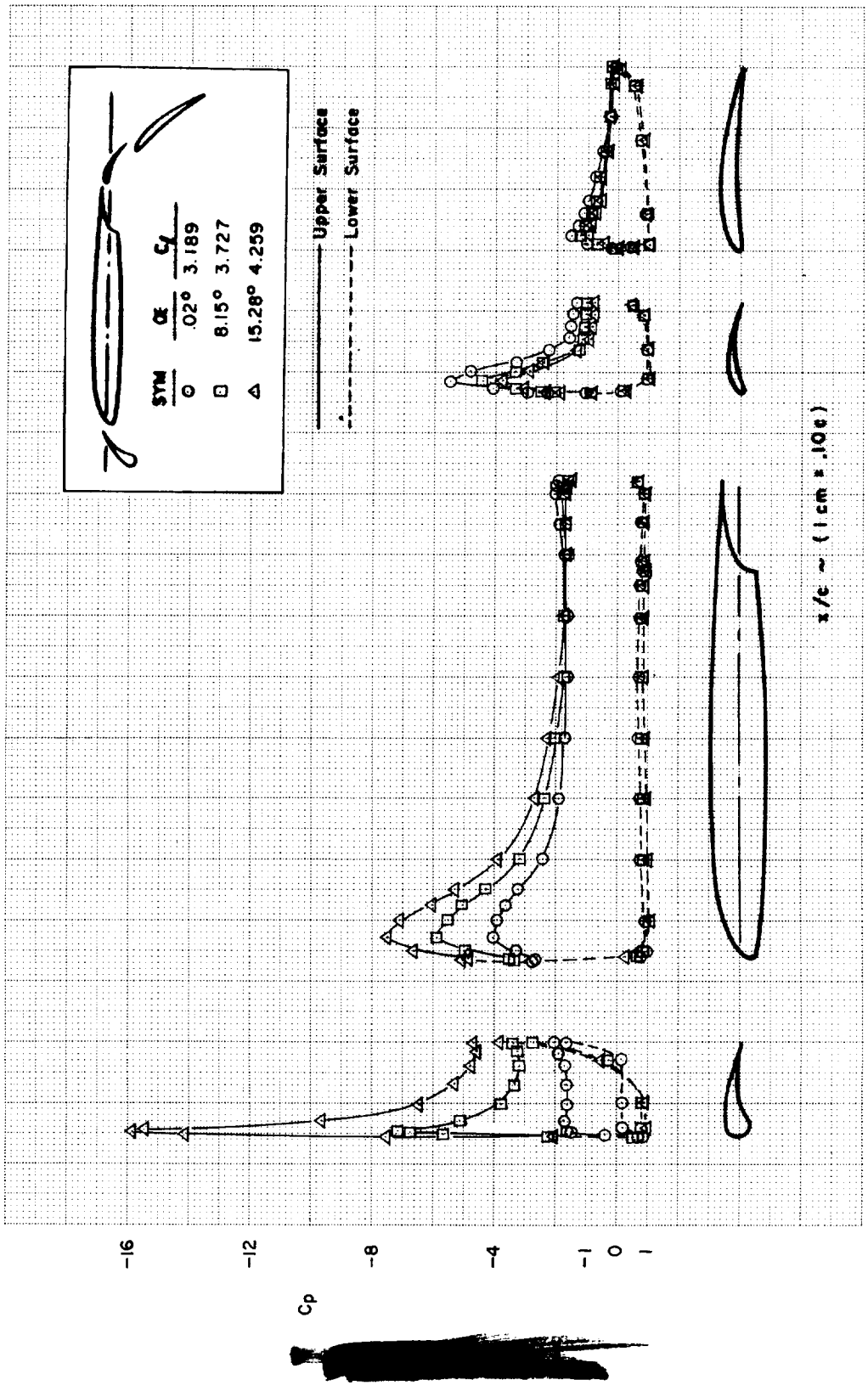

(b)

FIGURE C11.—Concluded

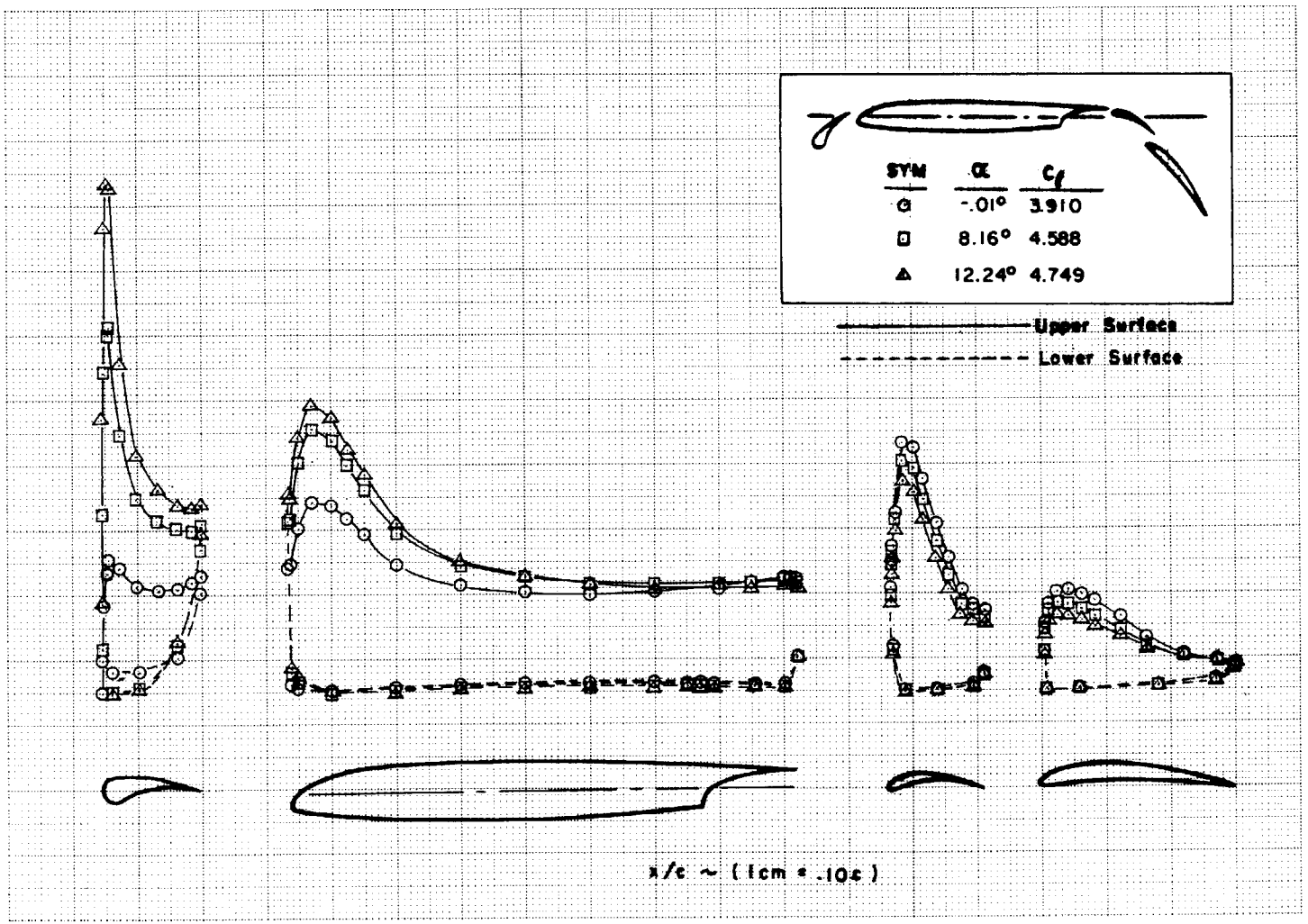

(a)

FIGURE C12.–EFFECT OF WING-VANE SLOT GAP AND OVERLAP–MODEL C ($\delta_{f_{eq}} = 44°$)

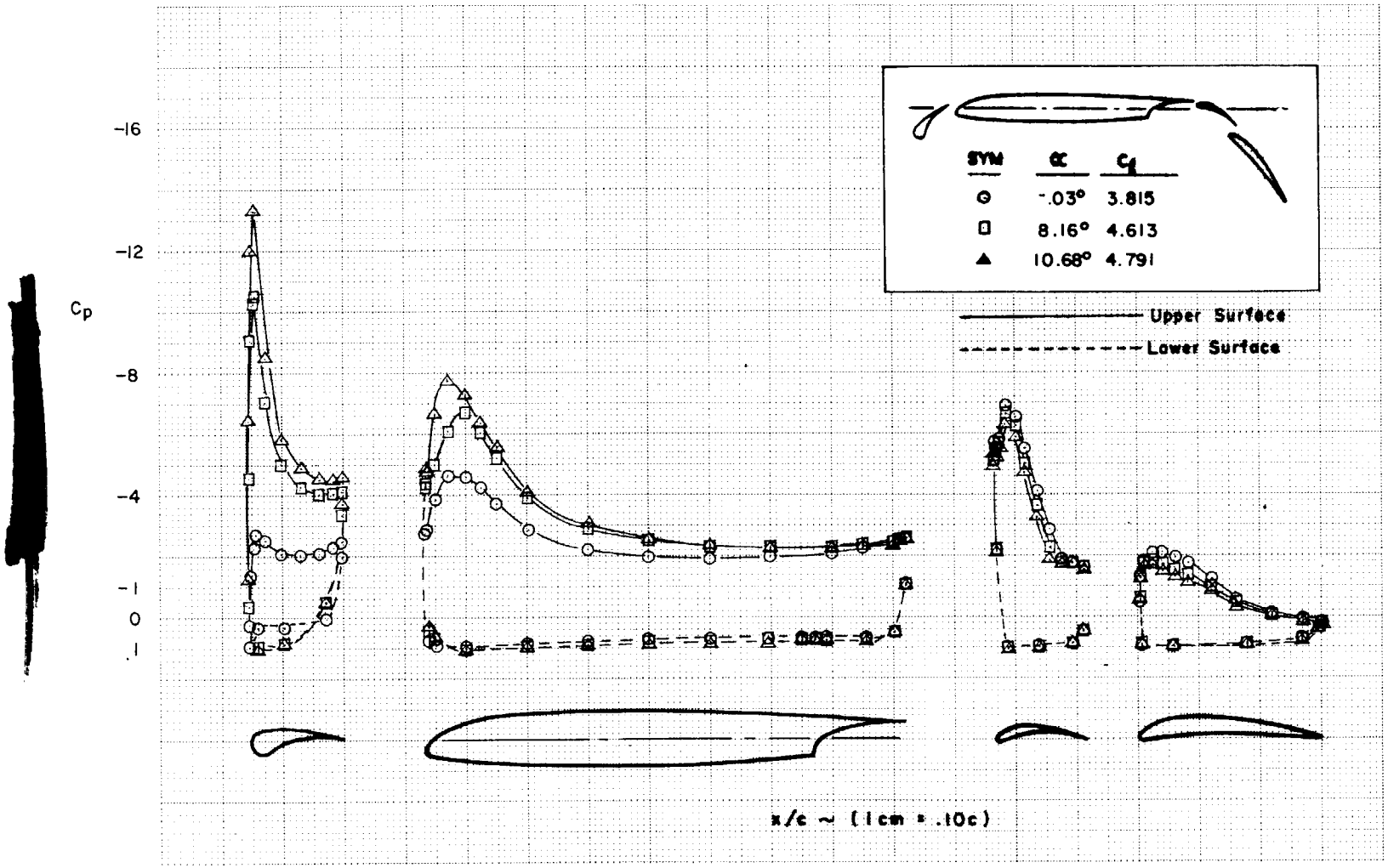

(b)

FIGURE C12.—Continued

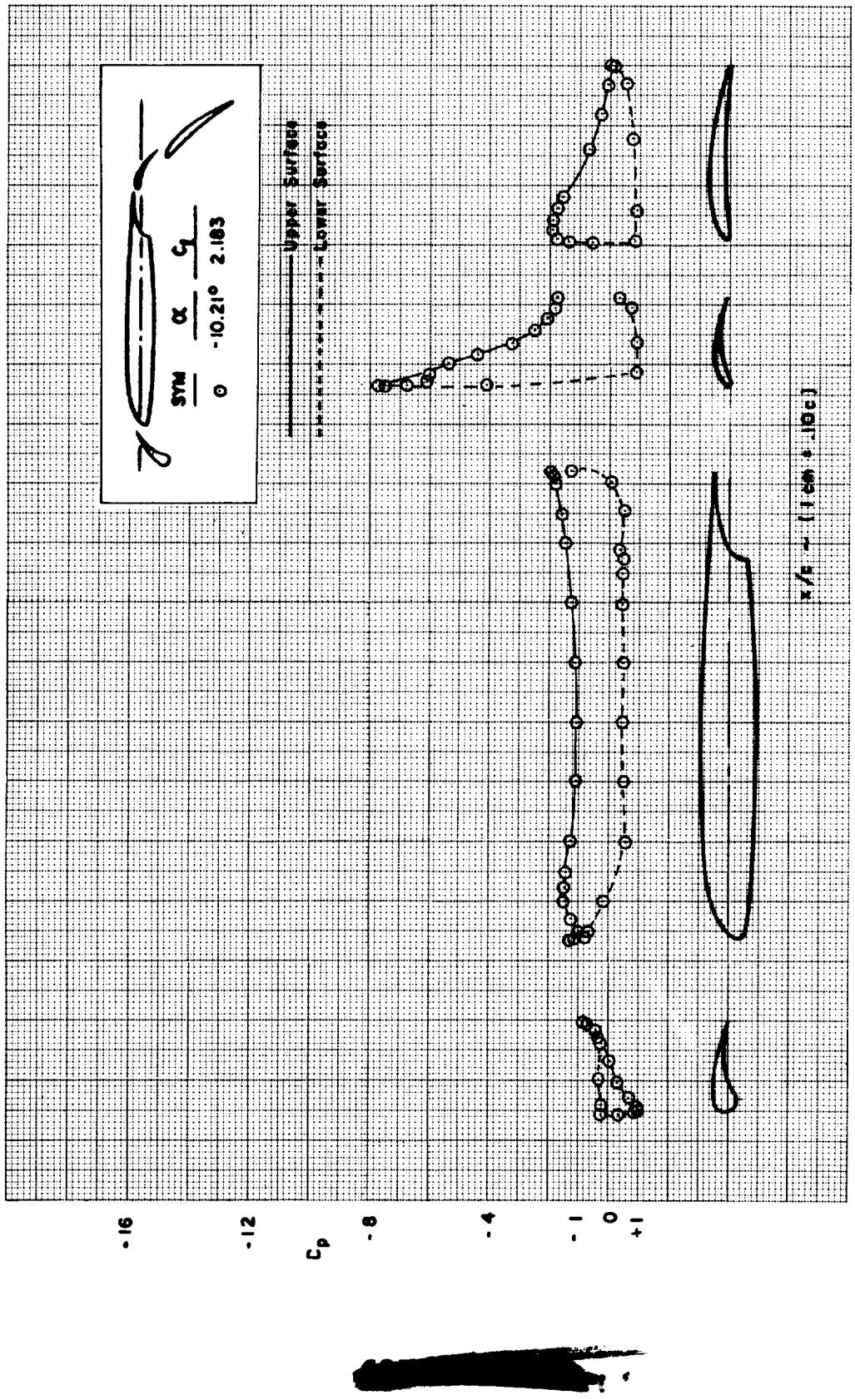

(c)

FIGURE C12.—Continued

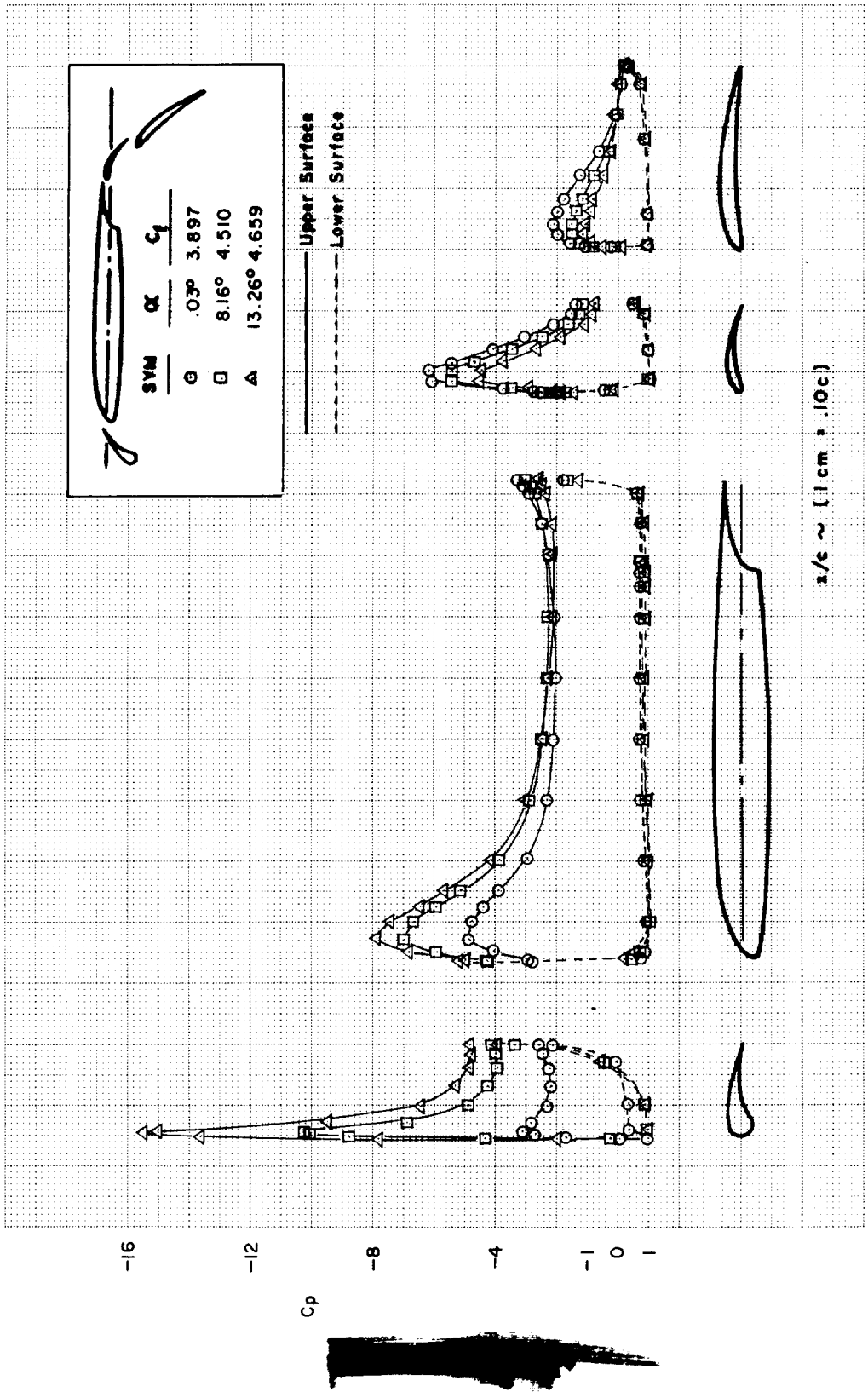

(d)

FIGURE C12.—Continued

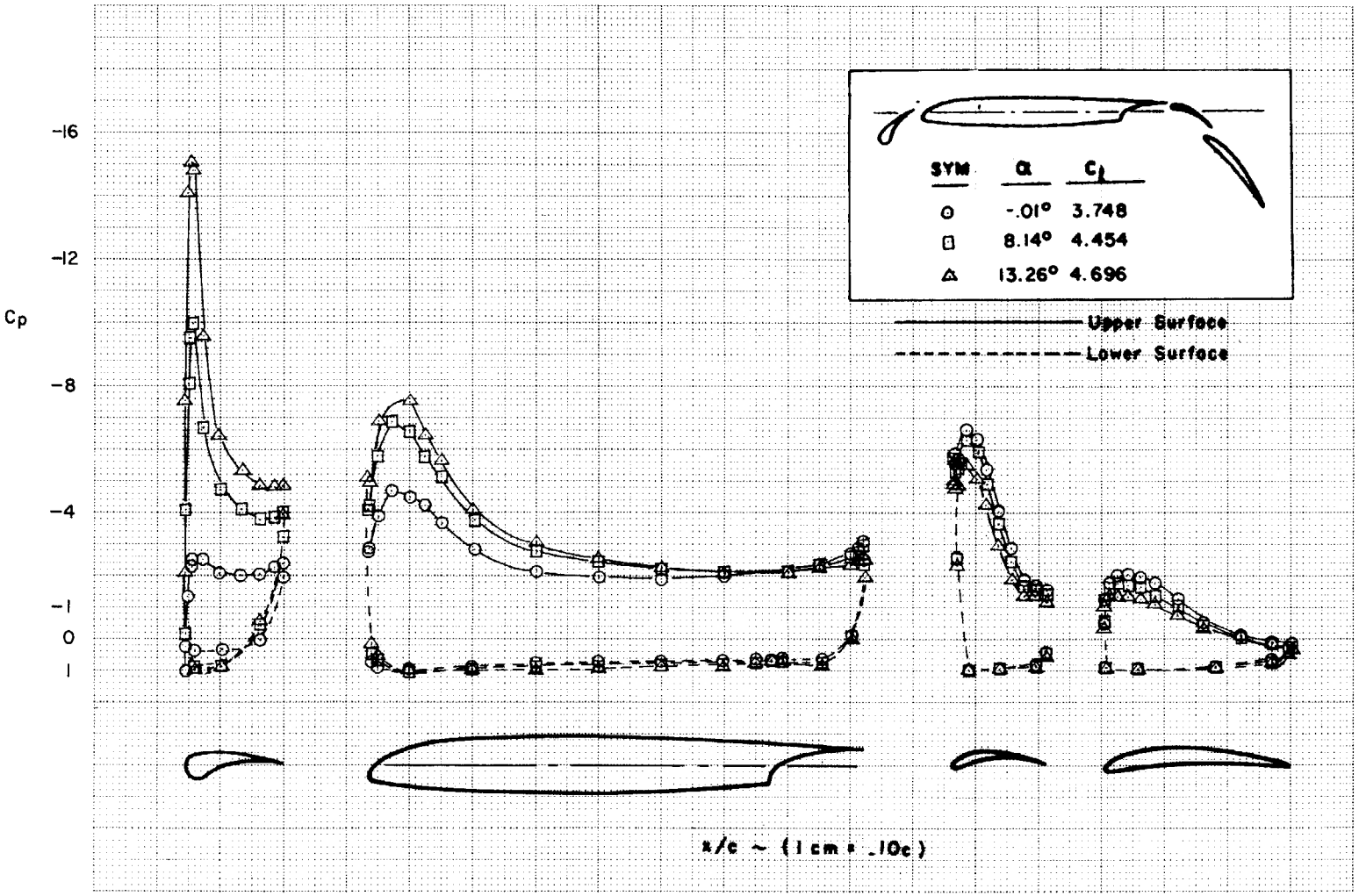

(e)

FIGURE C12.—Continued

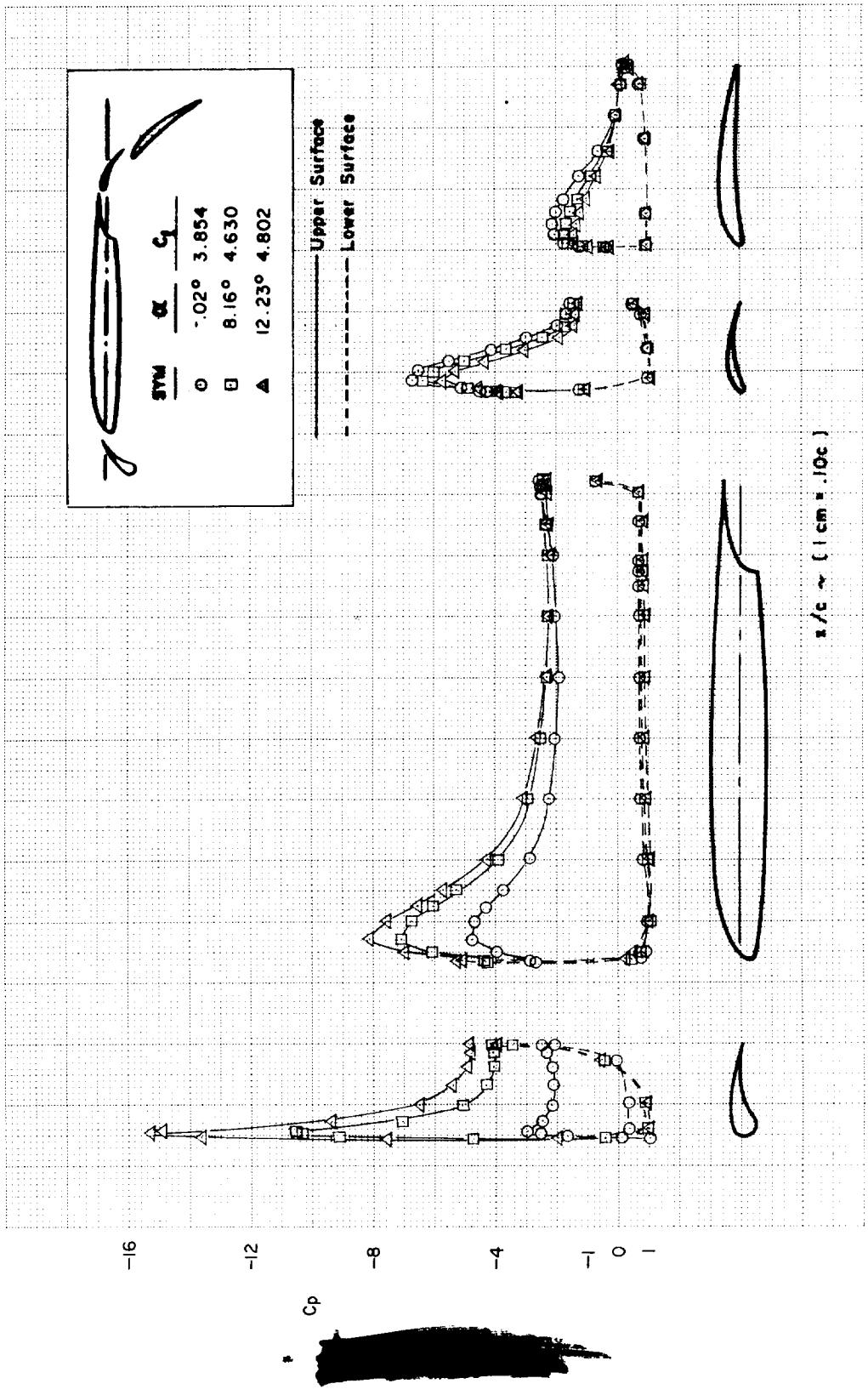

(f)

FIGURE C12.—Continued

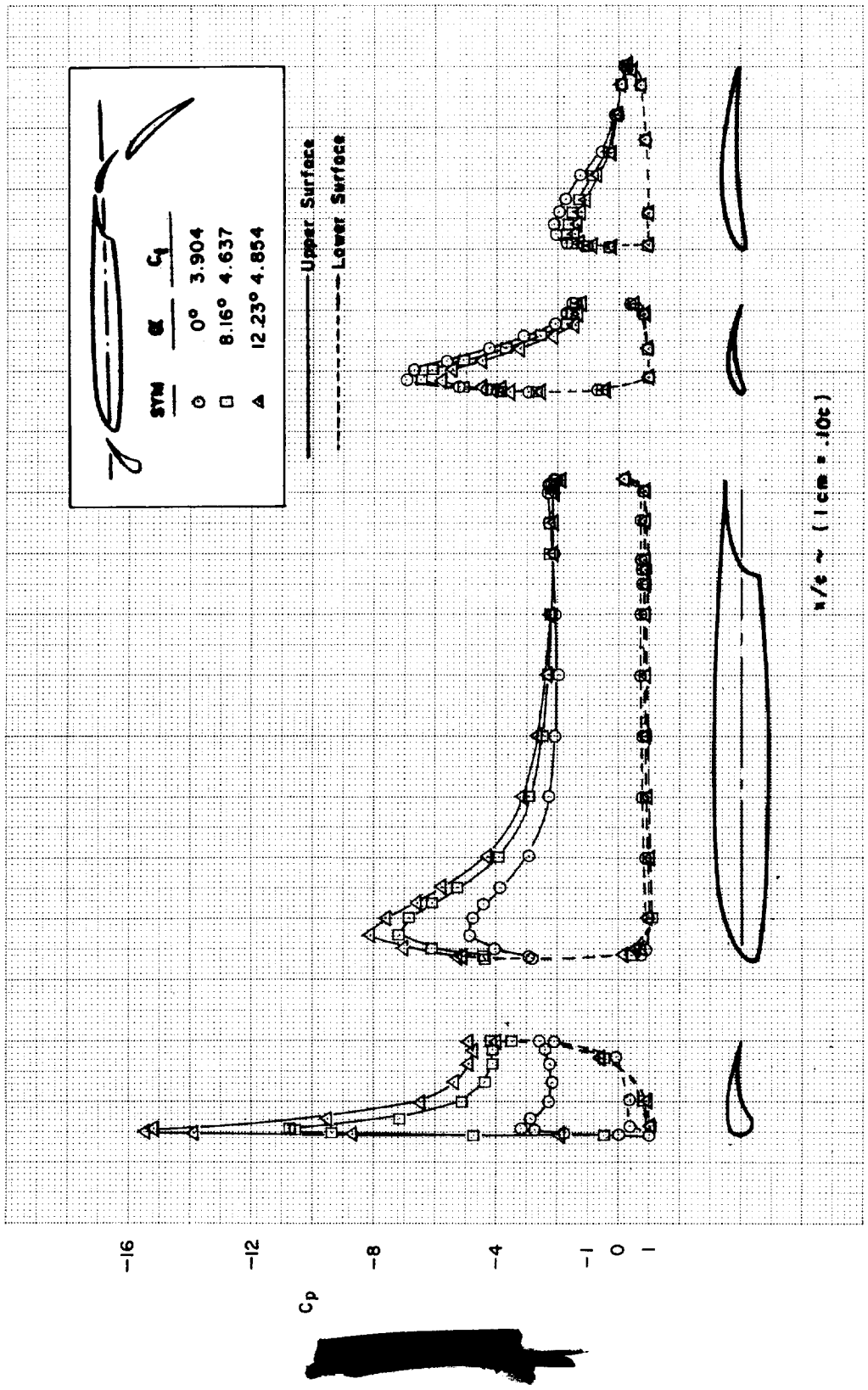

(g)

FIGURE C12.—Continued

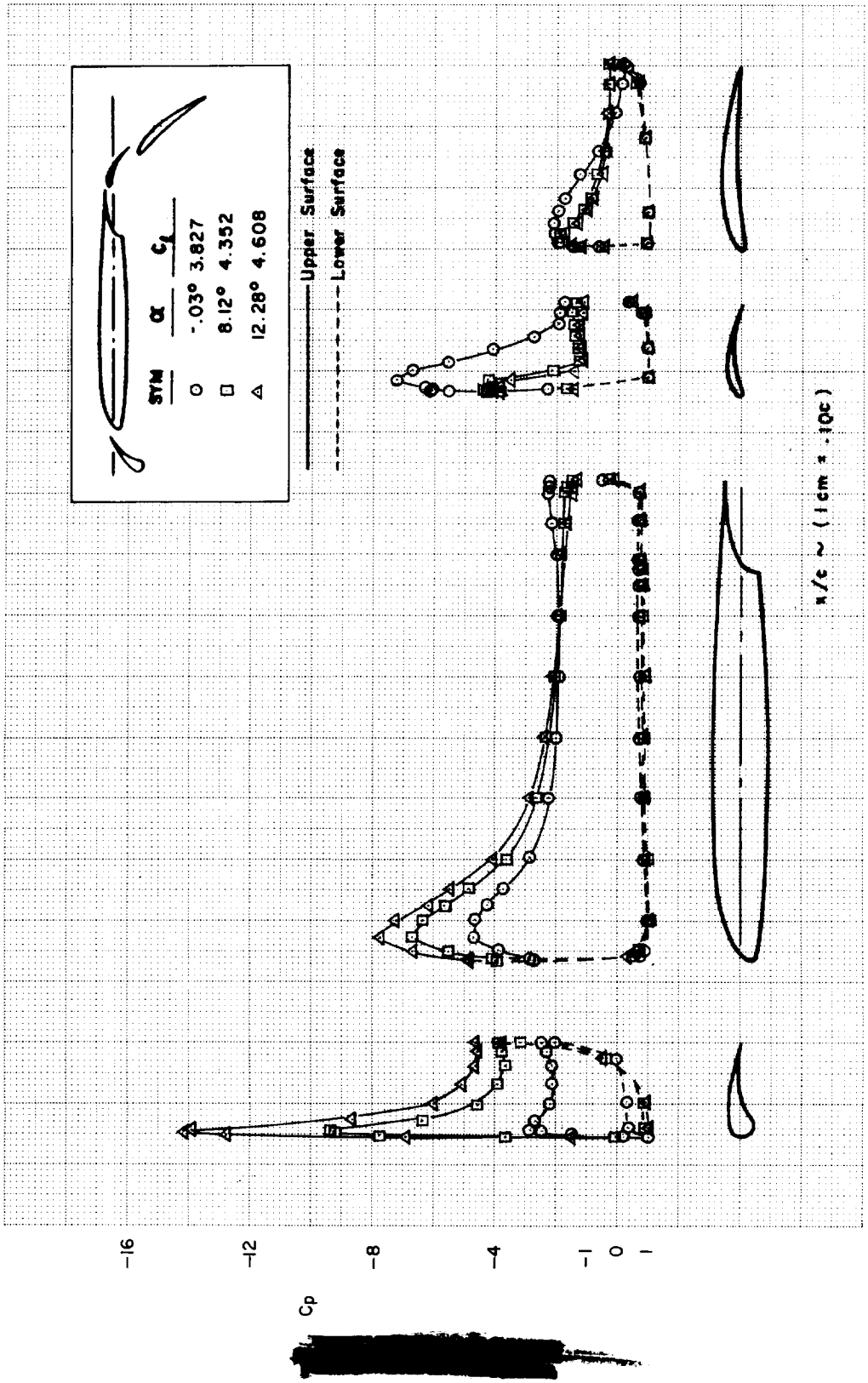

(h)

FIGURE C12.—Continued

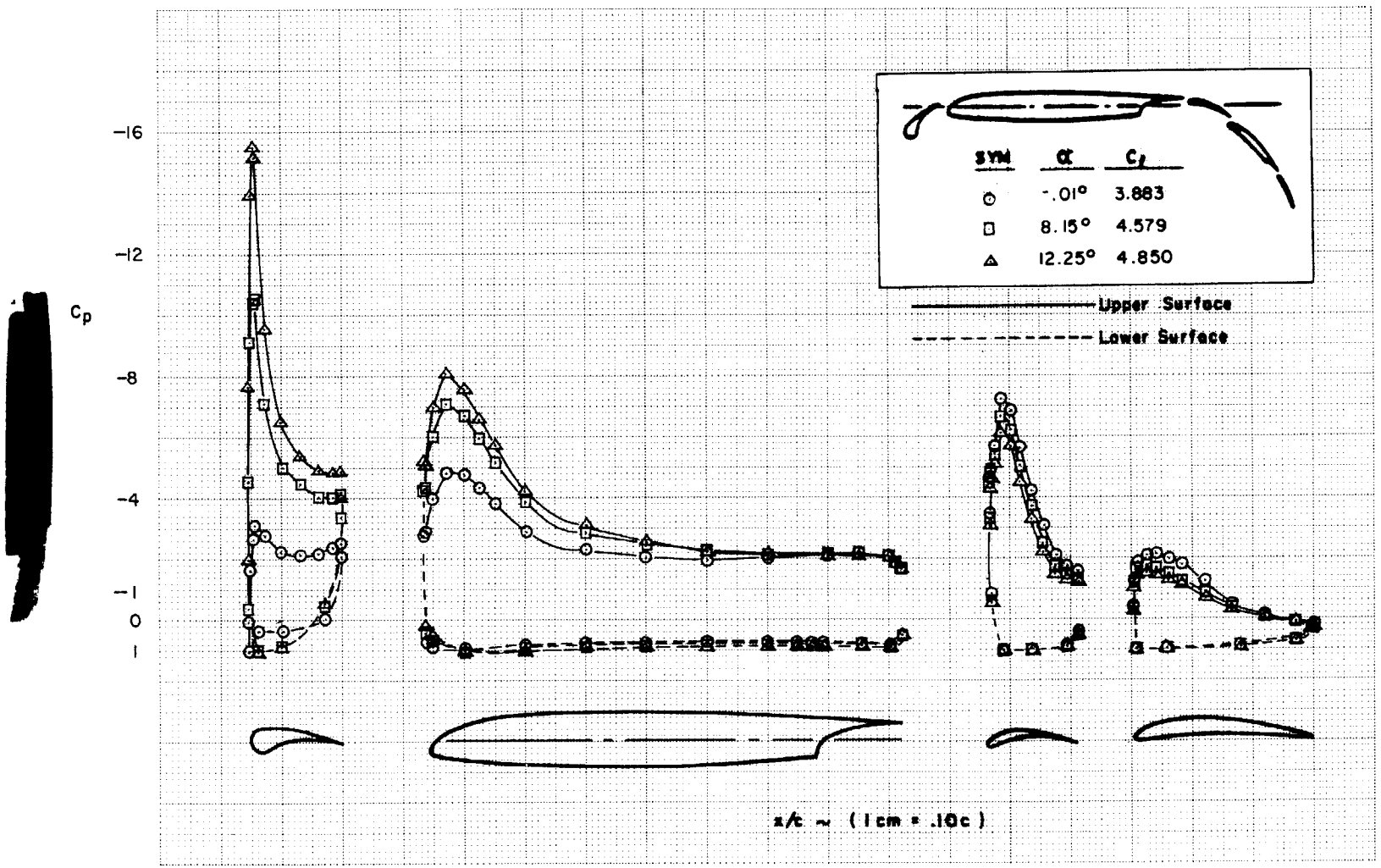

(i)

FIGURE C12.—Continued

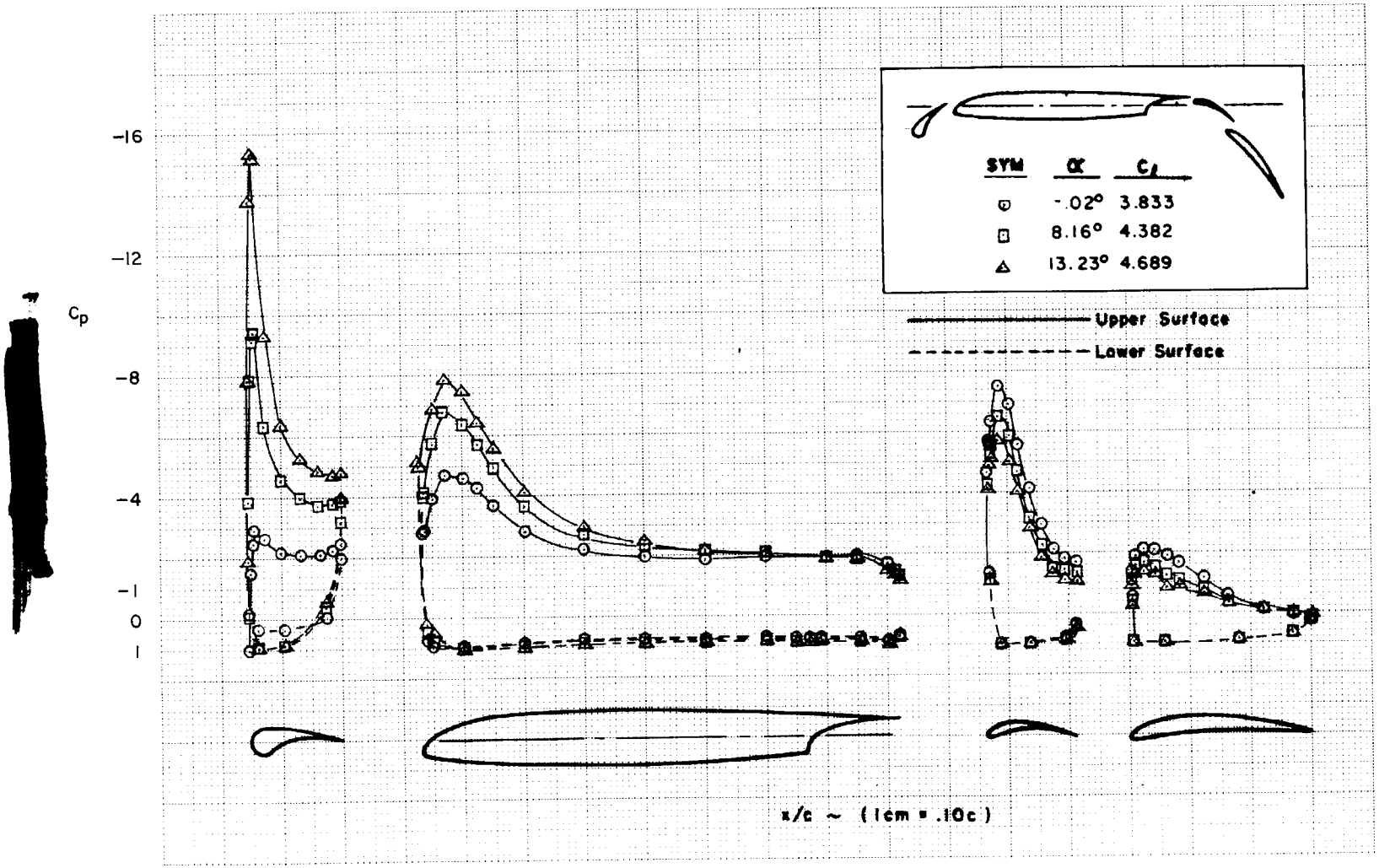

(j)

FIGURE C12.–Continued

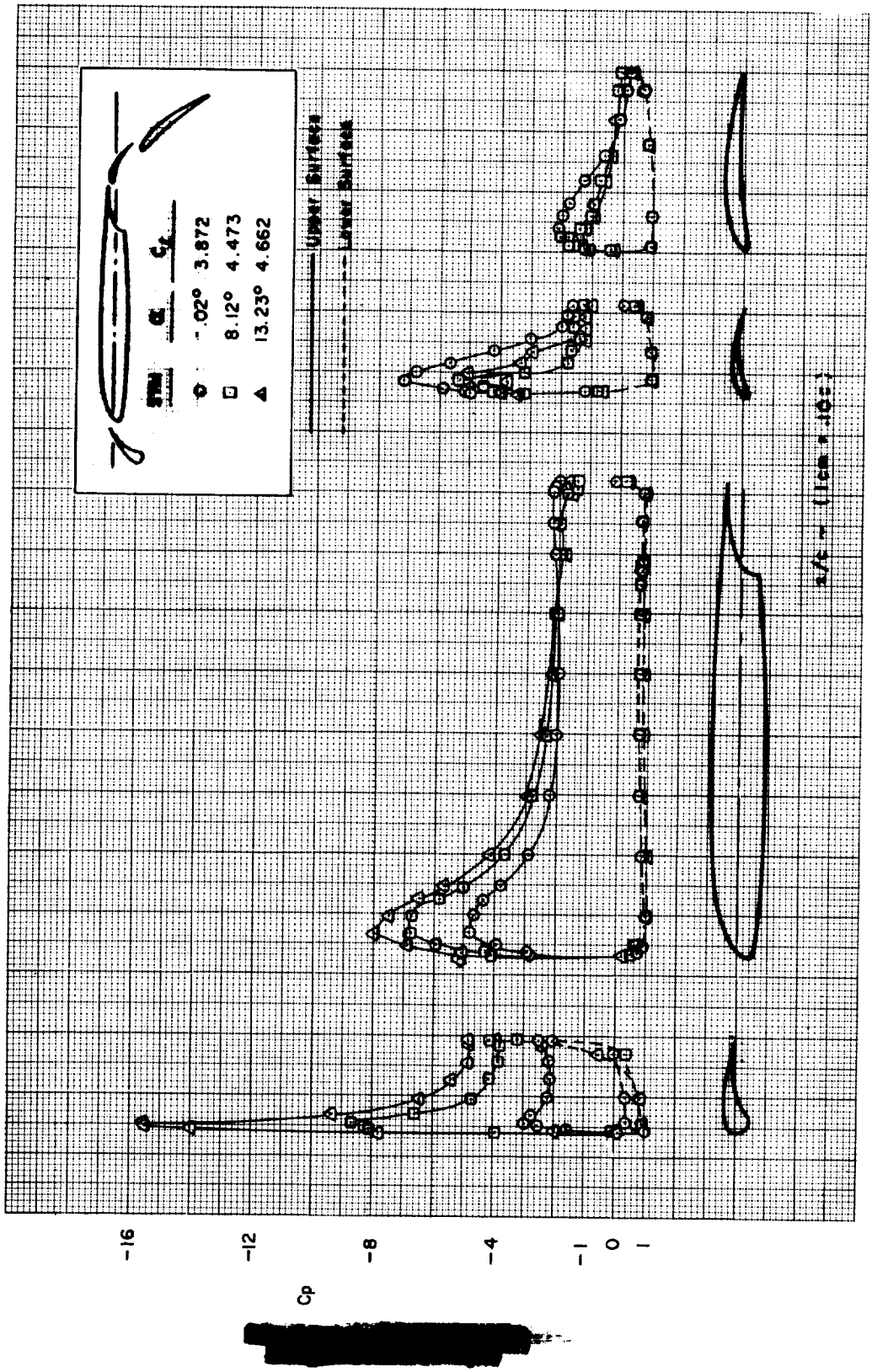

(k)

FIGURE C12.—Continued

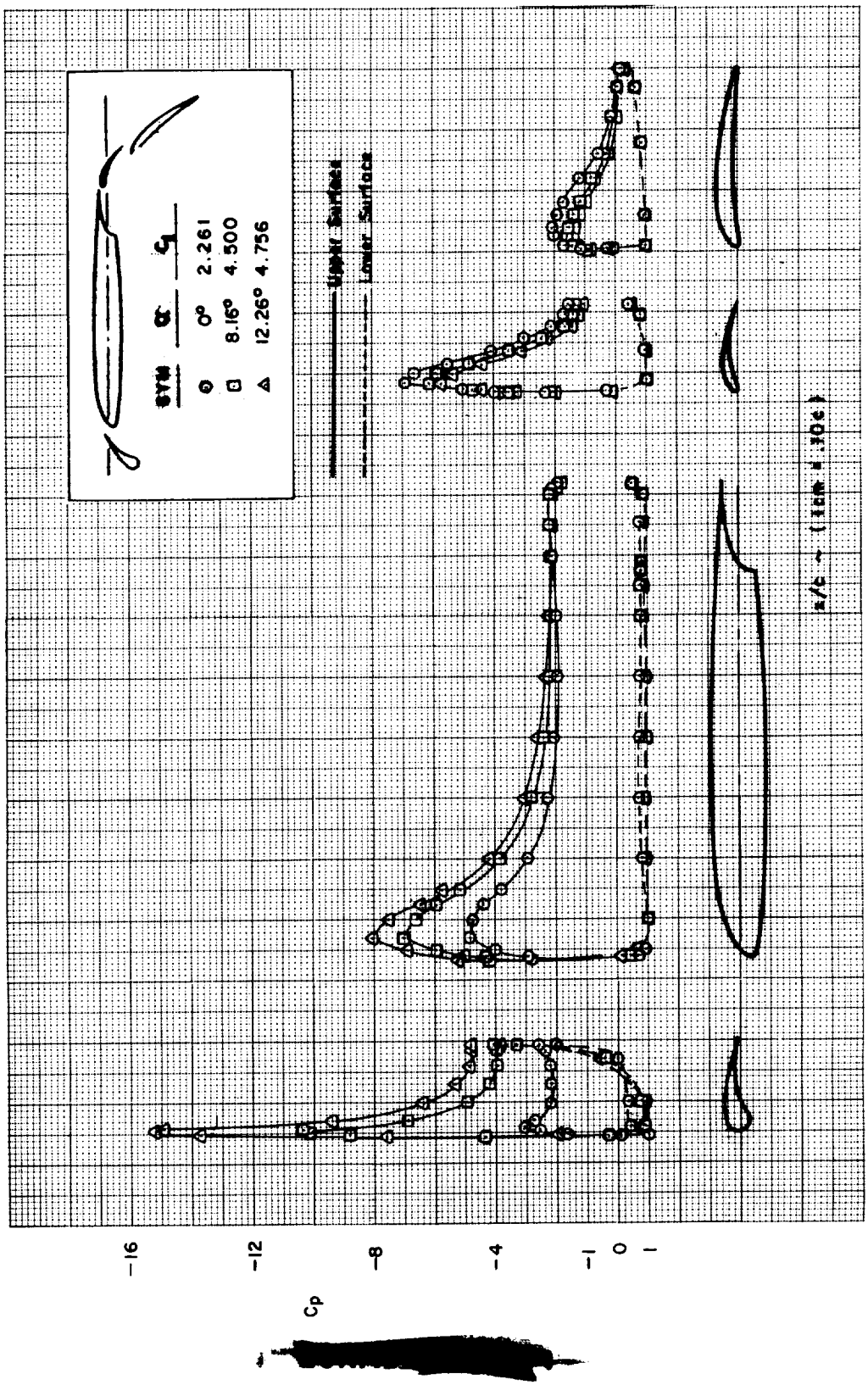

(l)

FIGURE C12.—Concluded

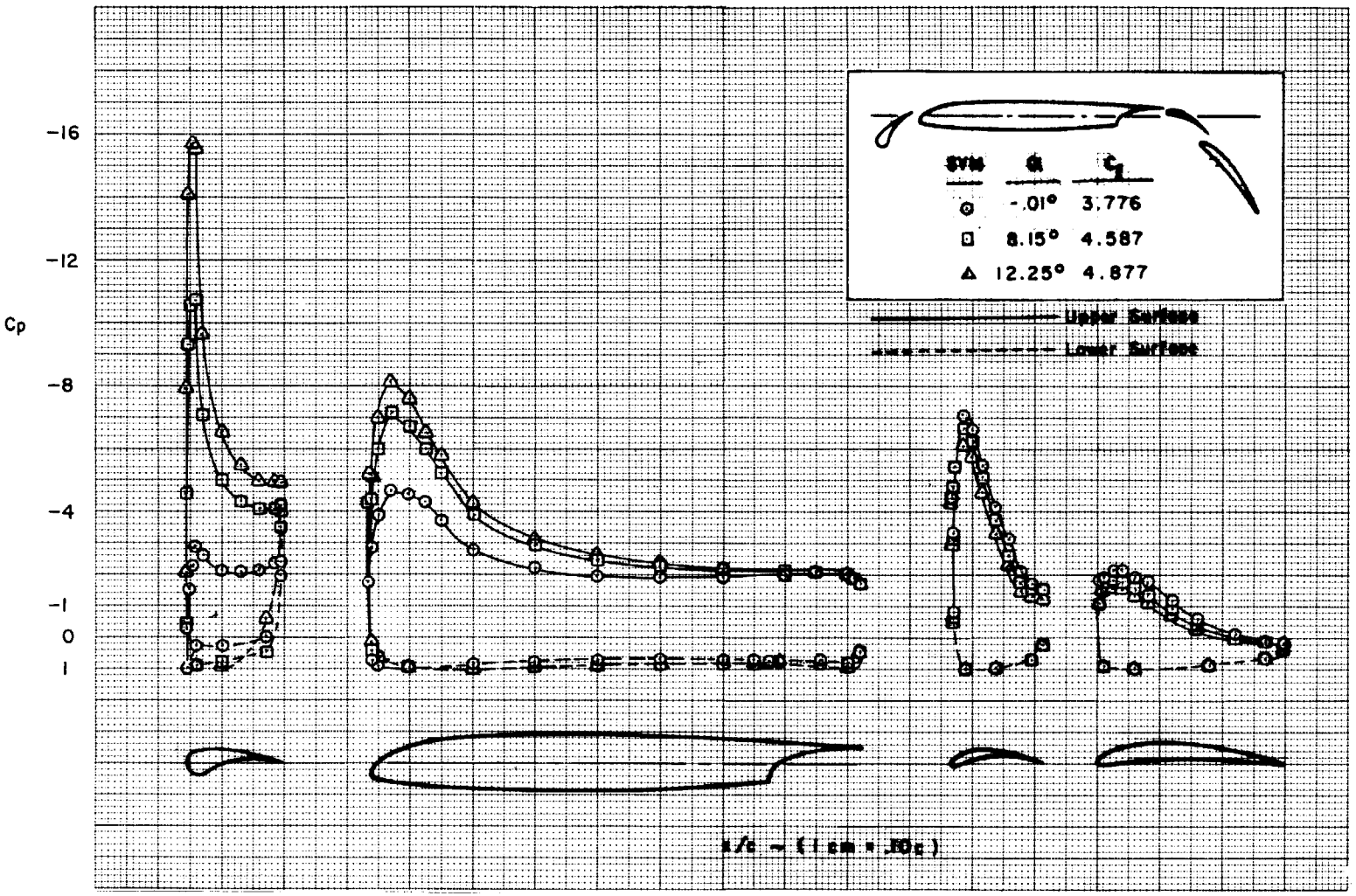

(a)

FIGURE C13.–EFFECT OF VANE-FLAP SLOT GAP AND OVERLAP–MODEL C ($\delta_{f_{eq}} = 44°$)

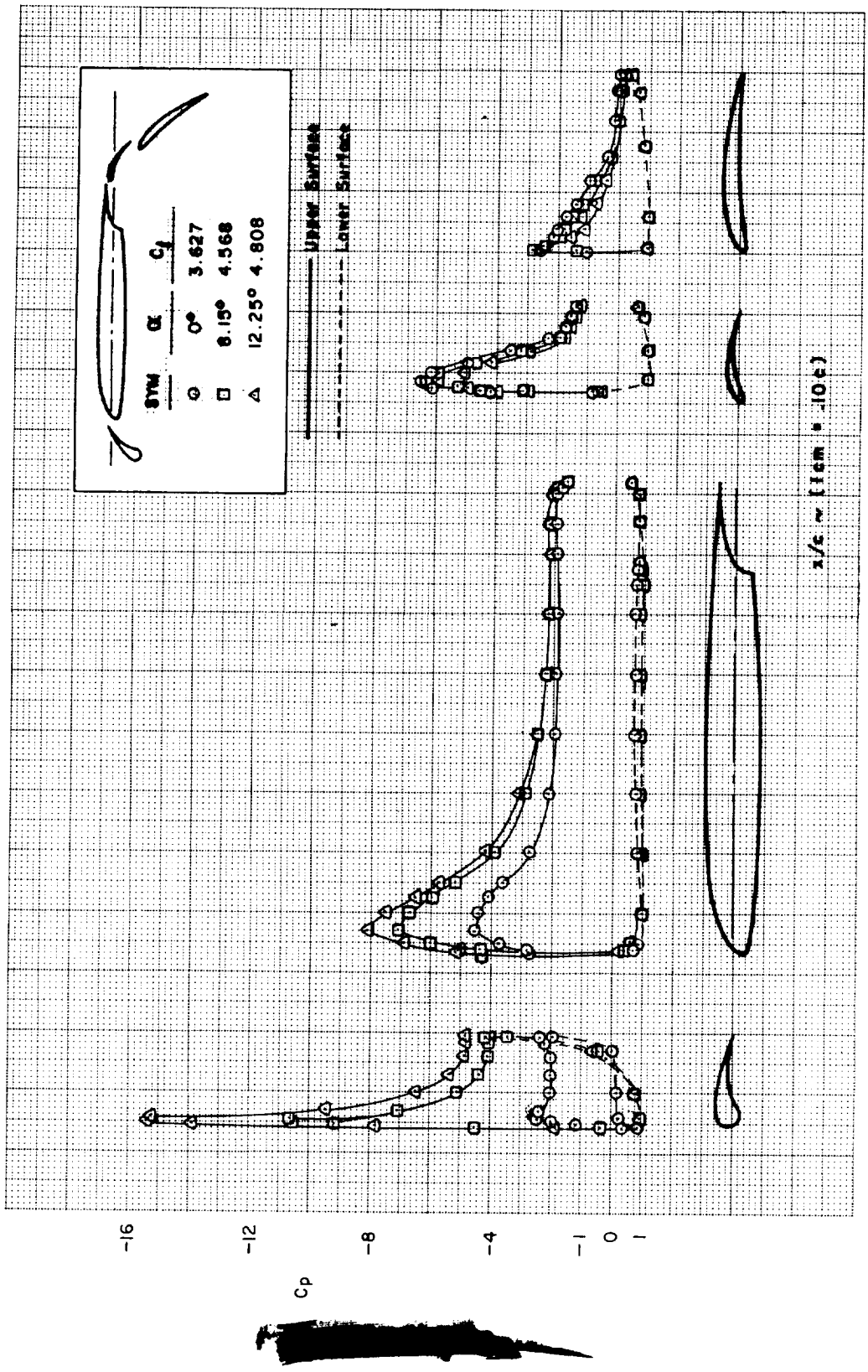

(b)

FIGURE C13.—Continued

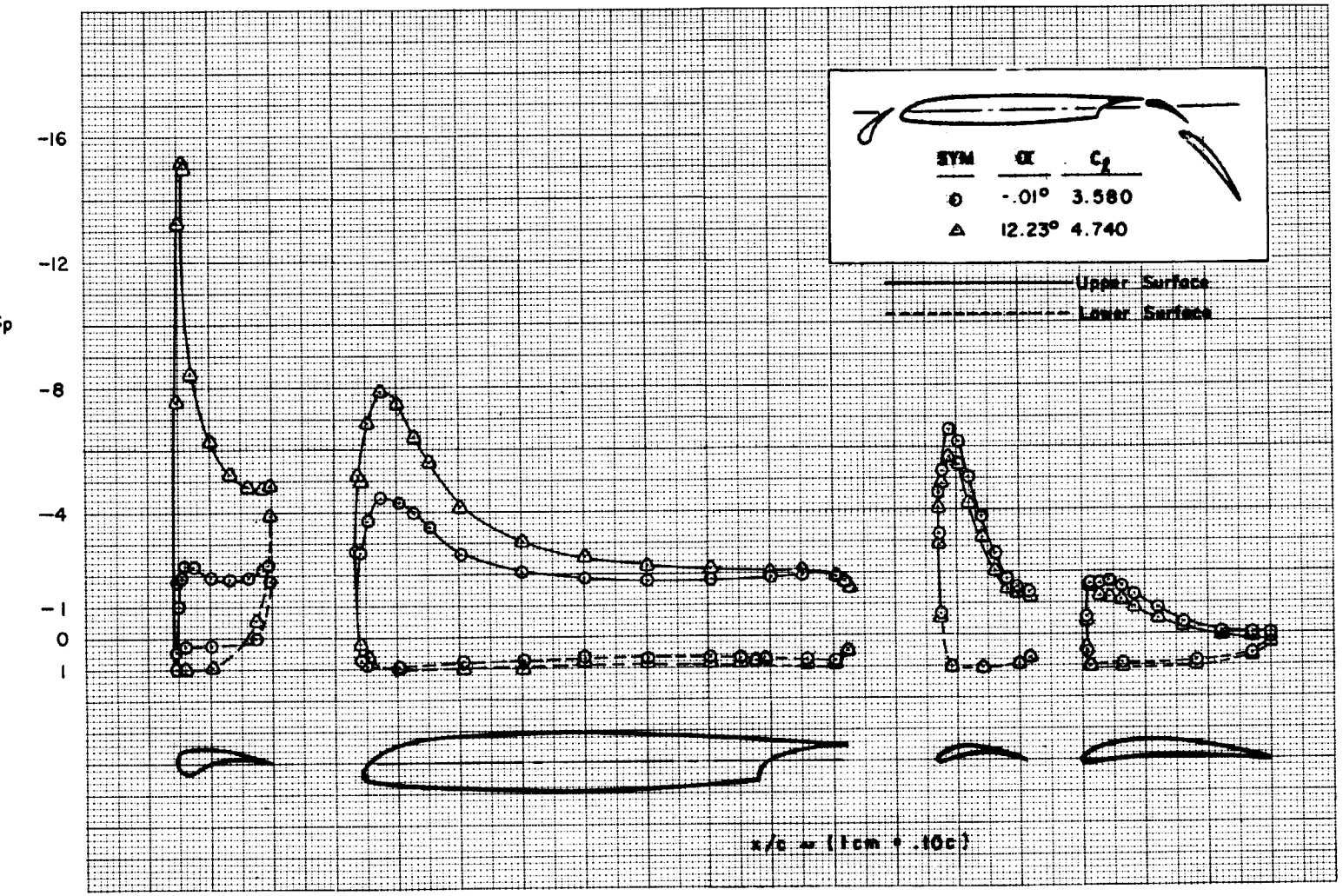

(c)

FIGURE C13.—Continued

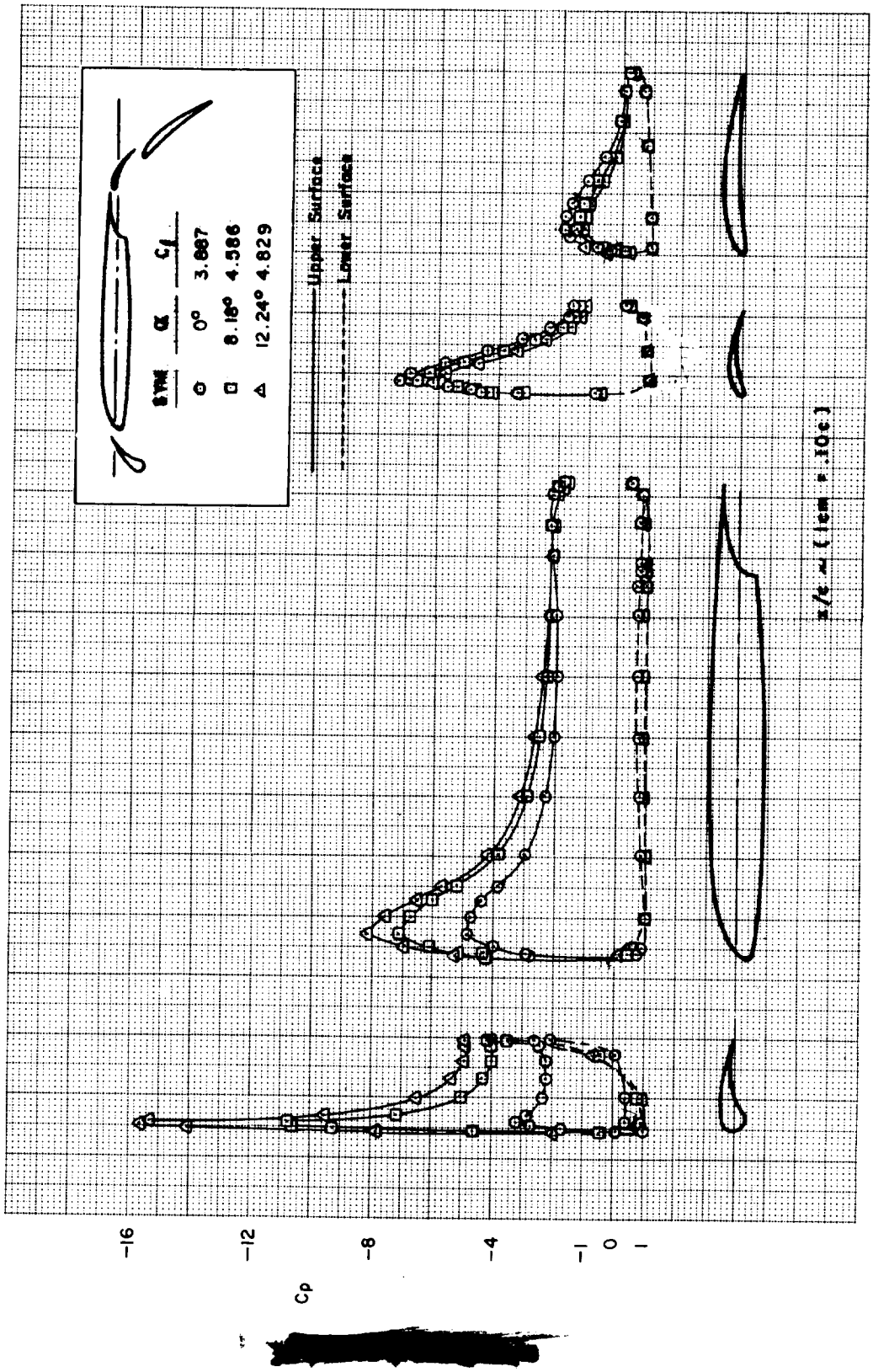

FIGURE C13.—Continued

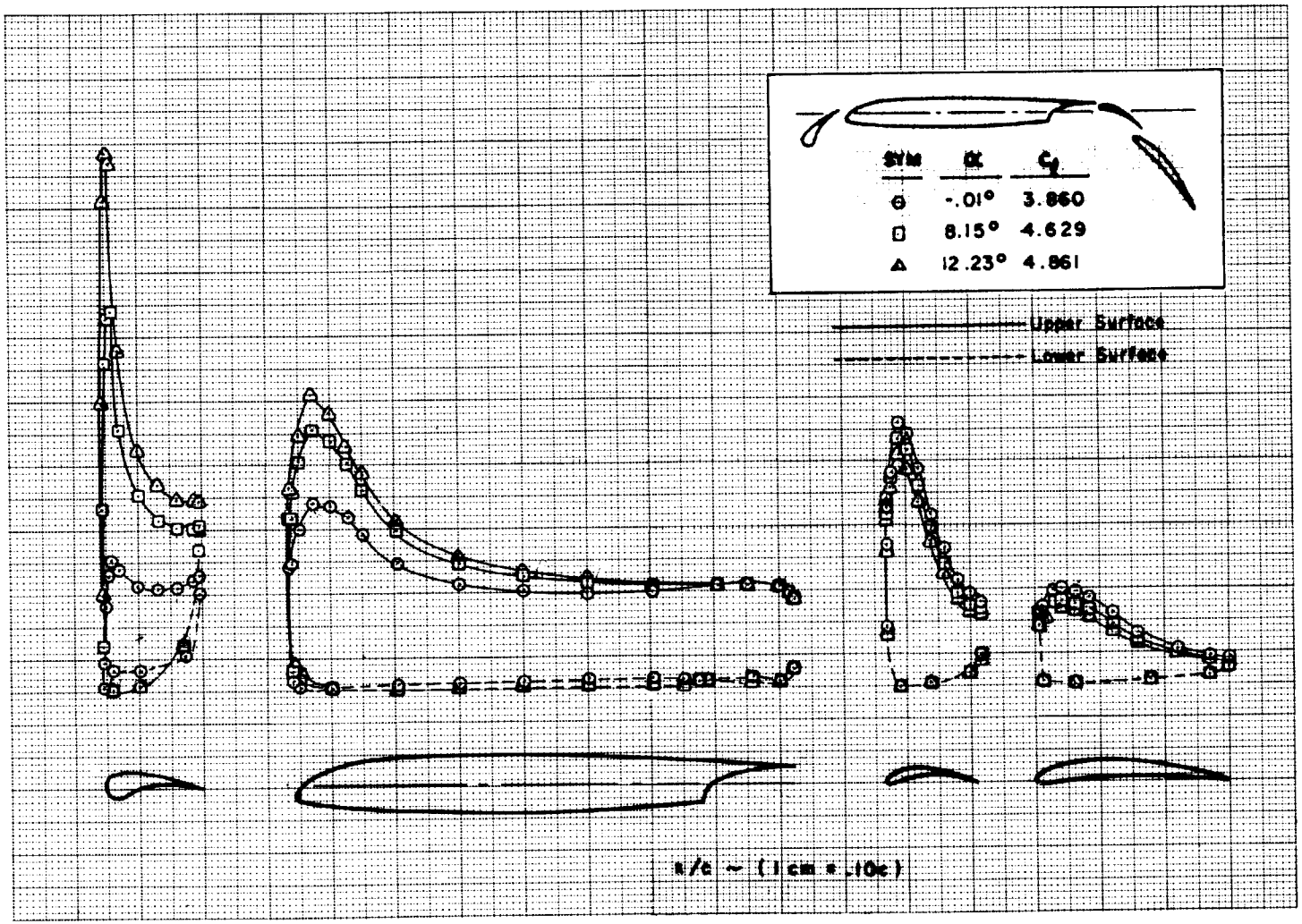

(e)

FIGURE C13.—Continued

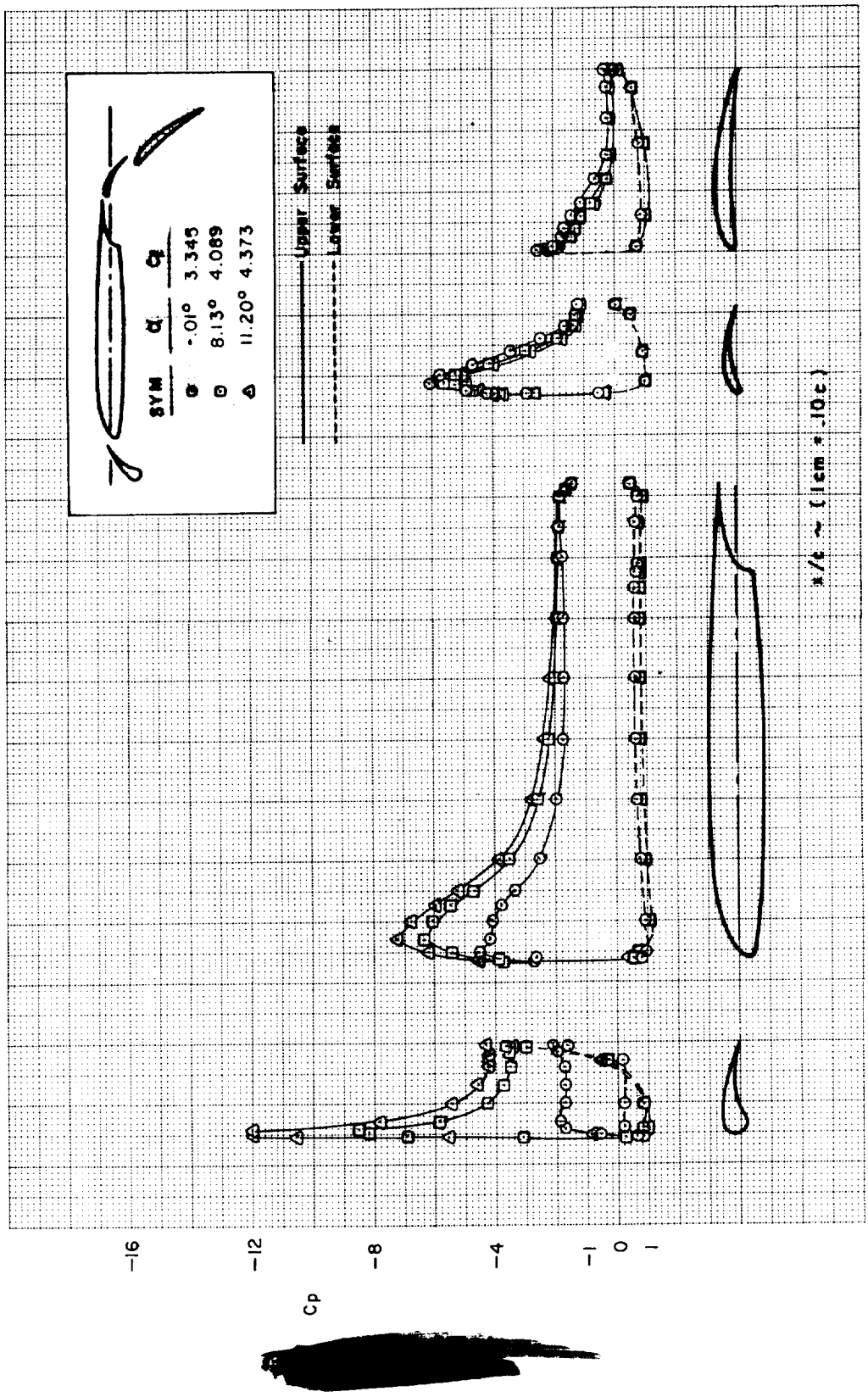

(f)

FIGURE C13.—Continued

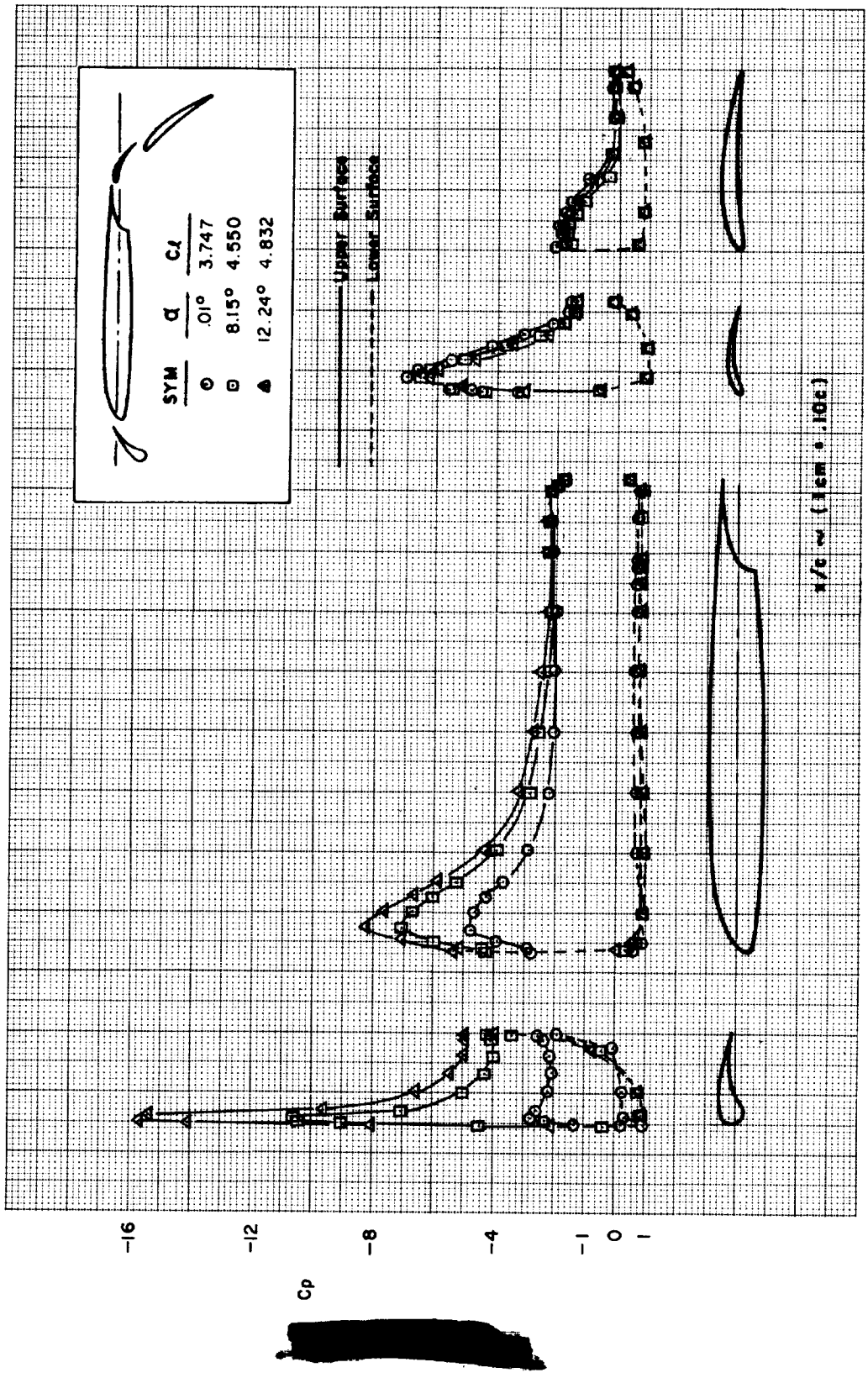

(g)

FIGURE C13.—Continued

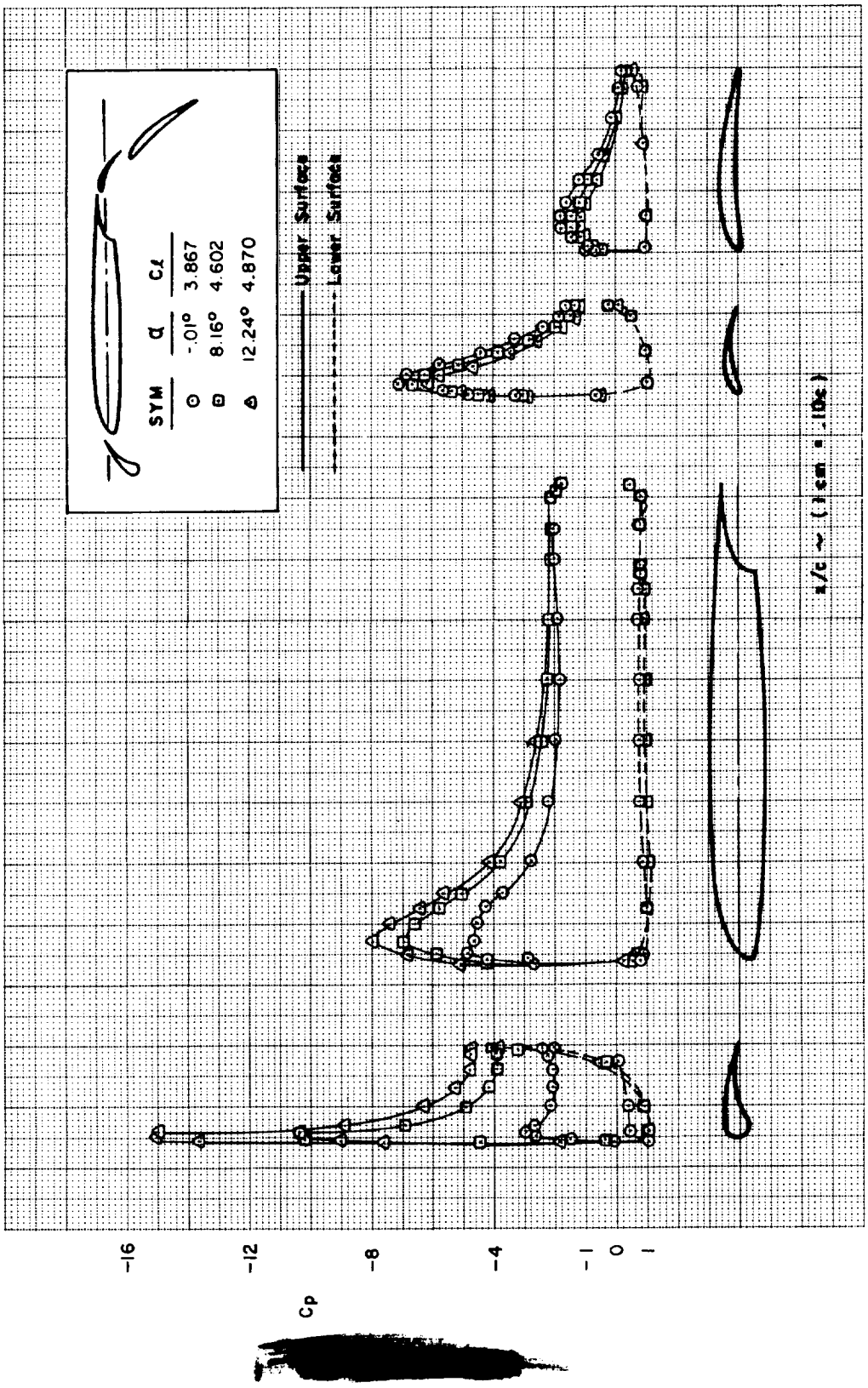

(h)

FIGURE C13.–Continued

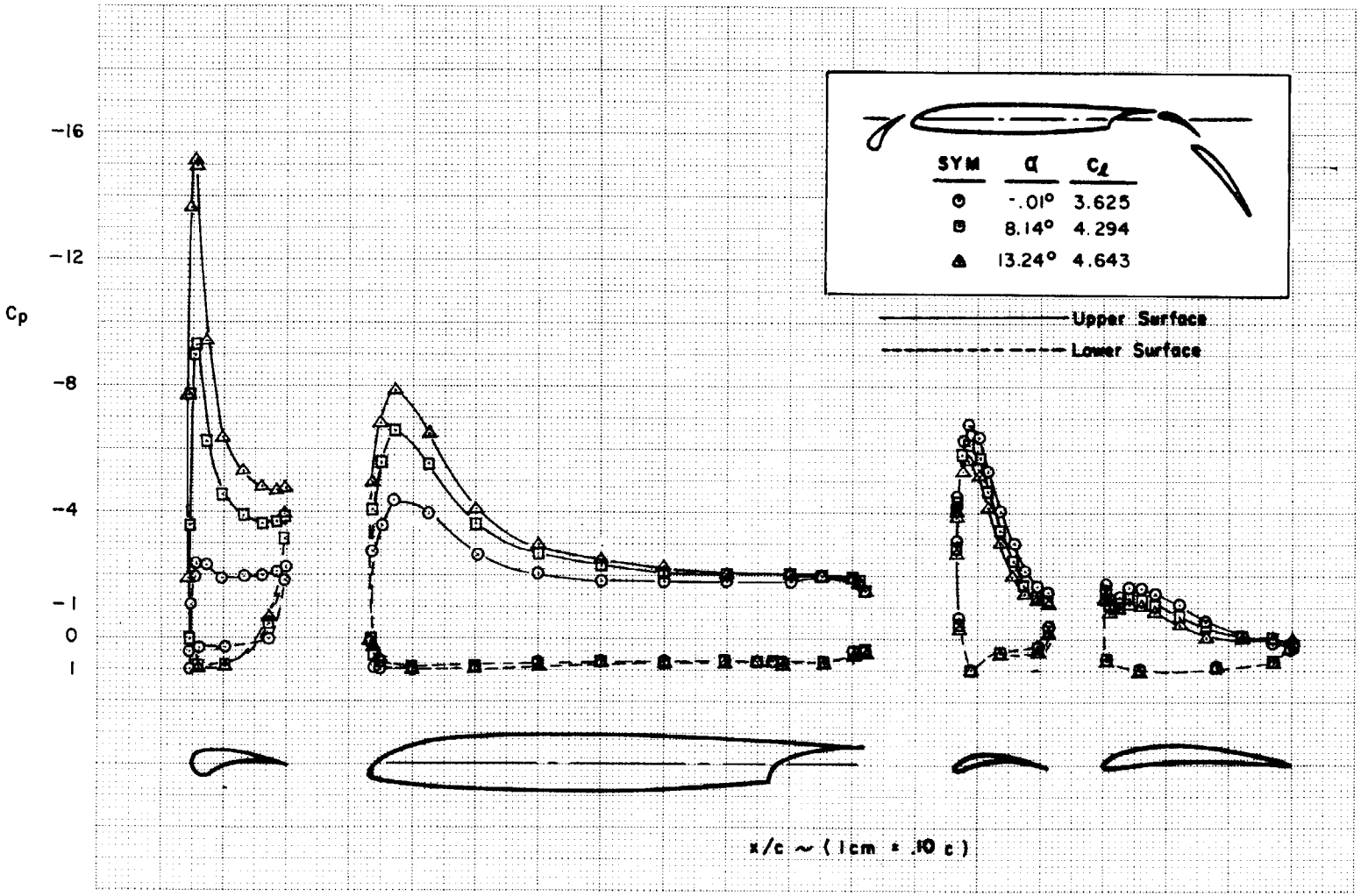

(i)

FIGURE C13.—Continued

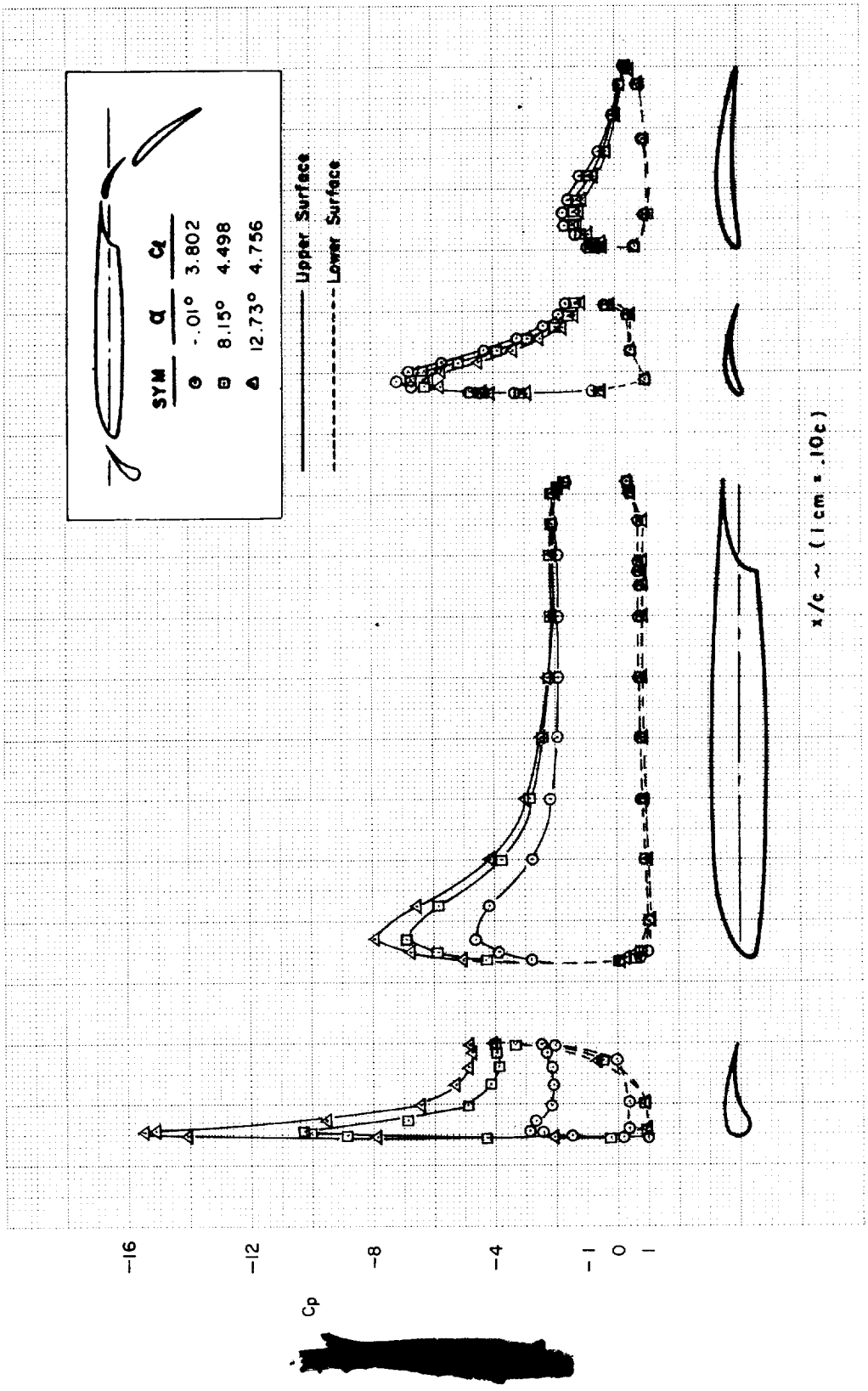

(j)

FIGURE c13.–Concluded

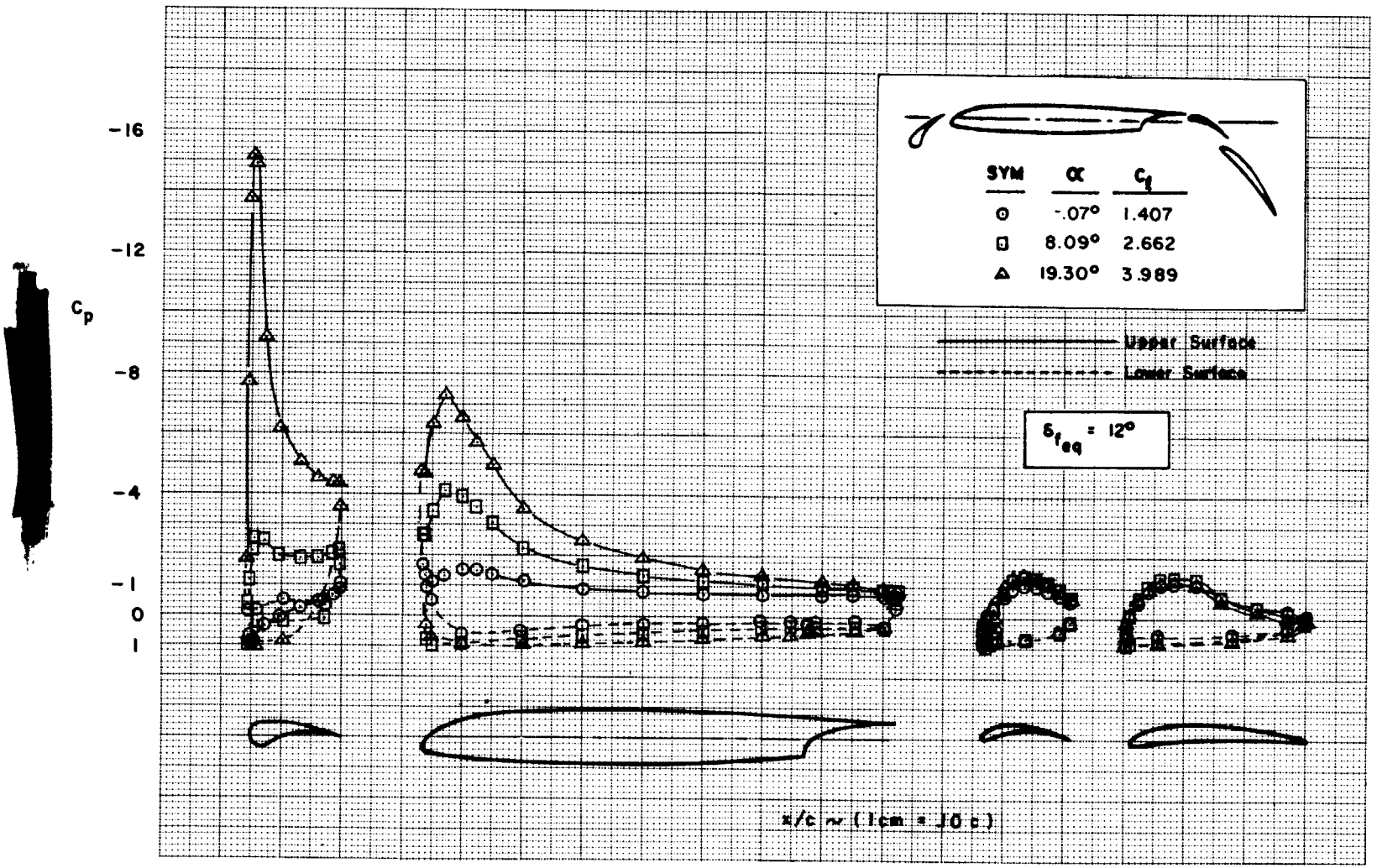

(a)

FIGURE C14.–EFFECT OF FLAP DEFLECTION ANGLE VARIATION–MODEL C

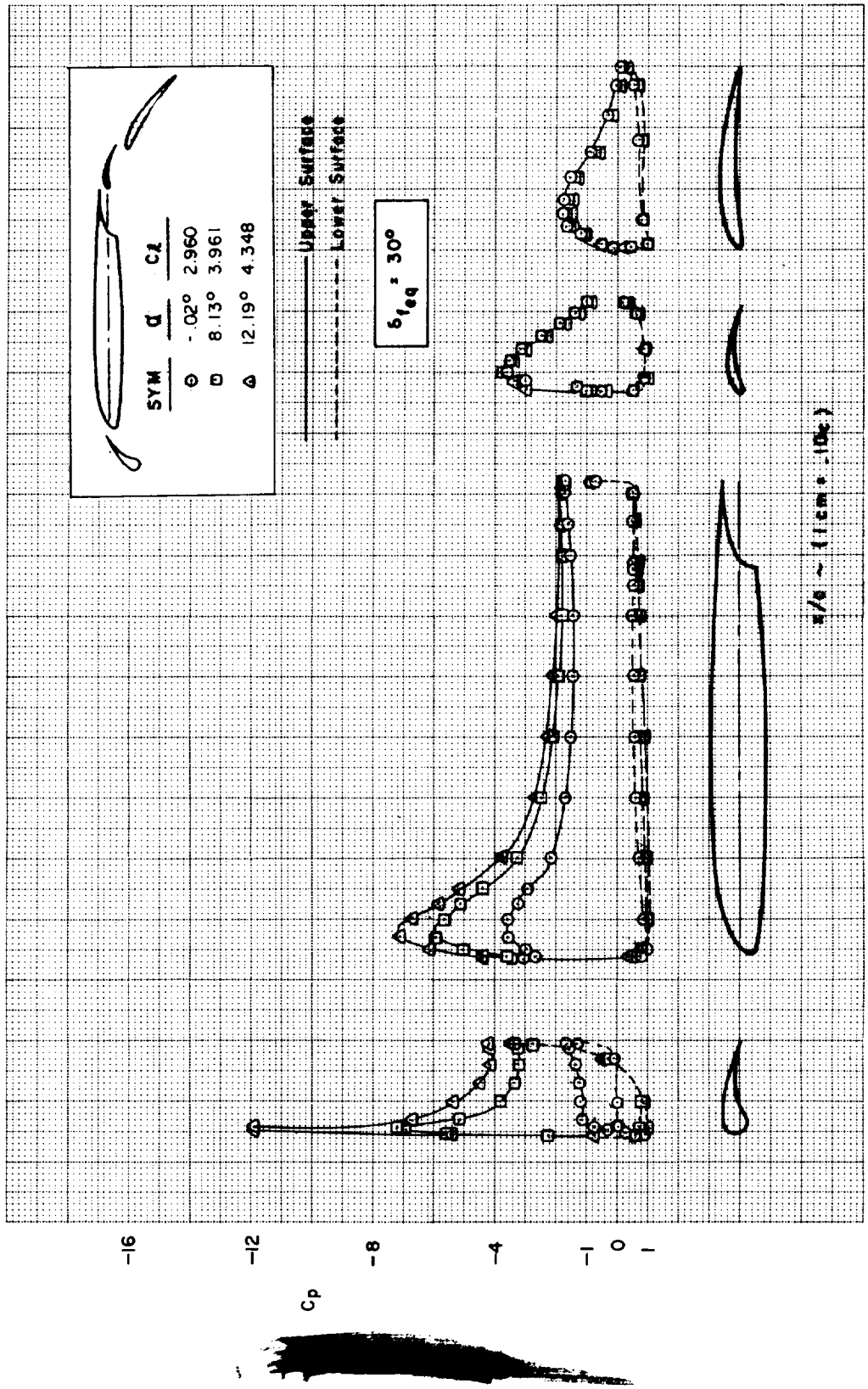

(b)

FIGURE C14.—Continued

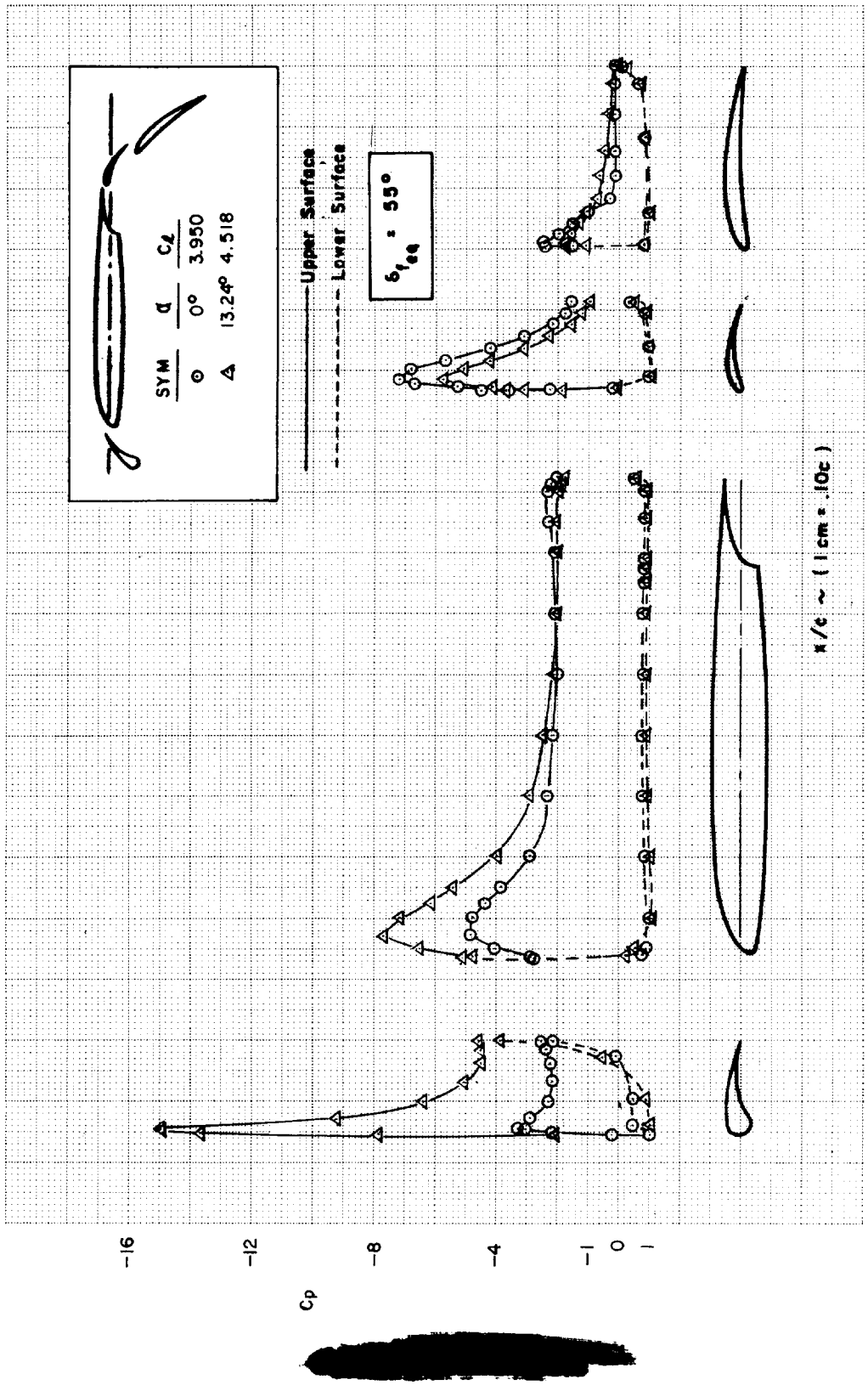

(c)

FIGURE C14.—Continued

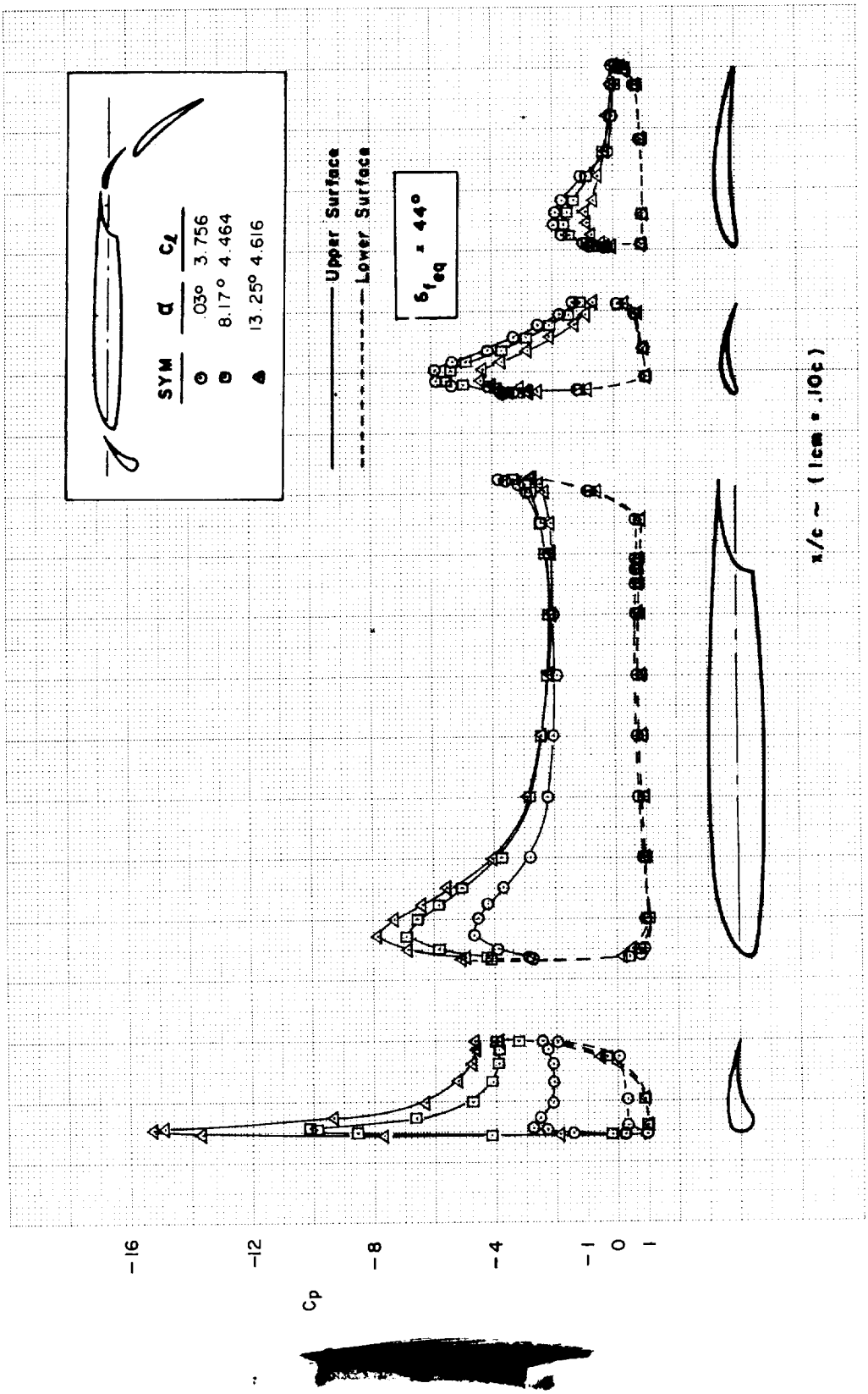

(d)

FIGURE C14.—Concluded

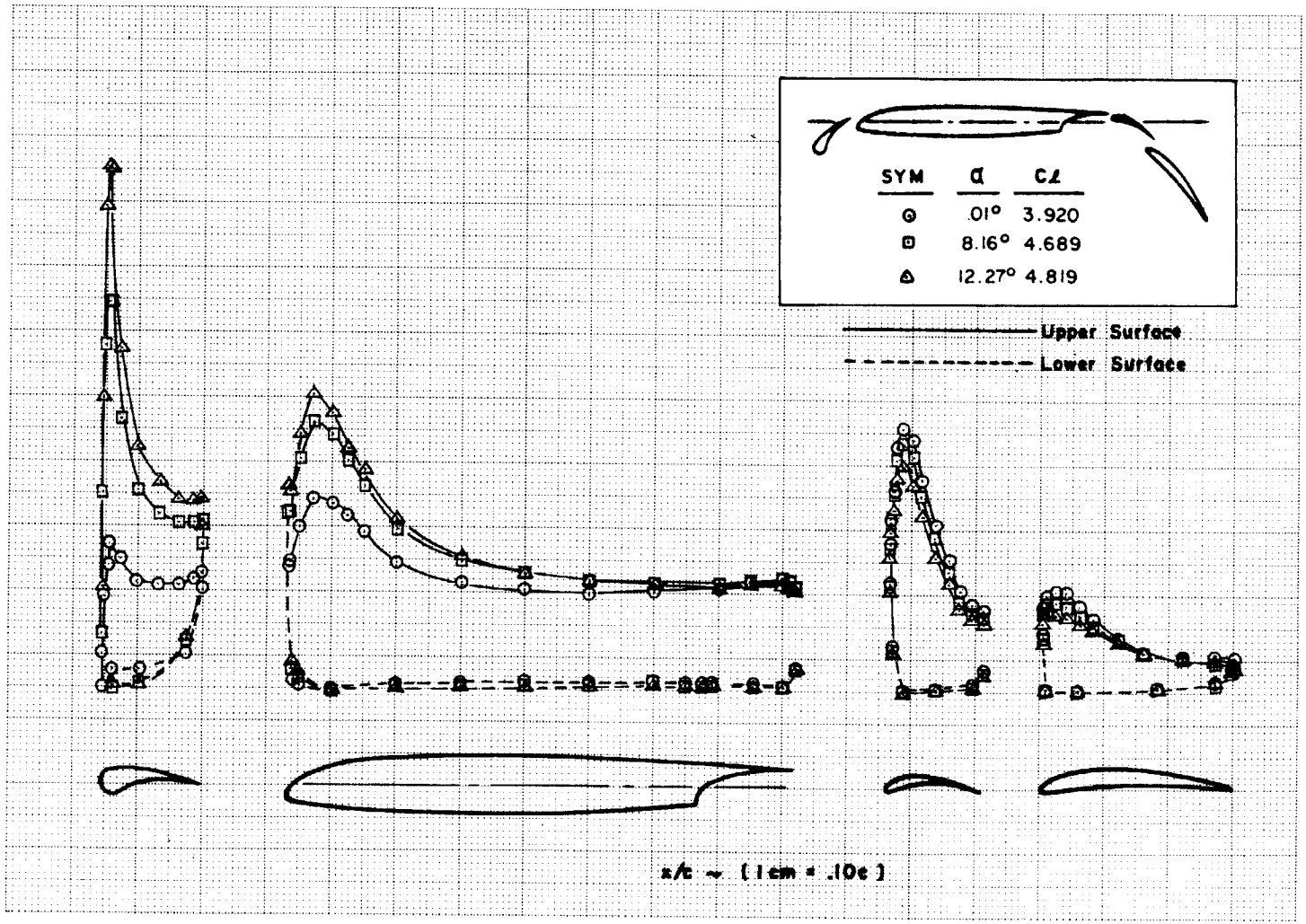

(a)

FIGURE C15.–EFFECT OF FLAP COMPONENT ANGLE COMBINATION AT CONSTANT $\delta_{f_{eq}}$ (49°)–MODEL C

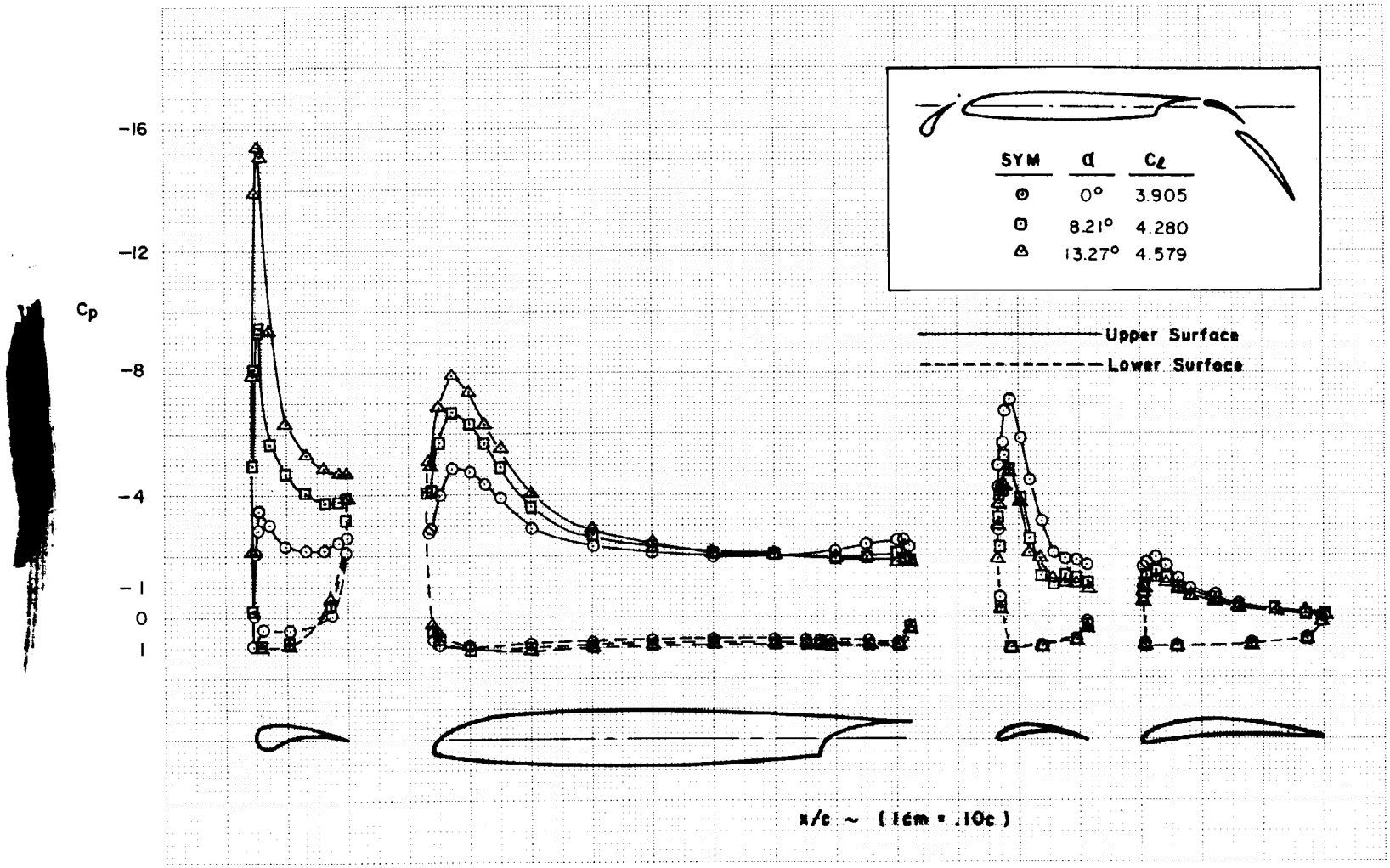

(b)

FIGURE C15.—Continued

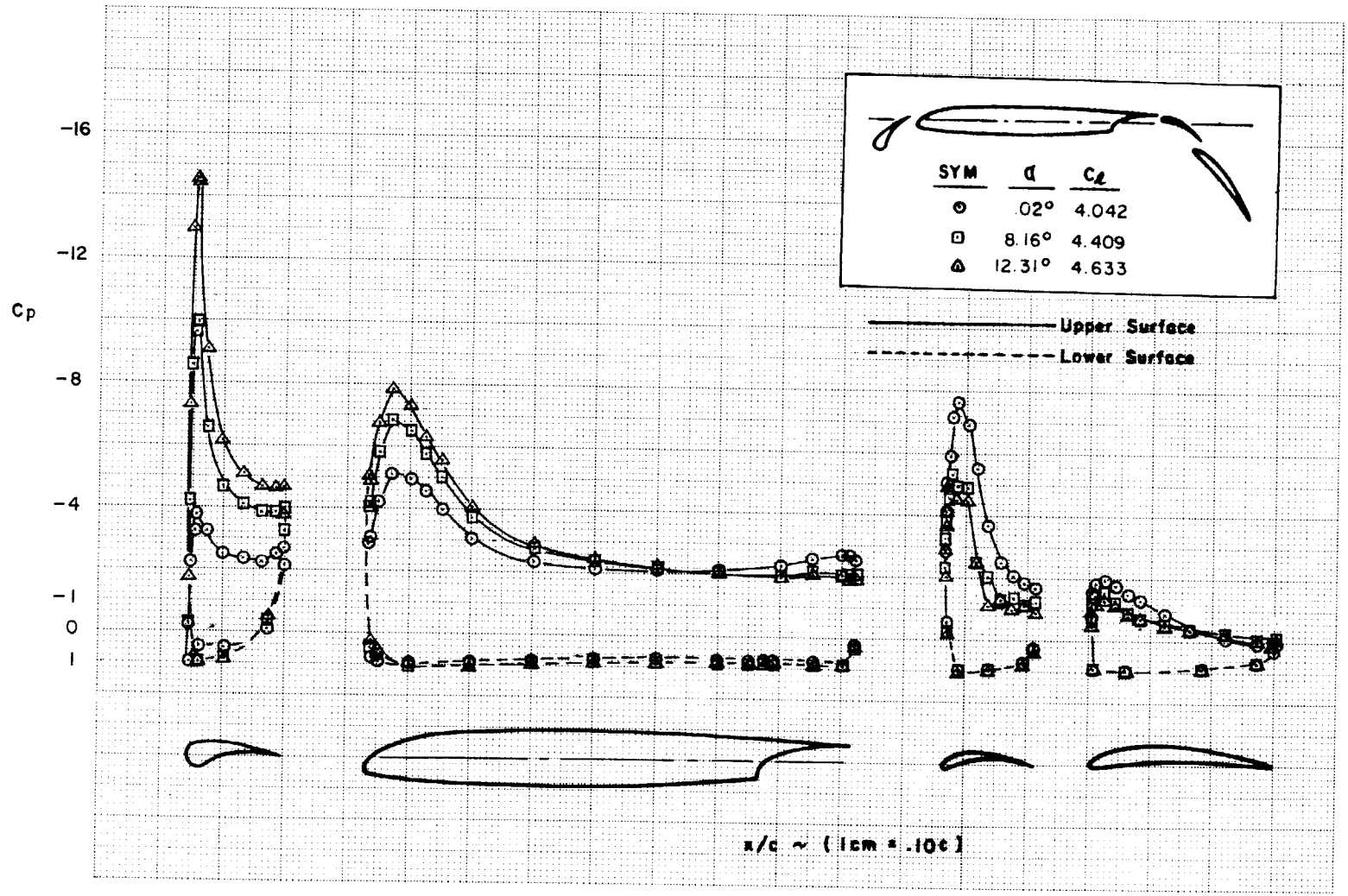

(c)

FIGURE C15.—Concluded

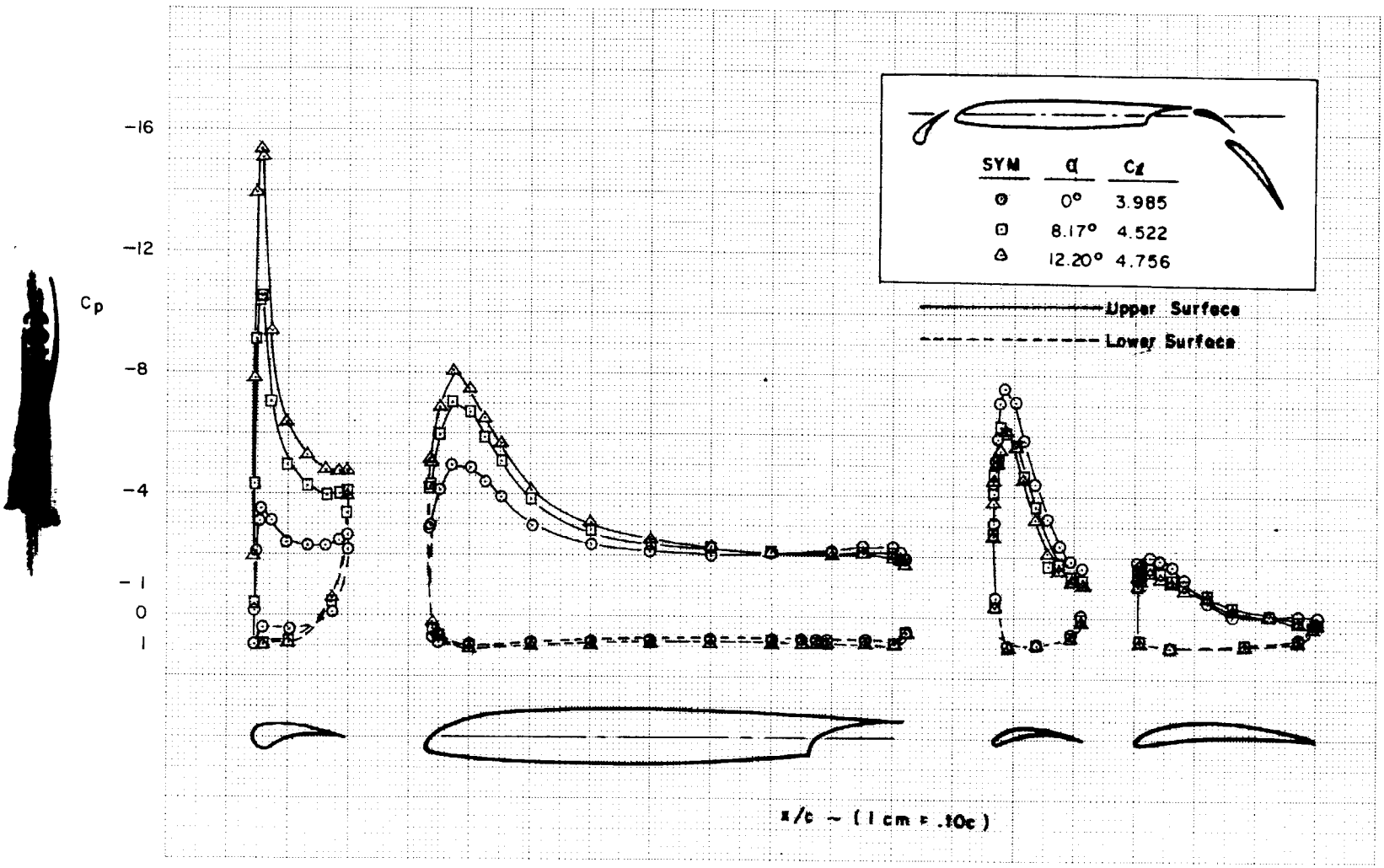

FIGURE C16.—EFFECT OF WING-VANE SLOT GAP AND OVERLAP—MODEL C ($\delta_{f_{eq}} = 49°$)

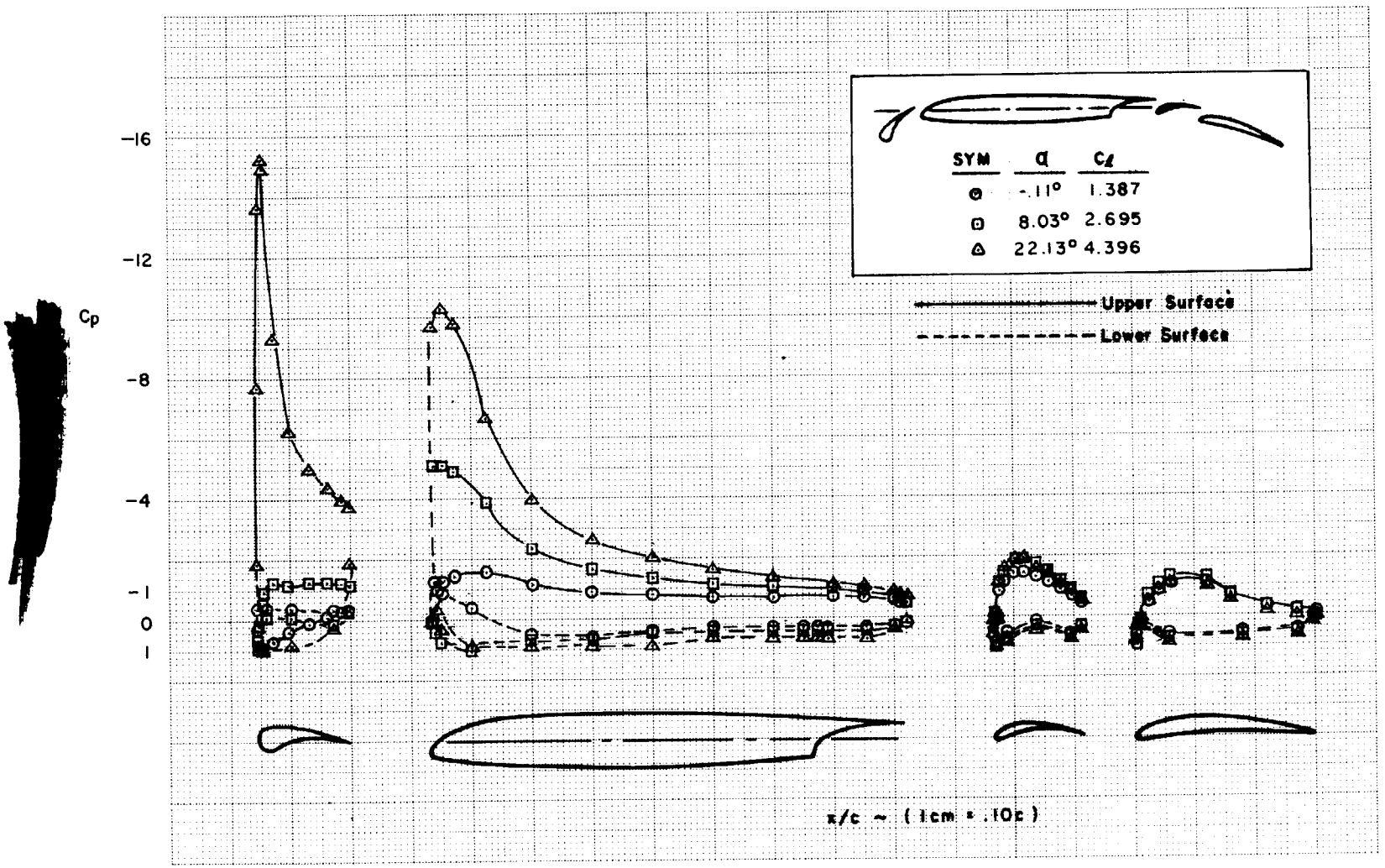

(a)

FIGURE C17.—FLAP DEFLECTION ANGLE STUDY—MODEL C ($\delta_{f_{eq}} = 15°$)

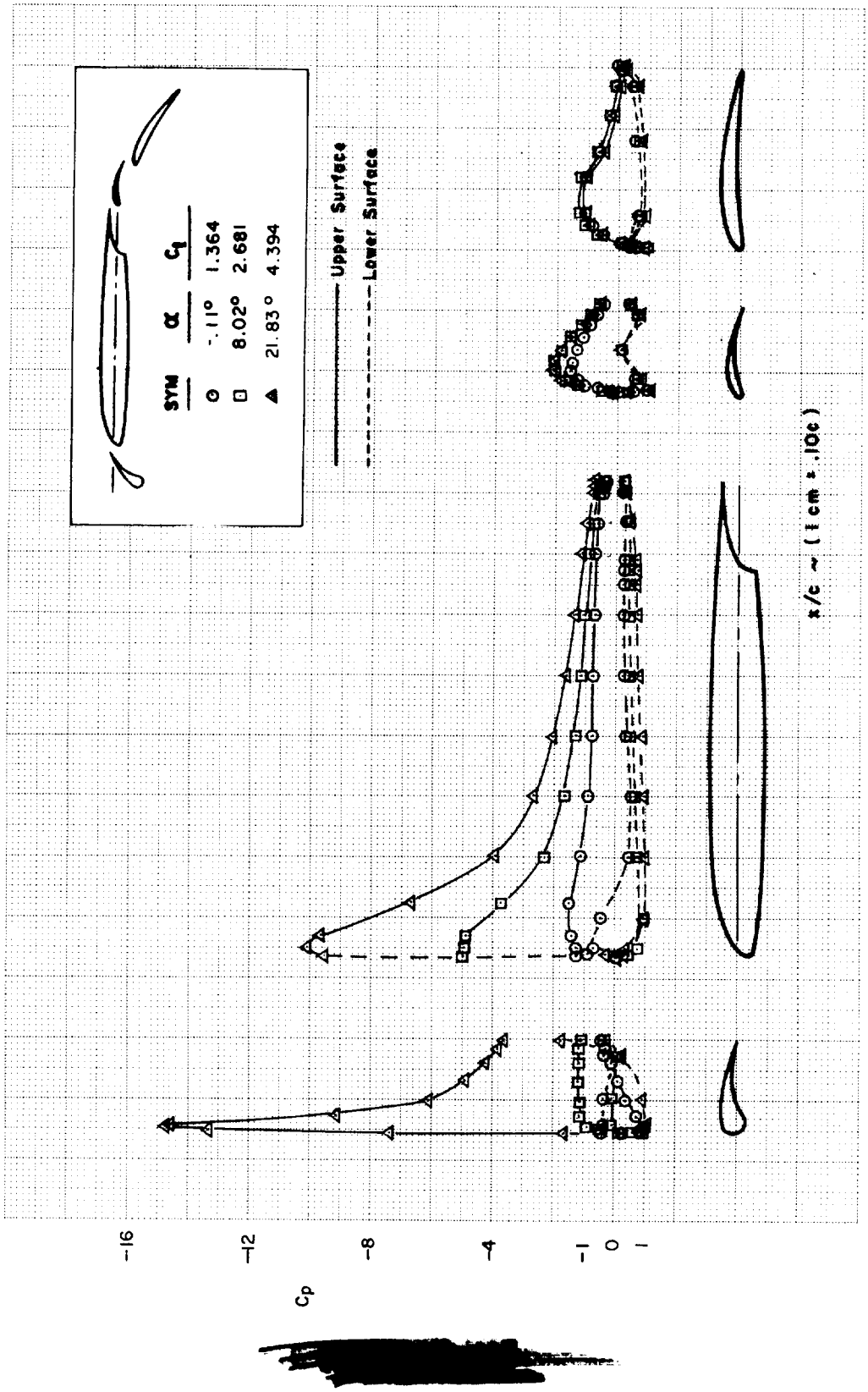

(b)

FIGURE C17.—Continued

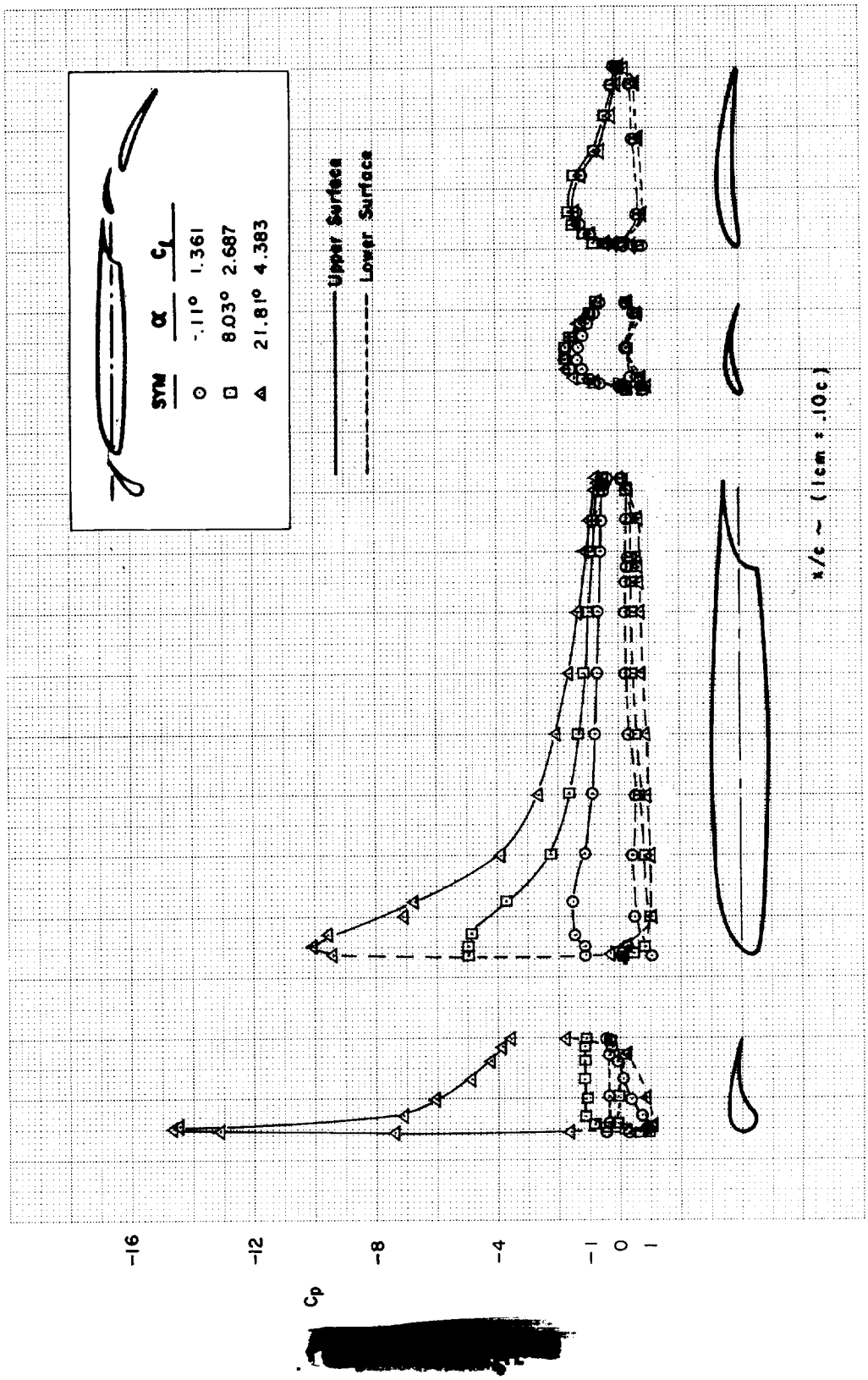

(c)

FIGURE C17.—Concluded

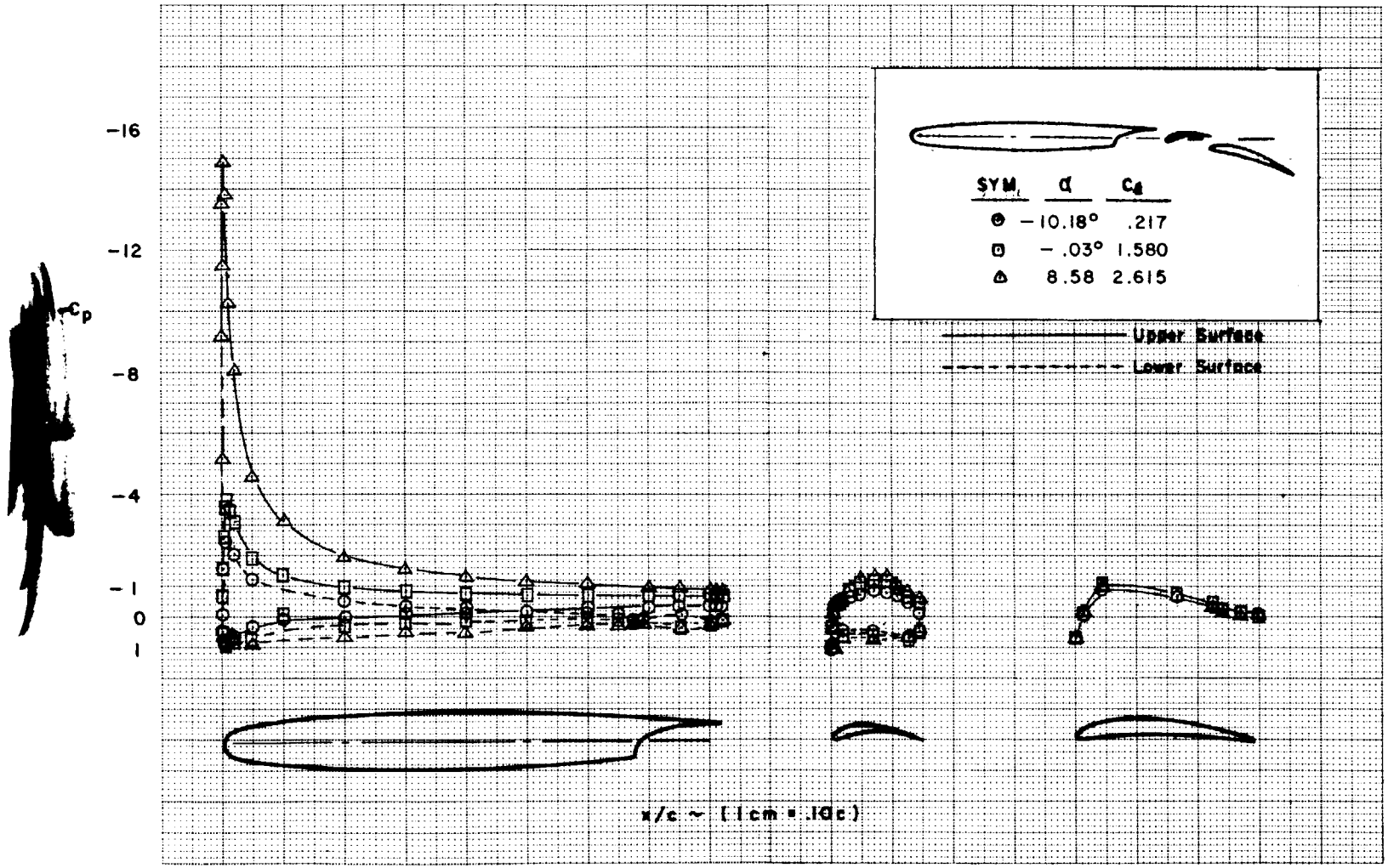

FIGURE C18.–EFFECT OF FLAP WITHOUT LEADING-EDGE DEVICE–MODEL C ($\delta_{f_{eq}} = 13°$)

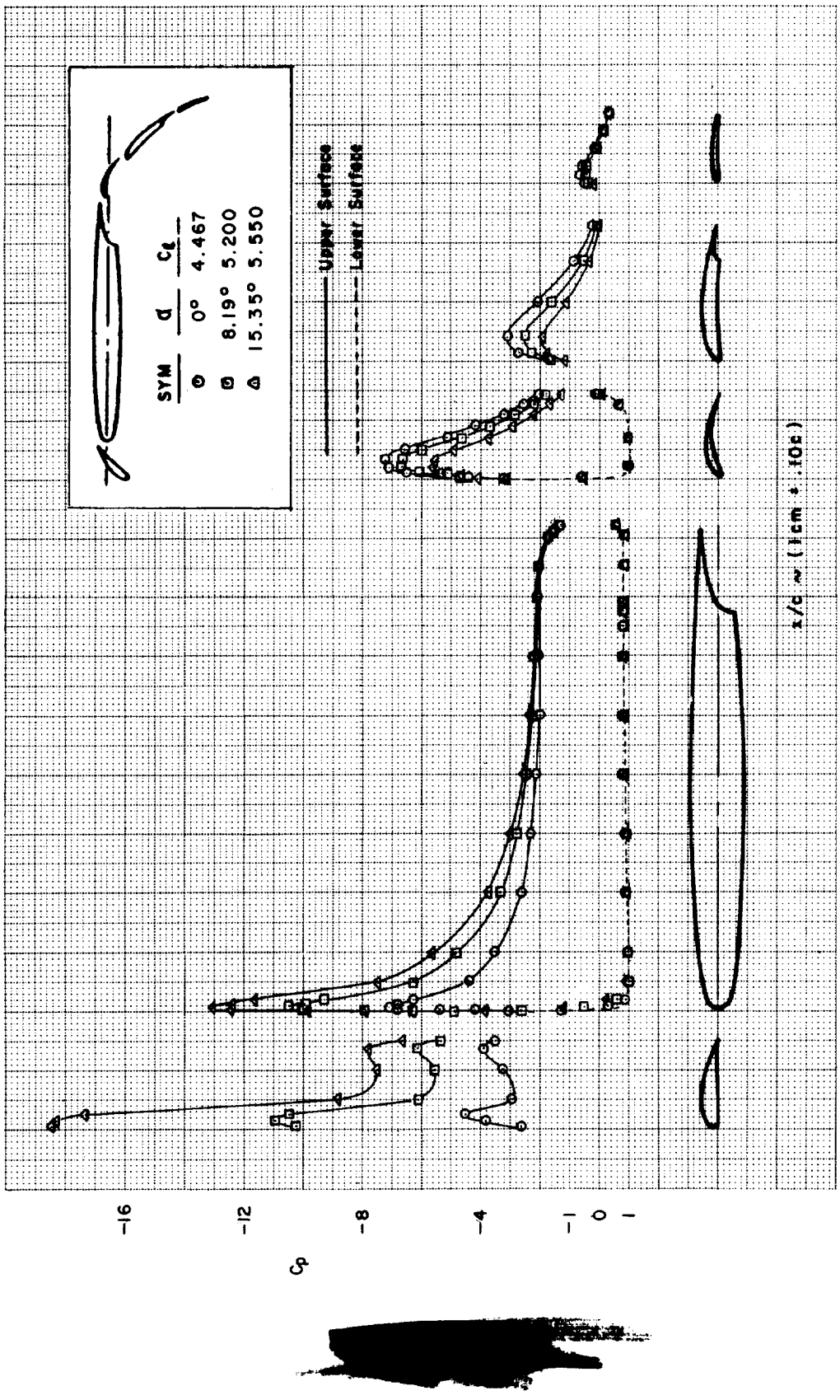

FIGURE C19.–OPTIMIZED CONFIGURATION–MODEL D ($\delta_{f_{eq}} = 46°$)

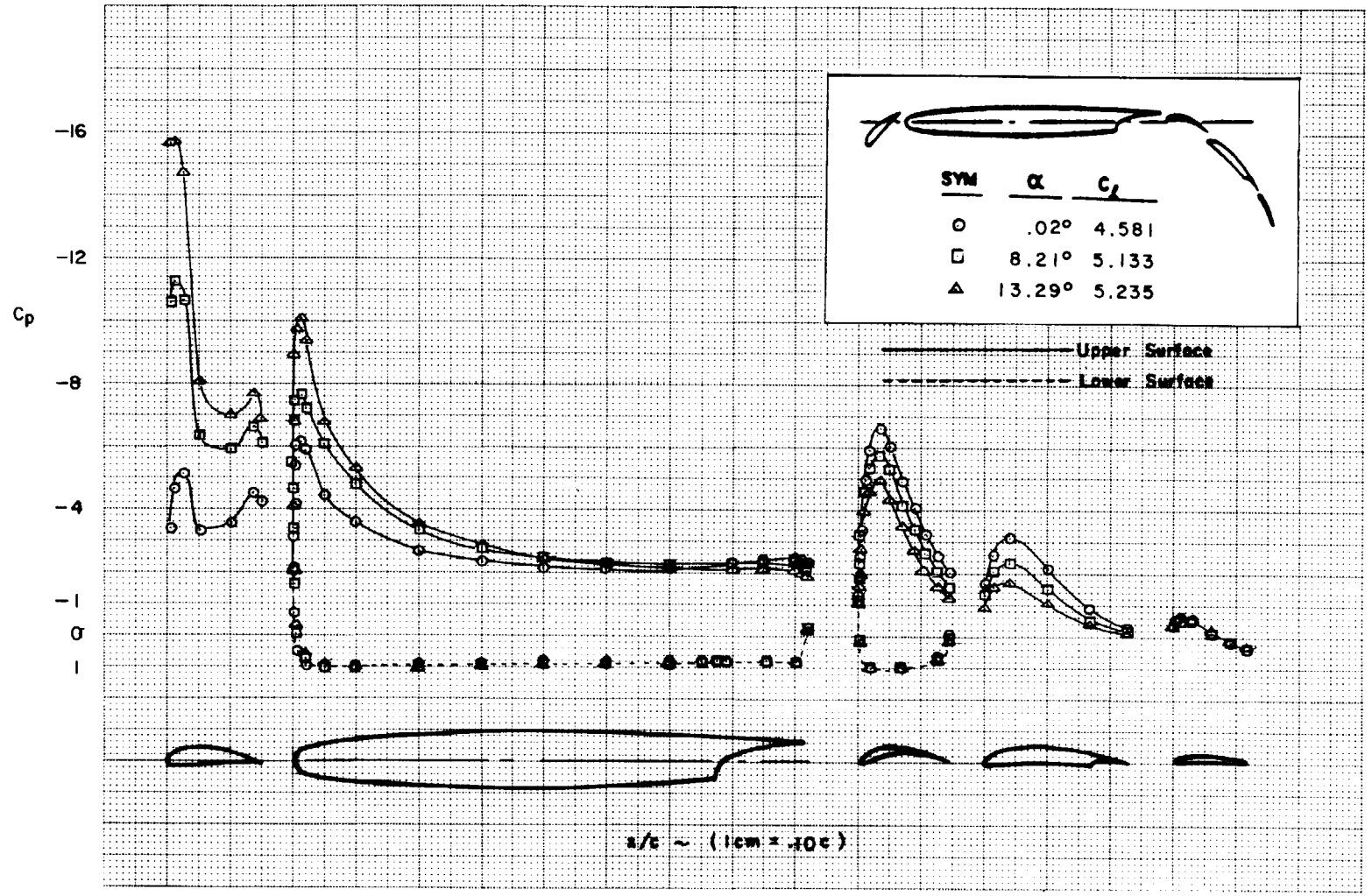

(a)

FIGURE C20.–EFFECT OF SLAT 2 DEFLECTION ANGLE VARIATION–MODEL D ($\delta_{f_{eq}} = 46°$)

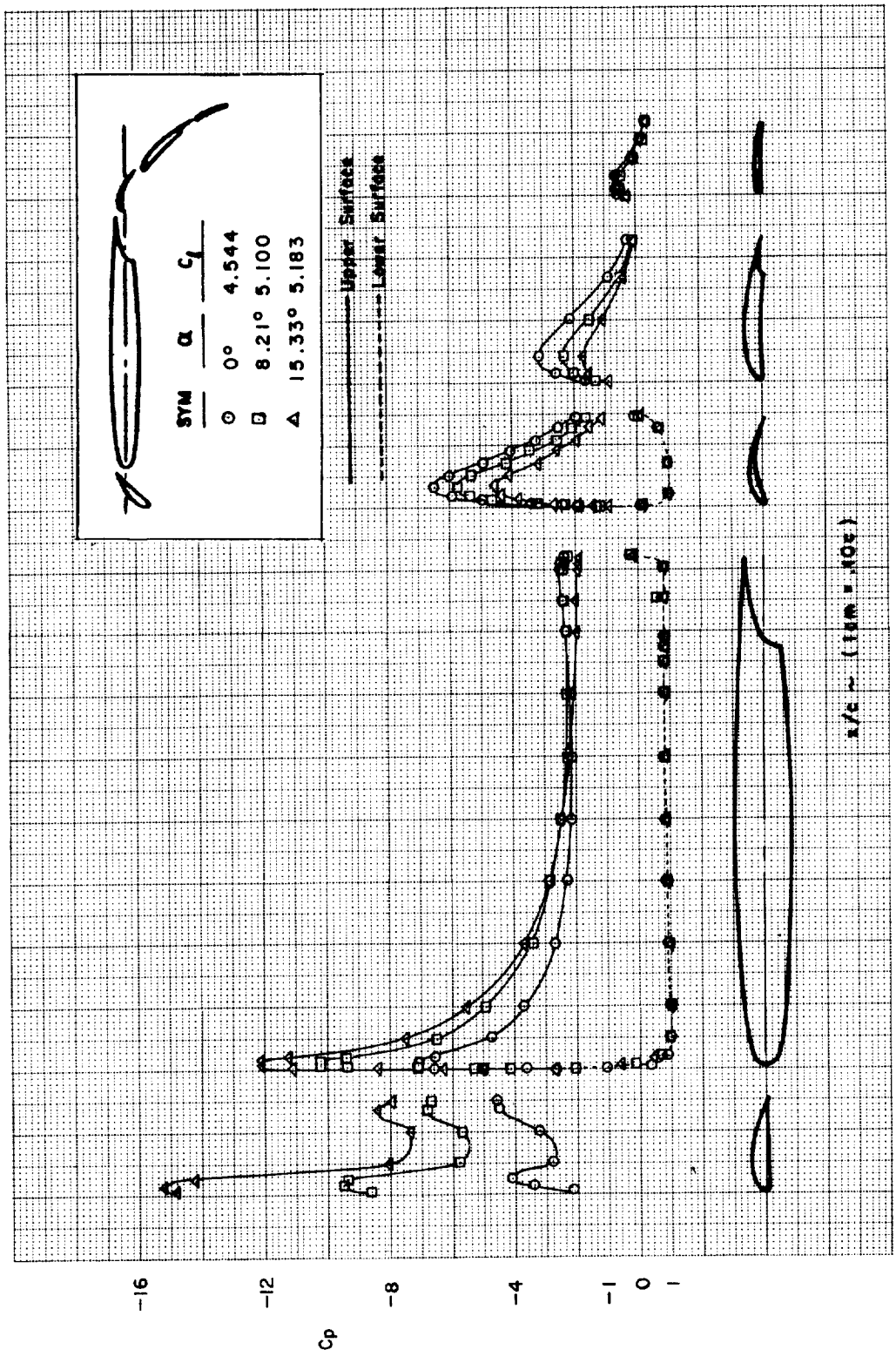

(b)

FIGURE C20.—Continued

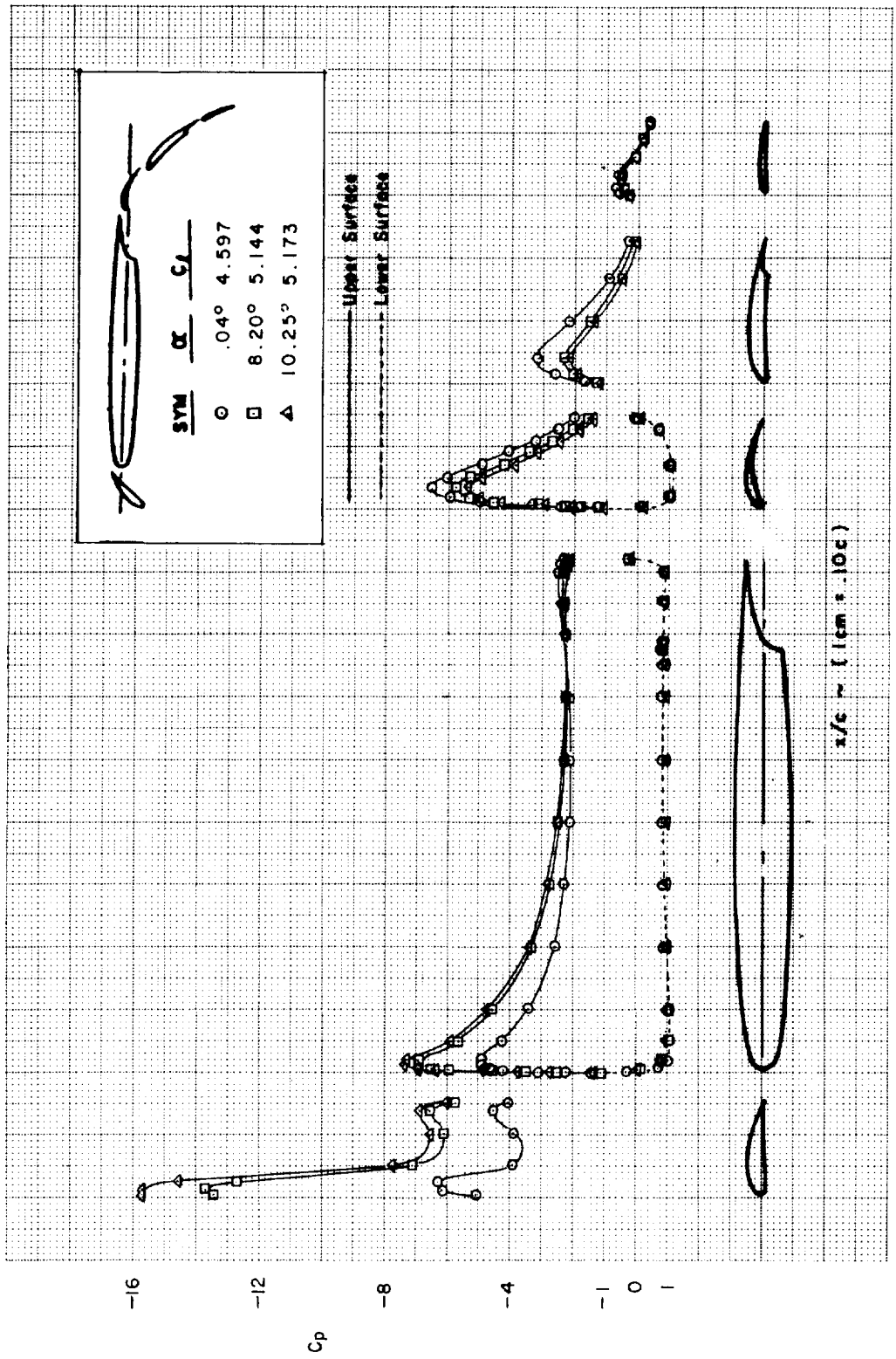

(c)

FIGURE C20.—Continued

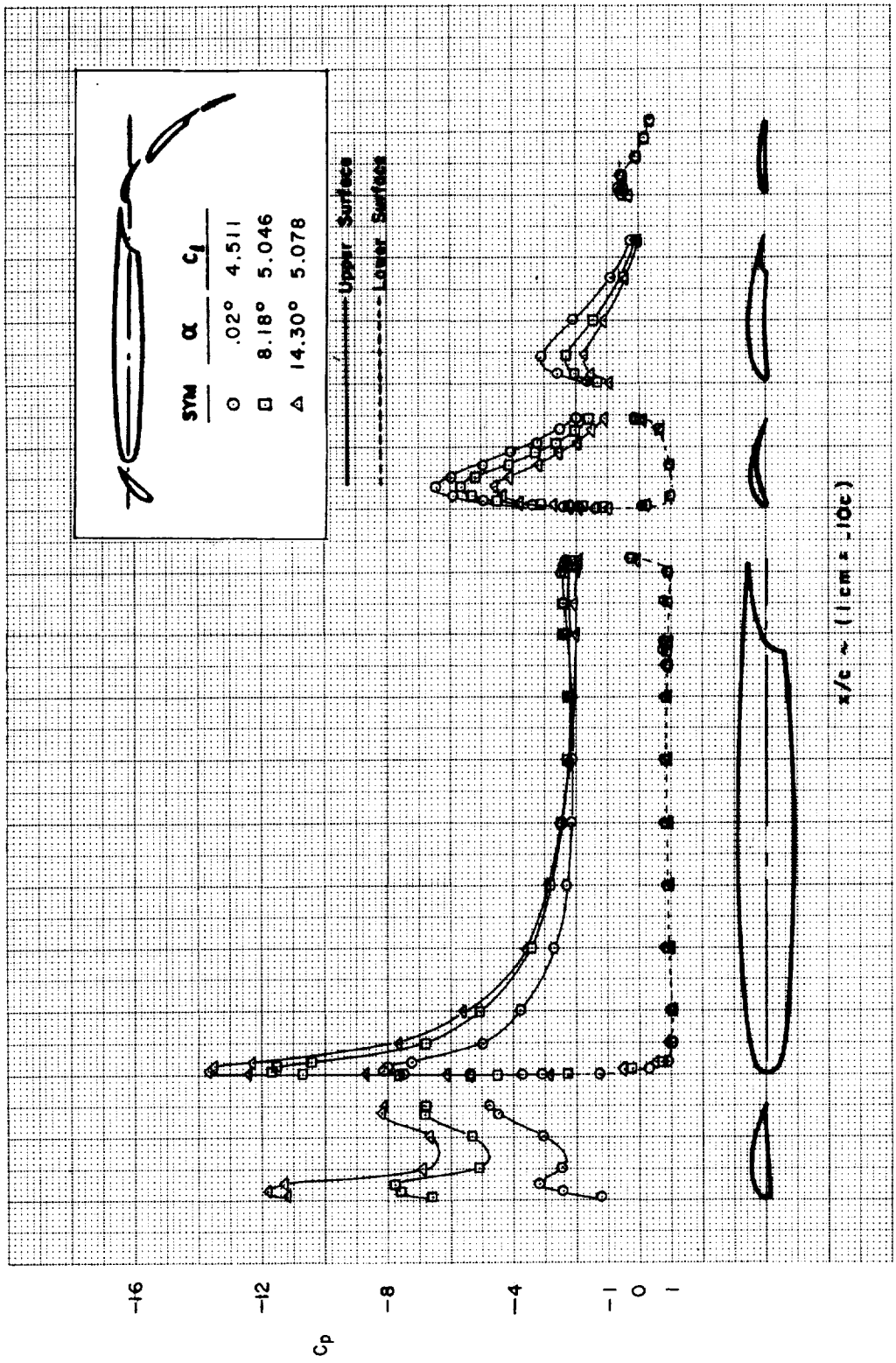

(d)

FIGURE C20.—Concluded

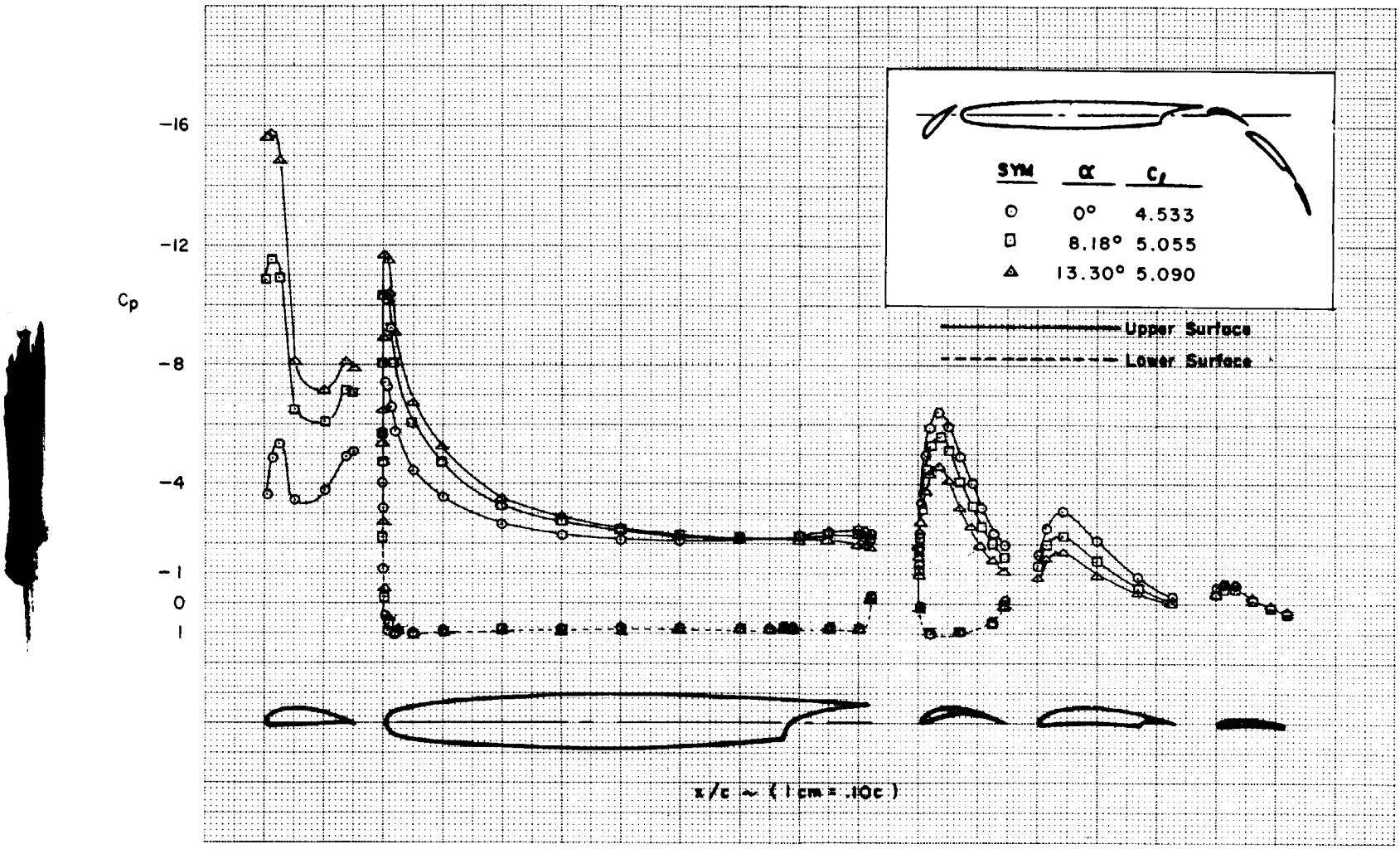

(a)

FIGURE C21.–SLAT 2 SLOT GAP AND HEIGHT OPTIMIZATION–MODEL D ($\delta_{f_{eq}} = 46°$)

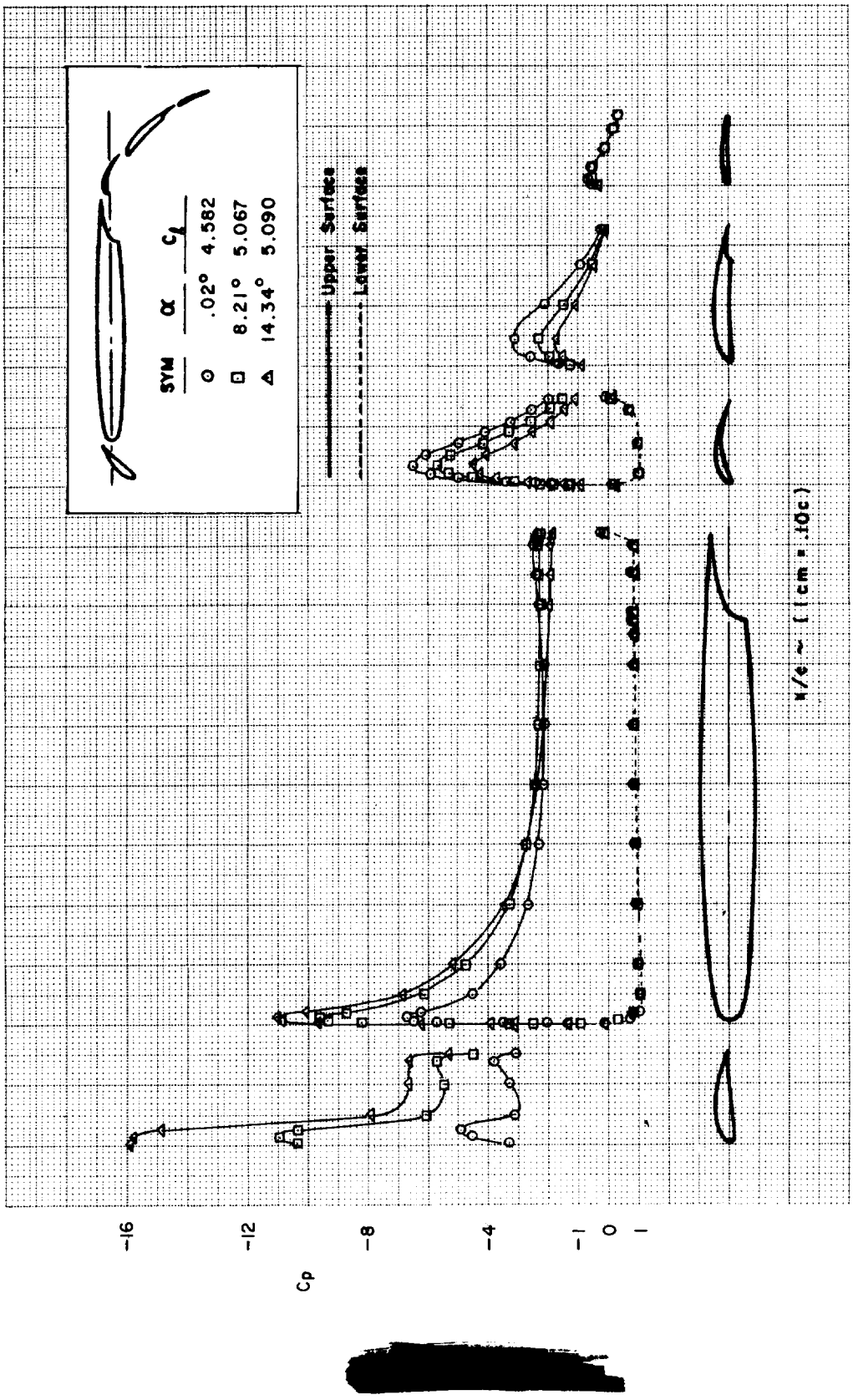

(b)

FIGURE C21.—Continued

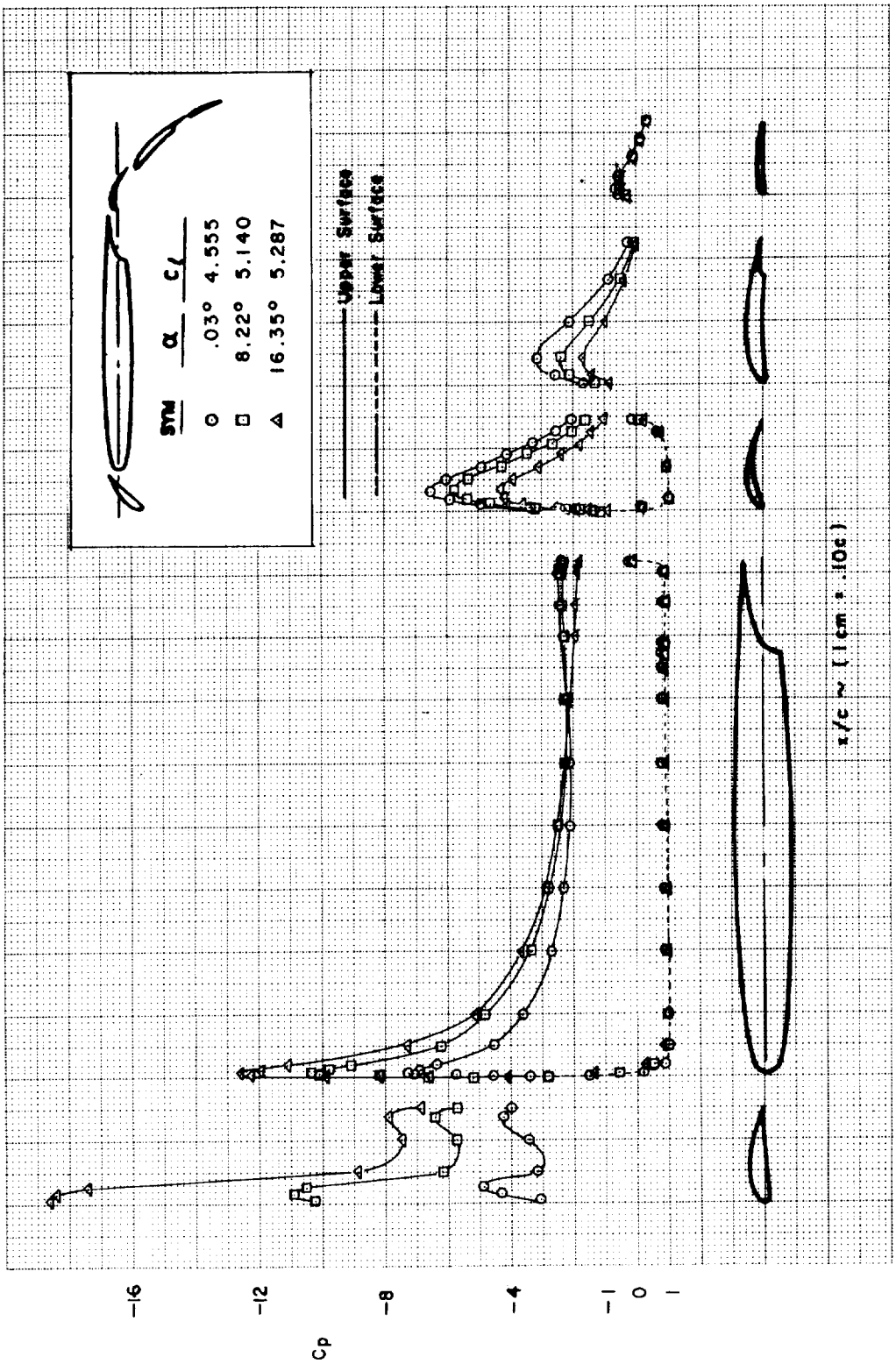

(c)

FIGURE C21.—Continued

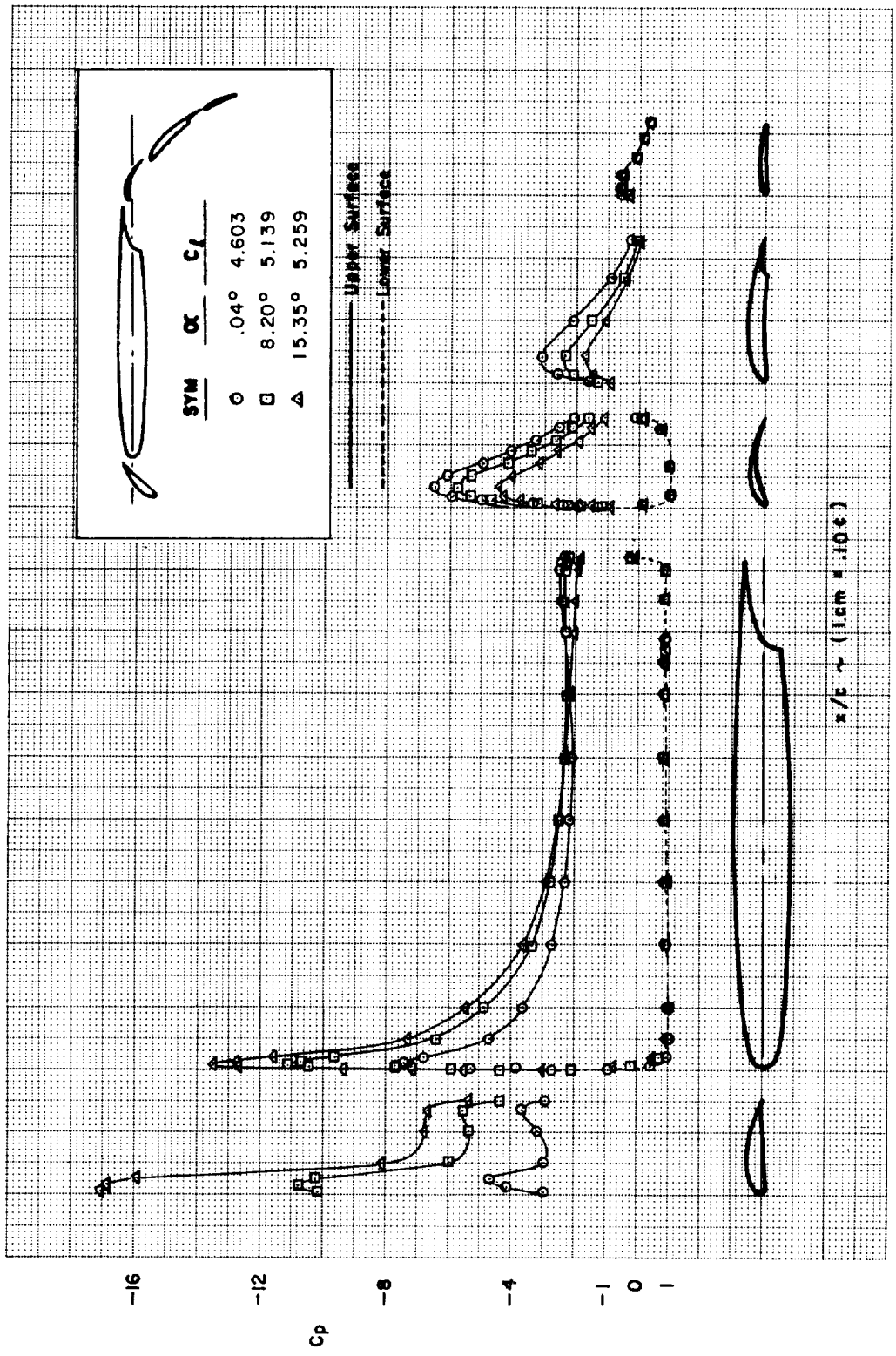

(d)

FIGURE C21.—Continued

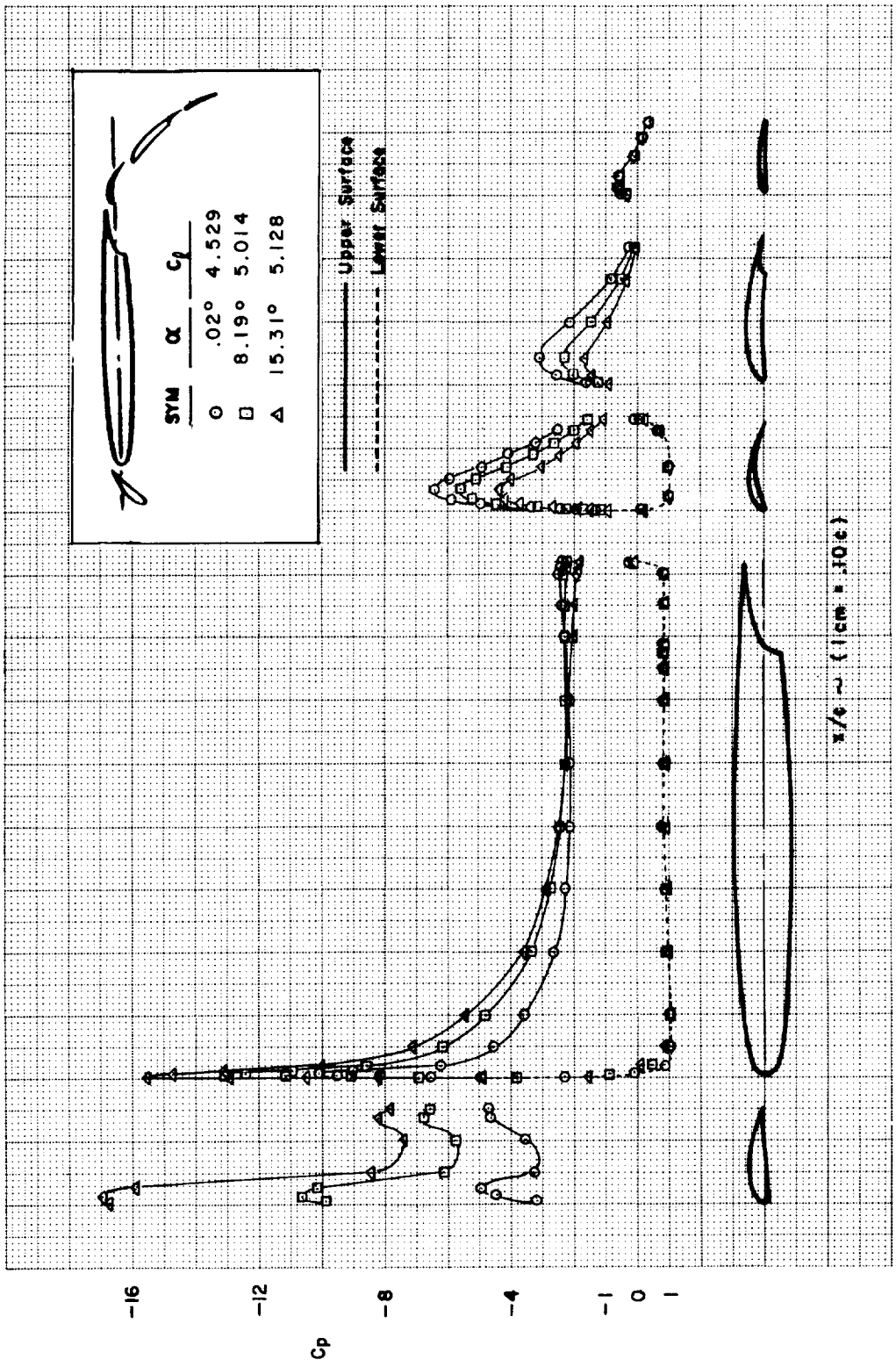

(e)

FIGURE C21.—Continued

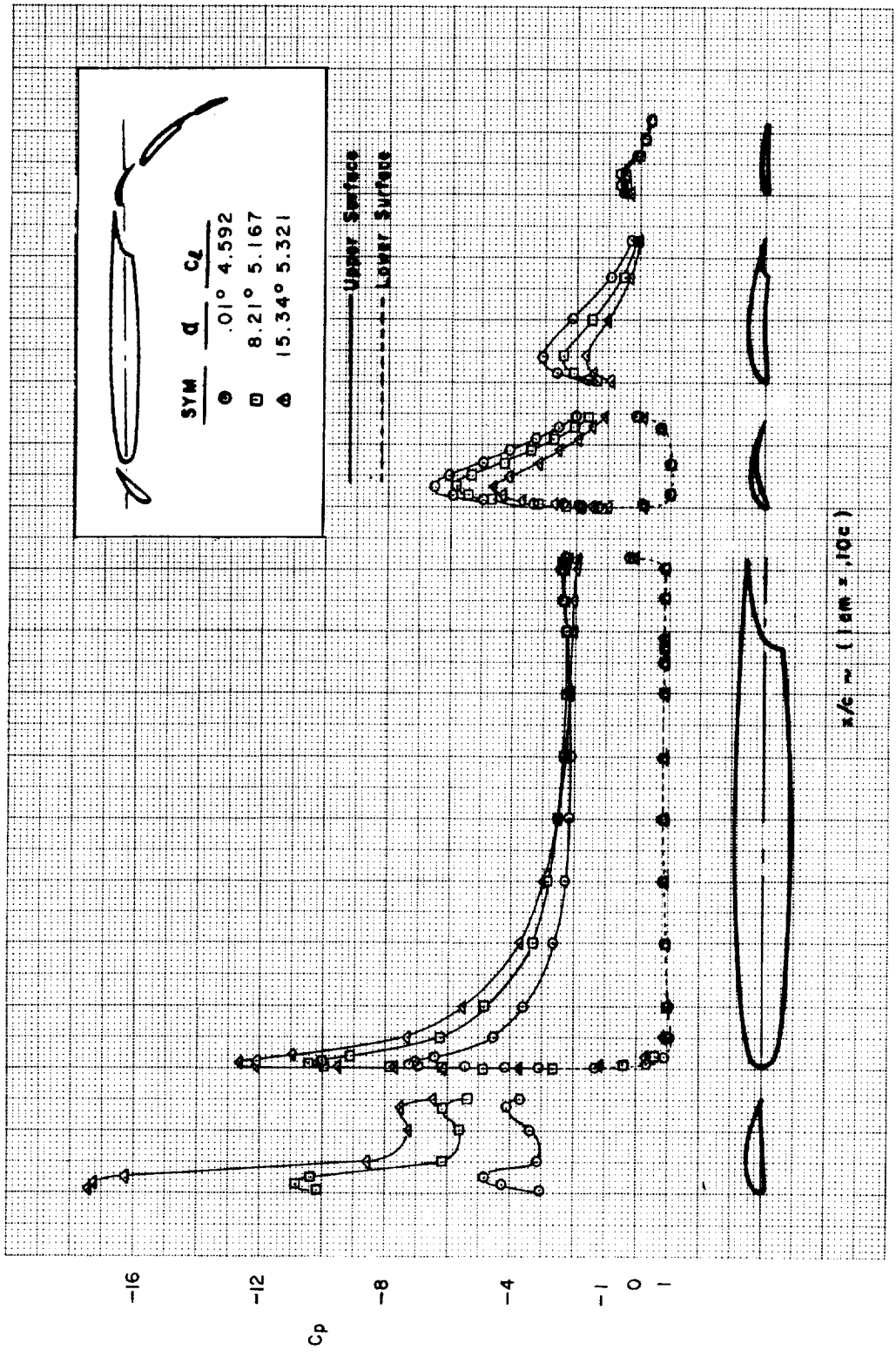

(f)

FIGURE C21.—Continued

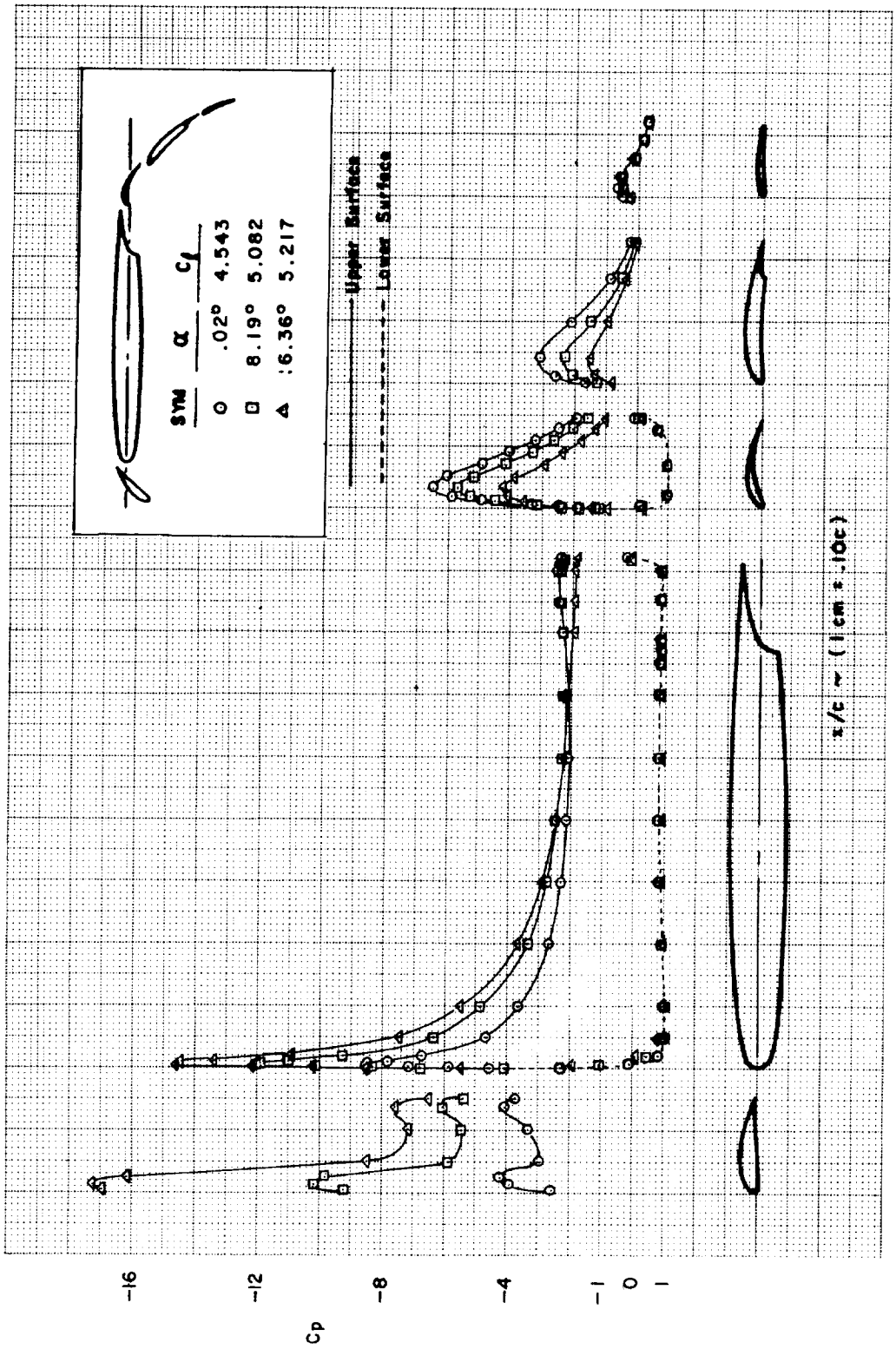

(g)

FIGURE C21.–Continued

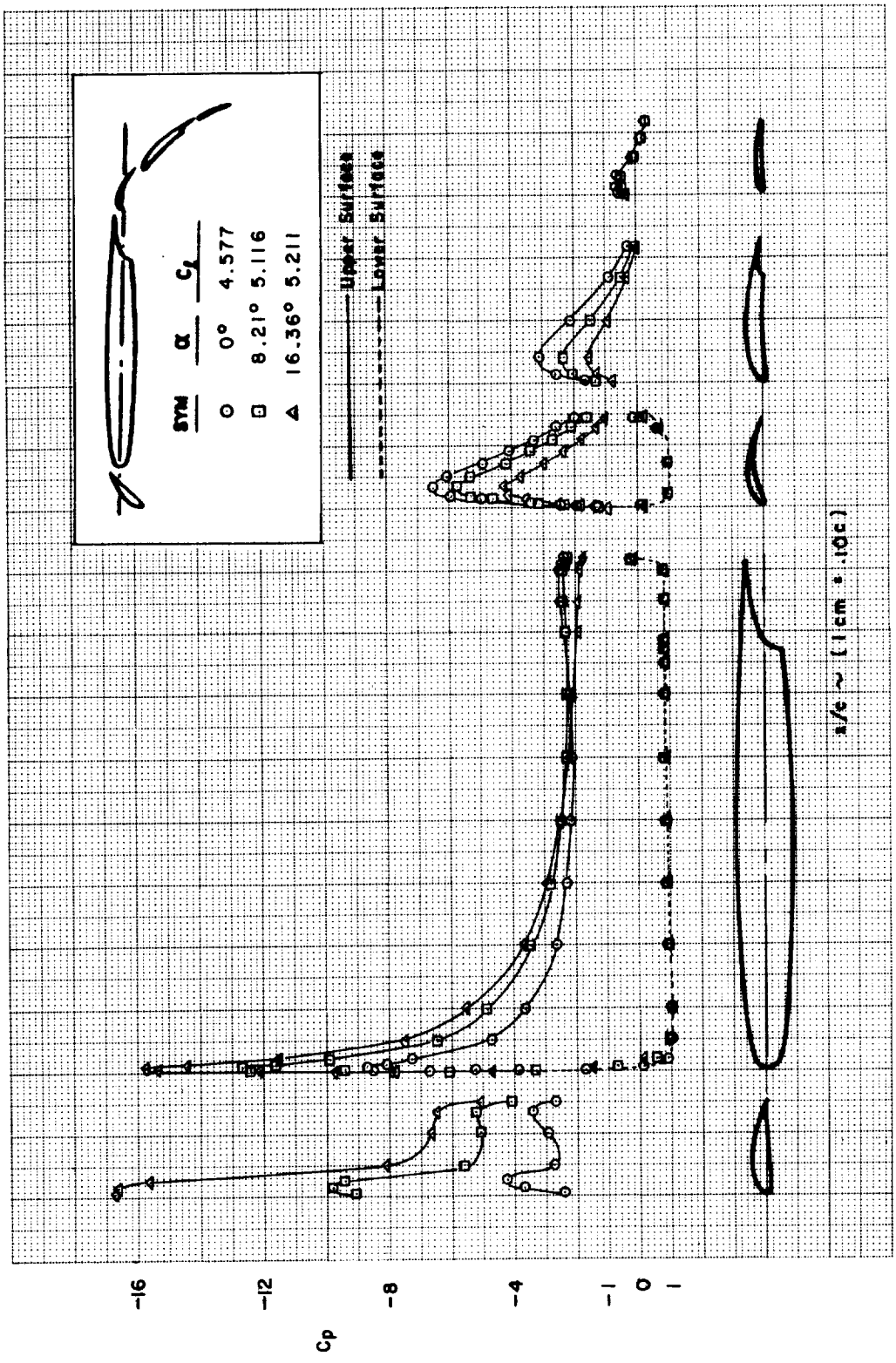

(h)

FIGURE C21.–Concluded

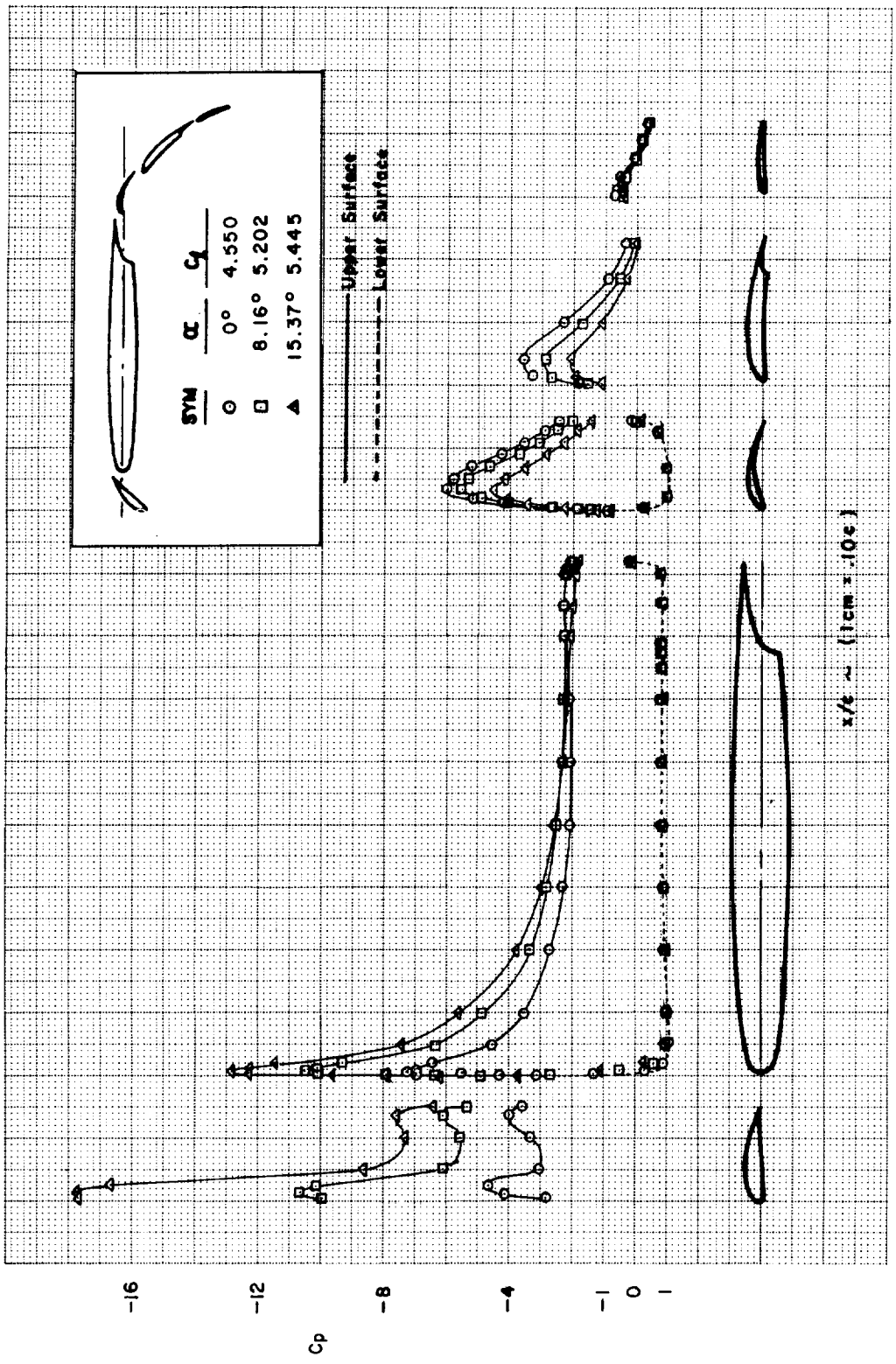

(a)

FIGURE C22.–EFFECT OF FLAP COMPONENT ANGLE COMBINATION AT CONSTANT $\delta_{f_{eq}}$ (46°)–MODEL D

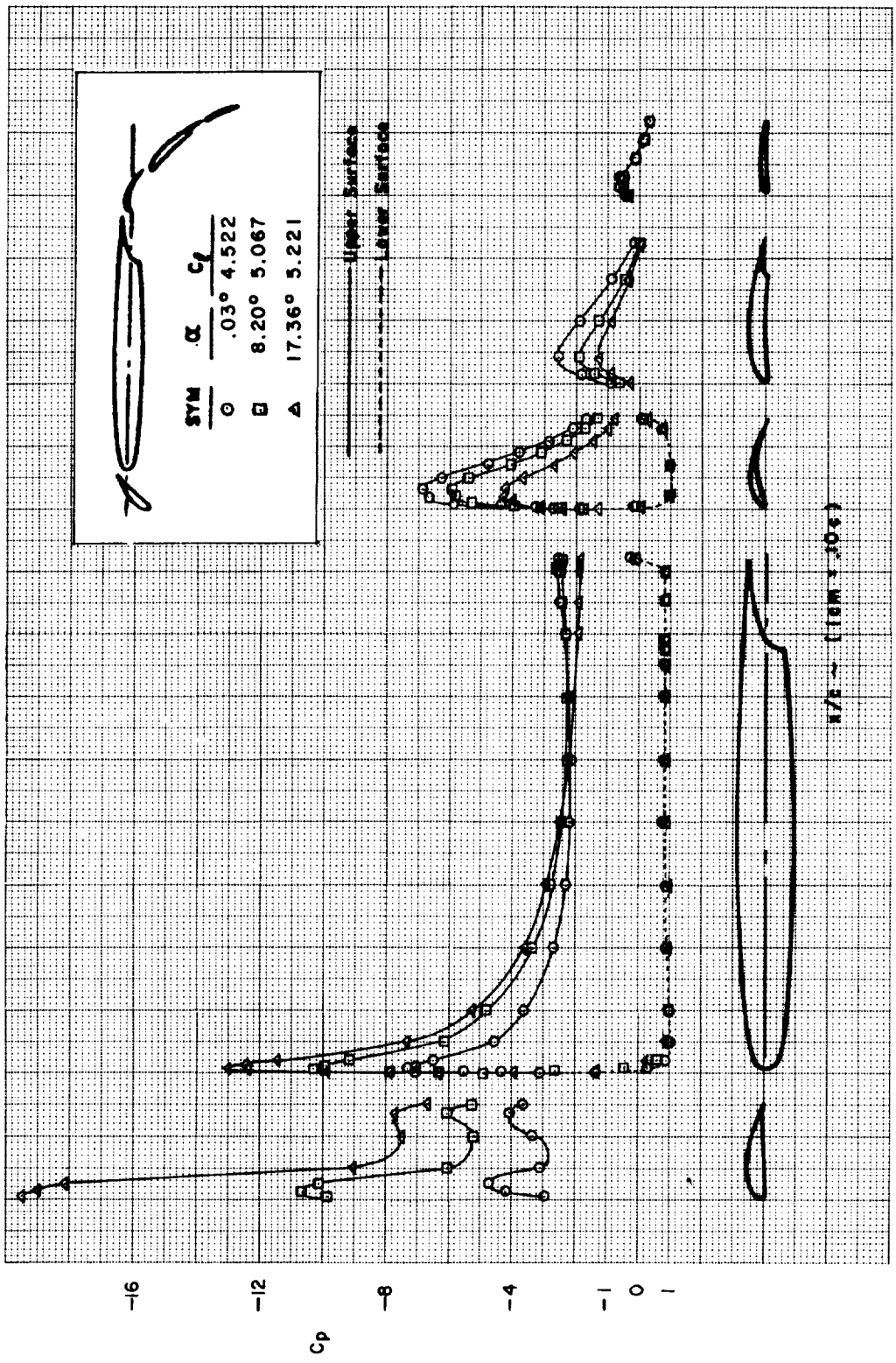

(b)

FIGURE C22.—Continued

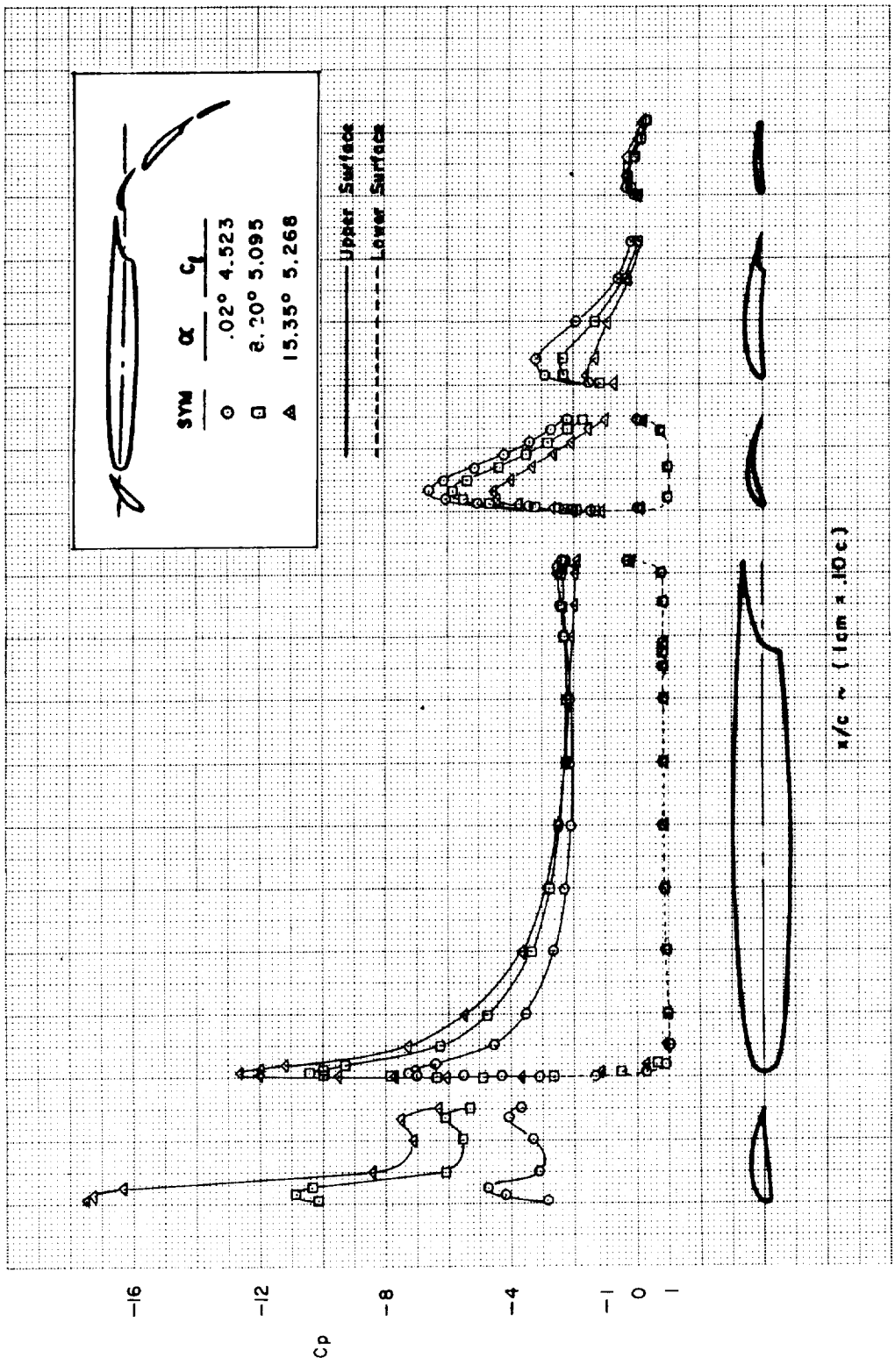

(c)

FIGURE C22.—Continued

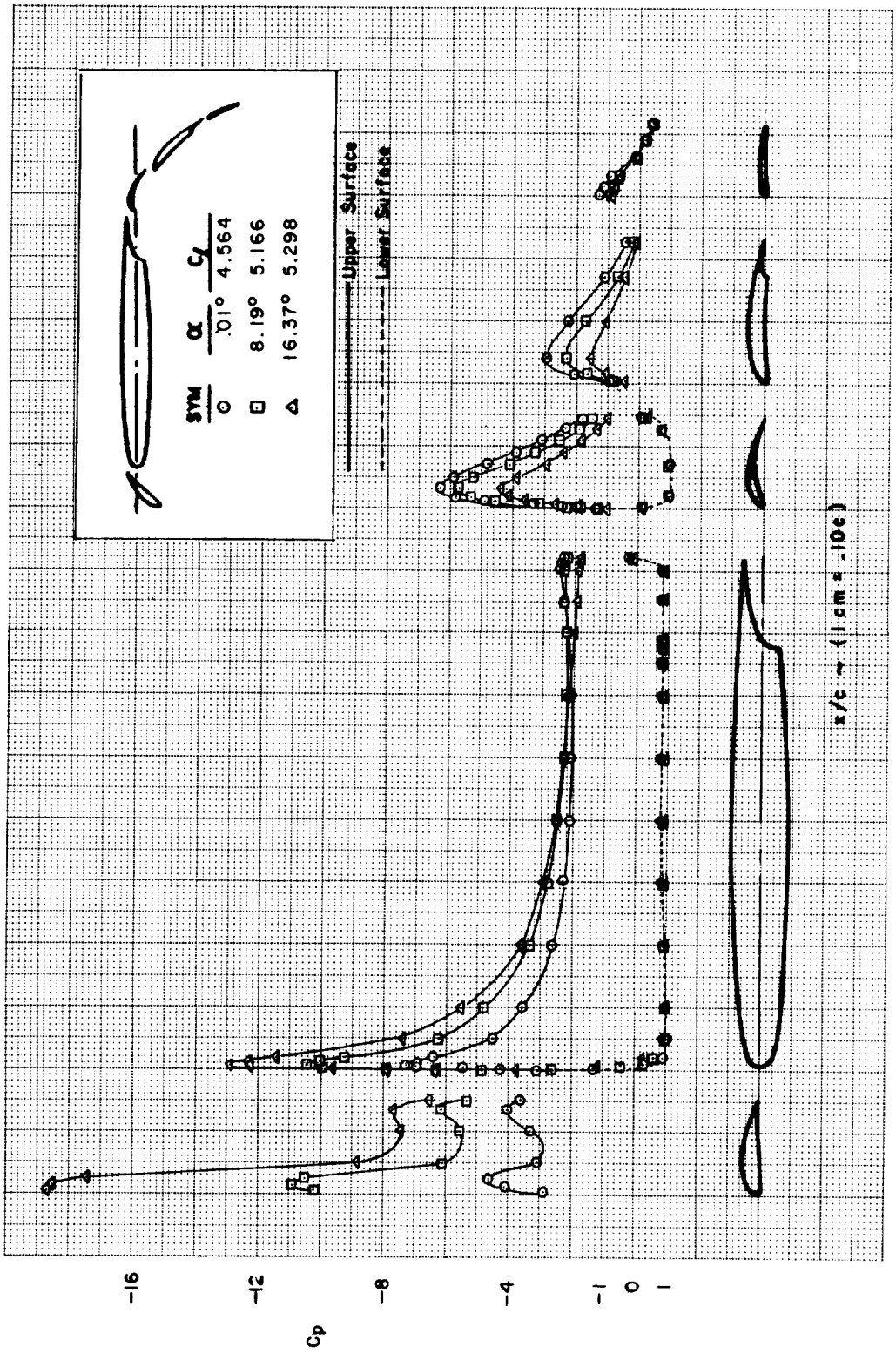

(d)

FIGURE C22.–Concluded

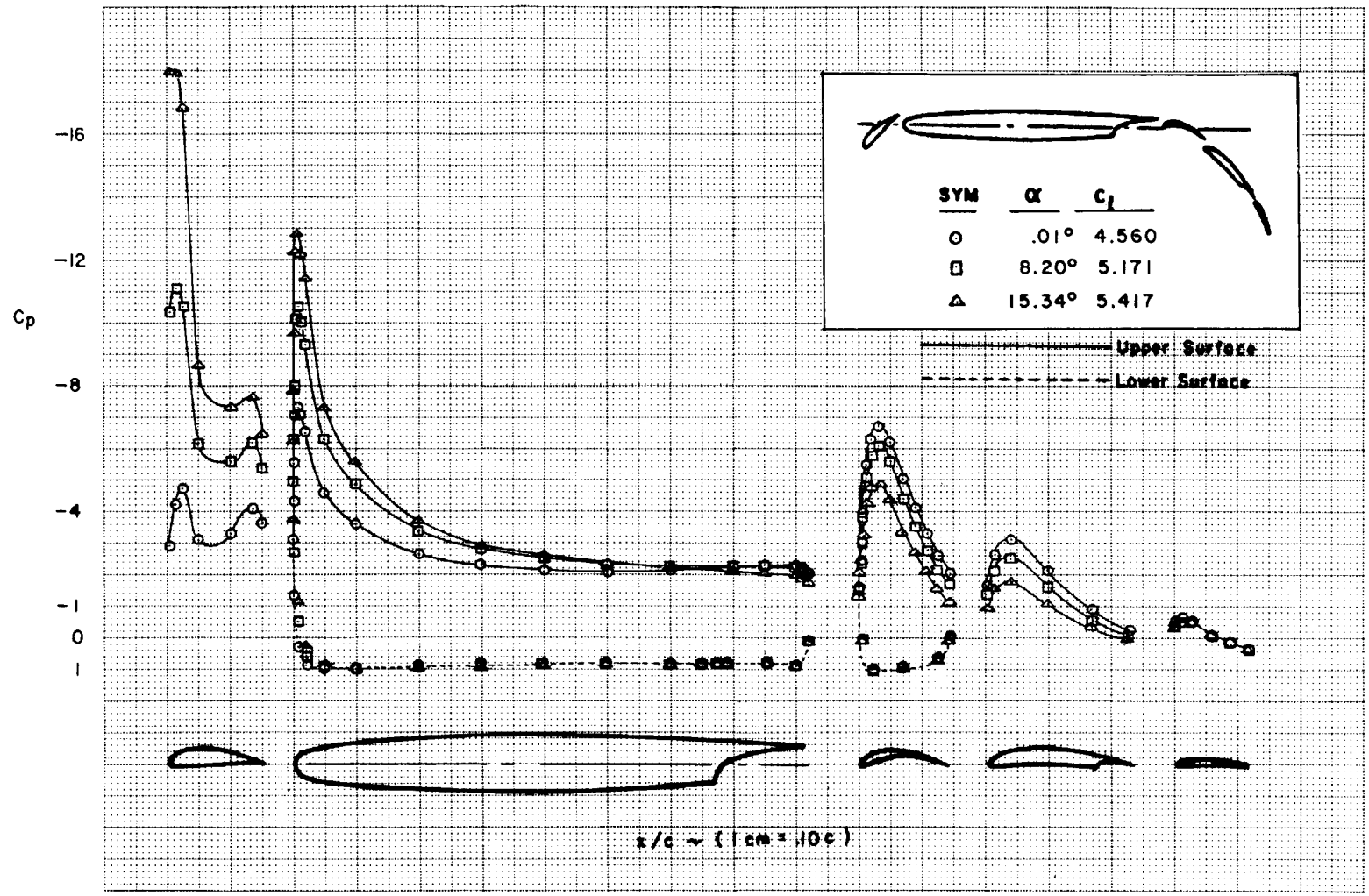

(a)

FIGURE C23.–EFFECT OF WING-VANE SLOT GAP AND OVERLAP–MODEL D ($\delta_{f_{eq}} = 46°$)

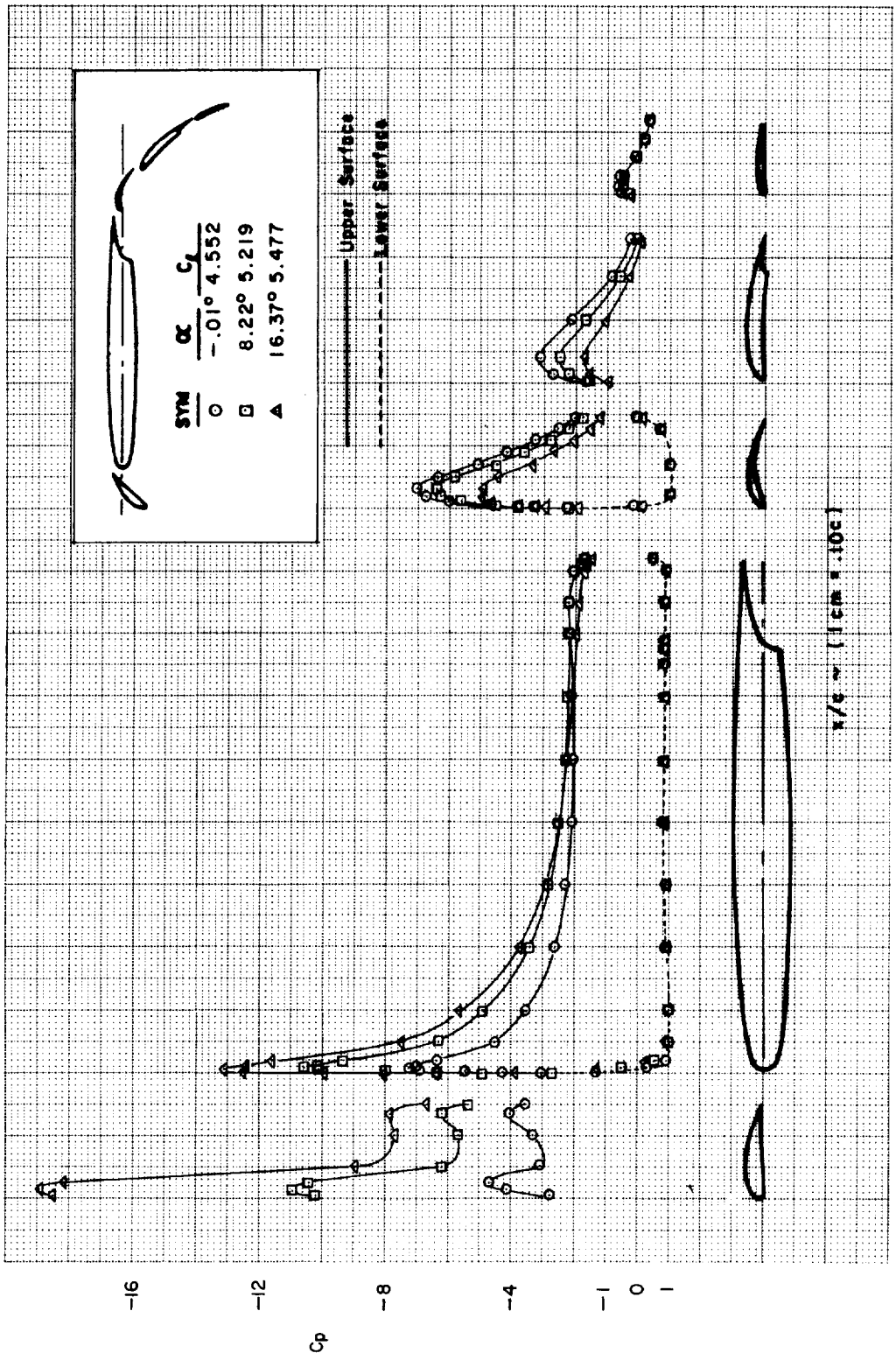

(b)

FIGURE C23.—Continued

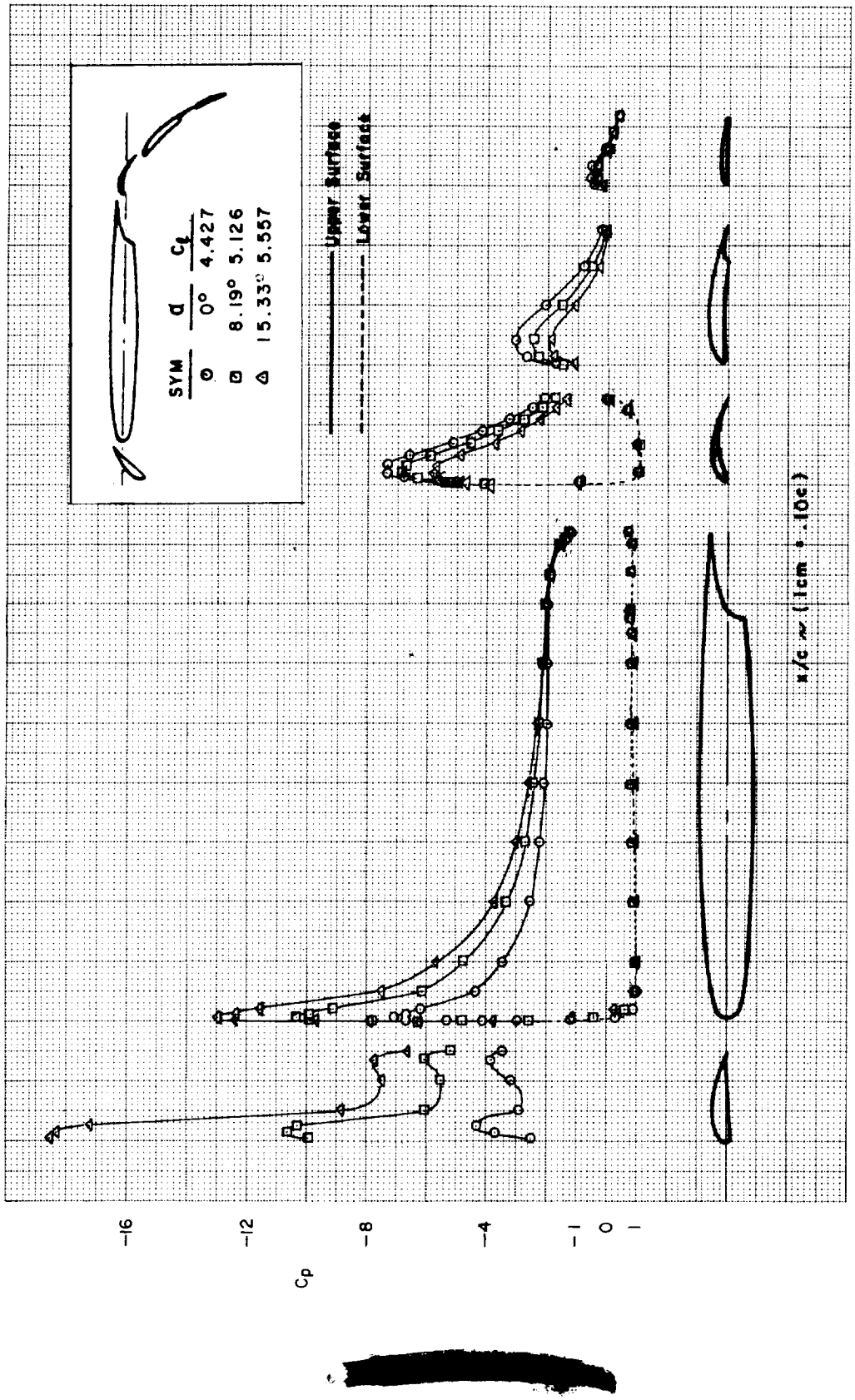

(c)

FIGURE C23.–Concluded

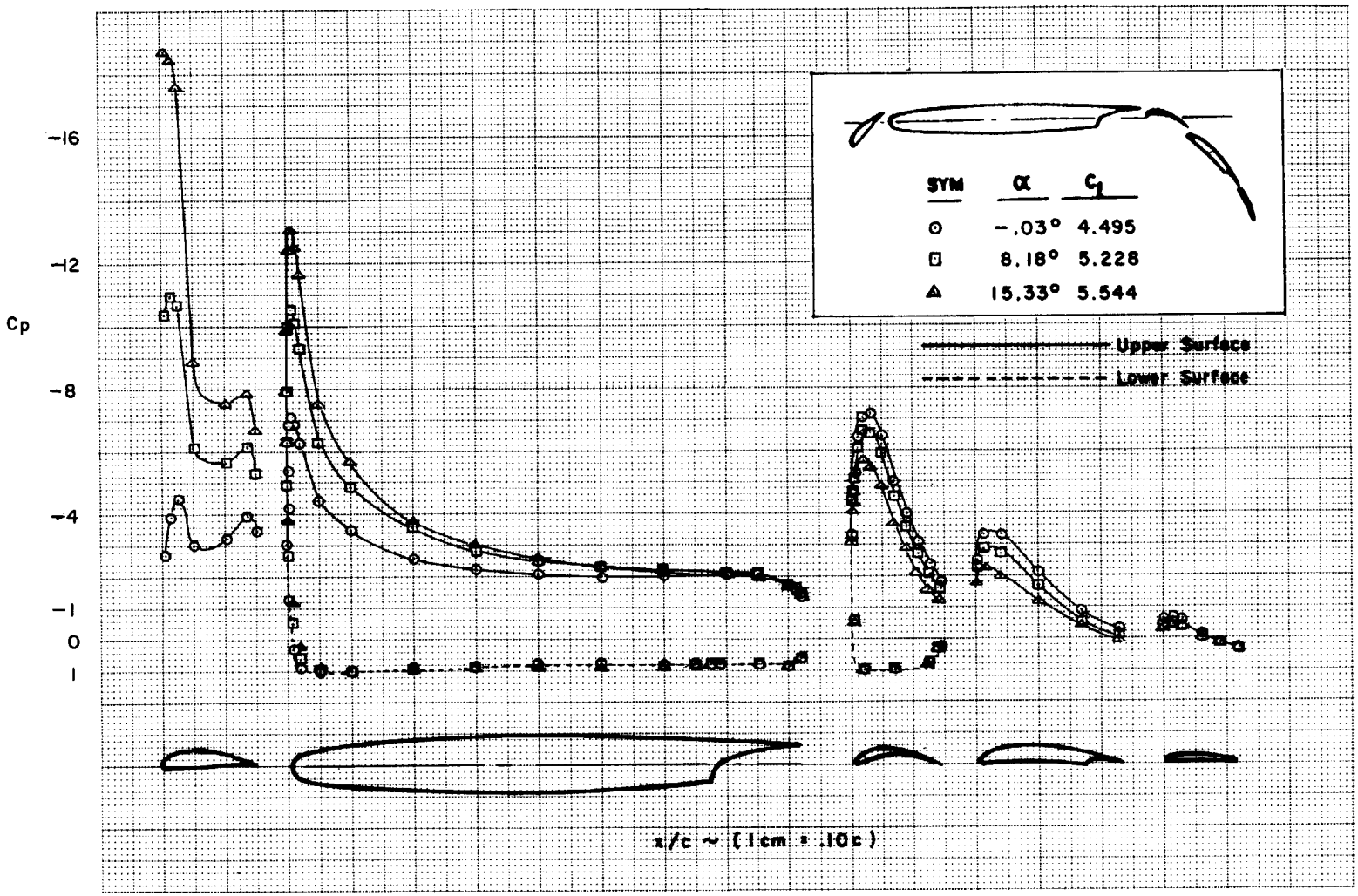

(a)

FIGURE C24.–EFFECT OF VANE-MAIN FLAP SLOT GAP AND OVERLAP–MODEL D ($\delta_{f_{eq}} = 46°$)

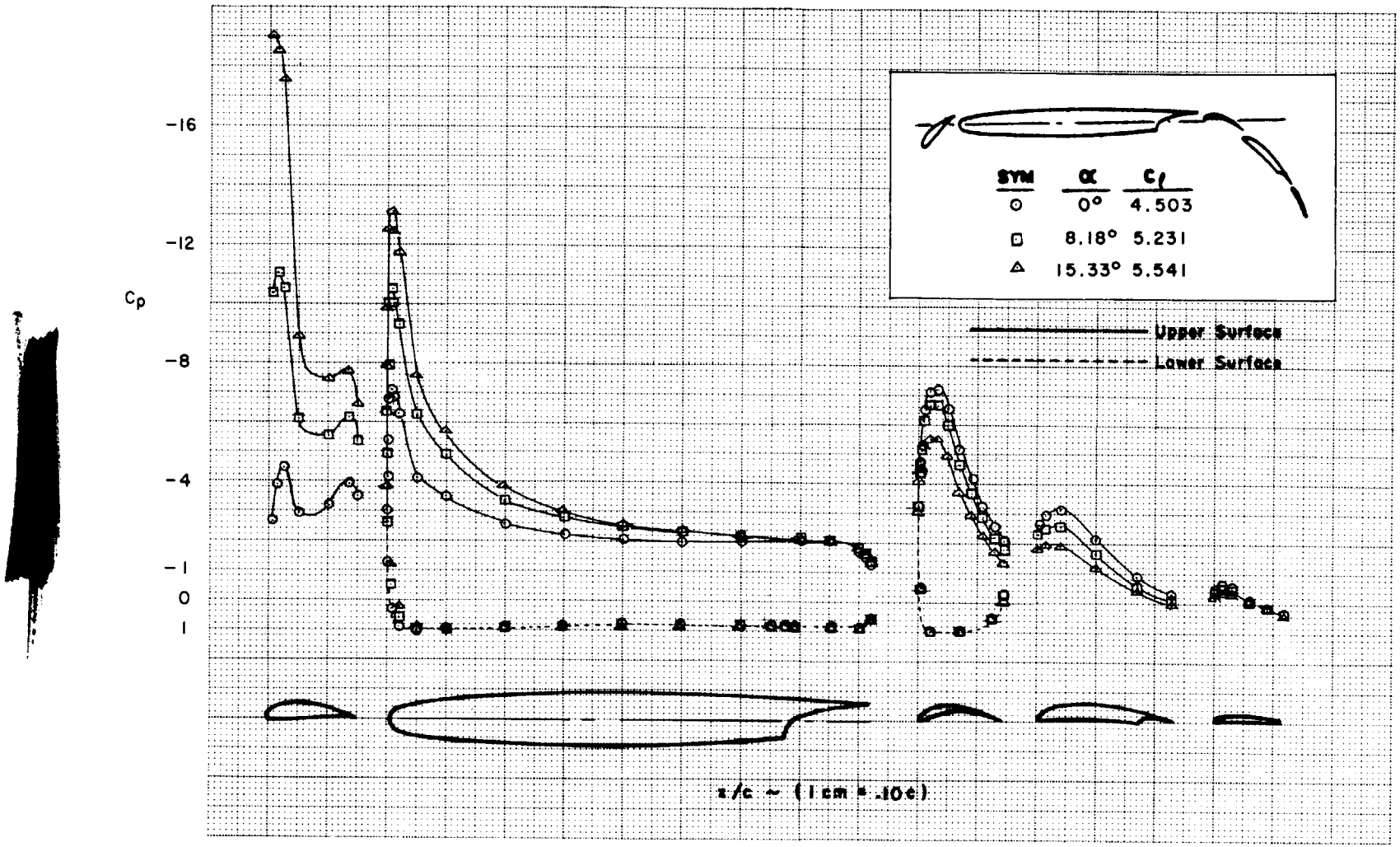

(b)

FIGURE C24.—Concluded

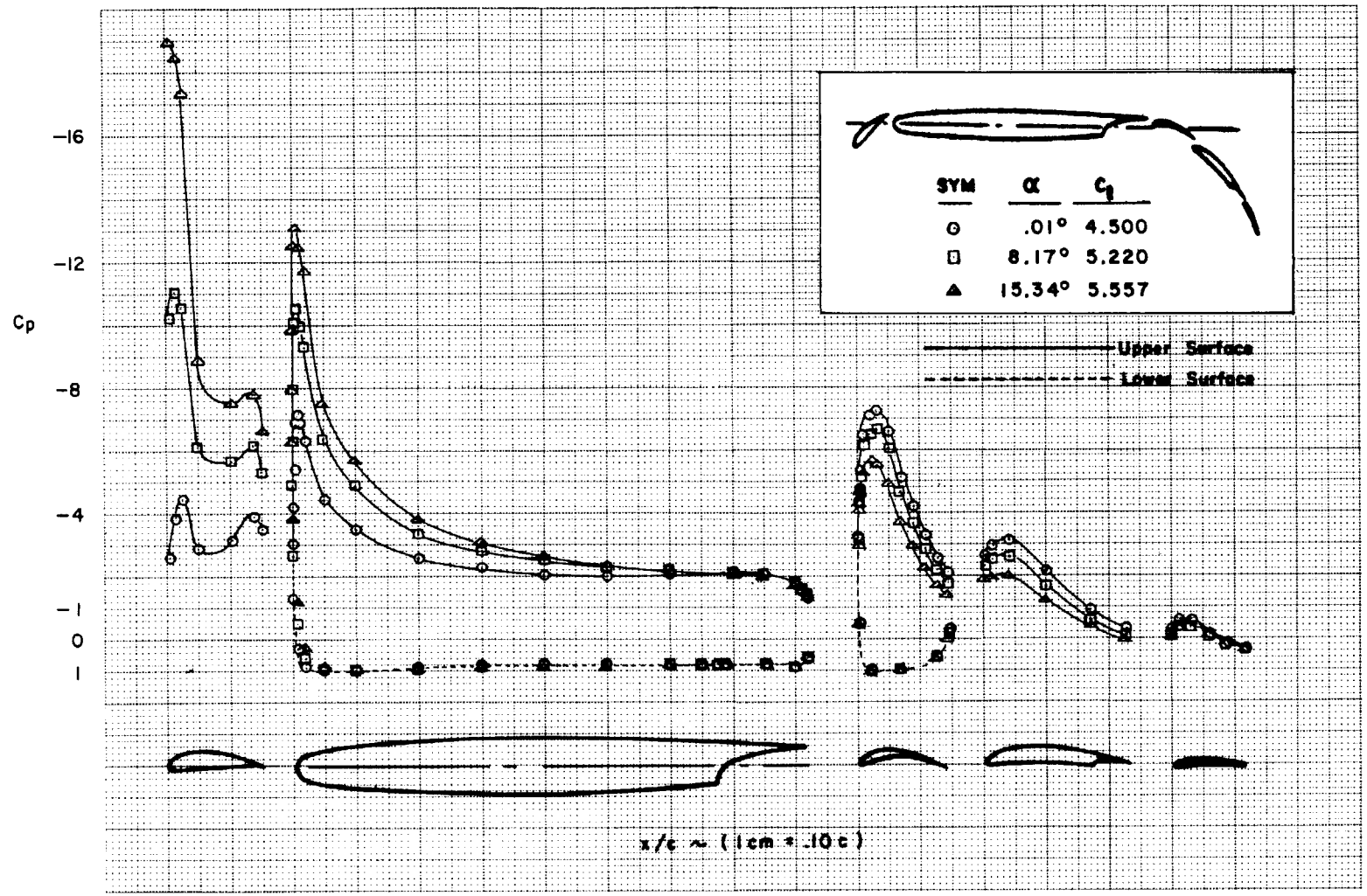

(a)

FIGURE C25.–EFFECT OF MAIN FLAP/AFT FLAP SLOT GAP AND OVERLAP–MODEL D ($\delta_{f_{eq}} = 46°$)

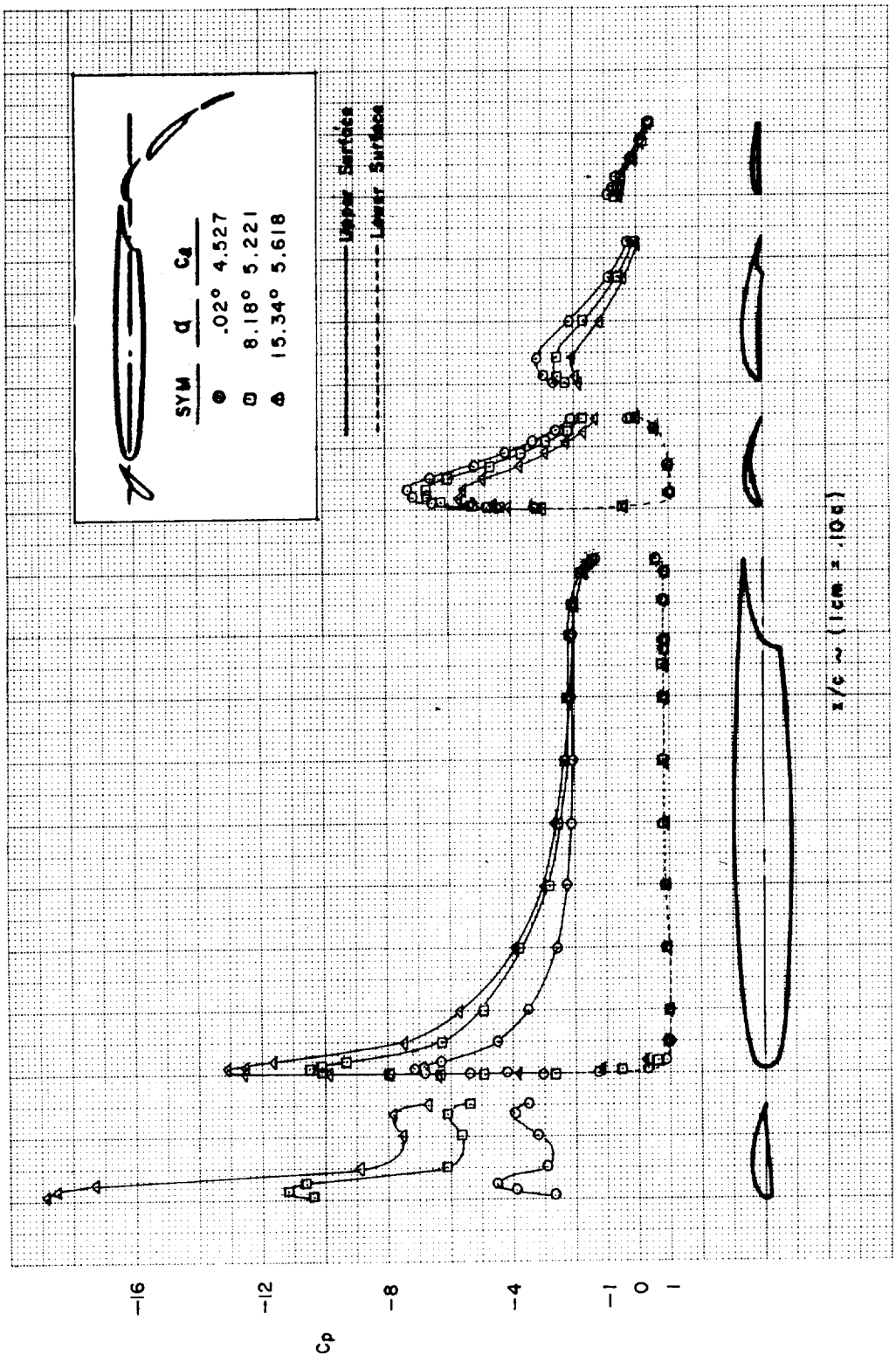

(b)

FIGURE C25.—Concluded

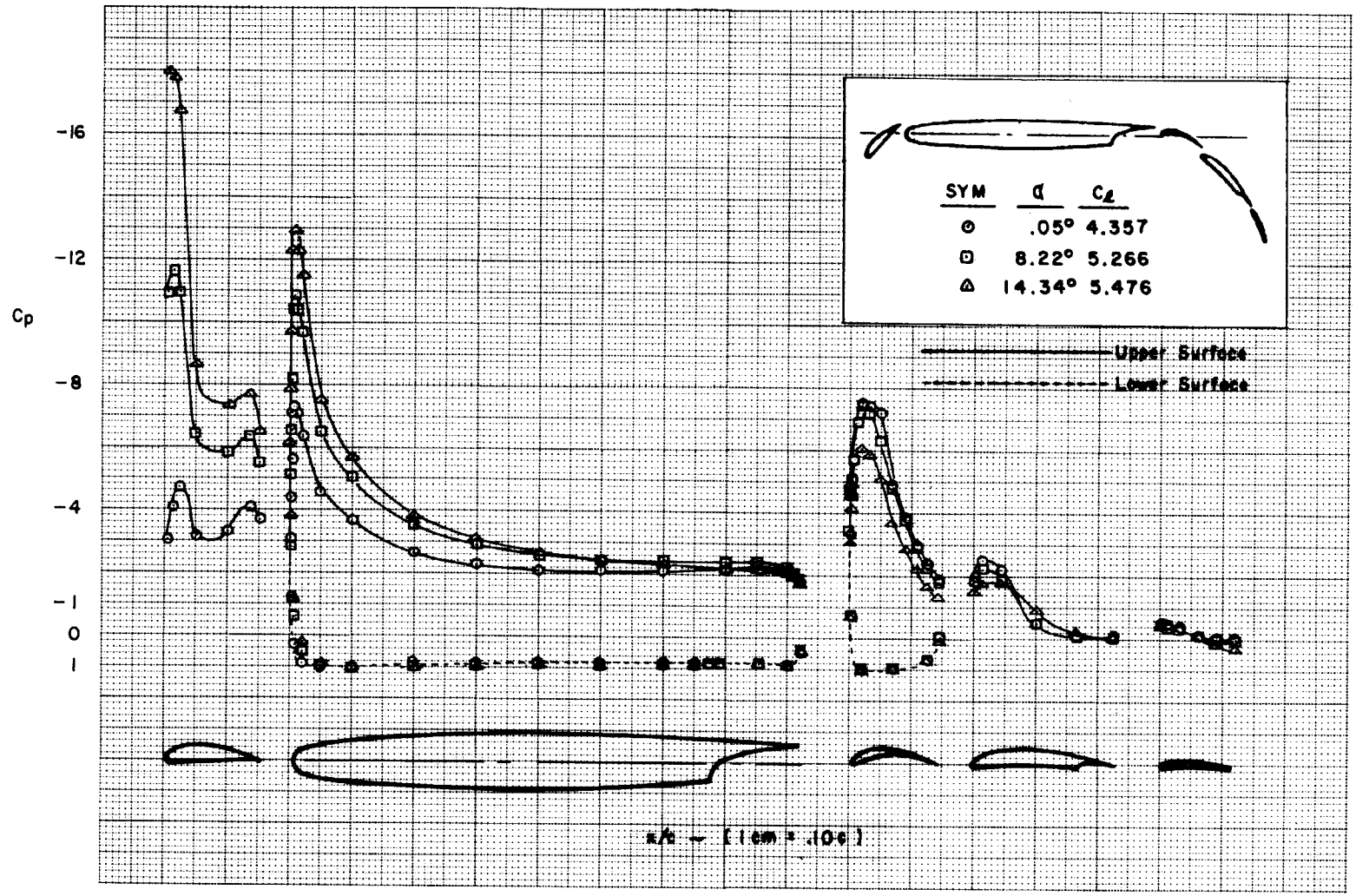

(a)

FIGURE C26.–EFFECT OF FLAP COMPONENT ANGLE COMBINATION AT CONSTANT $\delta_{f_{eq}}$ (53°)–MODEL D

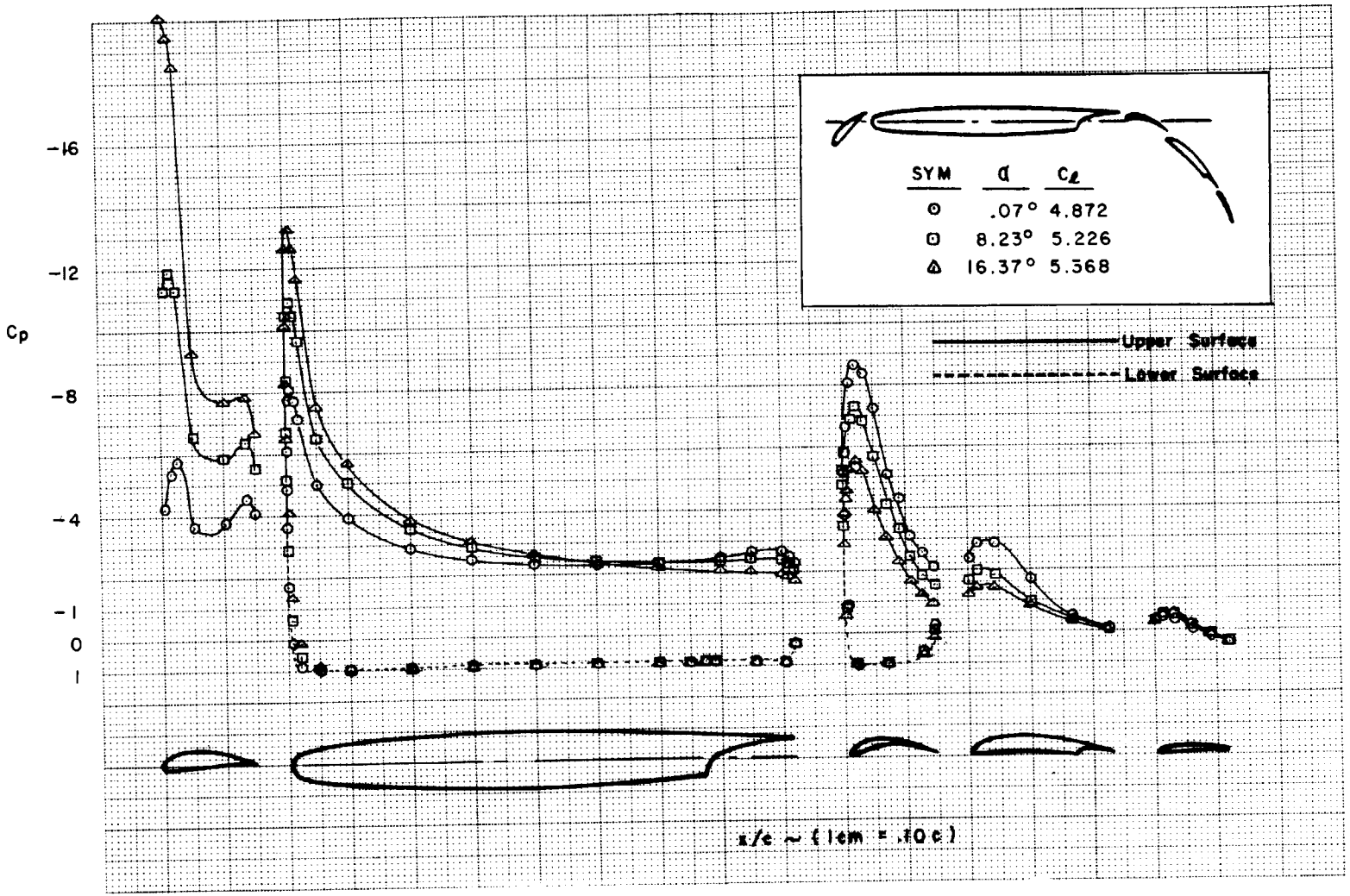

(b)

FIGURE C26.—Concluded

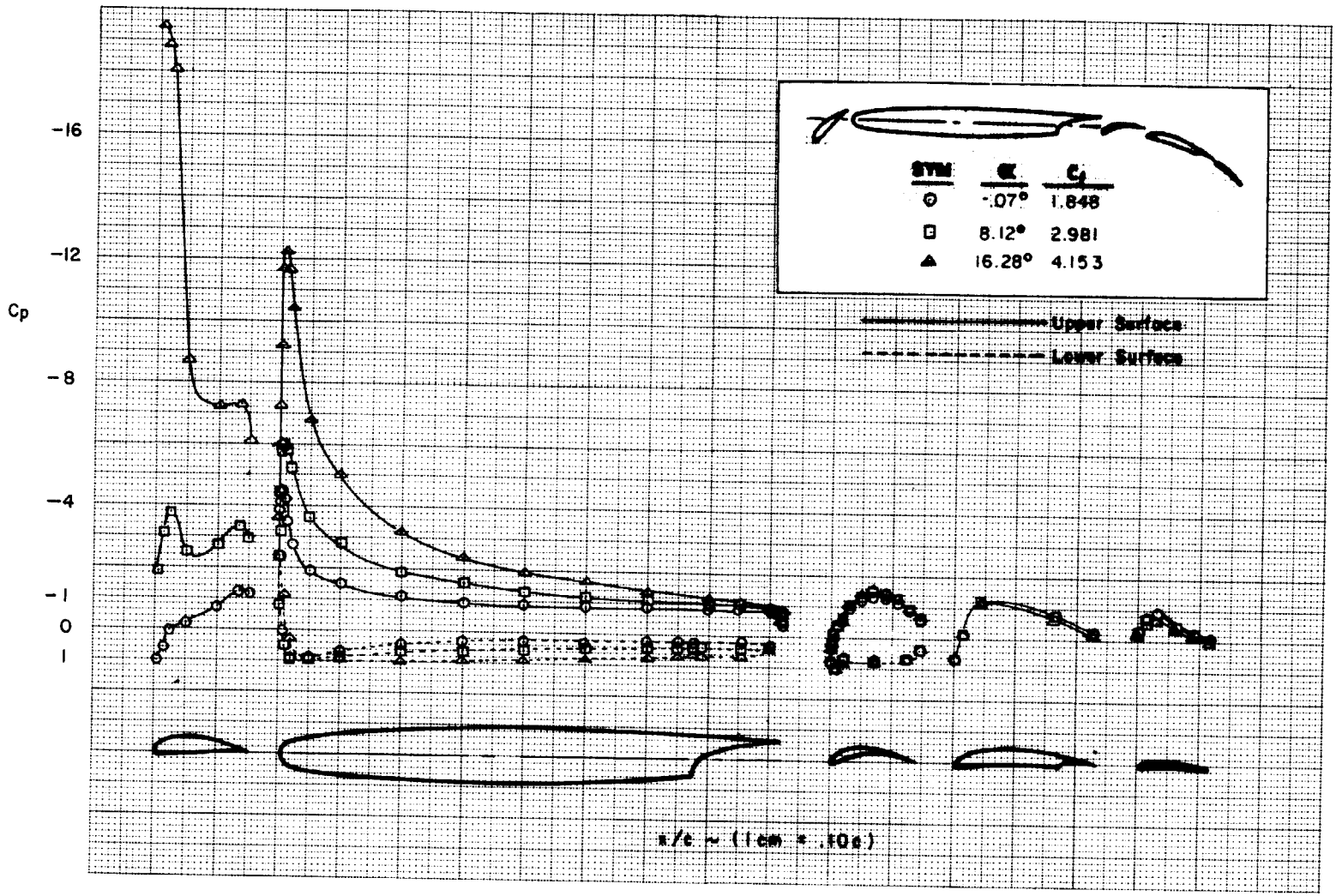

(a)

FIGURE C27.–EFFECT OF LEADING-EDGE DEVICE BRACKETS–MODEL D ($\delta_{f_{eq}} = 16°$)

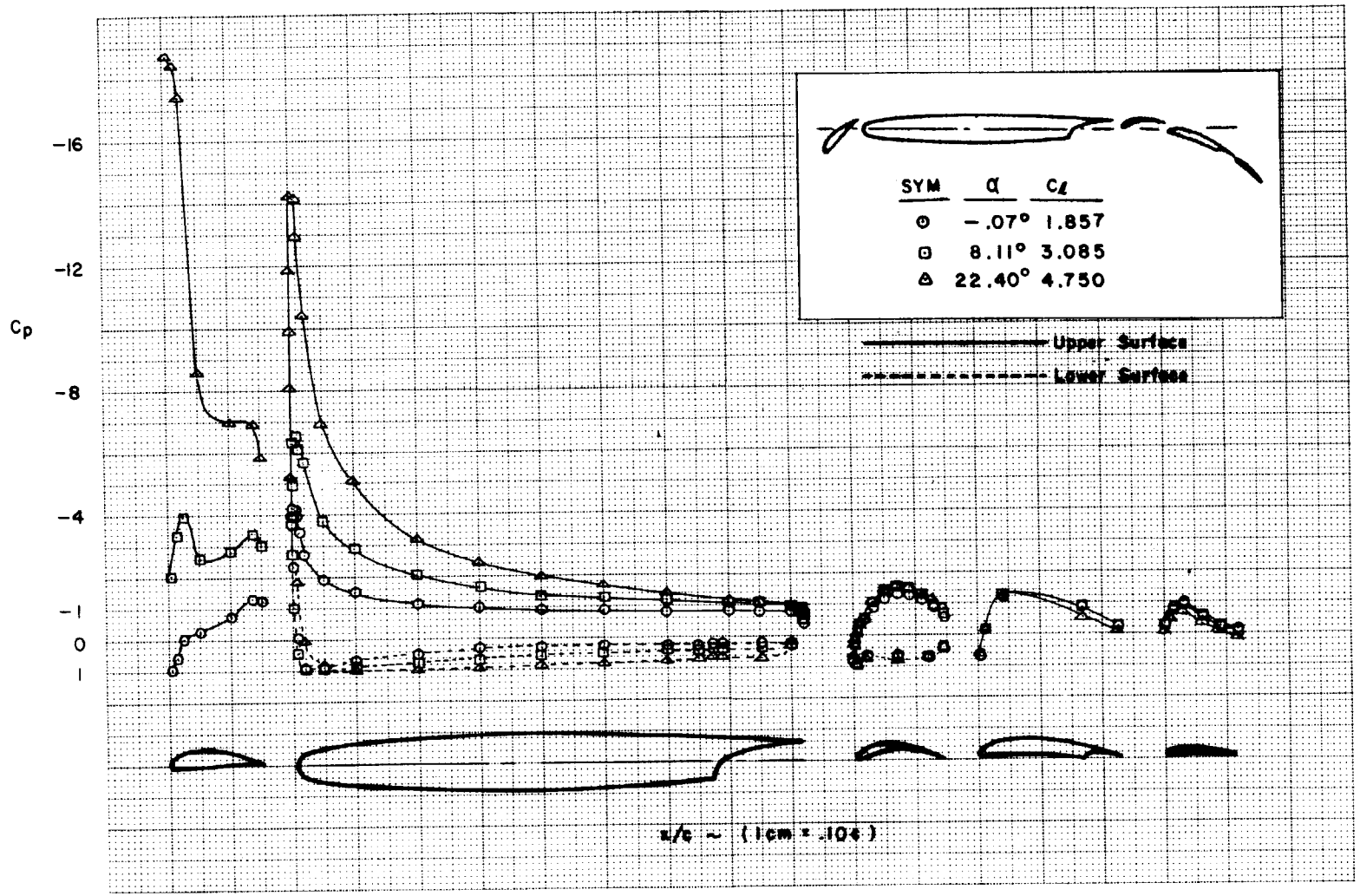

(b)

FIGURE C27.—Concluded

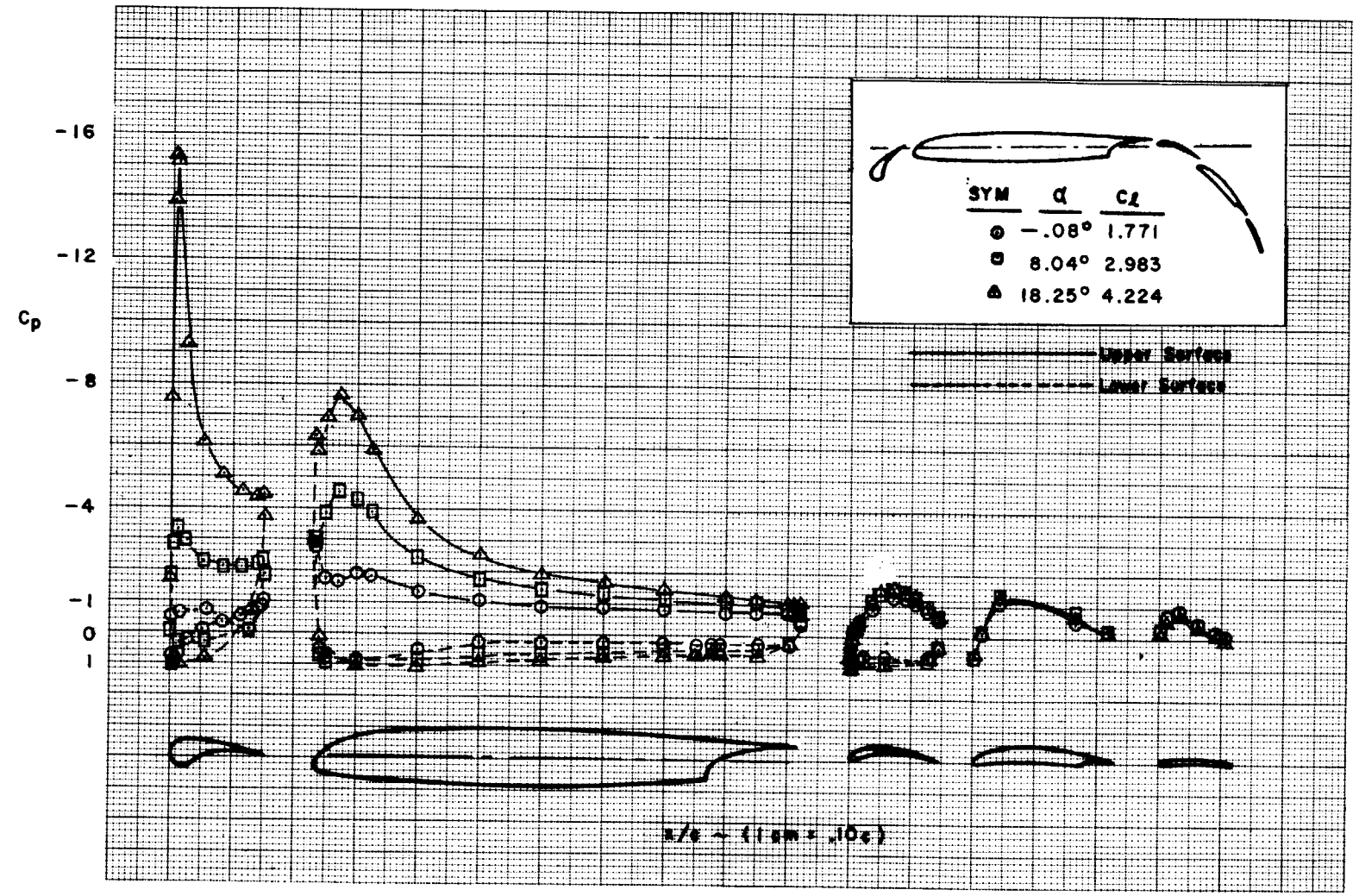

(a)

FIGURE C28.–EFFECT OF FLAP DEFLECTION ANGLE VARIATION WITH SLAT 1–MODEL D ($\delta_{f_{eq}} = 16°$)

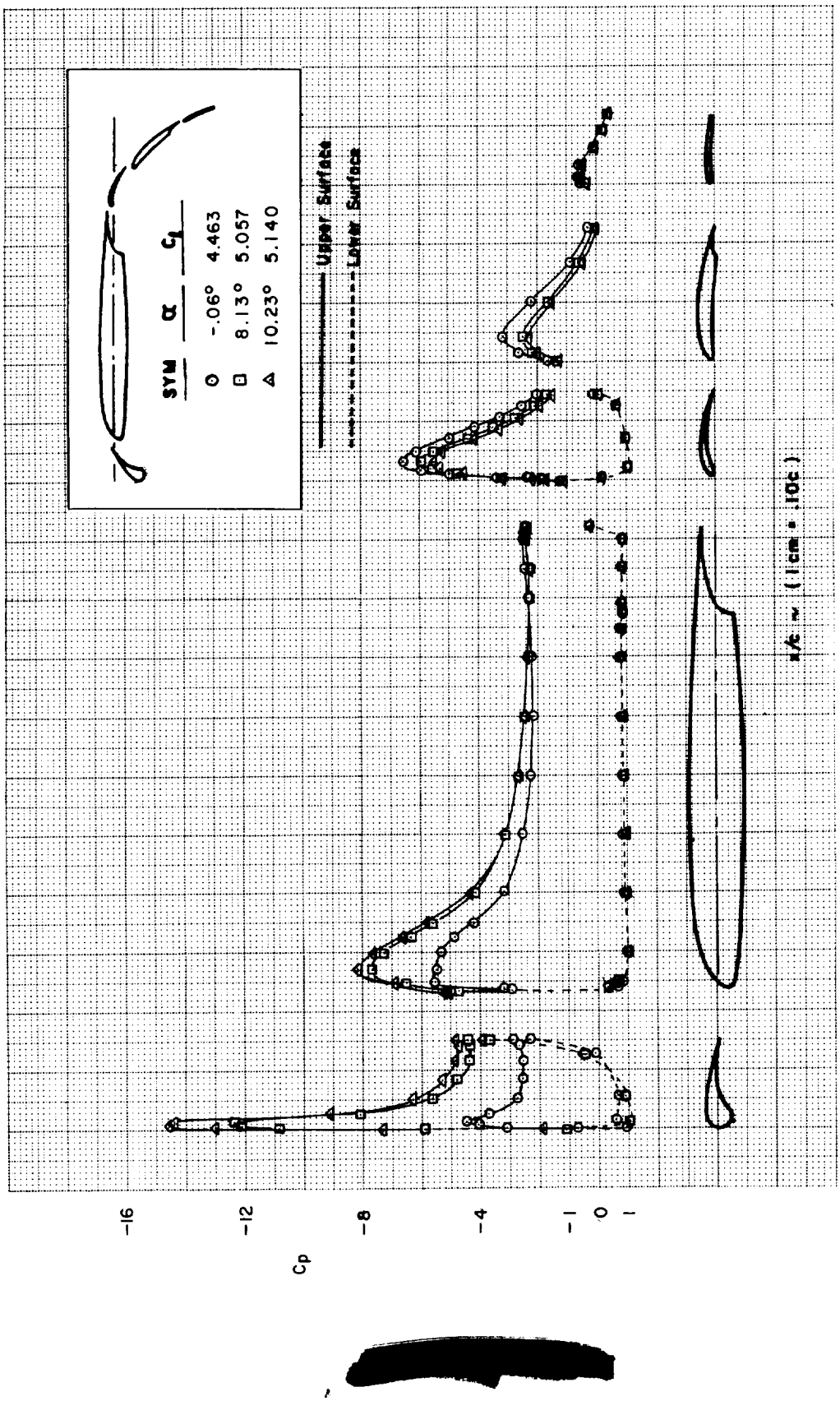

(b)

FIGURE C28.—Concluded

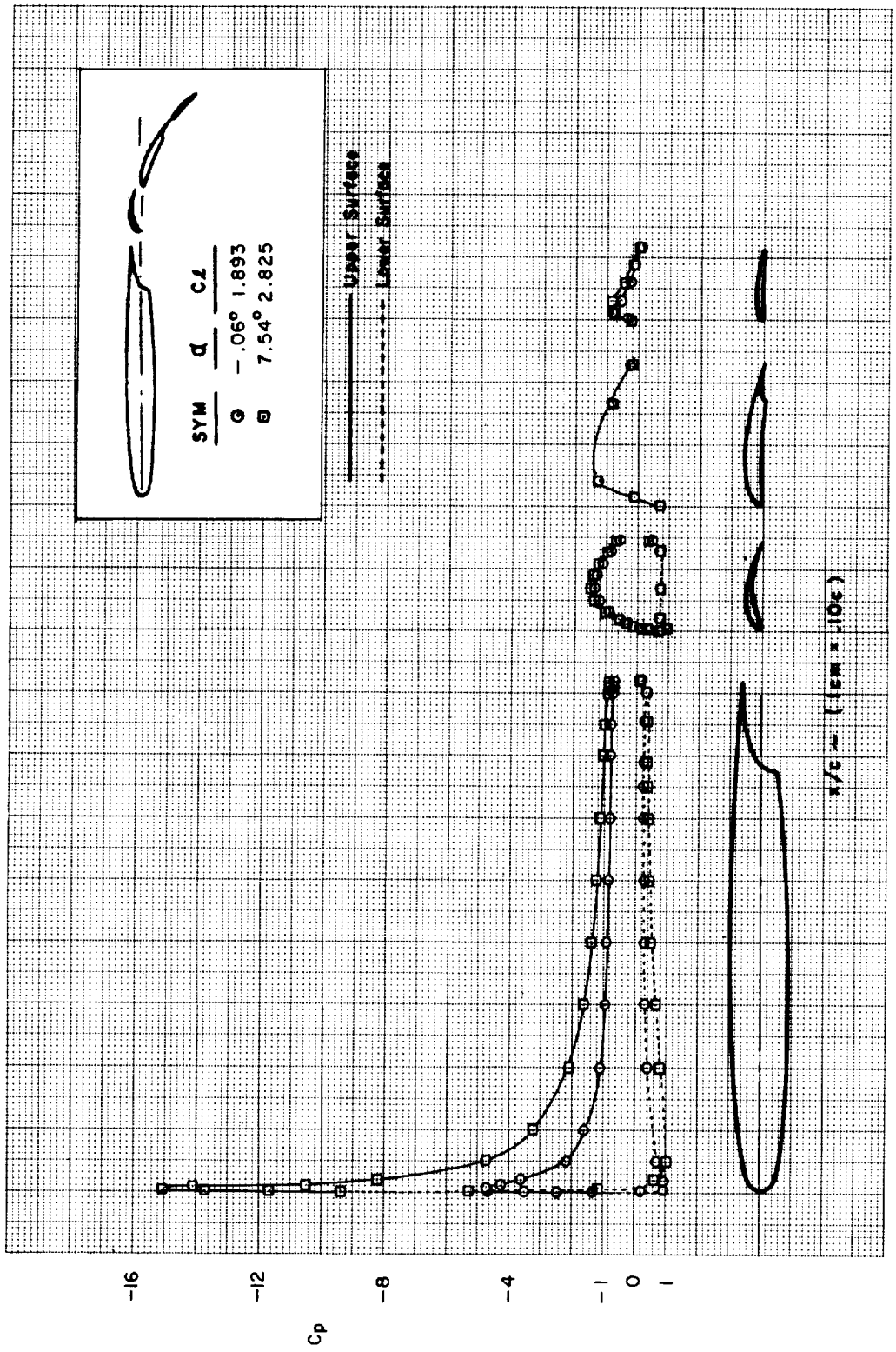

FIGURE C29.–EFFECT OF FLAP WITHOUT LEADING-EDGE DEVICE–MODEL D ($\delta_{f_{eq}}$ = 16°)

NASA-Langley, 1973 — 1 CR-2215